Wharton, Samuel James (2011) Susceptibility mapping in high field MRI. PhD thesis, University of Nottingham.

Access from the University of Nottingham repository:
http://eprints.nottingham.ac.uk/13074/1/555793.pdf

Copyright and reuse:

The Nottingham ePrints service makes this work by researchers of the University of Nottingham available open access under the following conditions.

- Copyright and all moral rights to the version of the paper presented here belong to the individual author(s) and/or other copyright owners.
- To the extent reasonable and practicable the material made available in Nottingham ePrints has been checked for eligibility before being made available.
- Copies of full items can be used for personal research or study, educational, or not-for-profit purposes without prior permission or charge provided that the authors, title and full bibliographic details are credited, a hyperlink and/or URL is given for the original metadata page and the content is not changed in any way.
- Quotations or similar reproductions must be sufficiently acknowledged.

Please see our full end user licence at:
http://eprints.nottingham.ac.uk/end_user_agreement.pdf

A note on versions:

The version presented here may differ from the published version or from the version of record. If you wish to cite this item you are advised to consult the publisher’s version. Please see the repository url above for details on accessing the published version and note that access may require a subscription.

For more information, please contact eprints@nottingham.ac.uk

The University of
Nottingham

School of Physics and Astronomy
Sir Peter Mansfield Magnetic Resonance Centre

Susceptibility Mapping in High Field MRI

by

Samuel Wharton

Thesis submitted to the University of Nottingham for
the degree of Doctor of Philosophy

August 2011

Contents

Abstract

Phase images of the human brain acquired using gradient echo based Magnetic Resonance Imaging techniques show excellent contrast at 7T. This contrast is attributed to small variations in magnetic susceptibility that perturb the main magnetic field and thus yield a spatial variation of the NMR frequency. The work described in this thesis is primarily concerned with mapping the distribution of magnetic susceptibility within the human brain using these phase images. The main technical challenges of the project were first to extract accurate field maps based on phase data, and then to solve the ill-posed problem of inverting these field maps to reconstruct susceptibility (χ) maps.

In initial work, simulations of field shifts based on known χ -distributions are compared to field maps acquired *in vivo* to highlight the non-local relationship between measured field offsets and the underlying susceptibility. These simulations were carried out using a recently derived Fourier method.

The bulk of the thesis is then devoted to a detailed study of the process of inverting field maps generated from phase data using the Fourier relationship to yield quantitative 3D χ-maps. Unfortunately, the inversion problem is ill-posed and requires careful conditioning, either through rotation of the sample being imaged or through regularisation. A simple *k*-space threshold is introduced to condition the inversion and the preliminary results of applying this method to brain data from healthy subjects and patients with Parkinson's disease and multiple sclerosis are presented. The results suggest that susceptibility mapping is sensitive to iron deposition and could be a useful tool in investigating the progression of neurodegenerative diseases.

Iterative inversion algorithms, which deal with noise more robustly and allow more sophisticated filtering techniques to be employed, are then presented. These powerful regularisation methods are compared to previously described techniques, and are shown to yield high quality whole-brain χ-maps.

Acknowledgments

I would like to thank my supervisor, Prof. Richard Bowtell, for his guidance and encouragement over the course of my PhD. I would also like to thank my co-supervisor, Prof. Penny Gowland, and all the staff at the SPMMRC in Nottingham.

A special thank you goes to my parents, whose support enabled me to start this work, and to Liz, who inspired me to complete it.

Collaborations

Much of the work described in this thesis involved collaborations with other scientists. The work described in Chapter 4 contained contributions from Dr Andreas Schäfer and formed the basis of a paper published in 2009 (see below) on which I and Dr Schäfer shared first author. The data listed in Chapter 6 for the Parkinson's disease study was acquired and analysed by Dr Ashley Lotfipour and formed the basis of a submitted paper, currently in press, on which I am second author. The data listed in Chapter 6 for the Multiple Sclerosis study was acquired and analysed by Dr Ali Al-radaideh and formed the basis of a submitted paper, currently in press, on which I am also second author.

Publications

Publications connected to work contained in this thesis are listed below.

Schäfer A, **Wharton S**, Gowland P, and Bowtell R, *Using magnetic field simulation to study susceptibility-related phase contrast in gradient echo MRI.* Neuroimage, 2009. 48(1): p. 126-137.

Al-radaideh A, **Wharton S**, Bowtell R, Gowland P, *High Resolution Magnetic Susceptibility mapping in deep grey matter structures in clinically isolated syndromes suggestive of MS at 7T MRI.* Radiology, (In Press).

Lotfipour A, **Wharton S**, Schwarz S, Gontu V, Schäfer A, Peters A, Bowtell R, Auer D, Gowland P, Bajaj N. *High Resolution Magnetic Susceptibility Mapping of the Substantia Nigra in Parkinson's Disease.* JMRI, (In Press).

Wharton S, Schäfer A, Bowtell R. *Susceptibility Mapping in the Human Brain using threshold based k-space division.* Magn Reson Med, 2010. 63:1292-1304

Wharton S, Bowtell R. *Whole Brain Susceptibility Mapping at High Field: A Comparison of Multiple and Single Orientation Methods.* Neuroimage, 2010. doi:10.1016/j.neuroimage.2010.06.070

CHAPTER 1

INTRODUCTION

1.1 Introduction

The work described in this thesis was carried out at the Sir Peter Mansfield Magnetic Resonance Centre at the University of Nottingham and began in September 2007. At ultra-high field strengths, gradient echo-based phase images of the brain exhibit excellent contrast due to differences in magnetic susceptibility across tissues. The focus of this work was to investigate this relatively new contrast mechanism using the 7T system at Nottingham, and eventually to form maps of susceptibility differences within the brain. The early stages of the project involved the development and optimisation of a threshold-based inversion technique for mapping susceptibility. The later stages were centred on the application of this technique, and the development of more sophisticated iterative methods for calculating susceptibility maps from phase images. Over the course of this project, the field of susceptibility mapping has become an important area of research, with several groups around the world committed to exploiting this rich source of quantitative information.

1.2 History of MRI

The phenomenon of Nuclear Magnetic Resonance (NMR) was first observed in 1946 by Purcell [1] and Bloch [2], who in separate experiments measured weak radiofrequency signals from atomic nuclei precessing in a magnetic field. Bloch and Purcell shared the Nobel prize in physics in 1952 for this work.

The birth of Magnetic Resonance Imaging (MRI) came in 1973 with the work of Mansfield [3] and Lauterbur [4]. At the time it was already well-known that the spins of protons would precess at the Larmor frequency in the presence of a magnetic field. Mansfield and Lauterbur proposed that a spatially varying magnetic field would yield a spatial variation of the Larmor frequency. They showed that separating and measuring the different frequency components could yield spatial information about the distribution of hydrogen nuclei within a sample. In 2003, Peter Mansfield and Paul Lauterbur were jointly awarded the Nobel prize for medicine for their discoveries concerning magnetic resonance imaging.

1.3 Thesis Overview

Chapter 2 describes the background theory of MRI. The key concepts of nuclear spin and its interaction with electromagnetic radiation are discussed, along with an introduction to the 3D gradient echo imaging technique used extensively in the work described in this thesis.

Chapter 3 contains theory specific to phase imaging. The non-local relationship between field measurements extracted from phase images and the underlying susceptibility distribution is described in detail. The derivation of a recently developed Fourier method for rapidly simulating field perturbations based on a susceptibility distribution with an arbitrary geometry is detailed. This is followed by a validation of the Fourier method based on susceptibility distributions with simple geometries and known analytical solutions.

In Chapter 4, the steps involved in creating field maps from phase data are outlined. The techniques for removing phase artefacts, such as discrete wraps and unwanted background fields, are described in detail. This is followed by a description of the results of simulation experiments utilising the Fourier method to simulate field shifts due to digitised models of the brain and deep grey matter structures. The results of these simulations are then compared to phase images acquired *in vivo* at 7 T. Through this comparison it is shown that susceptibility distributions with relatively simple geometries can create complex field maps.

The Fourier relationship between field and susceptibility can be inverted to allow reconstruction of susceptibility maps from phase data with appropriate conditioning. In Chapter 5, an inversion method incorporating a simple *k*-space threshold is presented. A novel filtering technique for removing unwanted background fields is also presented. This inversion method is applied to data acquired from a special phantom and is also used to analyze *in vivo* data. The advantages of measuring field data at multiple orientations to the main field are also investigated.

The preliminary results of applying the threshold based approach in clinical applications are presented in Chapter 6. As part of this work, software was developed to enable investigators with no specialist knowledge of susceptibility mapping to apply the threshold method to *in vivo* data from patients with multiple-sclerosis and Parkinson's disease. The results showed increased levels of iron in the deep grey matter structures of patients with these neurodegenerative diseases.

In Chapter 7, a new type of inversion method based on an iterative approach is introduced. Recently developed iterative techniques for creating susceptibility maps from phase data acquired at single- and multiple-orientations are described. These techniques, along with the threshold-based method, are then optimised for creating high quality, whole-brain, susceptibility maps based on phase and modulus data acquired at 7T. The resulting susceptibility maps are then compared in order to investigate the strengths and weakness of each technique.

The main outcomes and results of this thesis are summarised in Chapter 8. Possible future work on susceptibility mapping is also suggested. Finally, recently proposed phase contrast mechanisms that could lead to new areas of research are described.

1.4 References

1. Purcell, E.M., H.C. Torrey, and R.V. Pound, *Resonance Absorption by Nuclear Magnetic Moments in a Solid.* Physical Review, 1946. **69**(1-2): p. 37.
2. Bloch, F., *Nuclear Induction.* Physical Review, 1946. **70**(7-8): p. 460.
3. Mansfield, P. and P.K. Grannell, *NMR 'diffraction' in solids?* Journal of Physics C: Solid State Physics, 1973. **6**: p. L422.

4. Lauterbur, P.C., *Image formation by induced local interactions: Examples employing NMR.* Nature, 1973. **242**: p. 190.

CHAPTER 2

Nuclear Magnetic Resonance and Magnetic Resonance Imaging Theory

The theory of NMR is outlined in the first part of this chapter. Particular emphasis is placed on the ^1H nucleus due to its importance in MRI. The second section of the chapter describes the basic theory of MRI and includes a description of the imaging techniques relevant to this work.

2.1 Nuclear Magnetic Resonance

Nuclear Magnetic Resonance (NMR) describes the resonant behaviour of certain nuclei when placed in a magnetic field.

nucleus	spin	natural abundance	magnetogyric ratio γ/rad s^{-1} T^{-1}
^1H	1/2	~100%	267.522×10^6
^{12}C	0	98.9%	-
^{13}C	1/2	1.1%	67.283×10^6
^{14}N	1	99.6%	19.338×10^6
^{17}O	5/2	0.04%	-36.281×10^6
^{31}P	1/2	~100%	108.394×10^6

***Table 2.1** List of six atomic nuclei and their properties [1].*

2.1.1 Nuclear Spin and energy levels

Spin is a physical property associated with atomic nuclei. Like other properties of the nucleus, such as mass and electrical charge, spin is linked to the number of protons and neutrons inside the nucleus. Specifically, spin is related to the total angular momentum of a nucleus and is characterised using the spin quantum number, I. Both protons and neutrons have spin $I = 1/2$. The low energy state, or *ground* state, of a certain nucleus can either have half integer spin, $I = 1/2, 3/2, 5/2$...etc, or integer spin, $I = 0, 1, 2, 3$...etc. The nuclear spin for a number of different nuclei is listed in Table 2.1. The total angular momentum, $|\mathbf{p}|$, of a nucleus is quantised and related to the spin by

$$|\mathbf{p}| = \hbar\sqrt{I(I+1)} \qquad \text{Eq. 2.1}$$

where $\hbar = 1.054 \times 10^{-34}$ is Planck's constant divided by 2π. The measurable z-component of the angular momentum, p_z, is given by

$$p_z = \hbar m_z \qquad \text{Eq. 2.2}$$

where m_z is a quantum number that may take values $-I, -I + 1, ..., I$. The ^{1}H nucleus, consisting of a single proton, has spin $I = 1/2$ (see Table 2.1) and has two possible m_z values, $m_z = 1/2$ and $m_z = -1/2$. As a proton has a positive charge the ^{1}H nucleus also has an associated magnetic dipole moment parallel to $\mathbf{p}$ given by

$$\boldsymbol{\mu} = \gamma\mathbf{p} \qquad \text{Eq. 2.3}$$

where γ is the nucleus-specific gyromagnetic ratio (see Table 2.1) taking a value of $\gamma = 267.522 \times 10^6$ rad s^{-1} T^{-1} for ^{1}H. The z-component of the magnetic dipole moment is given by

$$\mu_z = \gamma p_z = \gamma\hbar m_z \quad . \qquad \text{Eq. 2.4}$$

In a magnetic field, B_0, the spin of a ^{1}H nucleus will tend to line up with the field, taking one of two possible states: firstly parallel to the direction of B_0 known as the 'up' state or $|\alpha\rangle$ state where $m_z = 1/2$, and secondly anti-parallel to the direction of B_0

known as the 'down' state or $|\beta\rangle$ state where m_z = -1/2. The energy of each state is given by

$$E = -\mu_z B_0 = -\gamma\hbar m_z B_0 \quad . \qquad \text{Eq. 2.5}$$

The energy difference between the two states is given by

$$\Delta E = \gamma\hbar B_0 \quad . \qquad \text{Eq. 2.6}$$

Applying electromagnetic waves at the correct frequency will induce transitions between the two states. The necessary frequency is called the Larmor frequency, ω_0, and is given by

$$\omega_0 = \gamma B_0 \quad . \qquad \text{Eq. 2.7}$$

For ^{1}H in the presence of a 7 Tesla (T) magnetic field ω_L = 298 MHz. This is in the radiofrequency (RF) range.

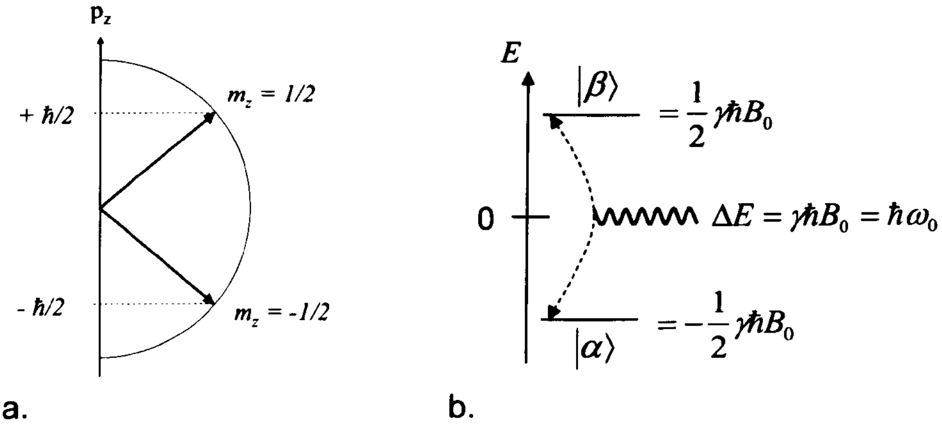

***Figure 2.1** (a) Illustration of z-component of quantised angular momentum, (b) illustration of energy levels for the two spin states of a ^{1}H nucleus.*

Transitions between states will only occur if RF photons at the Larmor frequency are applied. This resonance condition gives rise to the term nuclear magnetic resonance. Figure 2.1 shows an illustration of the discrete nature of the angular momentum and energy levels associated with a ^{1}H-nucleus.

Using a more classical approach, the time dependence of the nuclear magnetic moment in the presence of a magnetic field can be better characterised using

$$\frac{d}{dt}\boldsymbol{\mu} = \gamma\boldsymbol{\mu}\times\mathbf{B} \quad . \qquad \text{Eq. 2.8}$$

This expression means that the rate of change of **μ** is perpendicular to both **μ** and **B**. Assuming the direction of **B** is along the z-axis, $\mathbf{B} = B_z\mathbf{k}$, the solutions of Eq. 2.8 are given by

$$\begin{aligned} \mu_x(t) &= \mu_x(0)\cos(\gamma B_z t) + \mu_y(0)\sin(\gamma B_z t) \\ \mu_y(t) &= -\mu_x(0)\sin(\gamma B_z t) + \mu_y(0)\cos(\gamma B_z t) \\ \mu_z(t) &= \mu_z(0) \end{aligned} \quad . \qquad \text{Eq. 2.9}$$

The motion described by Eq. 2.9 is termed precession. The tip of the magnetic moment vector will follow a clockwise circular path, assuming $\gamma > 0$, around B_z at an angular frequency equal to the Larmor frequency (Eq. 2.7). This motion is illustrated in Figure 2.2.

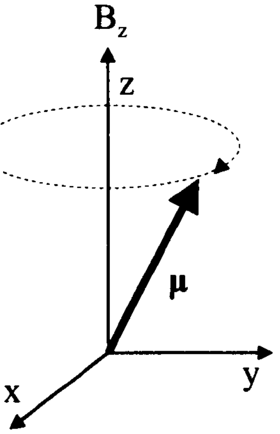

Figure 2.2 Illustration of the precession of the magnetic moment around a static magnetic field.

2.1.2 Bulk Magnetisation

In any sample of a reasonable size there is likely to be a large number of nuclei, and considering each spin separately is not a realistic option. The NMR properties of materials can instead be described by looking at a group of spins, known as a spin ensemble. In the presence of a static magnetic field, B_0, the sample will become magnetised. This induced bulk magnetisation is in the direction of the magnetic field and is due to differences in the populations of spin states. The populations of spin states can be determined via Boltzmann statistics given by

$$\frac{N^-}{N^+} = \exp\left(-\frac{\Delta E}{kT}\right) \qquad \text{Eq. 2.10}$$

where N^- is the number of nuclei in the high energy 'down'-state, N^+ is the number of nuclei in the low energy 'up'-state, ΔE is the energy difference between the states, $k = 1.38\times10^{-23}$ JK^{-1} is Boltzmann's constant, and T is the temperature of the system. In normal conditions the difference in the populations of the two states will usually be very small. For a sample of ^{1}H nuclei at room temperature in the presence of a 7 T magnetic field there will be ~1,000,048 nuclei in the low energy state for every

1,000,000 in the high energy state. This population difference gives rise to a small bulk magnetisation, **M**, orientated along the magnetic field as shown in figure 2.3.

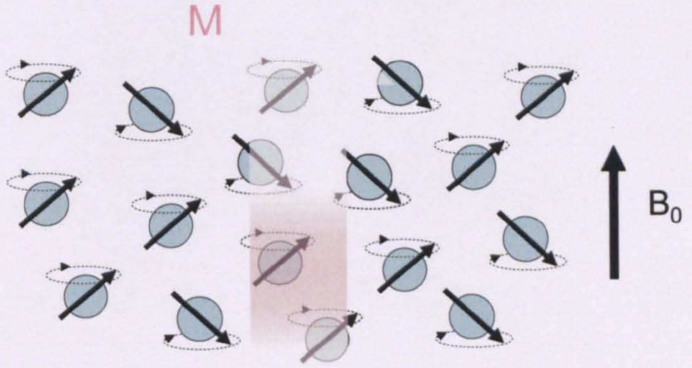

***Figure 2.3** Illustration of spin ensemble showing bulk magnetisation in the presence of a magnetic field, B_0. The magnetisation is due to the presence of slightly more 'up' spins than 'down' spins.*

Although the population difference is small there are Avogadro numbers (6×10^{23}) of spins per unit volume of sample. Assuming a spin density, ρ_0, the magnetisation induced is proportional to

$$|\mathbf{M}| \propto \rho_0 \Delta E \propto \rho_0 B_0 \qquad \text{Eq. 2.11}$$

where ΔE is the energy difference between the states. The dependence of the bulk magnetisation on B_0 is one reason for using powerful magnets when performing NMR and MRI experiments. The bulk magnetisation obeys the same classical equation of motion as the single magnetic moment described above (Eq.2.8) which is written as

$$\frac{d\mathbf{M}}{dt} = \gamma\, \mathbf{M} \times \mathbf{B} \qquad . \qquad \text{Eq. 2.12}$$

The induced magnetisation due to a static field is also referred to as the equilibrium magnetisation, $\mathbf{M}_0$.

2.1.3 Interaction of Magnetisation with Radio-Frequency Pulses

As described in section 2.1.1, RF fields oscillating at the Larmor frequency can be used to induce transitions between spin states. By changing coordinate systems, the effect of RF fields on the equilibrium magnetisation can be further investigated. Adopting a frame of reference rotating around the *z*-axis at the Larmor frequency yields a coordinate system given by

$$\begin{aligned} \hat{\mathbf{x}}' &= \hat{\mathbf{x}} \cos \omega_0 t - \hat{\mathbf{y}} \sin \omega_0 t \\ \hat{\mathbf{y}}' &= \hat{\mathbf{x}} \sin \omega_0 t + \hat{\mathbf{y}} \cos \omega_0 t \\ \hat{\mathbf{z}}' &= \hat{\mathbf{z}} \end{aligned} \quad . \qquad \text{Eq. 2.13}$$

In this rotating reference frame the spins no longer precess around $\hat{\mathbf{z}}$, but instead appear stationary. A quadrature, or 'left-circularly polarised', RF field is created by the superposition of two linearly polarised RF fields which have the same frequency and amplitude, but are perpendicular to each other and 90° out of phase. If the frequency is set to ω_0 the quadrature field is given by

$$B_1^{cir} = B_1 \left(\hat{\mathbf{x}} \cos \omega_0 t - \hat{\mathbf{y}} \sin \omega_0 t \right) \quad . \qquad \text{Eq. 2.14}$$

In the rotating reference frame this simplifies to

$$B_1^{cir} = B_1 \hat{\mathbf{x}}' \quad . \qquad \text{Eq. 2.15}$$

The evolution of the magnetisation, in the rotating reference frame, on the application of B_1^{cir}, assuming the RF field is applied for a short time, is described by

$$\frac{d\mathbf{M}'}{dt} = \gamma \mathbf{M}' \times B_1 \hat{\mathbf{x}}' \qquad \text{Eq. 2.16}$$

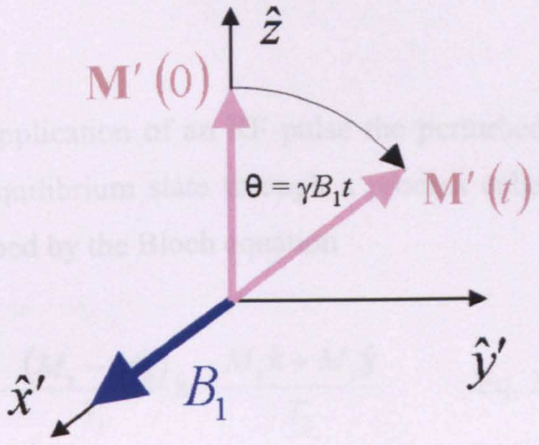

Figure 2.4 Illustration of the rotation of equilibrium magnetisation caused by the application of a quadrature RF field in the rotating reference frame.

and the solutions of Eq.2.15 are given by

$$\begin{aligned} M_{x'}(t) &= M_{x'}(0) \\ M_{y'}(t) &= M_{y'}(0)\cos\omega_1 t + M_{z'}(0)\sin\omega_1 t \\ M_{z'}(t) &= -M_{y'}(0)\sin\omega_1 t + M_{z'}(0)\cos\omega_1 t \end{aligned} \qquad \text{Eq. 2.17}$$

where $\omega_1 = \gamma B_1$. This motion, illustrated in Figure 2.4, is a rotation of $\mathbf{M}_0$ around $\hat{\mathbf{x}}'$ where the angle of rotation is defined by the amplitude of the RF field, B_1, and the duration of time, t, over which the field is applied. If viewed in a stationary frame of reference, this rotation would be visualised as a spiralling motion referred to as nutation. A special case is when an RF field is applied to a magnetised sample with sufficient power, and for a sufficient duration of time, to rotate the magnetisation into the transverse, x-y, plane. This is referred to as a '90°-pulse' or 'π/2-pulse'. In general, the angle through which the magnetisation is rotated is referred to as the 'flip-angle'.

2.1.4 Relaxation

Immediately after the application of an RF pulse the perturbed magnetisation will begin to return to its equilibrium state through a process called 'relaxation'. This relaxation can be described by the Bloch equation

$$\frac{d\mathbf{M}}{dt}=\gamma(\mathbf{M}\times\mathbf{B})-\frac{(M_z-M_0)}{T_1}\hat{\mathbf{z}}-\frac{M_x\hat{\mathbf{x}}+M_y\hat{\mathbf{y}}}{T_2} \qquad \text{Eq. 2.18}$$

where M_z is the z-component of the magnetisation which is also referred to as the 'longitudinal' magnetisation, M_x and M_y are the x- and y-components of the magnetisation which are also referred to as the 'transverse' magnetisation, T_1 is the spin-lattice relaxation constant which governs the recovery of the longitudinal magnetisation, T_2 is the spin-spin relaxation time that governs the decay of the transverse magnetisation. The solutions of Eq.2.17 are

$$\begin{aligned}
M_x(t)&=\exp\left(\frac{-t}{T_2}\right)\cdot\left(M_x(0)\cos\omega_0 t+M_y(0)\sin\omega_0 t\right)\\
M_y(t)&=\exp\left(\frac{-t}{T_2}\right)\cdot\left(M_y(0)\cos\omega_0 t-M_x(0)\sin\omega_0 t\right) \qquad \text{Eq. 2.19}\\
M_z(t)&=\exp\left(\frac{-t}{T_1}\right)M_z(0)+M_0\left(1-\exp\left(\frac{-t}{T_1}\right)\right)
\end{aligned}$$

.

Table 2.2 shows approximate values for T_1 and T_2 in brain tissues at 7 T. As the table shows, T_1 is generally considerably longer than T_2. Figure 2.5 shows the simulated evolution of the magnetisation, based on the solutions in Eq. 2.18, directly after a 90° RF pulse such that $M_z(0) = 0$, $M_y(0) = 0$, $M_x(0) = 1$, and setting the relaxation constants of T_1 and T_2 to 250ms and 60ms respectively. To make Fig.2.5 more easily interpretable the frequency of precession has been slowed down from $\omega_0 = 300$ MHz (^{1}H at 7 T) to $\omega_0 = 50$ Hz.

Tissue	T_1 (ms)	T_2 (ms)
grey matter	2000	60
white matter	1200	40

***Table 2.2* List of brain tissues and associated approximate T_1 and T_2 values at 7 T [22].**

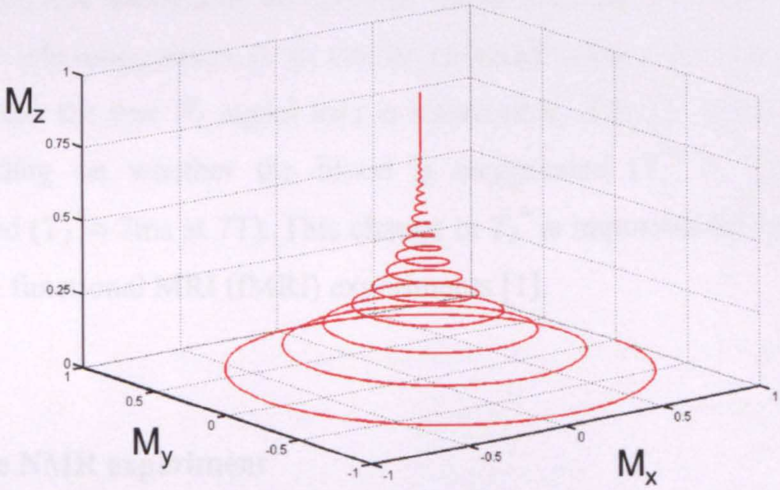

***Figure 2.5* Simulation of the evolution of magnetisation after 90^o pulse.**

The relaxation of spins is driven by dipole-dipole interactions. Each nucleus and its local molecular environment have associated dipolar magnetic fields. Thermal energy causes these dipoles to fluctuate causing small, time-dependent, changes in the direction, and magnitude, of the magnetic field, B_0, experienced by each nucleus. For the longitudinal relaxation, characterised by T_1, the energetic favourability of spin orientations parallel to B_0 (see Eq.2.5-6) drives the growth of longitudinal magnetisation to the equilibrium value. For the transverse relaxation, characterised by T_2, the dipolar fluctuations produce a distribution of precessions frequencies. This distribution of precession frequencies leads to spin dephasing, driving the decay of transverse magnetisation. In reality the transverse magnetisation relaxes at a quicker rate than predicted by pure T_2 relaxation alone. To describe the decay of transverse magnetisation, a composite relaxation constant, T_2^*, must be incorporated. This can be written as

$$\frac{1}{T_2^*} = \frac{1}{T_2} + \frac{1}{T_2'} \qquad \text{Eq. 2.20}$$

where the T_2' relaxation constant arises due to static inhomogeneities in B_0. These inhomogeneities can be caused by magnetic susceptibility differences, and result in a spatial variation of the Larmor frequency. This frequency variation leads to increased spin dephasing that accelerates the decay of transverse magnetisation. The dephasing due to static inhomogeneities in B_0 can be reversed using a spin echo (see Section 2.1.5); whereas the true T_2 signal loss is irreversible. The T_2^* values of blood can vary depending on whether the blood is oxygenated ($T_2^* \approx$ 15ms at 7T) or deoxygenated ($T_2^* \approx$ 7ms at 7T). This change in T_2^* is important for measuring brain activation in functional MRI (fMRI) experiments [1].

2.1.5 Simple NMR experiment

The precessing and decaying transverse magnetisation, occurring after a 90° pulse, can be used to produce a measurable NMR signal. The *emf* produced in a coil by a change in magnetic flux can be calculated using Faraday's Law of induction

$$emf = -\frac{d}{dt}\Phi_M(t) \quad , \qquad \text{Eq. 2.21}$$

where Φ_M is the flux through the coil due to a time dependent magnetisation and is given by

$$\Phi_M(t) = \int_{sample} \mathbf{M}(\mathbf{r},t)\cdot\mathbf{B}^{rec}(\mathbf{r})d^3r \qquad \text{Eq. 2.22}$$

where $\mathbf{M}(\mathbf{r},t)$ is the time dependent magnetisation at a point **r**, and $\mathbf{B}^{rec}(\mathbf{r})$ is the 'receive' field at a point **r** and is related to properties of the coil such as its geometry

[3]. In simple terms, ignoring the effects of sample volume and coil properties, the induced *emf*, or 'signal', is given by

$$signal \propto \omega_0 \sqrt{M_x^2 + M_y^2} \exp\left(\frac{-t}{T_2^*}\right) \sin(\omega_0 t + \phi) \quad . \qquad \text{Eq. 2.23}$$

As ω_0 is typically on the order of 100MHz (^{1}H) a demodulation step is used to reduce the frequency of oscillation. The demodulation step involves multiplying the rapidly varying NMR signal (Eq. 2.22) by a reference signal of frequency = $\omega_0 + \delta\omega$, where $\delta\omega$ is the 'offset' frequency from the Larmor frequency, ω_0.

$$\text{demodulated signal} \propto \text{reference signal} \times \text{NMR signal} \quad .$$

Both sinusoid and cosinusoid multiplication are carried out to form two data sets referred to as the 'real' and 'imaginary' signal channels. Assuming that the signal shows a frequency offset, $\delta\omega$, the real signal is given by

$$real\ channel \propto \sin(\omega_0 t + \delta\omega t) \cdot \sin(\omega_0 t + \phi) \qquad \text{Eq. 2.24}$$

rearranging Eq.2.24 using sin a sin b = 1/2(cos($a - b$) – cos($a + b$)) yields

$$real\ channel \propto \frac{1}{2}\left(\cos(\delta\omega t - \phi) - \cos((2\omega_0 t + \delta\omega t) + \phi)\right) \quad .$$

Eq. 2.25

The signal is thus made up of two parts, one oscillating at a relatively low frequency characterised by $\delta\omega$, and a high frequency component characterised by $2\omega_0$. On application of a low-pass filter, the real channel signal is then given by

$$real\ channel \propto \frac{1}{2}\cos(\delta\omega t - \phi) \quad . \qquad \text{Eq. 2.26}$$

In a similar way the demodulated 'imaginary' channel signal can be derived by multiplying the NMR signal by -cos($\omega_0 t + \delta\omega t$) to give

$$\text{imaginary channel} \propto \frac{1}{2}\sin(\delta\omega t - \phi) \quad . \qquad \text{Eq. 2.27}$$

The last step is to convert the analogue *emf* signal to a digital signal using an Analogue to Digital Converter (ADC). If a sample containing water, with two ^{1}H nuclei per H_2O molecule, is placed in a homogeneous magnetic field, B_0, the NMR signal of the ^{1}H nuclei can be measured after the application of a 90° RF pulse using a receiver coil. Figure 2.6 shows an illustration of the signal received from this simple NMR experiment.

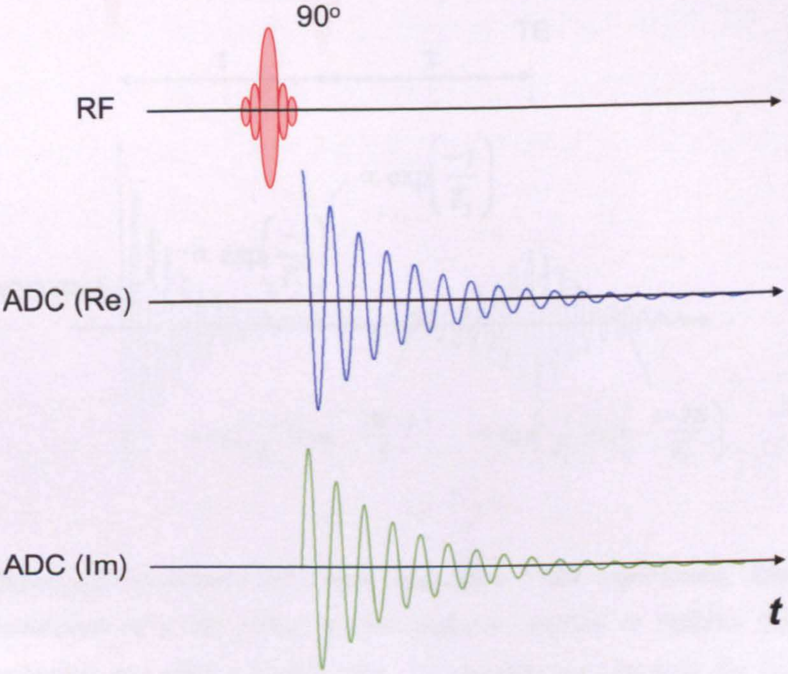

***Figure 2.6** Illustration of FID in simple NMR experiment after application of a 90° RF pulse.*

The oscillating exponential decay of the signal shown in Fig 2.6 is referred to as a Free Induction Decay (FID). A commonly used technique in NMR and MRI is the application of an additional 180° RF pulse to create a 'spin-echo' or 'Hahn-echo' [4]. Figure 2.7 shows an illustration of a simple spin echo experiment. If the 180° pulse is applied a time, τ, after the first 90° pulse, a signal echo will occur at a time, TE = 2τ.

The 180° pulse reverses the dephasing of spins due to static inhomogeneities in B_0, characterised by T_2' (Section 2.1.3), to yield a signal weighted by a pure T_2 decay at time = TE, corresponding to the centre of the spin-echo. The 180° pulse cannot reverse the dephasing caused by pure T_2 effects as this results from random, time-dependent, movements of spins. Fig 2.7 also shows the equations describing the signal 'envelopes' that characterise the exponential behaviour of the decay, and growth, before and after the application of the 180° RF pulse [2].

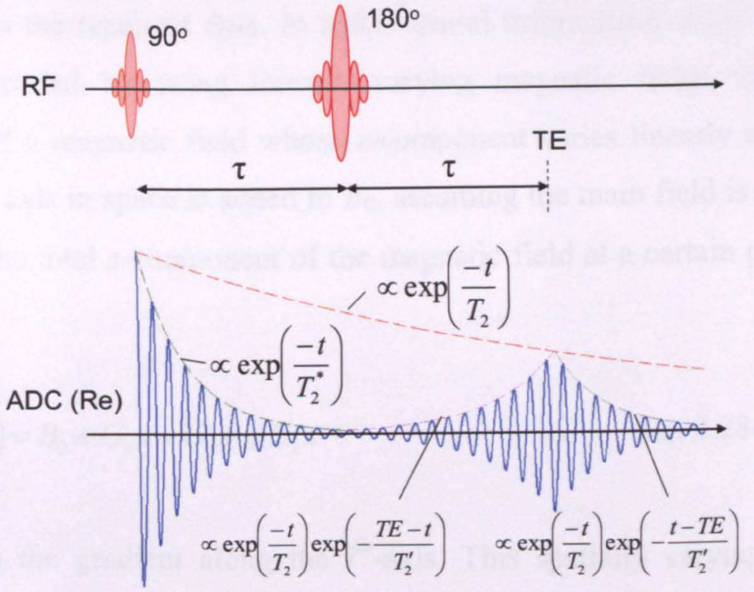

<u>Figure 2.7</u> Illustration of simple spin echo NMR experiment. After application of a 90° pulse, a 180° pulse is applied to refocus spin dephasing and yield a signal echo. To simplify the plot only the real channel is shown.

In reality, the simple spin echo experiment illustrated in Fig 2.7 is sensitive to water diffusion and will result in non-ideal signal envelopes. A series of 180° RF pulses can be used to suppress these diffusion effects. This approach is known as the Carr-Purcell Meiboom-Gill (CPMG) method [23].

2.2 Magnetic Resonance Imaging

Magnetic Resonance Imaging (MRI) is a non-invasive imaging method that over the last few decades has revolutionised the way researchers, and clinicians, visualise soft tissues in the human body and brain.

2.2.1 Spatial Localisation of Signal

To create any image, spatial information about the sample being analysed must be encoded into the received data. In MRI, spatial information about the locations of spins is encoded by using linearly varying magnetic fields, known as 'field gradients'. If a magnetic field whose *z*-component varies linearly in strength along an arbitrary axis in space is added to B_0, assuming the main field is orientated along the *z*-axis, the total *z*-component of the magnetic field at a certain point, $B(x,y,z)$, is given by

$$B(z) = B_0 + G_x x + G_y y + G_z z \quad . \qquad \text{Eq. 2.28}$$

where G_i is the gradient along the i^{th}-axis. This spatially varying magnetic field causes a spatial variation in the Larmor frequency of spins

$$\omega_0 = \gamma(B_0 + G_x x + G_y y + G_z z) \quad . \qquad \text{Eq. 2.29}$$

The ability to encode spatial position in the NMR signal using magnetic field gradients is the foundation of all MRI.

2.2.2 Slice Selection

The first stage of most MRI sequences is to select a slice, or slab, corresponding to the region of interest of the sample. This slice selection is carried out by applying an RF pulse in the presence of a field gradient, often varying in the *z*-axis. The Larmor frequency of spins in the presence of this field gradient is given by

$$\omega_0(z) = \gamma(B_0 + G_z z) \quad . \qquad \text{Eq. 2.30}$$

RF pulses can be tailored to excite a specific range of frequencies, Δω. This is often achieved by setting the RF pulse shape to that of a sinc function with a variable width and centre frequency, depending on the choice of Δω and slice position. Figure 2.8a shows the selection of a slice corresponding to the brain region of a human subject. Only the spins with precession frequencies in the Δω range have their magnetisation tipped into the transverse plane. Thus, only signal from the slice of choice will be measured by receiver coils. One problem associated with slice selection is the dephasing of spins due to the linear distribution of precession frequencies resulting from the field gradient applied during the RF pulse. To correct for this dephasing, a 'rephasing' gradient lobe is used. This is simply a field gradient of the opposite sign to that used for the slice selection. Assuming that the slice select gradient is applied for a time τ, and the slice selective RF pulse is applied at a time τ/2, after the gradient is switched on, the spins will dephase in the presence of the gradient, G_z, for a time = (τ-τ/2) = τ/2.

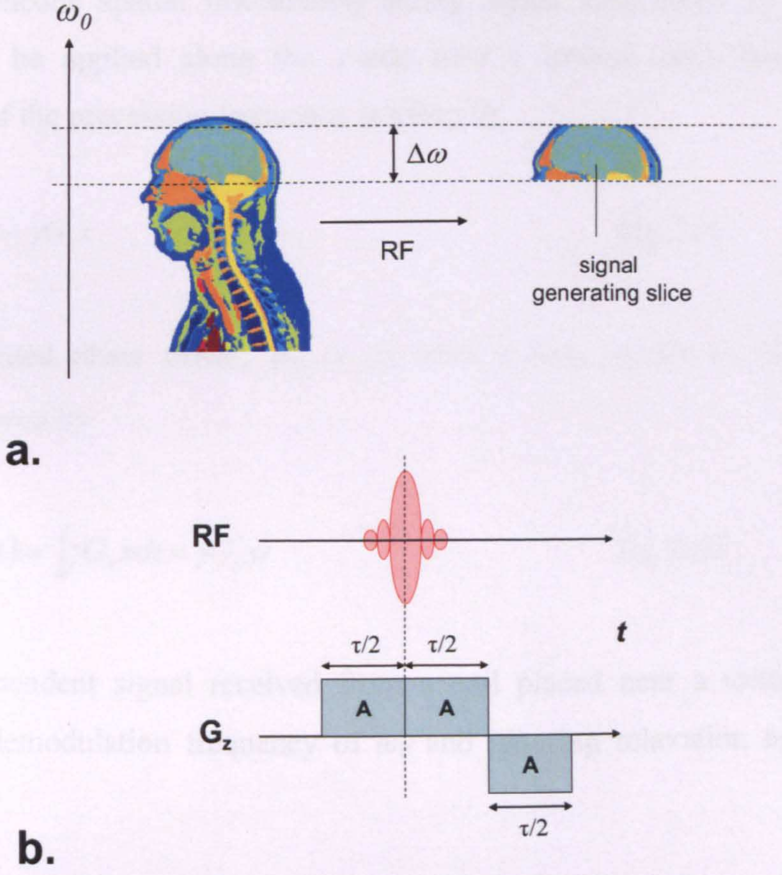

Figure 2.8 (a) Illustration showing slab excited by slice selective RF pulse in the presence of a field gradient, (b) Illustration of timings for RF pulse and gradient field lobes used for slice selection.

It then follows that to rephase the spins a field gradient of amplitude $-G_z$ must be applied for a time = τ/2. The RF pulse, and corresponding gradient lobes, used for slice selection are illustrated in Figure 2.8b. In the discussion above it was assumed that the two gradients had the same magnitude. In reality, the positive and negative gradient pulses can have different magnitudes. It is the combined quantity, $G \times t$, equal to the area under the gradient lobe, A (see Figure. 2.8), that is of importance. In the case of the slice select gradient, the area of the negative gradient lobe must equal half the area under the positive gradient lobe, to ensure the spins fully rephase.

2.2.3 Frequency Encoding

After slice selection, further spatial encoding can be carried out to measure the distribution of spins within the excited slab. Frequency encoding uses a field gradient to encode spatial information during signal acquisition [5, 6]. A field gradient can be applied along the *x*-axis over a sample such that the spatial dependence of the precession frequency is given by

$$\omega_0(x) = \gamma G_x x \qquad .$$

Eq. 2.31

The accumulated phase offset, ϕ_G (*x*, *t*), after a time, *t*, due to this frequency variation is given by

$$\phi_G(x,t) = \int_0^t \gamma G_x x dt = \gamma G_x x t \qquad .$$

Eq. 2.32

The time dependent signal received from a coil placed near a sample of spins, assuming a demodulation frequency of ω_0 and ignoring relaxation terms, is then given by

$$S = \int \rho(x) \exp(-i\phi_G(x,t)) dx = \int \rho(x) \exp(-i\gamma G_x t) dx \ ,$$

Eq. 2.33

where $\rho(x)$ is the spin density distribution, and the real and imaginary signal channels (Eq. 2.25-26) have been grouped into a single complex exponential. Probably the most important mathematical tool in MRI is the Fourier transform. It is a method for expressing a signal in terms of its frequency components. The 1D Fourier transform is given by

$$F(k) = FT(f(x)) = \int_{-\infty}^{\infty} f(x) \exp(-ikx) dx$$

Eq. 2.34

where *k* is a frequency variable, and $F(k)$ is the total frequency distribution. If Eq. 2.33 is compared to Eq. 2.34 a spatial frequency variable, *k*, can be defined such that

$$k = \gamma G t \qquad .$$

Eq. 2.35

The time dependent signal can then be written as,

$$S(k)=\int \rho(x)\exp(-ikx)dx \quad . \qquad \text{Eq. 2.36}$$

One of the main properties of the Fourier transform is its well defined inverse. This means that the original spin density distribution, $\rho(x)$, can potentially be retrieved from the NMR signal, $S(k)$, assuming sufficient frequency components are sampled, via an inverse Fourier transform given by

$$\rho(x)=FT^{-1}(F(k))=\frac{1}{2\pi}\int S(k)\exp(ikx)dk \quad . \qquad \text{Eq. 2.37}$$

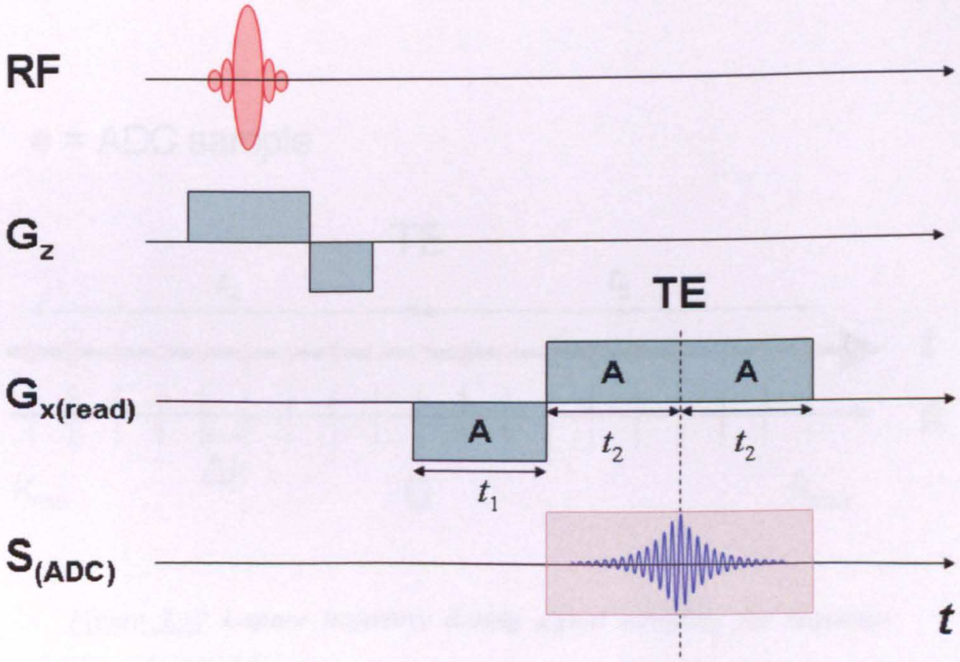

***Figure 2.9** Sequence diagram for frequency encoding along x-axis.*

Figure 2.9 shows a simple MRI experiment for carrying out frequency encoding along the x-axis. Firstly, the slice selective RF-pulse and gradients are applied to the sample to excite the slab of choice. A negative field gradient along the x-axis, $-G_x$, is then applied for a time, t_1. The magnetisation dephases in the field gradient according to its position in the sample. The negative gradient is then switched off and a positive gradient, $+G_x$, is switched on for a time, $2t_2$, where $t_2 = t_1$. The rephasing signal manifests itself as a 'gradient echo'.

The centre of this echo occurs at a time, TE = $2t_1$. This is the point in time when the area under the negative gradient lobe, $-G_x t_1$, is cancelled by the positive gradient lobe, $+G_x t_1$. The ADC is switched on to sample the signal during the positive gradient lobe, for a time = $2t_2$. During the negative gradient lobe $k_x = -\gamma G_x t$ (see Eq. 2.30), and then during the positive lobe $k_x = +\gamma G_x(t-t_1)$. The ADC is switched on during the positive gradient lobe to sample k-space. As the signal is 'read' while G_x is switched on, the field gradient used for frequency encoding is often referred to as the 'read-gradient'. The sampling of k-space, referred to as the k-space 'trajectory', during this period is shown in Figure 2.10.

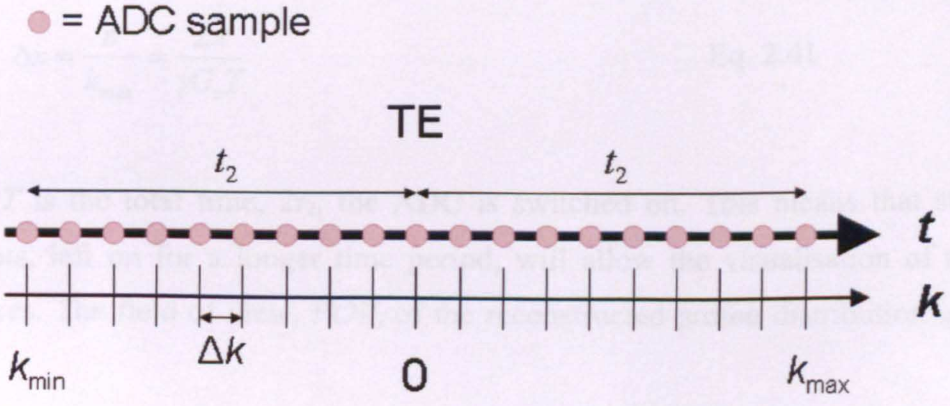

***Figure 2.10** k-space trajectory during signal sampling for sequence shown in Fig.2.9*

The sampling begins at the negative extreme of k-space, $k_{\min}$, given by

$$k_{\min} = -\gamma G_x t_1 \qquad .$$ Eq. 2.38

The signal is then sampled using the ADC at equally spaced points in time, Δt, to give a k-space sampling interval equal to

$$\Delta k = \gamma G_x \Delta t \qquad . \qquad \text{Eq. 2.39}$$

This sampling continues past the TE point at $k = 0$, until the positive extreme of k-space is reached, $k_{\max}$, given by

$$k_{\max} = +\gamma G_x t_2 \qquad . \qquad \text{Eq. 2.40}$$

The proton density, $\rho(x)$, can then be reconstructed from k-space using inverse fourier transformation (see Eq. 2.31). It should be noted that the previous discussion of Fourier transforms considered a continuous signal. The actual signal is, however, sampled discretely for N points over k_x. This means that a discrete Fourier transform must be used to reconstruct the signal. In the discrete regime, the spatial resolution, Δx, assuming $|k_{\max}| = |k_{\min}|$, and $t_1 = t_2$, is given by

$$\Delta x = \frac{\pi}{k_{\max}} = \frac{2\pi}{\gamma G_x T} \qquad \text{Eq. 2.41}$$

where T is the total time, $2t_2$, the ADC is switched on. This means that stronger gradients, left on for a longer time period, will allow the visualisation of smaller structures. The field of view, FOV, of the reconstructed proton distribution is given by

$$FOV = \frac{2\pi}{\Delta k} = \frac{2\pi}{\gamma G_x \Delta t} \qquad . \qquad \text{Eq. 2.42}$$

This means that the FOV is inversely proportional to the field gradient strength and the sampling time spacing. The bandwidth, BW, is the inverse of the time spacing,

$$BW = \frac{1}{\Delta t} \qquad . \qquad \text{Eq. 2.43}$$

In MRI the Signal to Noise Ratio (SNR) of the reconstructed spin distribution is ultimately dependent on the bandwidth. This is because of the well known signal averaging law stating that the longer each signal point is measured the less noisy the measurement will be, or written mathematically,

$$SNR \propto \sqrt{\Delta t} = \frac{1}{\sqrt{BW}} \quad . \qquad \text{Eq. 2.44}$$

Despite this relationship there are circumstances when a high bandwidth is preferable. Specifically, a high *bandwidth* is ideal if within a sample of spins there are two or more populations of spin frequencies due to chemical shift effects. In human imaging, protons within fatty tissues generally have a large chemical shift relative to protons within water rich tissues. A chemical shift is a change in the Larmor frequency of a nucleus due to its local chemical environment. If a single voxel contains both water and fat, the associated Larmor frequency will have two discrete values. For signal reconstruction, based on spatially dependent variations in the Larmor frequency, a large BW (relative to the chemical shift) is then necessary to allocate both the fat and water contributions to the same point in space. A balance must usually be made between high SNR and reduced chemical shift artefacts.

2.2.4 Phase Encoding

In the previous section the steps for reconstructing a 1D representation of a spin density distribution using frequency encoding were outlined. Phase encoding is a technique for providing information on the spatial distribution of spins in 2, or 3, dimensions. The basic principle of phase encoding is to use additional gradients, prior to the read gradient, to encode into the signal phase additional information about the spatial distribution of the spins. A 2D imaging sequence using phase encoding is shown in Figure 2.11. The sequence is identical to the 1D gradient echo (GE) sequence shown in Fig 2.9, with the addition of a gradient pulse, G_y, applied before the signal is acquired. This additional gradient field varies linearly in the y-axis or 'phase-encode' (PE) direction. The phase encode gradient sets the k_y coordinate before the read gradient is used to traverse a line of k-space in the k_x-direction. The k-space coordinates of the signal are given by

$$k_x = \gamma G_x t_x$$
$$k_y = \gamma G_y t_y \qquad \text{Eq. 2.45}$$

where G_x and G_y are field gradients varying linearly in the x- and y-axis respectively, and t_x and t_y is the effective duration of time each field gradient has been switched on, prior to the signal being acquired.

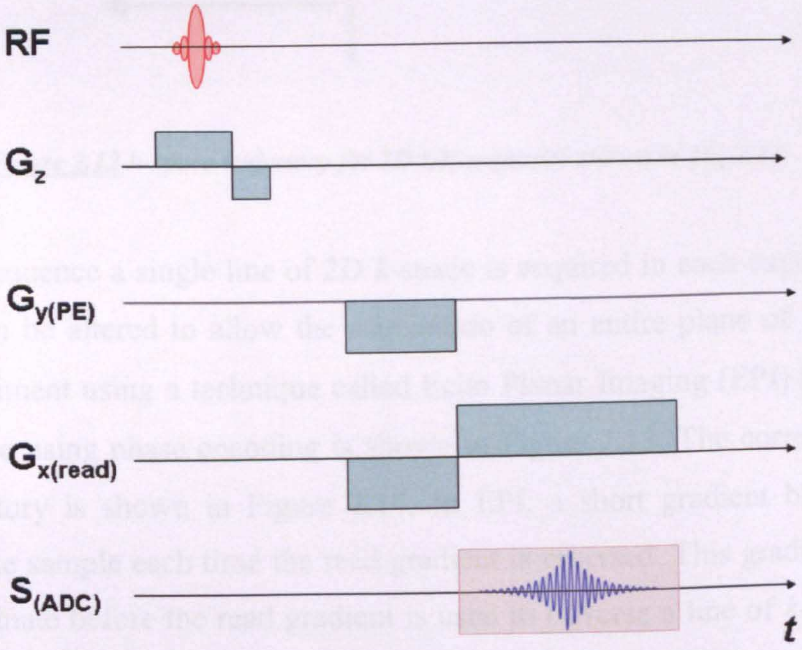

***Figure 2.11** Sequence Diagram for 2D GE with phase encoding*

The k-space trajectory for the 2D GE sequence, shown in Fig. 2.11, is depicted in Figure 2.12. The first stage of the sequence, after slice selection, is to set the starting point in k-space. The negative gradient lobe in G_y, corresponding to the large red arrow in Fig. 2.12, starts the acquisition at the negative extremity of k_y. Similarly, the negative lobe of G_x, corresponding to the black arrow at the bottom of Fig. 2.12, starts the acquisition at the negative extreme of k_x. Hence, the starting point for the k-space acquisition is $S(-k_{x,max},-k_{y,max})$. The read gradient is then applied to traverse a k_x-line, and the ADC is switched on to sample the gradient echo.

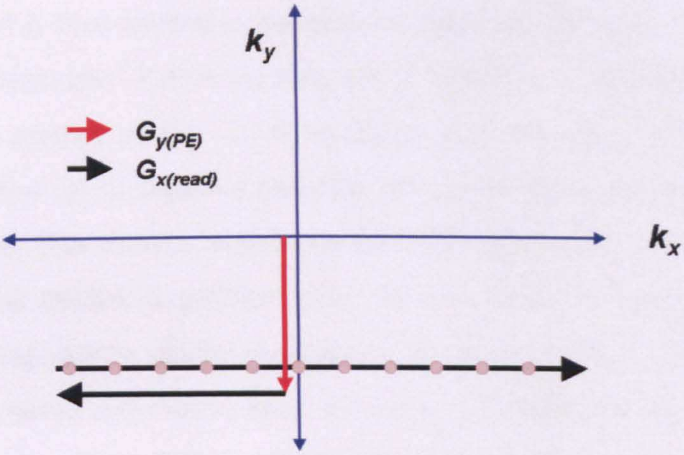

__Figure 2.12__ k-space trajectory for 2D GE sequence shown in Fig 2.11.

Using this sequence a single line of 2D *k*-space is acquired in each experiment. The sequence can be altered to allow the acquisition of an entire plane of *k*-space in a single experiment using a technique called Echo Planar Imaging (EPI) [7, 8]. A 2D EPI sequence using phase encoding is shown in Figure 2.13. The corresponding k-space trajectory is shown in Figure 2.14. In EPI, a short gradient blip, $G_y\Delta t$, is applied to the sample each time the read gradient is reversed. This gradient blip sets the k_y coordinate before the read gradient is used to traverse a line of *k*-space in the k_x-direction.

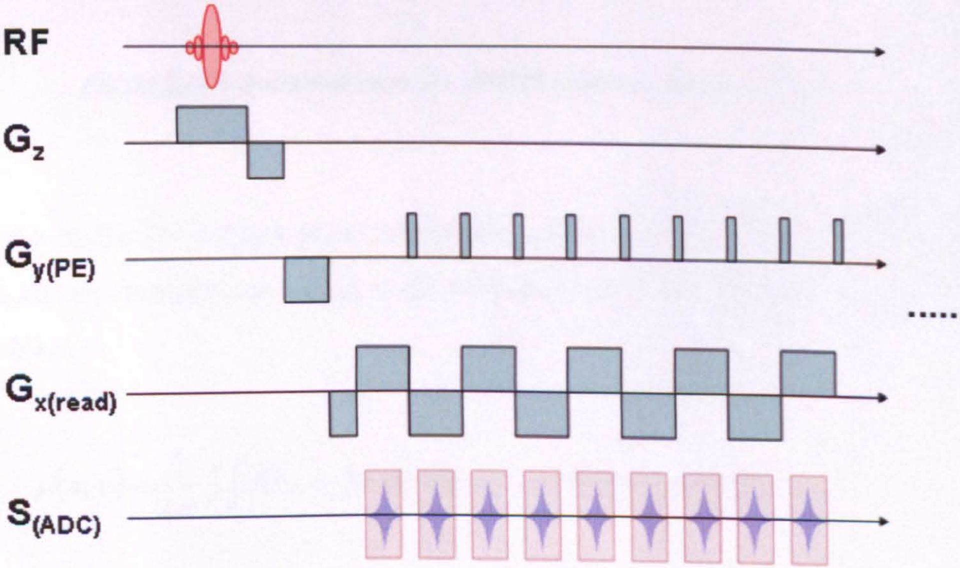

__Figure.2.13__ Sequence diagram of 2D EPI with phase encoding.

The read gradient is then applied to traverse a k_x-line, and the ADC is switched on to sample the gradient echo. Following this, the G_y gradient is switched on for a short time (small red arrows in Fig. 2.14) to move to a new k_y-coordinate. The read gradient is switched on to acquire a new line of k-space, but with opposite polarity to the previous lobe. This reverse in polarity allows the lines of k-space to be acquired quickly, and also creates a gradient echo for the ADC to sample. EPI has the advantage of being able to sample a complete 2D plane of k-space after a single RF-pulse. This high speed acquisition does, however, have disadvantages when it comes to its Signal to Noise Ratio (SNR), and its sensitivity to artefacts.

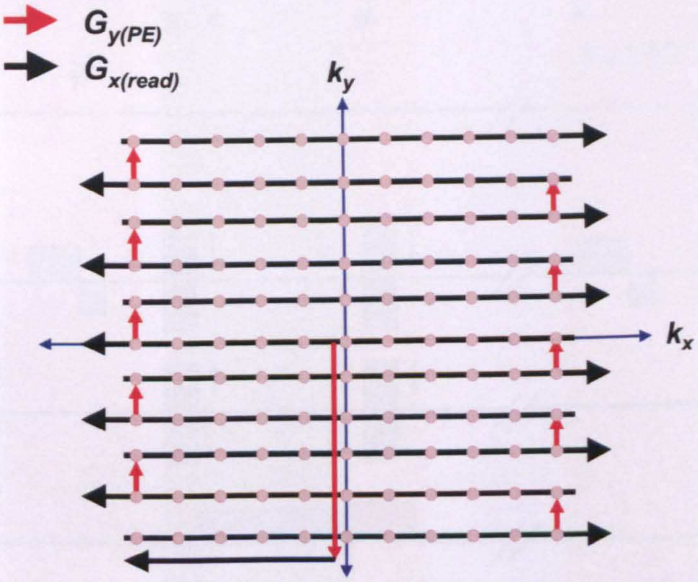

<u>Figure 2.14</u> k-space trajectory for 2D EPI sequence shown in Fig.2.11.

Once the entire 2D k-space plane has been sampled, the proton density distribution, $\rho(x,y)$, can be reconstructed using a 2D inverse Fourier transform similar to Eq. 2.31, given by

$$\rho(x,y)=\frac{1}{2\pi}\int\int S(k_x,k_y)\exp[-i(k_x x+k_y y)]dk_x dk_y \; . \quad \text{Eq. 2.46}$$

2.2.5 3D T2*-Weighted Imaging

In the previous sections the concepts of frequency encoding and phase encoding have been introduced, and their application to 1D and 2D imaging were discussed. Within this section, a fast 3D imaging technique that is used extensively for the work detailed in later chapters will be described. The sequence is a fast field echo (FFE) sequence, also called: a spoiled gradient recalled echo (SPGR), a fast low angle shot (FLASH) sequence, and spoiled gradient recalled acquisition in steady state (spoiled GRASS) [9-13]. Within this work it will be referred to as a FLASH sequence.

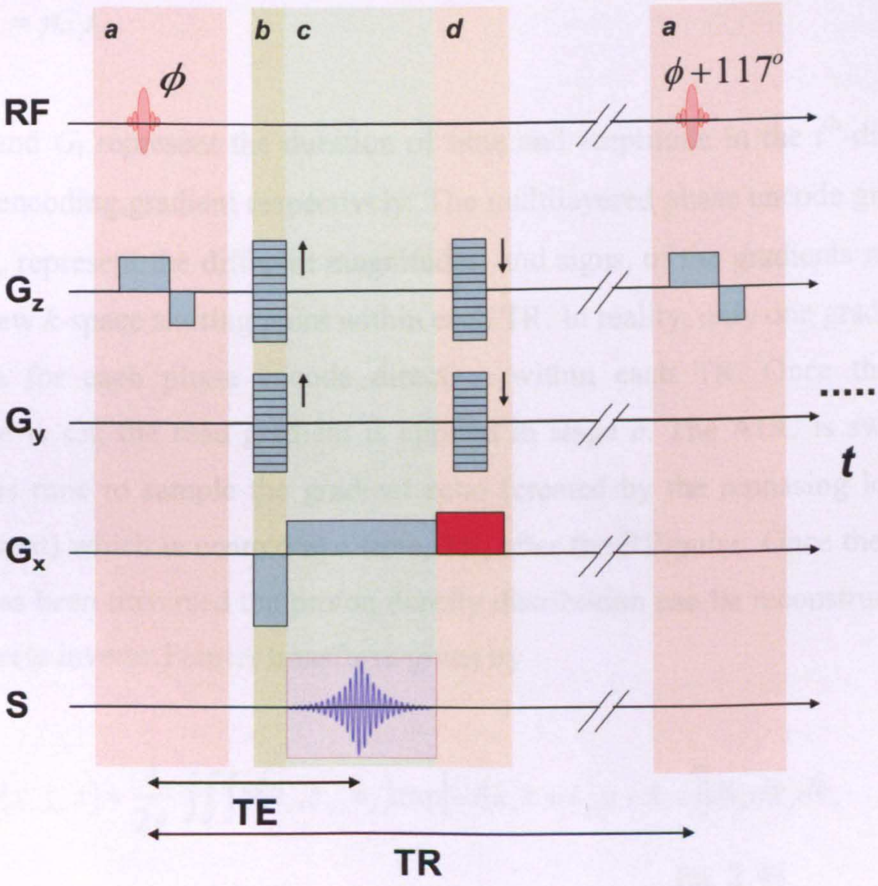

Figure.2.15 Sequence diagram for a 3D FLASH sequence.

The FLASH sequence diagram is shown in Figure 2.15. In this sequence one line of *k*-space is acquired for every RF-pulse. The acquisition is then repeated after a time, referred to as the repetition time (TR). Within each TR-period a new line of *k*-space is sampled until sufficient data have been acquired to span the whole of 3D *k*-space.

To simplify the explanation of this 3D FLASH sequence, the diagram in Fig. 2.15 has been divided into four parts, ***a***, ***b***, ***c***, and ***d***.

The first part, ***a***, in Fig. 2.15, is the slice selection stage involving an RF-pulse combined with a field gradient. The second stage, ***b***, involves the three field gradients, one for each axis/dimension, switched on simultaneously to select the starting point in *k*-space. The *k*-space coordinates in this case will be given by

$$\begin{aligned} k_x &= \gamma G_x t_x \\ k_y &= \gamma G_y t_y \\ k_z &= \gamma G_z t_z \end{aligned}$$

Eq. 2.47

where t_i and G_i represent the duration of time and amplitude in the i^{th}-direction of each pre-encoding gradient respectively. The multilayered phase encode gradients in G_z and G_y represent the different magnitudes, and signs, of the gradients required to select a new *k*-space starting point within each TR. In reality, only one gradient value is chosen for each phase encode direction within each TR. Once the starting coordinate is set, the read gradient is applied in stage ***c***. The ADC is switched on within this time to sample the gradient echo (created by the rephasing lobe of the read gradient) which is centred at a time, TE, after the RF-pulse. Once the whole of *k*-space has been traversed the proton density distribution can be reconstructed using a 3D discrete inverse Fourier transform given by

$$\rho(x,y,z) = \frac{1}{2\pi}\int\int\int S(k_x,k_y,k_z)\exp\left[-i(k_x x + k_y y + k_z z)\right]dk_x dk_y dk_z \quad .$$

Eq. 2.48

In the previous sections discussing imaging in 1D and 2D the effects of relaxation have been ignored. Here, the effect of relaxation on the sequence will be discussed as it is implicit to understanding the contrast seen in FLASH images. If TR is of the same order as T_2^* (section 2.1.3), some transverse magnetisation, resulting from the application of an RF-pulse, will still exist on the application of the following RF-pulse. Also, because in most cases TR < T_1, the longitudinal magnetisation will not fully recover between RF-pulses. This means the evolution of longitudinal and transverse magnetisation is dependent on the RF-pulse number and flip angle. Eventually, after sufficient RF-pulses have been applied the magnetisation available to one RF-pulse will be equal to the magnetisation available to the next RF-pulse. If this condition is satisfied the magnetisation is said to have reached 'steady-state'. The contrast seen in FLASH images is a complicated function of relaxation terms and flip angles. To simplify the contrast dependence of FLASH images, the transverse magnetisation, following an RF-pulse, can be effectively forced to zero before the application of next RF-pulse through 'spoiling'.

Spoiling mechanisms destroy any transverse magnetisation before the next RF-pulse is applied to the sample. The sequence used here (Fig. 2.15) incorporates RF-spoiling [14]. RF spoiling involves changing the phase of each RF pulse such that any transverse magnetisation will not add constructively to the signal measured after the following RF pulse. Through numerical methods, it can be shown that to ensure the transverse magnetisation is suitably spoiled a phase offset of 117° should be cumulatively added to each RF pulse such that the phase of the RF-pulse, $\phi_{RF}(n)$, as a function of pulse number, n, is given by

$$\phi_{RF}(n) = \phi_{RF}(n-1) + n \cdot 117^{o} \quad . \qquad \text{Eq. 2.49}$$

The RF spoiling is shown in part ***a*** of the 2nd TR-period in Fig. 2.15. Another important aspect of the sequence is that the phase encode gradients prior to the signal being read (***b***) are balanced by refocusing gradients of the opposite polarity, shown in ***d*** where the arrows signify reversed polarity. This *rewinding* is used to refocus the dephasing caused by the phase encoding gradients and is usually applied together with the gradient spoiling, as shown in ***d***. To further ensure that no transverse magnetisation exists for the following RF-pulse the read gradient is switched on for a period of time after the ADC is switched off. This is illustrated in Fig. 2.13, section *c*, as the G_x gradient shaded in red. This additional gradient, sometimes referred to as a 'crusher' gradient dephases any remaining transverse magnetisation [15]. Thus, through a combination of RF spoiling and the application of 'crusher' gradients, the transverse magnetisation induced in the n^{th} TR-period, for the FLASH sequence shown in Fig. 2.15, is destroyed before the $n+1^{th}$ TR-period.

A relatively simple expression can be formed to describe the signal strength in a FLASH sequence in terms of the RF flip angle and the transverse and longitudinal decay constants. Assuming that immediately before the n^{th} RF pulse the longitudinal magnetisation is equal to $M_z(TR_n-)$, the transverse magnetisation a time, t, following the n^{th} RF pulse, $M_z(TR_n+)$, is given by,

$$M_{xy}(TR_n+) = M_z(TR_n-)\sin\theta\exp\left(-\frac{t}{T_2^*}\right) \qquad \text{Eq. 2.50}$$

where θ is the RF flip angle. The time evolution of the remaining longitudinal magnetisation directly after the RF pulse is given by the solution of the Bloch equation (Eq. 2.19),

$$M_z(TR_n+) = M_0\left(1-\exp\left(-\frac{t}{T_1}\right)\right) + M_z(TR_n-)\cos\theta\exp\left(-\frac{t}{T_1}\right) \quad .$$

Eq. 2.51

Assuming the signal reaches steady state, the longitudinal magnetisation available to the n^{th} RF pulse is equal to the longitudinal magnetisation available a time TR later for the $n+1^{th}$ RF pulse. Thus, Eq.2.48 can be re-written as,

$$M_{ze} = M_0\left(1-\exp\left(-\frac{TR}{T_1}\right)\right) + M_{ze}\cos\theta\exp\left(-\frac{TR}{T_1}\right) \qquad \text{Eq. 2.52}$$

where $M_{ze} = M_z(TR_n-)$ is the equilibrium magnetisation available before each RF pulse. Grouping terms in Eq.2.49 leads to,

$$M_{ze} = \frac{M_0\left(1-\exp\left(-\frac{TR}{T1}\right)\right)}{\left(1-\cos\theta\exp\left(-\frac{TR}{T1}\right)\right)} \quad . \qquad \text{Eq. 2.53}$$

Substituting Eq. 2.53 into Eq. 2.50, and assuming M_{ze} is proportional to the spin density, $\rho(x,y,z)$, the steady-state signal strength, S, for a spoiled FLASH sequence is given by

$$S \propto \rho(x,y,z)\sin\theta \frac{1-\exp\left(\frac{-TR}{T_1}\right)}{1-\cos\theta\exp\left(\frac{-TR}{T_1}\right)}\exp\left(\frac{-TE}{T_2^*}\right)$$

Eq.2.54

where θ is the RF-pulse flip angle and M_0 is the equilibrium magnetisation [16]. Figure.2.16 shows plots of the signal dependence against flip angle for varying TR/T_1 ratios, and fixed $exp(TE/T_2^*) = 1$.

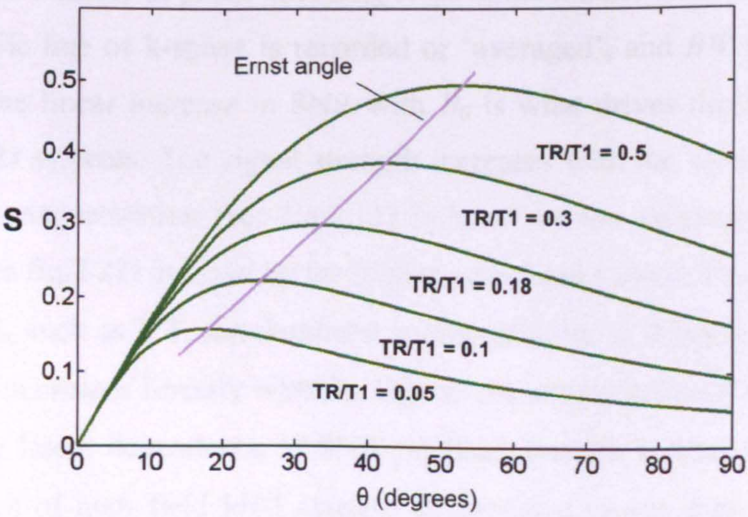

***Figure 2.16** Plot of signal strength, S, against flip angle, θ, for different TR/T_1 values. The purple line shows the maximum signal occurring at the Ernst angle.*

The maximum signal for a given TR/T_1 value occurs at the Ernst angle, θ_E, given by

$$\cos(\theta_E) = \exp\left(\frac{-TR}{T_1}\right) \quad . \qquad \text{Eq. 2.55}$$

In general, the signal strength reduces for low values of TR/T_1. This means a compromise between signal strength and scan time must normally be made. Once the TR value and flip angle are chosen, T_2^* can be made to dominate by choosing TE ≥ T_2^*. This is why spoiled gradient echo (GE) FLASH sequences are referred to as T_2^*-weighted. A long TE will result in images that are heavily T_2^*-weighted. Once the optimal TR and TE values are chosen, the SNR of the 3D scan can be derived using a fairly general expression,

$$SNR \propto B_0 V \sqrt{\frac{N_{PEy} \cdot N_{PEz} \cdot NEX}{BW}} \qquad \text{Eq. 2.56}$$

where V is the voxel volume, N_{PEy} is the number of phase encoding steps in the y-axis, N_{PEz} is the number of phase encoding steps in the z-axis, NEX is the number of times a specific line of k-space is recorded or 'averaged', and BW is the sampling bandwidth. The linear increase in SNR with B_0 is what drives the development of high field MRI systems. The signal strength increases with the square of B_0 due to the increased magnetization (see Eq.2.11) induced by the magnetic field and the higher *emf* (see Eq.2.21) induced by the higher associated Larmor frequency. At high field strengths, such as 7 T, the dominant source of noise is thermal noise from the sample which increases linearly with B_0. Due to the combination of these factors an approximately linear dependence of SNR on field strength is observed at 7 T [1]. One draw back of high field MRI systems is increased power deposition from RF fields into the body as heat. The Specific Absorption Rate (SAR) is a measure of power deposition and increases with B_0 [2]. This means careful consideration of SAR values must be undertaken when designing an imaging sequence at 7 T.

An increased voxel volume will contain a larger number of spins and thus will generate a greater signal strength. The square root arises from the well-known signal averaging law that, assuming the noise is random, the SNR will increase with the square root of the number of averages. The *BW* dependence is due to the signal averaging law, but through repeated sampling rather than repeated averages (see Eq. 2.44). Eq. 2.56 can be generalised further to

$$SNR \propto B_0 V \sqrt{\frac{time}{BW}} \qquad \text{Eq. 2.57}$$

where *time* is the duration of the scan. This expression represents a fundamental limitation on 3D imaging. If the voxel size is reduced to increase the imaging resolution, either the scanning time or the magnetic field strength must be increased. As scanning time is often limited in *in vivo* applications, higher magnetic field strengths are often the only option for increasing the resolution of MR images, while achieving an adequate signal to noise ratio.

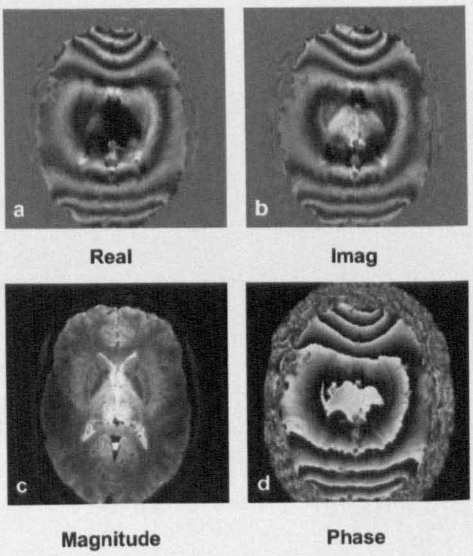

***Figure 2.17** Slice of 3D human brain data set acquired using spoiled gradient echo FLASH sequence at 7T with TE/TR = 20/150ms, showing: (a) real image; (b) imaginary image; (c) magnitude image; (d) phase image.*

Figure 2.17 shows example modulus and phase images of a human brain *in-vivo*, which were acquired using a 3D spoiled gradient echo FLASH sequence on a 7T whole-body MRI scanner. The origin of the modulus and phase images is in the complex NMR signal. In Section 2.1.5 the demodulation step of the signal acquisition was shown to generate a real (Re) and imaginary (Im) channel. This complex signal is then inverse Fourier transformed to yield a complex signal in image space. To extract useful information from the complex data, magnitude and phase images are calculated via

$$\begin{aligned} \text{Magnitude} &= \sqrt{\text{Re}^2 + \text{Im}^2} \\ \text{Phase} &= \arctan_{4q}\left(\frac{\text{Re}}{\text{Im}}\right) \end{aligned} \qquad \text{Eq. 2.58}$$

where *arctan*$_{4q}$ is the 4 quadrant arc-tan operator. This operator looks at the associated signs of Re and Im. This allows the reconstruction of the phase between $-\pi$ and π, as opposed to the $-\pi/2$ and $\pi/2$ range achievable with a standard arc-tan operation. The magnitude image yields information about the spatial distribution of signal strength (Eq.2.42). The phase image, measured in units of radians, yields information on the spatial distribution of local magnetic fields measured relative to B_0. The phase offset is given by

$$\phi(x,y,z) = -\gamma TE \Delta B(x,y,z) \qquad \text{Eq. 2.59}$$

where ΔB is the field shift relative to B_0. Small field shifts can result from susceptibility differences between tissues and from air/tissue interfaces [17, 18]. The steps used to process phase data to yield field maps will be discussed in later chapters.

2.2.6 Imaging Planes

As with other medical imaging modalities, in MRI there are conventions on how images are viewed and described. Figure 2.18 shows a 3D illustration of how the various imaging planes are described in this work relative to a human subject. The transverse plane may sometimes also be referred to as the 'axial' plane.

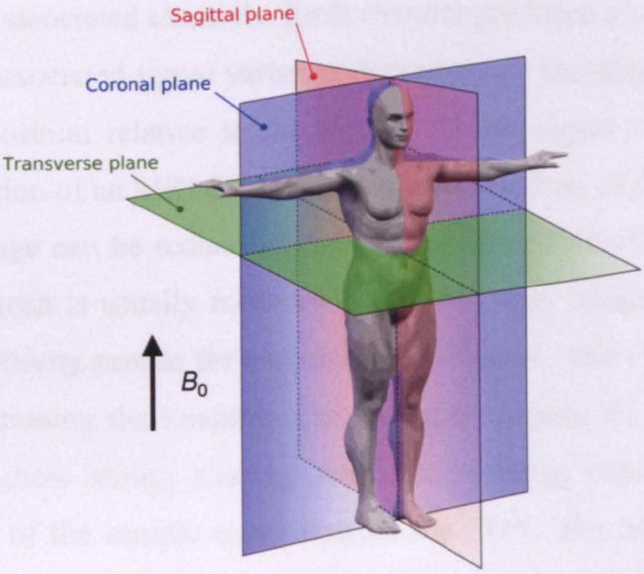

***Figure 2.18** – Illustration of imaging planes in MRI, adapted from [19].*

2.2.7 Accelerated Imaging

For many applications, especially involving human subjects, the time available to carry out MRI experiments is limited. While the FLASH sequence described previously uses short TR's, in some instances the imaging process must be accelerated if it is to be completed in a short enough time to be feasible for use in a clinical environment. There are two main acceleration options. These involve the use of: (i) EPI factors, and (ii) parallel imaging schemes. EPI factors combine the 3D FLASH sequence, in which a single line of k-space is read within each TR, with an EPI sequence, in which a whole plane of k-space is acquired as described in Section 2.2.4. The high SNR of the FLASH sequence must be balanced with the lower SNR, but increased speed, available using EPI schemes. For most of the *in vivo* imaging carried out in this thesis, the EPI factor was set to 3. This means within each TR multiple lines of k-space are read out using an EPI scheme similar to that described in Section 2.2.4, but with a smaller number of echoes such that only 3 lines are traversed. Introducing an EPI factor will make the reconstructed images more sensitive to field offsets producing distortion. Parallel imaging is an entirely different acceleration method. In modern MRI the NMR signal is measured using multiple receiver coils and associated channels. Each channel produces a separate image, but modulated by an associated signal variation dependent on the shape of the receiving element and its position relative to the sample. If this signal variation is known before the acquisition of an MRI data set, the number of lines of *k*-space required to reconstruct an image can be reduced, hence reducing the overall scanning time. A short 'reference' scan is usually recorded before the main image acquisition. This scan yields a sensitivity profile for each receiver channel. The FOV of the scan is then reduced, decreasing the imaging time, but also causing the image created by each channel to show strong aliasing artefacts. Aliasing occurs when a signal generating region of the sample exists outside the FOV. The NMR signal of this region is still read by the ADC and superimposed onto the signal generated within the FOV for each line of k-space. As the Fourier transform is a periodic function any signal beyond one extreme of the FOV will be wrapped back in on the opposite side. Although this is a severe problem, the sensitivity profiles can be utilised, in combination with reconstruction algorithms, to yield a composite image averaged over all of the channels that is free of aliasing. In much of the work presented in later chapters the parallel imaging factor was set to 2. This means that the number of k-space lines that were read by the ADC was reduced by a factor of 2. This was achieved based via the use of a 16 channel coil using the Sensitivity Encoding (SENSE) reconstruction algorithm [20]. For both acceleration techniques there is usually a decrease in SNR due to the reduction in total scan time (see Eq. 2.50).

2.2.8 Imaging Artefacts

For the 3D FLASH imaging and accelerated imaging, described in the previous section, there are associated sources of potential artefacts that can make accurate interpretation of the resulting data more difficult. The main sources of artefacts are: (i) chemical shifts, (ii) susceptibility related artefacts, (iii) aliasing, and (iv) Nyquist ghosting. As described in Section 2.2.2, the chemical shift of fat relative to water can cause the associated NMR signal to be localised to an incorrect region of space. Increasing the sampling bandwidth, BW, will reduce this problem at the cost of SNR. Susceptibility related artefacts are a result of the large susceptibility differences at air tissue interfaces. These differences induce strong dipolar magnetic fields near these surfaces. These dipolar fields then induce a spatial variation of the NMR frequency. Similar to the chemical shift effect, if the BW is too small the signal generated near these interfaces will be localised to incorrect points in space. Thus, another compromise between high BW, for reducing artefacts, and low BW, to increase SNR, must be made.

As described in the previous section, aliasing occurs when signal is generated from outside of the FOV. In terms of artefacts, it is signal being generated outside of the FOV in the phase encoding direction that can yield severe wrap around effects. If parallel imaging is utilised then signal outside the FOV in the direction of the associated phase encoding axis will cause artefacts. Thus, a compromise must be made between artefacts due to aliasing and a longer scan time due to an increased FOV. Imaging involving high EPI factors suffer from a different form of artefact known as the Nyquist Ghost. This ghosting is due to the rapid switching of gradient polarity necessary to traverse k-space in EPI, see Fig 2.14. If there are any errors in the sampling, or asymmetries in the gradients, aliasing will occur that can potentially overlap with the desired image data.

2.2.9 MRI System Layout

Figure 2.19 shows a schematic of a whole-body MRI scanner. The largest component of an MRI system is the main electromagnet. Generally, this consists of superconductive cylindrical current-carrying coils carefully positioned so as to achieve a strong, and homogeneous, magnetic field. To ensure the coils remain superconductive they are kept at a low temperature by a mixture of liquid helium, 4°K, liquid nitrogen, 77°K, and refrigeration units known as cryocoolers. Within the main magnet the next layer of current-carrying coils are called shim coils. These coils produce small magnetic fields that are used to increase the homogeneity of the main field. They can be adjusted to create a sample specific shim-field that, ideally, corrects for the field perturbations caused by susceptibility differences in the sample. The next layer of the MRI system is the gradient coils. These coils are designed to create linear spatially-varying magnetic fields that allow spins to be localised in space (see Section 2.2.1-2).

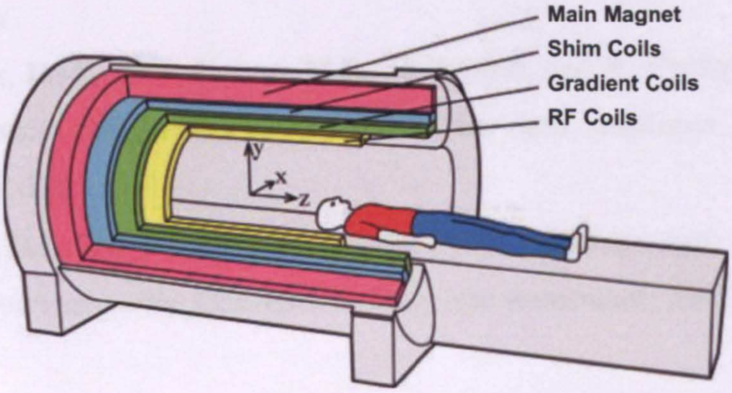

Figure 2.19 ***Schematic of a whole-body MRI scanner, reproduced from [21].***

The final layer is comprised of RF coils. These coils are designed to generate RF-fields that excite spins and flip longitudinal magnetisation into in the transverse plane (Section 2.1.2). These coils can also be set to receive the NMR signal, but in general, separate receiver coils are placed closer to the sample to increase signal strength. The subject is placed on a movable bed and slid into the centre of the MRI system. Aside from the components inside the MRI scanner, there are various pieces of equipment that must be placed away from the strong magnetic fields of the main magnet. These include: amplifiers, frequency synthesizers, duplexers, and the computer system that controls the scanner.

For the majority of work described in this thesis a 7T Philips Achieva scanner (Philips Medical Systems, Best, the Netherlands), situated in the Sir Peter Mansfield Magnetic Resonance Centre (SPMMRC) at Nottingham University, was used to acquire data.

2.3 References

1. Levitt, M.H., *Spin Dynamics: Basics of Nuclear Magnetic Resonance.* 2006: WILEY.
2. Haacke, E.M., R.W. Brown, M.R. Thompson, and R. Venkatesan, *Magnetic Resonance Imaging: Physical Principles and Sequence Design.* 1999: WILEY-LISS.
3. Hoult, D.I., *The principle of reciprocity in signal strength calculations—A mathematical guide.* Concepts in Magnetic Resonance, 2000. **12**(4): p. 173-187.
4. Hahn, E.L., *Spin Echoes.* Physical Review, 1950. **80**(4): p. 580.
5. Lauterbur, P.C., *Image formation by induced local interactions: Examples employing NMR.* Nature, 1973. **242**: p. 190.
6. Kumar, A., D. Welti, and R.R. Ernst, *NMR Fourier zeugmatography.* Journal of Magnetic Resonance (1969), 1975. **18**(1): p. 69-83.
7. Mansfield, P. and A.A. Maudsley, *Medical Imaging by NMR.* British Journal of Radiology, 1977. **50**(591): p. 188-194.
8. Mansfield, P., *Multi-planar image formation using NMR spin echoes.* Journal of Physics C: Solid State Physics, 1977. **10**(3): p. L55-L58.
9. Haase, A., J. Frahm, D. Matthaei, W. Hanicke, and K.D. Merboldt, *FLASH imaging. Rapid NMR imaging using low flip-angle pulses.* Journal of Magnetic Resonance (1969), 1986. **67**(2): p. 258-266.
10. Haase, A., *Snapshot Flash MRI. Applications to T1, T2, and chemical-shift imaging.* Magnetic Resonance in Medicine, 1990. **13**(1): p. 77-89.
11. Frahm, J., W. Hanicke, and K.-D. Merboldt, *Transverse coherence in rapid FLASH NMR imaging.* Journal of Magnetic Resonance, 1987. **72**(2): p. 307-314.
12. van der Meulen, P., J.P. Groen, A.M.C. Tinus, and G. Bruntink, *Fast Field Echo imaging: An overview and contrast calculations.* Magnetic Resonance Imaging, 1987. **6**(4): p. 355-368.
13. Haacke, E.M. and J.A. Tkach, *Fast MR imaging: techniques and clinical applications.* Am. J. Roentgenol., 1990. **155**(5): p. 951-964.

14. Zur, Y., M.L. Wood, and L.J. Neuringer, *Spoiling of transverse magnetization in steady-state sequences.* Magnetic Resonance in Medicine, 1991. **21**(2): p. 251-263.

15. Bernstein, M.A., K.F. King, and X.J. Zhou, *Handbook of MRI Pulse Sequences.* 2004: Elsevier.

16. Ernst, R.R. and W.A. Anderson, *Application of Fourier transform spectroscopy to magnetic resonance.* Review of Scientific Instruments, 1966. **37**(93).

17. Duyn, J.H., P. van Gelderen, T. li, J.A. de Zwart, A.P. Koretsky, and M. Fukunaga, *High-field MRI of brain cortical substructure based on signal phase.* PNAS, 2007. **104**(28): p. 11796-11801.

18. Collins, C.M., B. Yang, Q.X. Yang, and M.B. Smith, *Numerical calculations of the static magnetic field in three-dimensional multi-tissue models of the human head.* Magnetic Resonance Imaging, 2002. **20**(5): p. 413-424.

19. Wikipedia. Available from: http://en.wikipedia.org/wiki/File:Human_anatomy_planes.svg.

20. Pruessmann, K.P., M. Weiger, M.B. Scheidegger, and P. Boesiger, *SENSE: Sensitivity encoding for fast MRI.* Magnetic Resonance in Medicine, 1999. **42**(5): p. 952-962.

21. Poole, M., *Improved equipment and Techniques for dynamic Shimming in High Field MRI*, in *Physics*. 2007, University of Nottingham.

22. Wright, P., *Water proton T1 measurements in brain tissue at 7, 3, and 1.5T using IR-EPI, IR-TSE, and MPRAGE: results and optimization.* 2008, Magn Reson Mater Phy, 21:121–130.

23. Roebuck, J., *Carr-Purcell-Meiboom-Gill imaging of prostate cancer: quantitative T2 values for cancer discrimination.* 2008, MRI, 27 (2009) 497-502.

CHAPTER 3

Magnetic Susceptibility Induced Field Perturbation Theory

The first part of this chapter outlines theory describing magnetic field perturbations induced by magnetic susceptibility distributions. This is followed by examples demonstrating the practical application of a Fourier-based method for calculating field perturbations based on susceptibility distributions with simple geometries and known analytical solutions.

3.1 Field Perturbation Theory

Much of the work within this thesis has been motivated by recent advances in the simulation of magnetic field maps based on a known distribution of magnetic susceptibility. Specifically, the development of a fast Fourier based method has allowed researchers around the world to investigate field map data in ways that would have been difficult, if not impossible, using previous methods. The fast Fourier method was derived independently in 2003 by Salomir et al. [1] and Marques and Bowtell [2]. Interestingly, the paths by which the two groups arrived at the approach were virtually independent. Salomir et al. [1] started from an analysis of Maxwell's equations, while Marques and Bowtell [3] used a Fourier analysis of the dipole field due to a distribution of magnetic susceptibility. Here, both derivations will be outlined as each offers a different perspective on the non-local relationship between field perturbation and the underlying magnetic susceptibility distribution.

3.1.1 The Fourier Derivation

The magnetisation, **M**, induced within a sample by an applied magnetising field, **H**, is given by

$$\mathbf{M} = \chi\mathbf{H} \qquad \text{Eq. 3.1}$$

where χ is the volume magnetic susceptibility. Magnetic susceptibility describes how easily, and in what direction, a sample becomes magnetised in response to an applied magnetic field. Most molecules possess no intrinsic magnetic moment due to the net cancellation of the orbital and spin angular momentum of the electrons. In the presence of an applied magnetic field, the orbital moments of the electrons precess and generate a magnetic moment that is aligned opposite to the field [4]. This is known as the diamagnetic effect, and results in a negative magnetic susceptibility. For a small number of molecules, however, the angular momentum of the electrons does not cancel and forms an intrinsic dipole moment that will be oriented parallel to the applied field [4]. This is known as the paramagnetic effect, and results in a positive magnetic susceptibility. The magnetic induction, **B**, here-after referred to as the 'magnetic field', is related to **H** via,

$$\mathbf{B} = \mu_0(1 + \chi(\mathbf{r}))\mathbf{H} \qquad \text{Eq. 3.2}$$

where $\chi(\mathbf{r})$ is the spatial distribution of the magnetic susceptibility, and μ_0 is the permeability of free space = $4\pi \times 10^{-7}$ N/A^2. Substituting Eq. 3.2 into Eq. 3.1 gives,

$$\mathbf{M}(\mathbf{r}) = \chi(\mathbf{r})\frac{\mathbf{B}}{\mu_0(1 + \chi(\mathbf{r}))} \quad . \qquad \text{Eq. 3.3}$$

In MRI, the samples under investigation typically have magnetic susceptibilities approximately equal to that of water $\approx 9 \times 10^{-6}$ [5]. Assuming therefore $\chi \ll 1$, Eq.3.3 can be approximated as,

$$\mathbf{M}(\mathbf{r}) = \frac{1}{\mu_0}\chi(\mathbf{r})\mathbf{B} \quad . \qquad \text{Eq. 3.4}$$

The induced magnetisation will create its own magnetic field, $\mathbf{B}_d$. The magnetic field at a position **r**, due to a distribution of magnetisation, **M(r)**, is a complex function representing the summation of dipolar fields produced by each element of the magnetisation and is given by [3]

$$\mathbf{B}_d(\mathbf{r})=\frac{\mu_0}{4\pi}\int\frac{1}{|\mathbf{r}-\mathbf{r}'|^3}\times\left(3\frac{\mathbf{M}(\mathbf{r}')\cdot(\mathbf{r}-\mathbf{r}')}{|\mathbf{r}-\mathbf{r}'|^2}(\mathbf{r}-\mathbf{r}')-\mathbf{M}(\mathbf{r}')\right)d^3\mathbf{r}' \quad .$$

Eq. 3.5

Deville et al. [6] showed that this complex, non-local function becomes simple and local when calculated in the Fourier domain using k-space coordinates in the rotating reference frame, and is given by

$$\mathbf{B}_d(\mathbf{k})=\frac{\mu_0}{3}\frac{3\cos^2\beta-1}{2}\left(\mathbf{M}(\mathbf{k})-3M_z(\mathbf{k})\hat{\mathbf{z}}\right) \qquad \text{Eq. 3.6}$$

where β is the angle between the **k** vector and k_z such that,

$$\cos^2\beta=\frac{k_z^2}{k_x^2+k_y^2+k_z^2} \quad . \qquad \text{Eq. 3.7}$$

If a standard MRI reference frame is adopted where the main magnetic field, B_0, is orientated along **z**, and assuming that the magnetic susceptibility is isotropic, only the z-component of the magnetisation deviates significantly from zero, such that $\mathbf{M}(\mathbf{k}) = M_z(\mathbf{k})$ [3]. Eq.3.6 then becomes,

$$\mathbf{B}_{dz}(\mathbf{k})=\mathbf{B}_d(\mathbf{k})\cdot\hat{\mathbf{z}}=-\frac{\mu_0 M_z(\mathbf{k})}{3}\left(3\cos^2\beta-1\right) \quad . \qquad \text{Eq. 3.8}$$

Where $\mathbf{B}_{dz}(\mathbf{k})$ is the field perturbation along the z-axis. By substituting Eq. 3.4 into Eq. 3.8 and setting the magnetic field $\mathbf{B} = B_0\mathbf{z}$, an expression describing the field perturbation in k-space due to a susceptibility distribution, $\chi(\mathbf{k})$, can be formed and is given by

$$\mathbf{B}_{dz}(\mathbf{k})=B_0\chi(\mathbf{k})\left(\frac{1}{3}-\cos^2\beta\right) \quad . \qquad \text{Eq. 3.9}$$

Thus, the perturbation of the magnetic field is given by a simple Fourier expression involving the convolution of the k-space susceptibility distribution, $\chi(\mathbf{k})$, with the dipole field kernel.

3.1.2 Derivation based on Maxwell Equations

The magnetic field experienced by a nucleus, $\mathbf{B}_{nuc}$, is given by

$$\mathbf{B}_{nuc} = \left(1 - \frac{2}{3}\chi\right)\mathbf{B}_{mac} \qquad \text{Eq. 3.10}$$

where $\mathbf{B}_{mac}$ is the macroscopic field and is created by sources sufficiently far away from the nucleus to make $\mathbf{B}_{mac}$ homogeneous over this region of space. The $-2\chi/3$ correction in Eq.3.10 arises from the theoretical construct known as the sphere of Lorentz (SOL) [4, 7]. The SOL is a notional sphere drawn around the nucleus such that outside the SOL there is considered to be a uniform homogenous susceptibility. Inside the SOL, the nucleus is considered to reside in a vacuum surrounded by individual molecules whose net electromagnetic effect, after motional averaging on the microscopic scale, can be neglected as it is vanishingly small [4]. The analytical expression for the field perturbation within a sphere is known [8] and given by,

$$\mathbf{B}_{\mathrm{d}} = \mathbf{B}\frac{2}{3}\left(\chi_{in} - \chi_{ext}\right) \qquad \text{Eq. 3.11}$$

where χ_{in} is the internal susceptibility within the sphere and χ_{ext} is the external susceptibility outside the sphere. The derivation of the field perturbation due to a sphere is discussed in Section 3.2.2.1. Considering the nucleus within the SOL, $\chi_{in} = 0$ and $\chi_{ext} = \chi$ leading to an internal field offset due to the SOL of

$$\mathbf{B}_{\mathrm{d}} = -\mathbf{B}\frac{2}{3}\chi \quad . \qquad \text{Eq. 3.12}$$

The macroscopic field, $\mathbf{B}_{mac}$, in Eq. 3.10 can be written as

$$\mathbf{B}_{mac} = \mu_0(1+\chi(\mathbf{r}))(H_0 + H_{obj}) \qquad \text{Eq. 3.13}$$

where H_0 is the magnetising field due to B_0, and H_{obj} is the so called 'demagnetising field' due to the geometry of the objects making up the susceptibility distribution. Substituting Eq. 3.13 into Eq. 3.10 gives,

$$\mathbf{B}_{nuc} = \left(1-\frac{2}{3}\chi(\mathbf{r})\right)\mu_0(1+\chi(\mathbf{r}))(H_0 + H_{obj}) \quad . \qquad \text{Eq. 3.14}$$

As discussed in the previous section the magnitudes of susceptibilities relevant for MRI are measured in parts per million (ppm), and the demagnetising field, H_{obj}, will also be in this range. Thus, ignoring 2nd order terms and above in χ and H_{obj} will reduce the accuracy of the expression by a negligible amount, and doing this simplifies Eq. 3.14 to:

$$\mathbf{B}_{nuc} = \mu_0\left(1+\frac{1}{3}\chi(\mathbf{r})\right)H_0 + \mu_0 H_{obj} \quad . \qquad \text{Eq. 3.15}$$

Moving back to the macroscopic regime, Maxwell's equation for **H**, assuming no current density, becomes:

$$\nabla \times \mathbf{H} = 0 \quad . \qquad \text{Eq. 3.16}$$

This means a scalar field called the magnetic potential, Φ, exists such that

$$\mathbf{H} = -\nabla\Phi \quad . \qquad \text{Eq. 3.17}$$

Maxwell's equations also state,

$$\nabla \cdot \mathbf{B} = 0 \quad . \qquad \text{Eq. 3.18}$$

Substituting Eq.3.17 into Eq.3.13 and inserting into the expression above gives

$$\nabla \cdot \mathbf{B}_{mac} = \nabla \cdot \left(\mu_0 (1 + \chi(\mathbf{r}))(-\nabla\Phi_0 - \nabla\Phi_{obj})\right) = 0 \qquad \text{Eq. 3.19}$$

where,

$$\begin{aligned} H_0 &= -\nabla\Phi_0 \\ \Phi_0 &= -H_0\mathbf{z} \\ H_{obj} &= -\nabla\Phi_{obj} \end{aligned} \qquad \text{Eq. 3.20}$$

.

Expanding Eq.3.19 [1] leads to,

$$-\nabla\chi(\mathbf{r}) \cdot \left(\nabla\Phi_0 + \nabla\Phi_{obj}\right) + (1 + \chi(\mathbf{r}))\left(\nabla^2\Phi_0 + \nabla^2\Phi_{obj}\right) = 0 \ .$$

Eq. 3.21

Substituting Eq.3.20 into Eq.3.21, removing any second order terms, and noting that $\nabla^2\Phi_0 = 0$, leads to:

$$\nabla^2\Phi_{obj} = -H_0 \frac{\partial\chi}{\partial z} \quad . \qquad \text{Eq. 3.22}$$

Eq. 3.22 is of a similar form to Poisson's equation

$$\nabla^2 V = -\frac{\rho}{\varepsilon_0} \qquad \text{Eq. 3.23}$$

where V is the electric potential related to the electric field E via $E = -\nabla V$, ρ is the charge density, and ε_0 is the permittivity of free space. This means that the field perturbation caused by the demagnetising field, H_{obj}, is equivalent to the electric field created by a charge distribution proportional to the z-gradient of the susceptibility distribution. The Fourier transform of equation 3.22 leads to [1],

$$FT(\Phi) = -iH_0\left(\frac{k_z}{k_x^2 + k_x^2 + k_x^2}\right)FT(\chi) \quad . \qquad \text{Eq. 3.24}$$

As described previously, for MRI we are only interested in the z-component of H_{obj}. Thus, H_{obj} can be re-written from Eq.3.20 as,

$$H_{obj} = -\frac{\partial\Phi}{\partial z} = -FT^{-1}\left(i\left(k_z\right)FT(\Phi)\right) \qquad \text{Eq. 3.25}$$

where the derivative has been carried out using the Fourier derivative theorem. Substituting Eq.3.24 into Eq.3.25 gives,

$$H_{obj} = -H_0 FT^{-1}\left(\left(\frac{k_z^2}{k_x^2 + k_x^2 + k_x^2}\right)FT(\chi)\right) \quad . \qquad \text{Eq. 3.26}$$

Substituting Eq.3.26 into Eq.3.15 gives,

$$\mathbf{B}_{nuc} = \mu_0\left(1 + \frac{1}{3}\chi(\mathbf{r})\right)H_0 - \mu_0 H_0 FT^{-1}\left(\left(\frac{k_z^2}{k_x^2 + k_x^2 + k_x^2}\right)FT(\chi(\mathbf{r}))\right) .$$

Eq. 3.27

Grouping terms in Eq.3.27 and noting that $B_0 = \mu_0 H_0$ gives,

$$\mathbf{B}_{nuc} = B_0 + B_0 FT^{-1}\left(\left(\frac{1}{3} - \frac{k_z^2}{k_x^2 + k_x^2 + k_x^2}\right)FT(\chi(\mathbf{r}))\right) .$$

Eq. 3.28

Hence, the field perturbation relative to the main magnetic field is given by a convolution of the susceptibility distribution with the dipole field kernel. This agrees with the Fourier derivation described in the previous section. The Fourier derivation has the advantage of incorporating the SOL implicitly, and involves relatively fewer steps. However, the derivation based on Maxwell's equations highlights the relationship between the magnetic field perturbation caused by a susceptibility distribution and the electric field produced by a distribution charge.

3.2 Simulating Field Perturbations

The previous section described the derivation of a simple Fourier relationship between the field perturbation and underlying susceptibility distribution,

$$\Delta B = B_0 FT^{-1}\left(\left(\frac{1}{3} - \frac{k_z^2}{k_x^2 + k_y^2 + k_z^2}\right) FT(\chi(\mathbf{r}))\right) \quad . \qquad \text{Eq. 3.29}$$

This section describes how the mathematical expression in Eq. 3.29 can be applied to digitised models of 3D susceptibility distributions to produce accurate field perturbation maps. The validation of the method based on known analytical solutions is also described.

3.2.1 Practical Application of the Fourier Method

The expression in Eq. 3.29 describes the convolution of a 3D susceptibility distribution, $\chi(\mathbf{r})$, with the dipole field kernel. It is called the dipole field kernel as it is the Fourier transform of the z-component of the field produced by a point dipole, i.e:

$$\left(\frac{1}{3} - \frac{k_z^2}{k_x^2 + k_y^2 + k_z^2}\right) = FT\left(\frac{3}{|\mathbf{r}|^3}\left(\left(\frac{\mathbf{r}\cdot\hat{\mathbf{z}}}{|\mathbf{r}|}\right)^2 - \frac{1}{3}\right)\right)$$

Eq. 3.30

where $\mathbf{r}$ is the point in space being considered, and $\hat{\mathbf{z}}$ is the direction of B_0. One important observation is that the kernel becomes undefined at $k_x = k_y = k_z = 0$. This has important implications as the centre of k-space defines the average offset of the field perturbation. For an object residing in a large surrounding empty region the field perturbation should average out to zero, so setting **k**(0,0,0) = 0 is a sensible choice. Generally, it is more consistent to define field differences relative to some known reference value. For the work described in the later chapters the centre of k-space is always set to zero. Before Eq. 3.29 can be implemented on digitised susceptibility distributions, the continuous 3D Fourier transform (*FT*) must be replaced with a discrete Fourier transform (DFT). An efficient algorithm for computing DFT's is the Fast Fourier Transform (FFT) [9]. By utilising FFT's, a simple methodology can be formed for calculating field perturbations based on a known susceptibility distribution. The flowchart in Figure 3.1 shows the steps involved in creating a map of the field perturbation, $\Delta B(\mathbf{r})$, due to a digitised susceptibility distribution, $\chi(\mathbf{r})$.

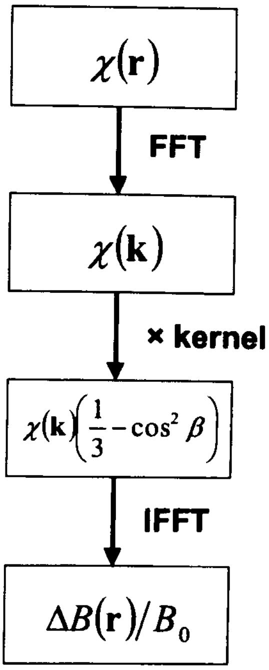

***Figure 3.1** Flow chart showing the three steps involved in simulating field maps based on known susceptibility distributions.*

Firstly, an FFT is applied to the digitised 3D susceptibility distribution. The k-space susceptibility distribution is then point-wise multiplied by the dipole field kernel. Lastly, an inverse FFT (IFFT) is applied to yield a 3D map of the field perturbation,

$\Delta B(\mathbf{r})/B_0$. To calculate a quantitative field map the field perturbation should be multiplied by the main magnetic field, B_0. Figure 3.2 shows an example of applying this methodology to the simple digitised susceptibility distribution of a sphere of homogeneous susceptibility residing inside a vacuum. A sphere, 10 voxels in radius, was set inside a 256 x 256 x 256 matrix. The voxels within the sphere were given a susceptibility of 1, while outside the sphere the susceptibility was set to zero as shown in Fig.3.2a. Figure 3.2 shows representative slices of the matrix after each of the different steps. The slices are taken from the central y-plane, since the susceptibility distribution, and the convolution kernel, are symmetric about the z-axis. The direction of the main magnetic field is set along the z-axis of the matrix. To make the images more easily interpretable, the Fourier space slices show the natural logarithms of the data values.

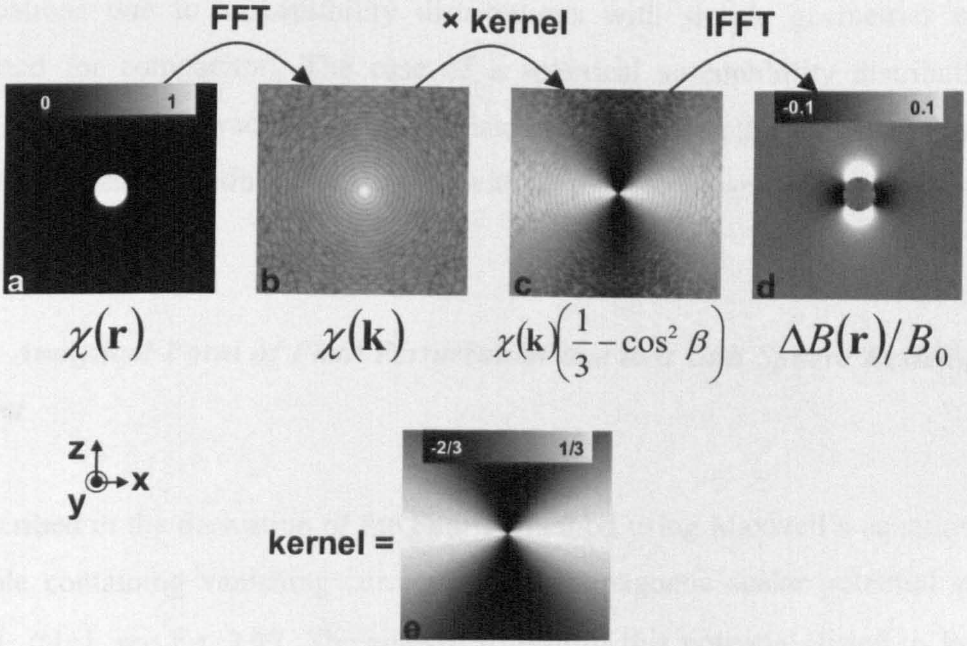

***Figure 3.2** Example of field perturbation calculation based on a spherical susceptibility distribution. Each image is a representative slice of a 3D volume taken from the central y-plane of: the spherical susceptibility distribution (a), FFT of (a) to give (b), (b) multiplied by the dipole field kernel (e) to give (c), IFFT of (c) to yield a field map (d).*

The field map shown in Fig. 3.2d, nicely demonstrates the non-local relationship between field maps and susceptibility maps. The well-defined, localised, spherical susceptibility map shown in Fig. 3.2a, after convolution with the dipole field kernel becomes spread out, and non-localised, in the field map shown in Fig. 3.2d. There is also a modulation of the sign of the field map around the sphere. This reflects the spatial variation of the convolution kernel shown in Fig. 3.2e. The simple Fourier methodology described above allows susceptibility maps defined on larger matrices to be analysed in a relatively short period of time. The main computational costs are the two FFT operations (*FFT* + *IFFT*), with the transform of a 256^3 matrix taking ≈ 5s on a PC with a 1.86 GHz dual-core processor and 2GB of RAM.

3.2.2 Validation of the Fourier Method

To validate the rapid Fourier method, the analytical solutions for the field perturbations due to susceptibility distributions with simple geometries can be calculated for comparison. The case of a spherical susceptibility distribution of radius a, residing in a vacuum will be considered first. Then the analytical forms for an infinite cylinder residing in a vacuum with its main axis parallel, and anti-parallel, to B_0 are described.

3.2.2.1 *Analytical Form of Field Perturbation due to a Unit Sphere Residing in a Vacuum*

As described in the derivation of the Fourier method using Maxwell's equations, for a sample containing vanishing current density a magnetic scalar potential can be utilised, $\Phi(\mathbf{r})$, see Eq. 3.17. The analytical form of this potential, listed in Jackson 1999 [8], is the sum of a volume integral and a surface integral given by

$$\Phi(\mathbf{r}) = -\frac{1}{4\pi}\int_V \frac{\nabla'\cdot\mathbf{M}(\mathbf{r}')}{|\mathbf{r}-\mathbf{r}'|}d^3r' + \frac{1}{4\pi}\oint_S \frac{\mathbf{n}'\cdot\mathbf{M}(\mathbf{r}')}{|\mathbf{r}-\mathbf{r}'|}da' \qquad \text{Eq. 3.31}$$

where $\mathbf{M}$ is the magnetisation distribution and $\mathbf{n}'$ is the surface normal of the magnetisation distribution. For a sphere with a homogeneous susceptibility, χ, surrounded by a vacuum, the first integral vanishes to leave only the surface integral. In biological samples the magnetisation is only along the z-axis such that

$$\mathbf{M}(\mathbf{r}') = M_0 \hat{\mathbf{z}} \quad . \qquad \text{Eq. 3.32}$$

For a sphere the dot product of the surface normal with the above magnetisation is given by

$$\mathbf{n}' \cdot \mathbf{M}(\mathbf{r}') = M_0 \cos(\theta) \qquad \text{Eq. 3.33}$$

where θ is the spherical polar coordinate such that $z = r\cos(\theta)$. Substituting Eq. 3.33 into Eq. 3.31, and using the polar coordinate expression for $da' = d\phi \sin\theta d\theta a^2$, where a is the radius of the sphere gives:

$$\Phi(\mathbf{r}) = \frac{M_0 a^2}{4\pi} \int d\theta' \sin\theta' d\phi' \frac{\cos(\theta')}{|\mathbf{r} - \mathbf{r}'|} \quad . \qquad \text{Eq. 3.34}$$

Further progress is made using a spherical harmonic expansion for the inverse distance [8]:

$$\frac{1}{|\mathbf{r} - \mathbf{r}'|} = 4\pi \sum_{l=0}^{\infty} \sum_{m=-l}^{l} \frac{1}{2l+1} \frac{r_<^l}{r_>^{l+1}} Y_{l,m}^*(\theta', \phi') Y_{l,m}(\theta, \phi) \qquad \text{Eq. 3.35}$$

where l and m index the spherical harmonic, $Y_{l,m}$, $r_>$ is equal to a and r for $r < a$ and $r > a$ respectively, and $r_<$ is equal to r and a for $r < a$ and $r > a$ respectively. For a spherical polar coordinate integration, the following identity is also valid [8]

$$\int_0^{2\pi} d\phi \int_0^{\pi} \sin\theta d\theta Y_{l,m}^*(\theta, \phi) Y_{l,m}(\theta, \phi) = \delta_{l'l} \delta_{m',m} \qquad \text{Eq. 3.36}$$

where $\delta_{l'l}\delta_{m',m}$ = 1 for $l'=l/m'=m$ and 0 for $l' \neq l/m' \neq m$. By substituting Eq. 3.36 and Eq. 3.35 into Eq. 3.34, noting that $Y_{10} = -\sqrt{(3/4\pi)}\cos\theta$, the scalar potential is given by

$$\Phi(\mathbf{r}) = \frac{1}{3} M_0 a^2 \frac{r_<}{r_>^2} \cos\theta \qquad \text{Eq. 3.37}$$

which for r < a (inside the sphere) this becomes

$$\Phi(\mathbf{r}) = \frac{1}{3} M_0 r \cos\theta = \frac{1}{3} M_0 \mathbf{z} \quad . \qquad \text{Eq. 3.38}$$

Substituting the expression above into Eq. 3.17, the so-called 'demagnetising field' inside the sphere is given by

$$\mathbf{H}_{obj=sphere} = -\frac{1}{3} M_0 \quad . \qquad \text{Eq. 3.39}$$

The expression for the macroscopic field, $\boldsymbol{B}_{mac}$, given in Eq. 3.13 can be re-written, ignoring 2nd order terms, as,

$$\Delta\mathbf{B}_{mac} = B_0\chi + \mu_0 H_{obj} \quad . \qquad \text{Eq. 3.40}$$

Substituting Eq. 3.39 into Eq. 3.40 and noting $\mu_0 M_0 = B_0$ gives,

$$\Delta\mathbf{B}_{mac} = B_0\chi - \mu_0 \frac{1}{3} M_0 = \frac{2}{3} B_0\chi \quad . \qquad \text{Eq. 3.41}$$

The microscopic effect of the SOL must now be added to the field above. Substituting Eq. 3.12 into Eq. 3.41 gives

$$\Delta\mathbf{B}_{in} = \left(\frac{2}{3}\chi B_0\right)_{mac} + \left(-\frac{2}{3}\chi B_0\right)_{SOL} = 0 \quad . \qquad \text{Eq. 3.42}$$

Interestingly, as the expression above indicates, the internal field offset for a spherical geometry is zero. The potential outside the sphere, when r > a, from Eq. 3.37 is given by

$$\Phi(\mathbf{r}) = \frac{1}{3} M_0 a^3 \frac{\cos\theta}{r^2} \quad . \qquad \text{Eq. 3.43}$$

This is the potential of a dipole field with dipole moment [8],

$$\mathbf{m} = \frac{4\pi a^3 M_0}{3}\mathbf{z} = \frac{4\pi a^3 \chi B_0}{3\mu_0}\mathbf{z} \quad . \qquad \text{Eq. 3.44}$$

The magnetic field due to a dipole orientated along the *z*-axis with moment, **m**, is given by [8],

$$\Delta\mathbf{B}_{out} = \mu_0 \frac{\mathbf{m}}{4\pi} \frac{1}{|\mathbf{r}-\mathbf{r}_d|^3}\left(\left(\frac{(\mathbf{r}-\mathbf{r}_d)\cdot\hat{\mathbf{z}}}{|\mathbf{r}-\mathbf{r}_d|}\right)^2 - \frac{1}{3}\right) \qquad \text{Eq. 3.45}$$

and substituting Eq. 3.44 into Eq. 3.45 yields a magnetic field outside the sphere equal to

$$\Delta\mathbf{B}_{out} = \chi B_0 \frac{a^3}{|\mathbf{r}-\mathbf{r}_d|^3}\left(\left(\frac{(\mathbf{r}-\mathbf{r}_d)\cdot\hat{\mathbf{z}}}{|\mathbf{r}-\mathbf{r}_d|}\right)^2 - \frac{1}{3}\right) \quad , \qquad \text{Eq. 3.46}$$

or equivalently, in spherical polar coordinates with the sphere placed at the origin,

$$\Delta\mathbf{B}_{out} = \chi B_0 \frac{a^3}{r^3}\left(\cos^2\theta - \frac{1}{3}\right) \quad . \qquad \text{Eq. 3.47}$$

3.2.2.2 *Analytical Form of Field Perturbation due to an Infinite Cylinder Residing in a Vacuum with its Main Axis Perpendicular to B_0*

In the case of an infinite cylinder of radius a with a homogeneous susceptibility equal to χ residing in a vacuum and with its main axis perpendicular to B_0, the resulting field perturbation is similar to that of the spherical case compressed into 2D space [10-12]. Assuming the cylinder is orientated along the x-axis, the field perturbation outside the cylinder is given by [10],

$$\Delta\mathbf{B}_{out} = \frac{\chi}{2} B_0 \frac{a^2}{\left(y^2 + z^z\right)}\left(z^2 - y^2\right) \qquad \text{Eq. 3.48}$$

or written in polar coordinates,

$$\Delta\mathbf{B}_{out} = \frac{\chi}{2} B_0 \frac{a^2}{r_{yz}^2}\left(2\cos^2\theta_{yz} - 1\right) \qquad \text{Eq. 3.49}$$

where $r_{yz} = (y^2+z^2)$, and $\theta_{yz} = \text{atan}(y/z)$. The demagnetising field within the cylinder is given by,

$$H_{obj=cylinder-perp} = -\frac{1}{2} M_0 \quad . \qquad \text{Eq. 3.50}$$

The macroscopic field in then given by,

$$\Delta\mathbf{B}_{mac} = B_0\chi - \mu_0 \frac{1}{2} M_0 = \frac{1}{2} B_0 \chi \quad . \qquad \text{Eq. 3.51}$$

Finally, adding the microscopic SOL effect to Eq. 3.51 leads to an internal magnetic field perturbation within the cylinder given by,

$$\Delta\mathbf{B}_{in} = \left(\frac{\chi}{2} B_0\right)_{mac} + \left(-\frac{2\chi}{3} B_0\right)_{SOL} = -\frac{\chi}{6} B_0 \quad . \qquad \text{Eq. 3.52}$$

3.2.2.3 *Analytical Form of Field Perturbation due to an Infinite Cylinder Residing in a Vacuum with its Main Axis Parallel to B_0*

For the case of an infinite cylinder parallel to $B_0\mathbf{z}$, the z-gradient of the susceptibility distribution is equal to zero for all points in space. Hence, from Eq. 3.22 it can be inferred that H_{obj} is zero for all points in space and the macroscopic field is local and given by,

$$\Delta\mathbf{B}_{mac} = B_0\chi - \mu_0(0) = B_0\chi \quad . \qquad \text{Eq. 3.53}$$

This means that outside the cylinder, where in a vacuum $\chi = 0$, the field perturbation is also zero ($\Delta\mathbf{B}_{out} = 0$). Finally, adding the microscopic SOL effect to Eq. 3.53 leads to an internal magnetic field perturbation within the cylinder given by,

$$\Delta\mathbf{B}_{in} = (\chi B_0)_{mac} + \left(-\frac{2\chi}{3}B_0\right)_{SOL} = \frac{\chi}{3}B_0 \quad . \qquad \text{Eq. 3.54}$$

3.2.2.4 *Comparison of Fourier Method Results to Analytical Forms*

Within this section, the results of applying the Fourier method to susceptibility distributions with simple geometries are compared to the associated analytical forms. The analytical expressions, described in the previous section, for a sphere and an infinite cylinder (perpendicular and parallel to B_0) are summarised in Table 3.1. To use the Fourier method, 3D digitised susceptibility distributions must be constructed. For the spherical case, a 256x256x256 matrix was populated with a sphere of radius 20 voxels and χ values = 1. Outside the sphere, the susceptibility was set to zero. Similarly, for the infinite cylinder case a 256^3 matrix was populated with a cylinder of 256 voxels in length, radius 20 voxels, and $\chi = 1$. For the anti-parallel and parallel cases, the cylinders were orientated along the *x*-axis and *z*-axis, respectively. The direction of B_0 was set parallel to the *z*-axis, and the field strength was set equal to unity (1T).

Geometry	**Internal field offset** $\Delta B_{in}\ (r < a)$	**External field offset** $\Delta B_{out}\ (r > a)$
Sphere	0	$\chi B_0 \frac{a^3}{r^3}\left(\cos^2\theta - \frac{1}{3}\right)$
Cylinder $\perp B_0$ (along x-axis)	$-B_0\frac{\chi}{6}$	$\frac{\chi}{2}B_0\frac{a^2}{r_{yz}^2}\left(2\cos^2\theta_{yz} - 1\right)$
Cylinder $\parallel B_0$ (along z-axis)	$B_0\frac{\chi}{3}$	0

***Table 3.1** Analytical expressions for the field perturbation due to spherical and cylindrical distributions of homogeneous susceptibility, χ, and radius, a, residing in a vacuum. B_0 is assumed to be parallel to the z-axis.*

The results of the Fourier method and the associated analytical fields are shown in Figure 3.3a-f. Also shown in Fig. 3.3g-l are difference plots taken along a 1D line at the centre of the matrix along the z-axis for the sphere and perpendicular cylinder, and the *x*-axis for the parallel cylinder. There are two difference plots for each susceptibility distribution, one with a scale from -0.4 to 0.4 (Fig. 3.3g-i), and the other with a zoomed scale (Fig.3.3j-l).

In general, there is good agreement between the results of the Fourier method and the analytical forms. However, the difference plots in Fig. 3.3g&h for the sphere and perpendicular cylinder show small errors, highlighted by arrows in the figure, at the boundaries of the susceptibility distribution. These errors are due to the discrete nature of the FFT's used to calculate the field maps in the Fourier method. At a discrete jump, like the boundary of the susceptibility distribution, the FFT operation generates ringing artefacts due to Gibbs phenomena [13]. This is a problem inherent in the Fourier method, and is difficult, if not impossible, to avoid. Aside from the large ringing artefacts at the boundaries of the susceptibility distributions, reduced ringing can be observed further away from the edges as shown by the dotted arrow in

Fig. 3.3j. These smaller ringing artefacts can often persist over large spatial areas despite being remote from boundaries.

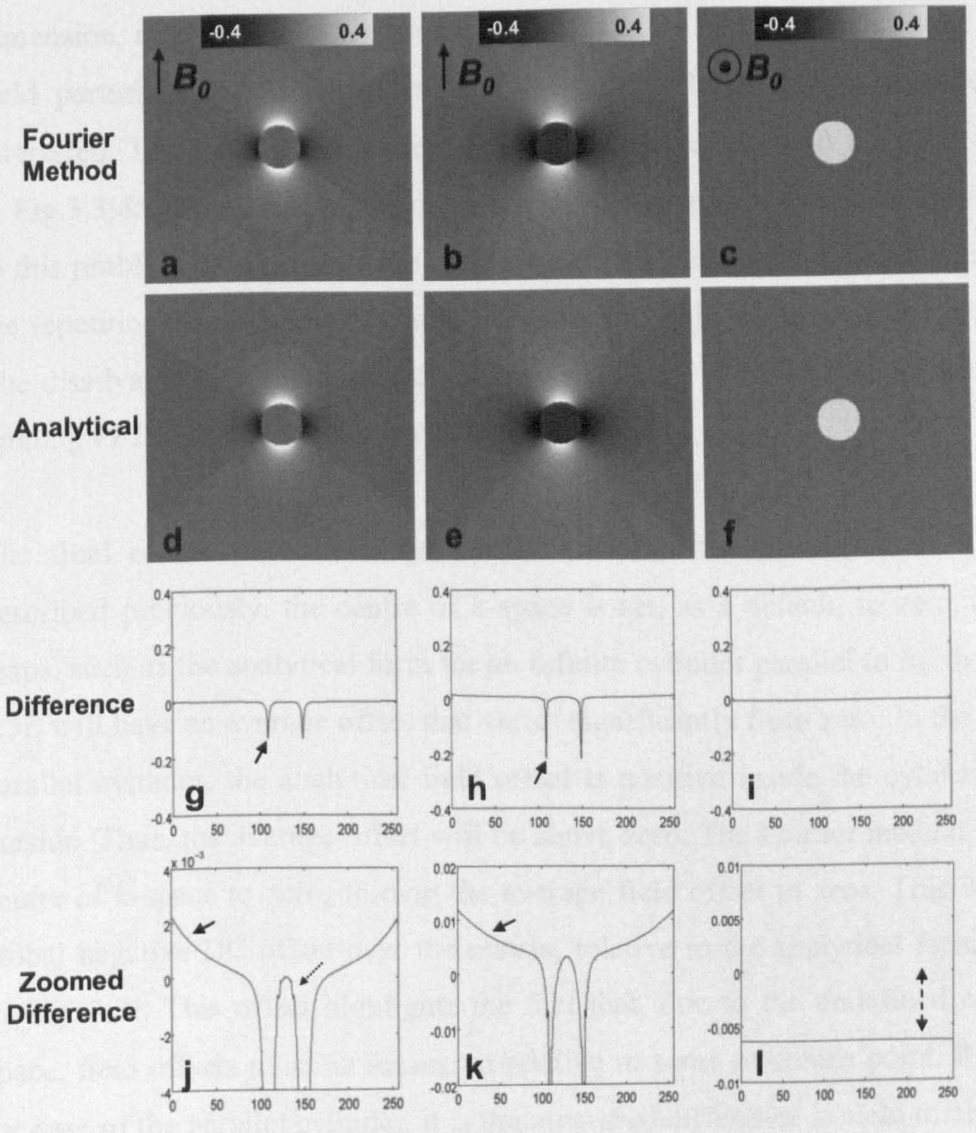

***Figure 3.3** Representative slices of simulated field perturbations using the Fourier method (a-c) and analytical fields (d-f) for: a sphere (a,d), an infinite cylinder perpendicular to the field (b,e), and an infinite cylinder parallel to the field (c,f). Also shown are two 1D difference plots, one large scale and one zoomed version, of the errors between the Fourier results and the analytical fields for the: sphere (g,j), perperndicular cylinder (h,k), and parallel cylinder (i,l).*

Another, more subtle effect, is the errors at the edge of the field of view (FOV), shown in the zoomed difference plots in Fig. 3.3j&k (see arrows). This effect is again due to the discrete Fourier transforms utilised by the Fourier method. A DFT has the effect of introducing repetitions of the susceptibility distribution in each dimension, so as to create a periodic spatial pattern [3]. These repetitions produce a field perturbation that interferes with the central field pattern in which we are interested. The interference pattern manifests itself as errors in the difference maps in Fig.3.3j&k, increasing as the edge of the FOV is approached. One simple solution to this problem is to increase the matrix size. This introduces a buffer region to shift the repetitions, and their associated interference fields, away from the central field. The disadvantage of increasing the matrix size is the growing computational cost of running FFT's on a large number of voxels.

The final source of error is the undefined value for the centre of k-space. As described previously, the centre of k-space is set, as a default, to zero. Some field maps, such as the analytical form for an infinite cylinder parallel to B_0 shown in Fig. 3.3f, will have an average offset that varies significantly from zero. In the case of the parallel cylinder, the analytical field offset is positive inside the cylinder and zero outside. Thus, the average offset will be above zero. The Fourier method will set the centre of k-space to zero, forcing the average field offset to zero. This will cause a global negative DC offset over the matrix, relative to the analytical form, as shown in Fig. 3.3l. This offset highlights the fact that, due to the undefined centre of k-space, field offsets must be measured relative to some reference point. Returning to the case of the parallel cylinder, it is the measured difference in field offsets between the external and internal compartments that should be used for comparison between the results of the Fourier method and the analytical form. Looking at differences between field offsets is an approach that is used extensively within this thesis and in other work investigating field maps generated from MRI phase data [14, 15].

3.2.2.5 *Improving the Fourier Method*

Some of the errors inherent in the basic Fourier method, highlighted in the previous section, can be reduced through the addition of a few extra steps. Firstly, the introduction of spatial smoothing with a Gaussian kernel can remove small ringing artefacts. The smoothing kernel can be multiplied directly by the dipole field kernel to yield the following expression for the field perturbation,

$$\Delta B = B_0 FFT^{-1}\left(\left(\frac{1}{3}-\frac{k_z^2}{k_x^2+k_y^2+k_z^2}\right)\exp\left(-\frac{\left(k_x^2+k_y^2+k_z^2\right)}{2\sigma^2}\right)FFT(\chi(\mathbf{r}))\right)$$

Eq. 3.55

where σ is the variable that controls the width of the Gaussian. Specifically, the full width at half maximum (FWHM) in k-space is given by,

$$\Delta k_{FWHM} = 2\left(\sqrt{2\ln 2}\right)\sigma \quad .$$

Eq. 3.56

A more sophisticated modification to the basic Fourier method is to tailor the dipole field kernel for a particular matrix/FOV size, so as to avoid aliasing artefacts. This approach was introduced by Cheng et al. [16] and requires the formation of the point-dipole field in image space before applying an FFT. The field due to a point dipole, given in Eq. 3.30, is placed at the centre of a matrix the same size as the matrix being used to carry out the field calculation. This field distribution is then Fourier transformed using an FFT to yield a field kernel that will, in theory, correct for the effect of aliasing. The disadvantage of this method is the increased computational effort required for calculating the extra FFT. The calculation of a field map including the smoothing kernel and tailored dipole kernel is then given by,

$$\Delta B = B_0 FFT^{-1}\left(FFT(Dipfield(\mathbf{r}))\exp\left(-\frac{\left(k_x^2+k_y^2+k_z^2\right)}{2\sigma^2}\right)FFT(\chi(\mathbf{r}))\right)$$

Eq. 3.57

where *Dipfield*(**r**) in spherical coordinates is given by,

$$Dipfield(\mathbf{r}) = \frac{3\cos^2\theta-1}{r^3} \quad .$$

Eq. 3.58

Figure 3.4 shows the new difference plot comparing the analytical field to the results of applying the adjusted Fourier method (Eq.3.57) to the spherical susceptibility distribution. The plots show a significant improvement in the accuracy of simulated field when using the smoothing kernel and tailored dipole field kernel.

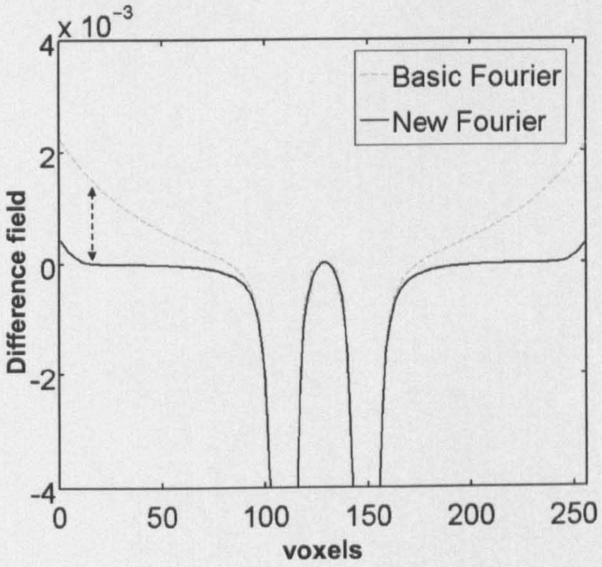

Figure 3.4 ***Plots of the field differences between the analytical field for a sphere in a vacuum and the simulated field created by: the basic Fourier method (grey dotted line), and the smoothed tailored dipole method (solid line).***

3.3 References

1. Salomir, R., B.D. De Senneville, and C.T.W. Moonen, *A fast calculation method for magnetic field inhomogeneity due to an arbitrary distribution of bulk susceptibility.* Concepts In Magnetic Resonance Part B-Magnetic Resonance Engineering, 2003. **19B**(1): p. 26-34.
2. Marques, J.P. and R. Bowtell, *Evaluation of a Fourier based method for calculating susceptibility induced magnetic field perturbations.* Proc ISMRM, 2003. **11**(1020).
3. Marques, J.P. and R. Bowtell, *Application of a Fourier-based method for rapid calculation of field inhomogeneity due to spatial variation of magnetic*

susceptibility. Concepts In Magnetic Resonance Part B-Magnetic Resonance Engineering, 2005. **25B**(1): p. 65-78.

4. Durrant, C.J., M.P. Hertzberg, and P.W. Kuchel, *Magnetic susceptibility: Further insights into macroscopic and miroscopic fields and the sphere of lorentz.* Concepts In Magnetic Resonance Part A, 2003. **18A**(1): p. 72-95.
5. Collins, C.M., B. Yang, Q.X. Yang, and M.B. Smith, *Numerical calculations of the static magnetic field in three-dimensional multi-tissue models of the human head.* Magnetic Resonance Imaging, 2002. **20**(5): p. 413-424.
6. Deville, G., M. Bernier, and J.M. Delrieux, *Nmr Multiple Echoes Observed In Solid He-3.* Physical Review B, 1979. **19**(11): p. 5666-5688.
7. Lorentz, H.A., *The Theory of Electrons and Its Application to the Phenomena of Light and Radient Heat.* 2nd Ed. 1915, New York: Dover.
8. Jackson, J.D., *Classical Electrodynamics.* 3rd ed. 1999: John Wiley and Sons, Inc.
9. Cooley, J.W. and J.W. Tukey, *An Algorithm for the Machine Computation of the Complex Fourier Series.* Mathematics of Computation, 1965. **19**: p. 297-301.
10. Haacke, E.M., R.W. Brown, M.R. Thompson, and R. Venkatesan, *Magnetic Resonance Imaging: Physical Priciniples and Sequence Design.* 1999, New York: WILEY-LISS.
11. Koch, K.M., X. Papademetris, D.L. Rothman, and R.A. de Graaf, *Rapid calculations of susceptibility-induced magnetostatic field perturbations for in vivo magnetic resonance.* Physics In Medicine And Biology, 2006. **51**(24): p. 6381-6402.
12. Bowtell, R., S. Gutteridge, and C. Ramanathan, *Imaging the Long-Range Dipolar Field in Structured Liquid State Samples.* Journal of Magnetic Resonance, 2001. **150**(2): p. 147-155.
13. Gibbs, J.W., *Fourier Series.* Nature, 1898. **59**.
14. Hammond, K.E., M. Metcalf, L. Carvajal, D.T. Okuda, R. Srinivasan, D. Vigneron, S.J. Nelson, and D. Pelletier, *Quantitative In Vivo Magnetic Resonance Imaging of Multiple Sclerosis at 7 Tesla with Sensitivity to Iron.* Annals Of Neurology, 2008. **64**(6): p. 707-713.

15. Duyn, J.H., P. van Gelderen, T.Q. Li, J.A. de Zwart, A.P. Koretsky, and M. Fukunaga, *High-field MRI of brain cortical substructure based on signal phase.* PNAS, 2007. **104**(28): p. 11796-11801.
16. Cheng, Y.C.N., J. Neelavalli, and E.M. Haacke, *Limitations of calculating field distributions and magnetic susceptibilities in MRI using a Fourier based method.* Physics in Medicine And Biology, 2009. **54**(5): p. 1169-1189.

CHAPTER 4

Using Simulations to Study Contrast in Field Maps based on Phase Data

The first part of this chapter discusses the steps required to extract field maps from phase data. The second section of this chapter describes how the Fourier based method, described in the previous chapter, can be used to simulate field perturbations in the human brain. This work uses segmented susceptibility distributions derived from magnitude image data acquired *in vivo*. These simulations are then compared to the field maps generated from *in vivo* phase data.

4.1 Processing Phase Data to yield Field Maps

In the early 1990's, phase images acquired using gradient echo techniques were starting to be utilised as a means of deriving field perturbations arising from paramagnetic contrast agents [1]. By arranging these paramagnetic agents in long thin cylinders, the measured field perturbation could be fitted to the analytical form of the field generated by an infinite cylinder to form an estimate of the magnetic susceptibility of the sample. These techniques developed further, and at the beginning of this century, the increased availability of high field MRI scanners led to the first *in vivo* measurements of susceptibility related phase contrast [2]. In 2004, Haacke et al. [3] introduced a technique called Susceptibility Weighted Imaging (SWI). The SWI method involves multiplying a filtered field map, derived from phase data, into the associated magnitude data a set number of times. The resulting SWI image will then show the susceptibility related contrast that is present in the field map, but will also include the structural information resulting from the magnitude signal. Specifically, the ability of SWI images to yield high quality maps of venous blood vessels in the brain and body has allowed the technique to develop into a widely used clinical tool [4, 5]. With the introduction of ultra high field (7T and above) whole body scanners, there was an anticipation that high resolution phase imaging would reveal new information about brain anatomy and physiology due to the increased susceptibility related field shifts associated with the higher B_0. A 2007 publication by Duyn et al. [6] was the first to demonstrate the potential of phase imaging at 7 T to yield exquisite contrast in the human brain. Phase imaging is now at the forefront of high resolution MRI [7-14], and with the seemingly never ending drive for higher and higher field strengths, the importance of understanding the contrast seen in field maps based on phase data cannot be underestimated.

4.1.1 The Problem with Phase Data: Wraps

In many fields of science and engineering there are often fundamental limitations on the ability of techniques to extract information from its sources. This is particularly true with phase imaging in MRI. The specific limitation on phase information is that, by definition, the measured phase will always lie between $-\pi$ and $+\pi$ relative to some reference frequency. In gradient echo based sequences, like the 3D FLASH sequence described in Section 2.2.5, the small field perturbations due to susceptibility differences cause spatial variation of the Larmor frequency. The effect, though much smaller in comparison, is similar to the spatial encoding carried out using linearly varying gradient fields. These small frequency shifts are accumulated within each TR for a time TE between the application of the RF pulse and the sampling of the centre of k-space. Generally, but not always, the frequency shift is smaller than the pixel bandwidth. Hence, the signal from a particular voxel is still localised to approximately the right point in space, and the associated magnitude data set will remain relatively unchanged. The measured phase is, however, highly sensitive to the small accumulated frequency offsets, $freq_{off}$, and is given by,

$$\phi = 2\pi freq_{off} TE = -\gamma \Delta B TE \qquad \text{Eq. 4.1}$$

where ΔB is the susceptibility related field offset. As described above, the phase can only be assigned to a range of values,

$$|\phi| \leq \pi \quad . \qquad \text{Eq. 4.2}$$

Figure 4.1 shows phase and magnitude data from a human brain acquired *in vivo* using a 3D FLASH sequence at 7T with TE = 15ms. The modulus data in Fig 4.1.a shows excellent structural detail of the human brain. The corresponding phase data, however, is dominated by discrete jumps or wraps. These wraps are a consequence of the phase measurements being limited to values in the range -π to +π. Outside of the head the phase data appears to show structured noise. This is due to ringing artefacts that emanate from sharp edges in the image such as the air/skull interface.

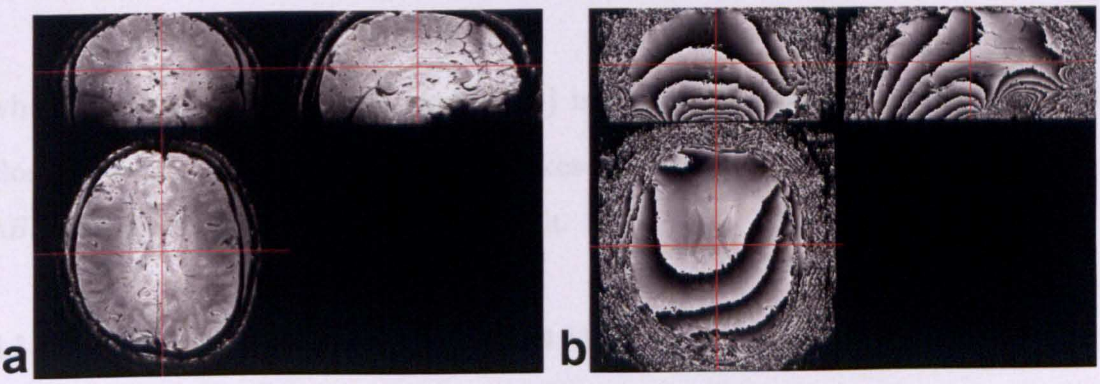

Figure 4.1 ***3D MRI data acquired using a FLASH sequence at 7T with TE=15ms. Representative slices in the transverse, coronal, and sagittal planes of the modulus data (a) and phase data (b).***

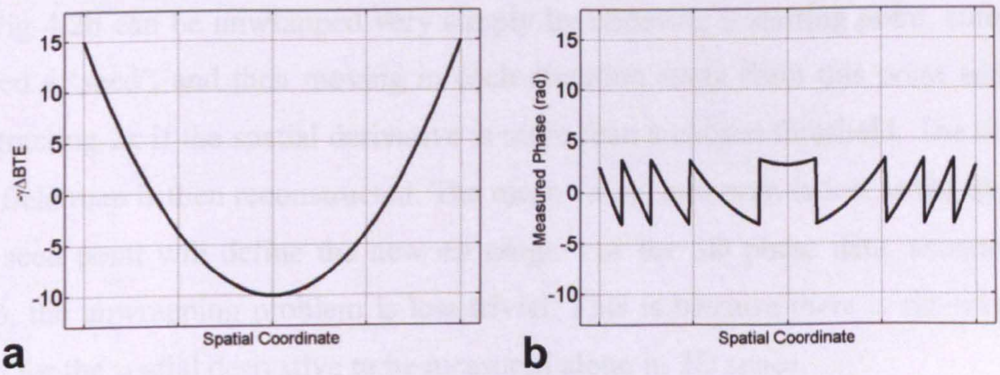

Figure 4.2 ***1D example of phase wrapping. The quadratic function representing the true scaled field map, -γΔBTE, (a) is discretely wrapped between –π and π when the phase in measured (b).***

Figure 4.2 shows a simple 1D example of phase wrapping. A quadratic function has scaled field map values (-$\gamma\Delta BTE$) ranging between -10 and 15 rad along an arbitrary spatial coordinate, see Fig 4.2a. The resulting measured phase values, lying in the ±π range, are shown in Fig 4.2b. The phase measurement compresses the true scaled field map such that the original field values are lost. As the true quadratic function evolves beyond the +π limit, the measured phase will take values close to –π creating a discrete jump of approximately 2π. The measured phase, $\phi_{measured}$ is given by,

$$\phi_{measured} = \phi_{true} - 2\pi \times \mathrm{int}\left[\frac{\phi_{true}}{2\pi}\right] \qquad \text{Eq. 4.3}$$

where ϕ_{true} is the true phase, and int[...] is an operator that rounds values to the closest integer. This wrapping effect makes a direct measurement of the field map, ΔB, from the measured phase data difficult.

4.1.2 Phase Unwrapping to yield a Field Map

Phase data sets containing wraps can be adjusted, through a process known as unwrapping [15], to yield a field map free from discrete jumps. Generally, unwrapping algorithms attempt to add integer multiplies of 2π to the measured phase to reconstruct a field map with a smooth spatial derivative. The 1D phase data shown in Fig 4.2b can be unwrapped very simply by choosing a starting point, sometimes called a 'seed', and then moving in each direction away from this point adding or subtracting 2π if the spatial derivative is more than a chosen threshold. The shape of the field map is then reconstructed. The mean value, however, is lost as the choice of the seed point will define the new ±π range. For the 3D phase data, shown in Fig 4.1b, the unwrapping problem is less trivial. This is because there is no unique 1D path for the spatial derivative to be measured along in 3D space.

The most widely used phase unwrapping algorithm for MRI data is the Phase Region Expanding Labeller for Unwrapping Discrete Estimates (PRELUDE) [15]. This algorithm groups the phase data into regions with similar phase values. It then merges them via the addition or subtraction of an integer multiple of 2π at the borders between regions. This unwrapping technique is robust, but can take on the order of 10 hours to process a 256 x 256 x 256, high-resolution data set with a large number of phase jumps. One way of speeding up the algorithm is to unwrap the data only within a mask of the brain. Brain masks can be produced via brain extraction algorithms such as the Brain Extraction Tool (BET) [16].

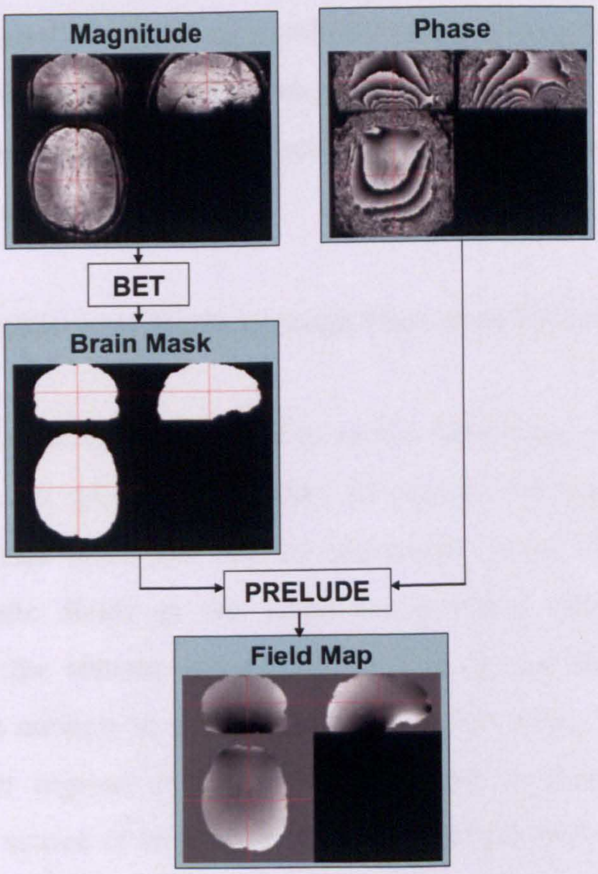

***Figure 4.3** Flow chart showing unwrapping methodology of using PRELUDE to unwrap phase data with the added input of a brain mask created using BET. The final field map is free of discrete 2π jumps.*

Figure 4.3 shows the results of applying the BET algorithm to the magnitude data shown in Fig. 4.1a. The result of unwrapping the phase data shown in Fig 4.1b using PRELUDE, with the BET mask as an extra input, is also shown in Fig 4.3. Both PRELUDE and BET are obtainable in the freely available FSL software package [17, 18]. The output of the PRELUDE algorithm is then a scaled field map ($-\gamma \Delta BTE$), free of phase jumps (Fig 4.3). A normalised field map can then be created by scaling the unwrapped phase data via,

$$\Delta B_{normalised} = \frac{\Delta B}{B_0} = \frac{\phi_{unwrapped}}{-\gamma TEB_0} \quad . \qquad \text{Eq. 4.4}$$

This normalised field map is then a dimensionless quantity, often measured in ppm ($1\text{x}10^{-6}$) due to the relatively small susceptibility values of materials relevant to MRI. This field map is independent of B_0, and can be used to evaluate susceptibility related contrast. Further references to 'field maps' within this work will assume the field map has been normalised.

4.1.3 Removing Background Fields through High-Pass Filtering

After unwrapping and scaling phase data to yield a field map, a new problem arises. Invariably, field maps will be dominated by slowly varying large length-scale background fields that mask the desired anatomical detail. One source of large length-scale magnetic fields is the large susceptibility difference at air/tissue interfaces found in the sinuses and ear canals. The dipolar fields created at these interfaces are large enough to be measured inside the brain, and are particularly strong in the lower regions of the brain which are in closer proximity to the interfaces. Another source of large scale background field shifts present in the brain is field inhomogeneities due to imperfections in the manufacture of the scanner. MR scanners are designed to have a very homogeneous B_0, but phase imaging is sensitive to very small variations in field strength. Shimming coils are often used to correct these spatial variations in B_0, and while they do reduce the field inhomogeneities it is generally the case that some unwanted field shifts remain.

Generally, the unwanted background fields show a slow spatial variation, while the desired anatomical contrast varies at higher spatial frequency. Due to this difference, high-pass filtering can be employed to remove the background fields. In most clinical applications of field maps, the data are analyzed slice by slice in the transverse plane (i.e. in the 2D plane normal to the magnetic field). The two main methods for filtering phase data are: (i) subtraction of a field map that has been smoothed via Fourier methods [19], and (ii) subtraction of a fitted 2D polynomial [6]. Figure 4.4 shows the methodology for filtering field maps using both the Fourier and the polynomial methods. For the Fourier smoothing method, the field map is convolved with a smoothing kernel, characterised by its Full Width at Half Maximum (FWHM). Gaussian smoothing kernel with a FWHM of 16 voxels was used to produce the results shown in Fig 4.4. For the 2D polynomial fit, polynomials up to and including the 8th order were used. The results of applying the 2 filters to a mid-brain slice and a lower slice (more towards the feet) are shown.

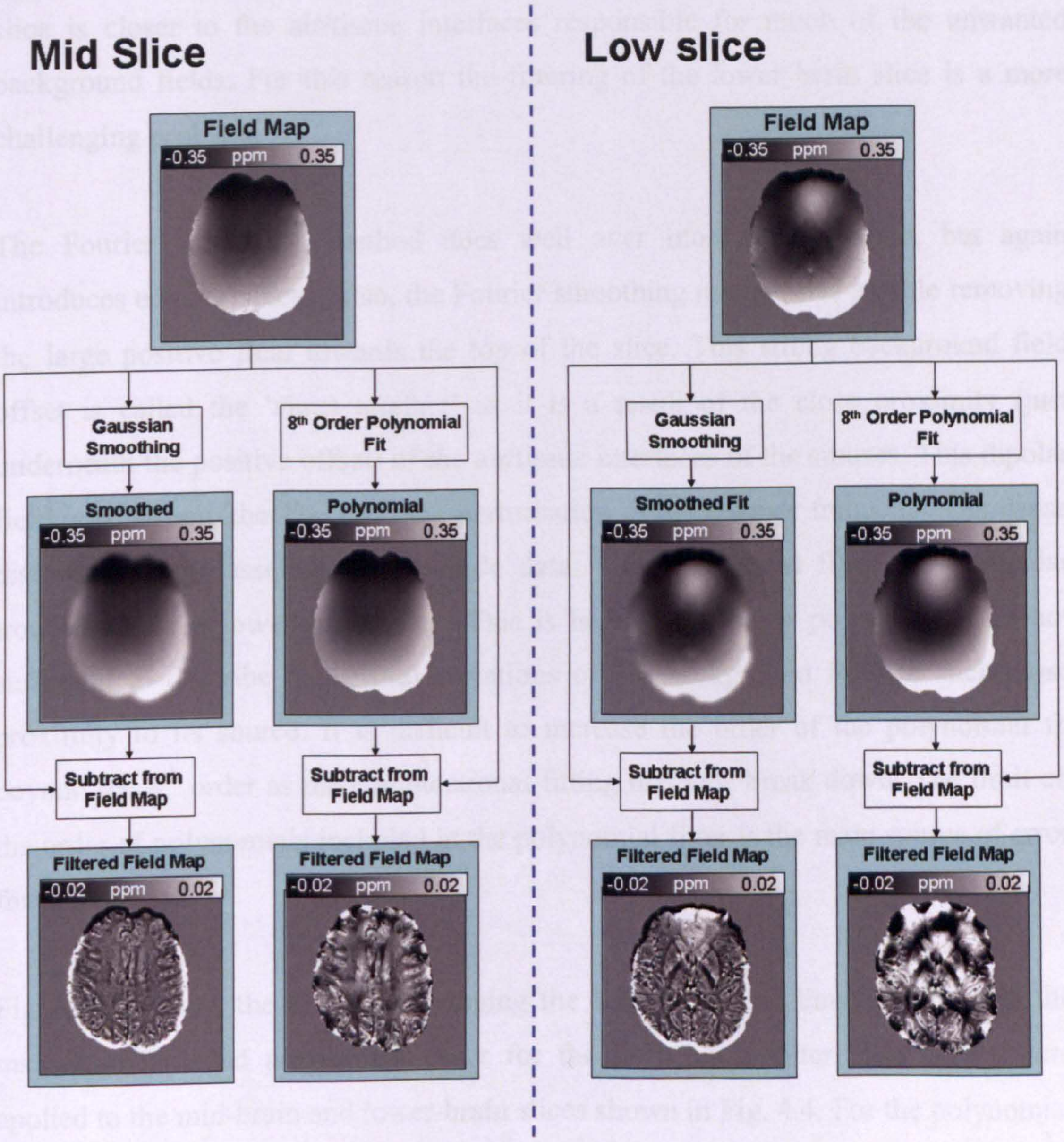

***Figure 4.4** Methodology for 2D high-pass filtering of field map data using polynomial fitting (8^{th} order) and Fourier smoothing (FWHM = 8mm). The results of applying the two filters to transverse slices of the mid-brain and lower brain are shown for comparison.*

For the mid-brain slice, both methods work fairly well. The large length-scale fields have been removed over the bulk of the slice to yield the desired anatomical detail. At the edges of the slice, however, the performance of the filtering is less impressive. The Fourier smoothing introduces strong edge artefacts. This is due to the smoothing kernel mixing information inside the brain with the zeros outside the brain. The polynomial method produces better results, with some anatomical detail visible at the edge of the brain, but large field offsets remain in some locations. The lower brain slice is closer to the air/tissue interfaces responsible for much of the unwanted background fields. For this reason the filtering of the lower brain slice is a more challenging problem.

The Fourier smoothing method does well over most of the brain, but again introduces edge artefacts. Also, the Fourier smoothing method has trouble removing the large positive field towards the top of the slice. This strong background field offset is called the 'sinus artefact' as it is a result of the close proximity (just underneath the positive offset) of the air/tissue interfaces of the sinuses. This dipolar field is so strong, that the resulting perturbation of the Larmor frequency can cause distortion in the associated magnitude data. The polynomial filter has particular trouble with the lower brain slice. This is because 8th order polynomials are not sufficient to describe the spatial variations of the background field in such close proximity to its source. It is difficult to increase the order of the polynomial fit beyond the 8th order as the computational fitting methods break down. The limit on the order of polynomials included in the polynomial filter is the main source of error for this method.

Figure 4.5 shows the effect of changing the FWHM of the Fourier filter and the maximum included polynomial order for the polynomial filter. The filters were applied to the mid-brain and lower-brain slices shown in Fig. 4.4. For the polynomial filter, the results show that increasing the order of the maximum included polynomial allows the background field to be mapped more accurately. On increasing the polynomial order, the filtered field maps become flatter and the desired anatomical detail starts to become more visible. However, for the low brain slice the sinus artefact is rapidly spatially varying and, as discussed above, cannot be accurately mapped by even the 8th order polynomial.

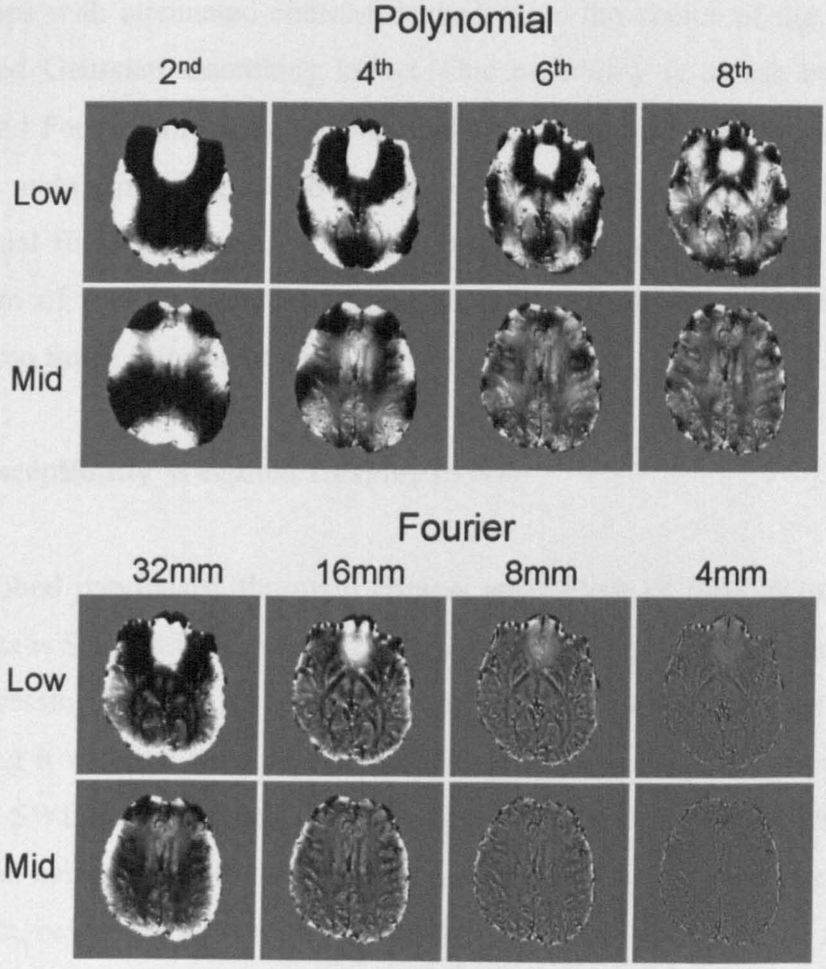

***Figure 4.5** Comparison of Polynomial and Fourier filter methods. The FWHM (mm) and the order of the maximum included polynomial were varied for the Fourier and Polynomial filter respectively. The filters were applied to a mid brain slice and a lower brain slice.*

For the Fourier filter, the results show that reducing the FWHM of the Gaussian smoothing kernel allows the unwanted background field to be modelled more accurately. However, as the FWHM is decreased so is the contrast in the final filtered field map. This is a result of the Gaussian kernel, used to smooth the field maps, removing frequency information associated with the desired anatomical detail as well as the unwanted background field. This 'blind' removal of frequency components is a severe limitation of the Fourier filter. To summarise, the polynomial filter is ideal for removing unwanted background fields in regions where the background field is slowly spatially varying. The Fourier filter is more robust than the polynomial filter in dealing with rapidly spatially varying field, but will yield field maps with attenuated contrast dependent on the choice of the FWHM of the associated Gaussian smoothing kernel. One possibility is to use both polynomial fitting and Fourier smoothing in combination. This would possibly give small gains for data exhibiting large-scale spatial variations that vary too quickly for the polynomial filter to accurately remove, but still vary slow enough for the FWHM maximum of the Gaussian smoothing kernel to be set at a level which will not remove too much information.

4.1.4 Susceptibility Weighted Imaging (SWI)

As described previously, the main clinical application of field maps derived from phase data is Susceptibility Weighted Imaging (SWI) [3, 5]. SWI is, essentially, a 2D post-processing method for extracting useful information from phase images, and combining it with the structural information present in magnitude images. The first stage of SWI image formation is high-pass filtering. Generally, this filtering is carried out using a Fourier smoothing filter applied directly to the original measured phase data, before the unwrapping procedures described above. While this avoids the lengthy unwrapping procedure, the FWHM of the smoothing kernel is generally smaller relative to that which is used on unwrapped data [8]. This is a disadvantage, as smaller kernel values reduce contrast. An investigation of the exact effect of different FWHM values on the contrast seen in field maps is described in the next section. The 'badly behaved' discrete phase jumps described previously, can be avoided by expressing the phase as a complex number,

$$Z = \mathrm{Re} + i\,\mathrm{Im} \qquad . \qquad \text{Eq. 4.5}$$

The real and imaginary parts are given by,

$$\begin{aligned} \mathrm{Re} &= \cos(\phi) \\ \mathrm{Im} &= \sin(\phi) \end{aligned} \qquad \text{Eq. 4.6}$$

where ϕ is the measured phase. The Fourier smoothing is then applied to both the *Re* and *Im* images, separately. These smoothed images are then used to form a low-pass complex image, given by:

$$Z_{low-pass} = \mathrm{Re}_{smoothed} + i\,\mathrm{Im}_{smoothed} \quad . \qquad \text{Eq. 4.7}$$

A high-pass complex image is then created via complex division of the original complex phase with the low-pass filtered complex image,

$$Z_{high-pass} = \frac{Z}{Z_{low-pass}} = \frac{\mathrm{Re} + i\,\mathrm{Im}}{\mathrm{Re}_{smoothed} + i\,\mathrm{Im}_{smoothed}} \quad . \qquad \text{Eq. 4.8}$$

The high-pass filtered phase can then be extracted from this complex image using a four quadrant arctangent operation. Generally, the filtered phase is not scaled, as described previously for field maps, but instead left in units of radians (rad). The next stage in SWI image formation is to use the filtered phase to create a mask of blood vessels carrying deoxygenated blood. Before going further, the theoretical basis for creating the mask will be described.

For veins carrying deoxygenated blood, the internal susceptibility will be strongly paramagnetic, relative to the surrounding tissue [1]. By convention, SWI of the human brain is carried out using 2D transverse (constant z-plane normal to B_0) slices. For this reason, the technique is mainly focused on blood vessels perpendicular to the main field with a main axis in the transverse plane. For modelling the field variation, these blood vessels can be represented as infinite cylinders of unit susceptibility orientated perpendicular to B_0. Figure 4.6a shows the associated analytical field map in a plane normal to the axis of the cylinder (using the expression given in Table 3.1 of Chapter 3). The measured phase inside a specific voxel is given by the ratio of the *Re* to *Im* signals after Fourier reconstruction of the NMR signal, see Eq. 2.58. If we assume the voxel can be split up into N smaller chunks, or 'sub-voxels', then the measured complex signal inside the large voxel is given by

$$Z_{measured} = \mathrm{Re} + i\,\mathrm{Im} = \sum_{i=1}^{N} S_i \exp(i\gamma TE \Delta B) \qquad \text{Eq. 4.9}$$

where S_i is the signal strength of the ith sub-voxel which, as discussed in Section 2.2.4, ignoring differences in proton density and T_1 is given by:

$$S_i \propto \exp\left(-\frac{TE}{T^*_{2\,i}}\right) \qquad \text{Eq. 4.10}$$

where $T_2^*{}_i$ is the T_2^* decay constant specific to a certain sub-voxel.

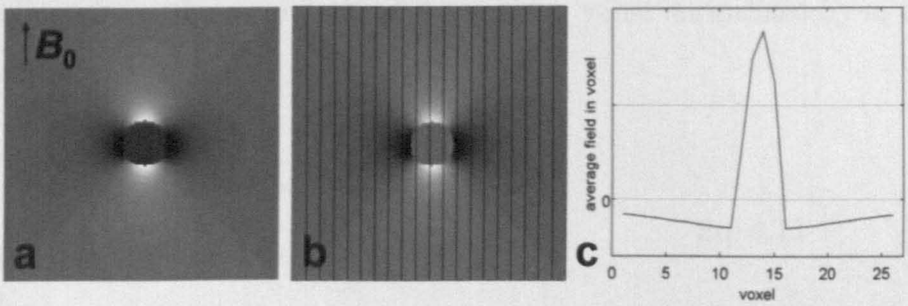

***Figure 4.6** Plots showing the theoretical basis for vessel isolation in SWI masks. Shown is the field map due to an infinite cylinder perpendicular to B_0 (a), the contributing field where the internal field is masked (b), the long-thin voxels (lines in b), and the field profile sampled by the voxels.*

The T_2^* value for deoxygenated blood (≈ 7ms) is considerably shorter than that of the surrounding tissue (≈ 30ms) [4]. Thus, at a sufficiently long TE the signal from sub-voxels inside the blood vessel will have decayed to zero, while those in the surrounding tissue will still have some associated signal. The averaged complex signal of the large voxel will then only depend on the field map outside the blood vessel. Returning to the cylindrical model, the external field map region contributing to the average complex signal is shown in Fig 4.6b, with the cylinder interior set to zero. This masked field map is then sampled using voxels that are large relative to the diameter of the cylinder in the z-axis (B_0 direction), but small enough in the x-axis and y-axis (transverse plane) to give at least one voxel lying entirely within the cylinder dimensions. These Long Thin (LT) voxels are represented by the faint lines in Fig 4.6b. The profile of the measured field map, after sampling with the LT voxels, is shown in Fig 4.6c. The resulting field profile is positive in voxels containing the vessel/cylinder, but negative outside. The optimum height to width ratio of LT voxels, when the aim is to highlight cylindrical blood vessels, is approximately 2 [14].

Returning to SWI image formation, a mask of venous blood vessels can be constructed based on the filtered phase, assuming the height to width ratio of the imaging voxels is ≥ 2. The vessel mask is constructed using two simple rules: (i) negative field offsets are set to 1, and (ii) positive field offsets are set to a value that depends linearly on the magnitude of the positive value normalised by π, or written mathematically:

$$\begin{aligned} Vesselmask(\Delta\phi \le 0) &= 1 \\ Vesselmask(\Delta\phi > 0) &= \frac{\pi - \Delta\phi}{\pi} \end{aligned} \qquad \text{Eq. 4.11}$$

where $\Delta\phi$ is the filtered phase in radians, sampled using LT voxels. The resulting vessel mask is then multiplied into the associated magnitude data an integer, *m*, number of times to yield a SWI image, such that

$$SWI = Magnitude \times \left(Vesselmask^{m}\right) \qquad \text{Eq. 4.12}$$

The optimal value of *m* is dependent on the SNR of the MRI data [3], and is generally determined through trial and error. Figure 4.7 shows the results of each step in SWI image formation for a FLASH data set with TE = 15 ms and voxel dimensions = 0.7 x 0.7 x 1.4mm^3 which was acquired at 7T. Thus the height to width ratio of the LT voxels used in this imaging sequence was 2. Fig. 4.7a shows a slice at the mid-brain level of the magnitude data set. The associated measured phase is shown in Fig. 4.7b. The phase of the low-pass filtered complex image, $Z_{low\text{-}pass}$, is shown in Fig. 4.7c. The filtered phase, extracted after the division of the complex image based on the original phase by the complex image based on the low-pass phase, is shown in Fig 4.7d. The *Vesselmask* based on the filtered phase is shown in Fig. 4.7e. The SWI image, using $m = 5$, is shown in Fig. 4.7f. After 5 multiplications with the *Vesselmask*, the magnitude data shows improved vessel contrast with vessels shown as 'dark' hypo-intense regions.

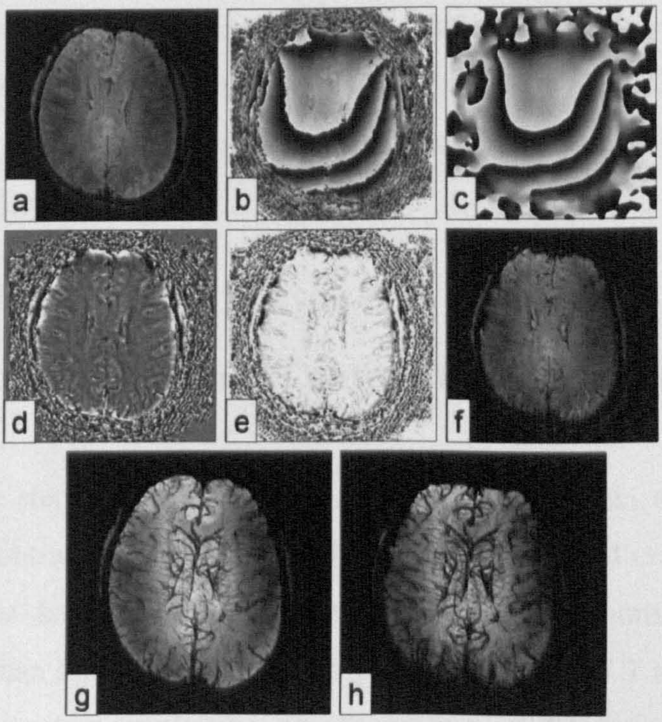

<u>Figure 4.7</u> Images showing the results of each step in SWI image formation: original magnitude data (a) and measured phase image (b), the low-pass filtered phase image (c), the high-pass filtered phase image using a smoothing kernel with FWHM = 8mm based on (b) and (c) shown in (d), the Vesselmask based on (d) shown in (e), the SWI image (f), the MIP over 10 slices for the original magnitude data (g) and for the SWI data (h).

A widely used method for vessel visualisation is the formation of Minimum Intensity Projection (MIP) images. The minimum intensity at a certain x-y voxel location is measured over a number of slices to yield a single composite image. To demonstrate the improved vessel contrast of SWI images the MIP created using the modulus data, measured over 10 slices, is shown in Fig. 4.7g. For comparison, the corresponding SWI MIP over the same volume is shown in Fig. 4.7h. As the images show, the MIP based on the SWI data shows vessels more clearly with a large number of small vessels evident. While SWI images are useful, the technique is limited to visualising small structures aligned perpendicular to the main magnetic field. This is because the assumption that positive contrast in field maps corresponds to a local increase in positive magnetic susceptibility is only valid when sampling is carried out using LT voxels, ideally larger than the structure being investigated. The second part of this chapter uses simulations to explore the relationship between susceptibility distributions with simple geometries and their associated field maps. This investigation will highlight the limitations and dangers of using 2D SWI images to investigate larger brain structures.

4.2 Using Simulations to Study Contrast in Field Maps

In Section 4.1 the steps for creating field maps from phase data were discussed. In this section, the contrast seen in these field maps is investigated using simulations of field perturbations based on known susceptibility distributions. The increasing availability of human scanners operating at magnetic fields of 7 T and above, has led to a growing interest in exploiting phase contrast in anatomical and functional imaging [6, 13, 14, 20, 21]. In particular, phase images obtained at 7 T have been shown to provide enhanced grey to white matter contrast compared with modulus data and to allow the delineation of cortical sub-structure [6], including the stria of Gennari. Phase imaging at 7 T has also recently been used to probe changes in the magnetic susceptibility in a range of brain areas resulting from multiple sclerosis [8]. The latter study forms part of a growing body of work in which phase values read off from anatomically defined regions of interest in phase maps are used to characterize regional changes in magnetic susceptibility that may be related to variations in iron content [22-25].

4.2.1 Phase Contrast at 7 T

Figure 4.8 shows example transverse, phase images and corresponding modulus data acquired at 7 T from the human brain in a superior slice at the level of the motor cortex and a more inferior slice spanning the lateral ventricles. Prior to display, the phase data have been subject to the post processing described in the previous section to yield a field map. This processing involved phase unwrapping to eliminate discontinuities in the calculated phase, followed by high-pass filtering to remove the effects of large length-scale magnetic field inhomogeneities.

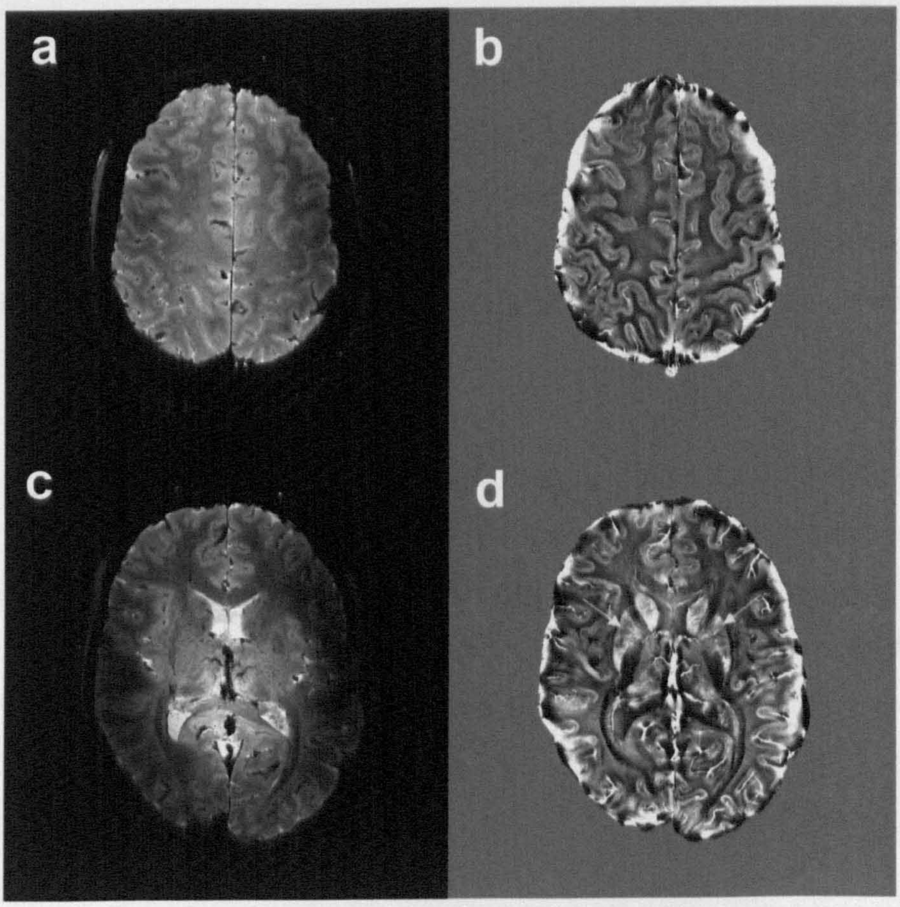

Figure 4.8 ***Representative phase and corresponding magnitude images ($0.25\times0.25\times1.5$ mm^3) resolution acquired from the human brain at 7 T using a three dimensional gradient echo sequence with TE/TR=20/45 ms. The phase images have been unwrapped and high-pass filtered using a filter kernel with an 8 mm FWHM. (a) and (b) show magnitude and phase images from a superior axial slice, whilst (c) and (d) are taken from a more inferior region. The arrows in (d) mark a region where the phase is affected by the presence of the putamen, even though the putamen is not evident in the corresponding modulus image (c).***

The resulting field maps display key features including; clearly delineated small veins; sharp boundaries between grey matter (GM) and white matter (WM), and between grey matter and cerebro-spinal fluid (CSF) in cortical regions; larger phase differences between deep grey matter structures and surrounding white matter; field offsets following the ordering CSF < WM < cortical GM < deep GM < veins; regions of reduced field in the optic radiations. In the inferior slice, it is also evident that some structures which appear in the phase image are not clearly delineated in the corresponding modulus data. In particular the arrows in Fig. 4.8d mark a region of the map where the phase is affected by the presence of the putamen, even though this structure is not clearly depicted in the corresponding modulus image. Despite the significant literature on the use of susceptibility induced phase effects in biomedical imaging and the growing interest in the exploitation of the enhanced phase changes that occur at high static field, the basic features of susceptibility-related phase contrast have not been explored in detail and in particular important questions remain about the level of spatial localization and quantification that phase contrast provides.

From the above discussion, it is evident that a fuller understanding of the characteristics of susceptibility-induced phase contrast would be valuable. In this section the results of utilising the Fourier-based method for rapidly simulating the field perturbations produced by a general distribution of magnetic susceptibility are presented and used to explore the relationship between the form of the susceptibility distribution and the resulting phase image contrast.

4.2.2 Phantom Validation of Fourier Method

Before simulated field maps can be compared to *in-vivo* MRI data, the Fourier method for calculating field perturbations must be validated by comparison with measurements from a known susceptibility distribution. For this purpose, a 10-cm-diameter spherical agar phantom, containing a random arrangement of small, cylindrical sections of agar that had been doped with an iron oxide based contrast agent, was created. In separate experiments the susceptibility of the agent was measured to be 0.15±0.01ppm/mM at 7T. These experiments involved doping a long thin cylinder with varying concentrations of the contrast agent and comparing the measured MRI phase images with the analytical form for a parallel cylinder (see Chapter 3). Cylindrical sections containing two different concentrations (0.5 mM and

1 mM) of the contrast agent were used, yielding a test sample showing a structured variation of magnetic susceptibility that spanned a similar range of values to those found in the human brain. Gradient echo images (phase and magnitude) of the phantom were acquired using a FLASH sequence with 0.5 mm isotropic resolution and a field of view of 128×128×65 mm^3, using TE/TR values of 16/45 ms and a nominal flip angle of 16°.

The phase images were masked using BET and unwrapped using PRELUDE, before elimination of large length-scale phase variation. The latter was accomplished by fitting and subtracting a 2D, 3rd order polynomial from each slice of the phase data. A 3rd order polynomial was chosen through trial and error as the lowest order polynomial that best fitted, and removed, the large length-scale phase variation. After this processing, the phase images were scaled to yield field maps of the field perturbation offset in parts per million (ppm). To test the validity of the field calculations, the field perturbation produced by the structured phantom was simulated. In order to do this, the modulus images of the phantom were segmented by hand into three compartments, corresponding to undoped agar and agar doped with the two different concentrations of contrast agent (χ=0.15 and 0.075 ppm). This yielded a susceptibility distribution spanning a region of 170×170×100 voxels extent which was inserted into a 400×400×400 matrix and surrounded by voxels of zero susceptibility. The Fourier method was used to simulate the field map due to this digitised susceptibility distribution. Specifically, the field map was simulated using Eq.3.51 (Chapter 3) with spatial smoothing using a filter with a FWHM of 1.5 voxels.

Figure 4.9 shows magnitude images and phase/field data acquired from the structured phantom, along with the corresponding simulated data. Figs. 4.9a and f show magnitude images from central transverse and axial slices, whilst corresponding slices from the susceptibility distribution which was used in the simulations are shown in Figs. 4.9c and h. High-pass filtered field maps measured from the same slices are shown in Figs. 4.9b and g (in ppm), whilst the calculated maps are shown with the same scaling in Figs. 4.9d and i. There is good agreement between the measured and simulated maps. This is particularly evident from Figs.

4.9e and j which show the differences between the measured and calculated field maps.

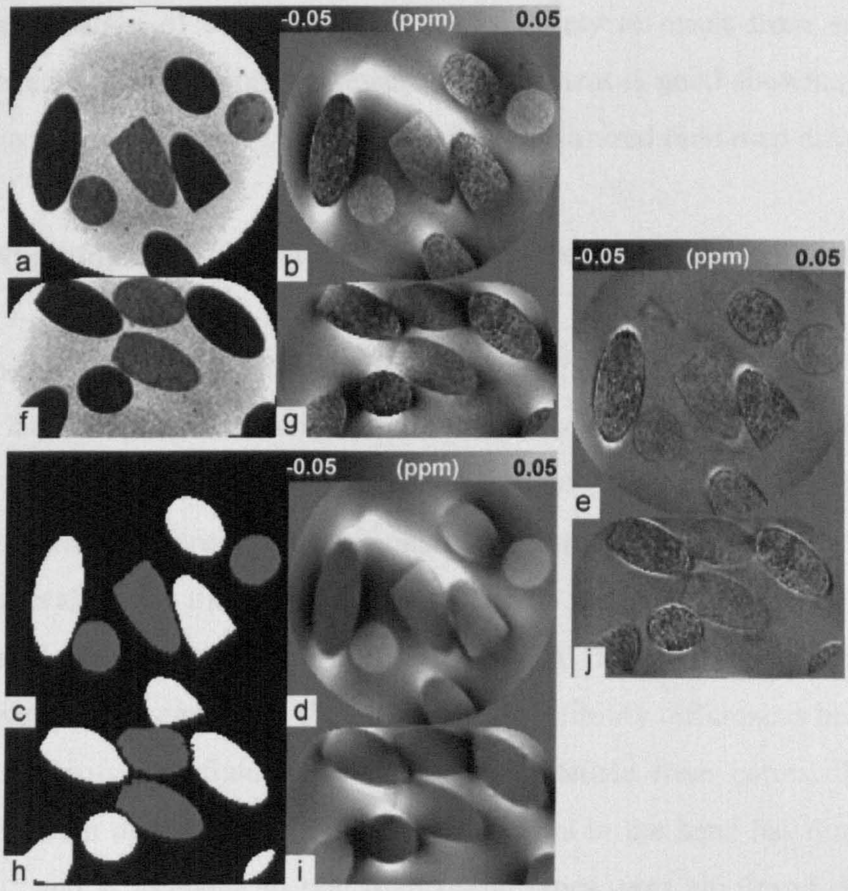

<u>Figure 4.9</u> Measured and simulated data from a structured phantom consisting of short cylindrical sections of iron oxide loaded agar inside a 10 cm diameter undoped agar sphere. (a) and (f) show experimentally acquired magnitude data from central, axial and coronal slices (0.5×0.5×0.5mm3 voxel size). (b) and (g) show corresponding experimentally measured frequency maps (in ppm) after high-pass filtering .(c) and (h) show similar slices in the model data that was generated by segmenting the magnitude images. (d) and (i) show simulated frequency maps, whilst (e) and (j) show the difference between measured and simulated frequencies, using the same scaling.

From these difference maps it can be seen that the largest discrepancies occur adjacent to the sharp boundaries between regions of different magnetic susceptibility. This is likely to result from errors in segmenting the magnitude images (Figs. 4.9a and f) to form the model structure (Figs. 4.9c and h), and the finite resolution of the digitized model, compounded by the apodisation that has to be employed to avoid sharp truncation at the edge of k-space, as described in Section 3.2.2.4. There also appears to be a general negativity in the cylinders doped with the higher concentration of contrast agent. This is likely to result from errors in the doping procedure. In general, however, the agreement is good showing that useful comparisons can be made between simulated and measured field map data.

4.2.3 Investigating the Effect of Gaussian High-Pass Filtering on Phase Contrast

As described in Section 4.1 the field maps must be high-pass filtered to remove unwanted, large length-scale background fields. To investigate the effect that Fourier high-pass filtering using a Gaussian kernel has on phase contrast, the results of simulations were compared to *in vivo* data. This comparison was also used to infer approximate values for the susceptibility differences between GM and WM in the human brain. The digitized HUGO body model (Medical VR Studio GmbH, Lörrach) was used in simulating the effect of susceptibility differences between GM, WM and cerebro-spinal fluid on phase images obtained from cortex. The highest resolution version of the model in which each voxel in the head has dimensions of $1\times1\times1$ mm^3 and is assigned to one of 6 tissue types, was employed. In previous simulation work by Collins et al. [26] the susceptibilities of tissues were calculated relative to each other based on tissue composition. These values are largely based on estimates of lipid content and do not take account of any effect of iron concentration or other factors. In the case of GM, WM and CSF (GM: −8.97; WM: −8.80; CSF: −9.04 in ppm) the values are not consistent with experimental data [6, 23] since they imply that GM has a more negative (less paramagnetic) susceptibility than WM. In the simulations described here, GM and WM and CSF values were therefore set to −8.995, −9.045 and −9.04 ppm respectively, which are based on estimates from recent experimental work [6]. In this study, the magnetic susceptibility of the bone, fat, muscle and air surrounding the brain was set to −9.02 ppm, the average of brain tissue. Although obviously unrealistic, this eliminated the large length-scale field variation due to air-tissue boundaries, allowing us to focus on the effect of the variation of magnetic susceptibility in the cortex. A 10 cm thick section of the brain spanning 100 slices was inserted into a 400×400×400 matrix for these calculations.

The field simulations were carried out using Eq.3.51, as described in the previous section.

Figure 4.10 demonstrates the effect of varying the width of the spatial filter (4, 8 and 16 mm FWHM) on simulated and measured data from similar superior cortical slices. The phase data were scaled to Hz in this example, as this is the unit most commonly used to measure field differences in the literature [6]. Table 4.1 lists the average GM/WM frequency differences in the experimental and simulated data for the different filtering conditions.

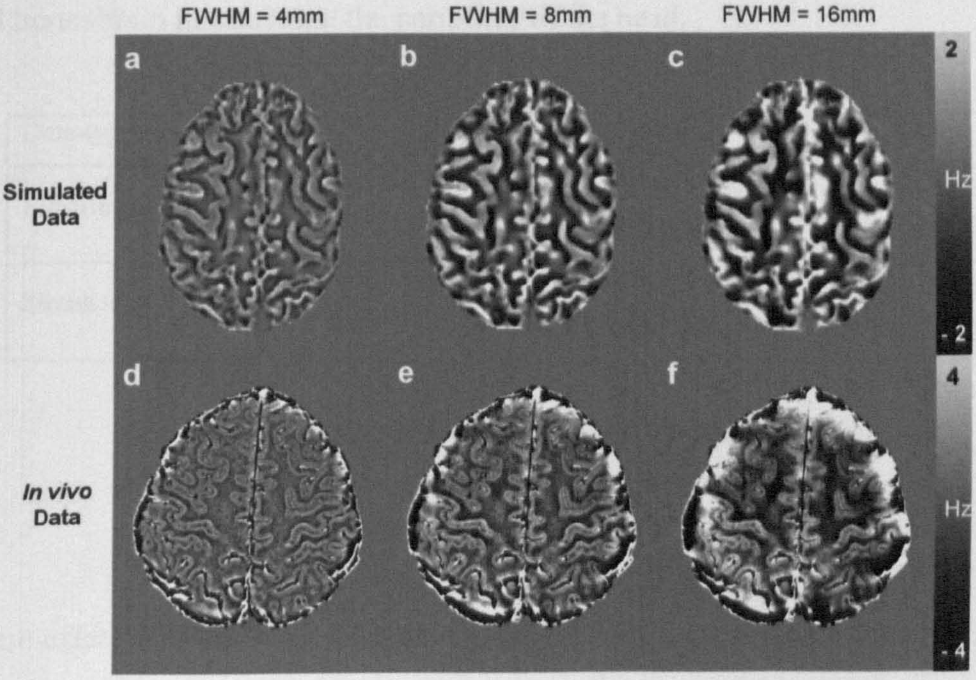

Figure 4.10 Effect of varying the degree of high-pass filtering applied to simulated (a–c) and experimentally acquired (d–f) frequency maps (in Hz) from a representative axial slice. Filter kernels of 4 mm (a and d), 8 mm (b and e) and 16 mm (c and f) were used. It should be noted that the scales used for the simulated data (±2Hz) and the in vivo data (±4Hz) are different.

These values were calculated using multiple ROI positioned in adjacent GM and WM regions in the central slices of the simulated and measured data sets. It is evident from the images shown in Fig. 4.10 and the values listed in Table 4.1, that the average difference in frequency (and phase) values in GM and WM is greater in the experimental measurements than in the simulated data and that in both cases this difference decreases as the degree of high-pass filtering is increased. The reduction in GM/WM phase contrast as the filter kernel width is varied from 16 to 4 mm results from the fact that the stronger high-pass filtering attenuates spatial variations occurring on the length-scale of 3–5 mm that characterizes the width of the GM layer on the cortical surface [22, 27]. This demonstrates that in making comparisons of frequency offsets measured in different studies it is very important to ensure that similar spatial filtering is always applied. As the degree of spatial filtering is reduced, the experimental data in Fig. 4.10 shows the effects of localised field variations produced by large susceptibility differences at the air–scalp, scalp–bone and bone–brain interfaces at the periphery of the head.

Data-type/filter FWHM	4mm	8mm	16mm
Experimental *in vivo*	1.8±0.9 Hz (0.006±0.003ppm)	2.9±0.9 Hz (0.0097±0.003 ppm)	3.0±1.0 Hz (0.010±0.004 ppm)
Simulated	0.9±0.5 Hz (0.003±0.002ppm)	1.5±1.0 Hz (0.005±0.003 ppm)	1.7±1.1 Hz (0.006±0.004 ppm)

Table 4.1 Average GM/WM field difference in Hz (ppm) measured from experimental and simulated data that have been subjected to varying degrees of high-pass filtering.

These effects are not evident in the simulated data, because the susceptibility of the region around the brain was artificially set to the average of the GM, WM and CSF susceptibility values. The smaller GM/WM frequency difference found when comparing the simulated data to the experimental measurements implies that a difference in GM and WM susceptibility which is larger than the 0.05 ppm value used here is needed to explain the experimentally measured effects.

The GM/WM/CSF susceptibility values that we employed in the simulations were based on scaling by a factor of three the frequency differences (in ppm) which Duyn et al. [6] measured experimentally. Such scaling is based on the assumption that the resonant offset in a region whose susceptibility is different from its surroundings by an amount, $\Delta\chi$, is given by $\gamma B_0 \Delta\chi/3$. However, this is only strictly true in a long cylinder which is oriented parallel to the applied field (see Table 3.1). In a spherical region for example, the field shift is zero, whilst in a long cylinder perpendicular to the field it takes a value of $-\gamma B_0\Delta\chi/6$ (Table 3.1). It is reasonable therefore to expect that in a complex structure, the average frequency difference should be less than $\gamma B_0\Delta\chi/3$. In these simulations the difference ranged from approximately 20 to 40% of the value of $\gamma B_0\Delta\chi/3$ as the filter kernel was varied. By simply taking the ratio of the measured and simulated frequency differences it can be estimated that a GM/WM susceptibility difference of about 9×10^{-8} would be needed to explain the effects which we measured at 7 T. A greater susceptibility difference, of approximately 16×10^{-8} would be needed to explain the data of Duyn et al. who measured an average GM/WM frequency difference of about 5 Hz in motor cortex at 7 T [6].

4.2.4 Phase Contrast in the Red Nucleus and Substantia Nigra

In phase images of lower regions of the human brain, the deep grey matter structures known as the red nucleus (RN) and substantia nigra (SN) show particularly strong phase contrast effects [23]. These strong field offsets are attributed to the large concentrations of non-heme iron that are known to exist within these structures [23, 28]. In SWI, phase images are multiplied directly into magnitude data to create contrast enhancement (see Section 4.1.4). To investigate whether phase contrast originating from large brain structures provides a good representation of localised susceptibility differences, simulations of the strong magnetic field perturbations generated by the RN and SN were carried out. A human subject was scanned using the 3D FLASH sequence, described in the previous section, to yield magnitude and phase data over the RN and SN brain region. The magnitude images were segmented by hand to produce a simple model structure defined using cubic voxels of 0.5 mm side, spanning the red nuclei, substantia nigra and surrounding white matter. The red nuclei and substantia nigra were allocated susceptibility values that were 0.09 and 0.14 ppm different from the surrounding white matter, based on comparison of simulations and experimental measurements. These structures occupied a region of approximately 60×60×30 voxels extent in a 200×200×200 matrix. As in the previous section, the field map associated with this geometry was then simulated using

Eq.3.51. The phase was high-pass filtered via 2D Gaussian smoothing in the transverse plane with a FWHM of 8mm.

Figure 4.11 shows the experimental and simulated data spanning the SN and RN. Figs. 4.11a and f show modulus data from transverse and coronal slices upon which the area that was studied in detail (Figs. 4.11b and g) is marked.

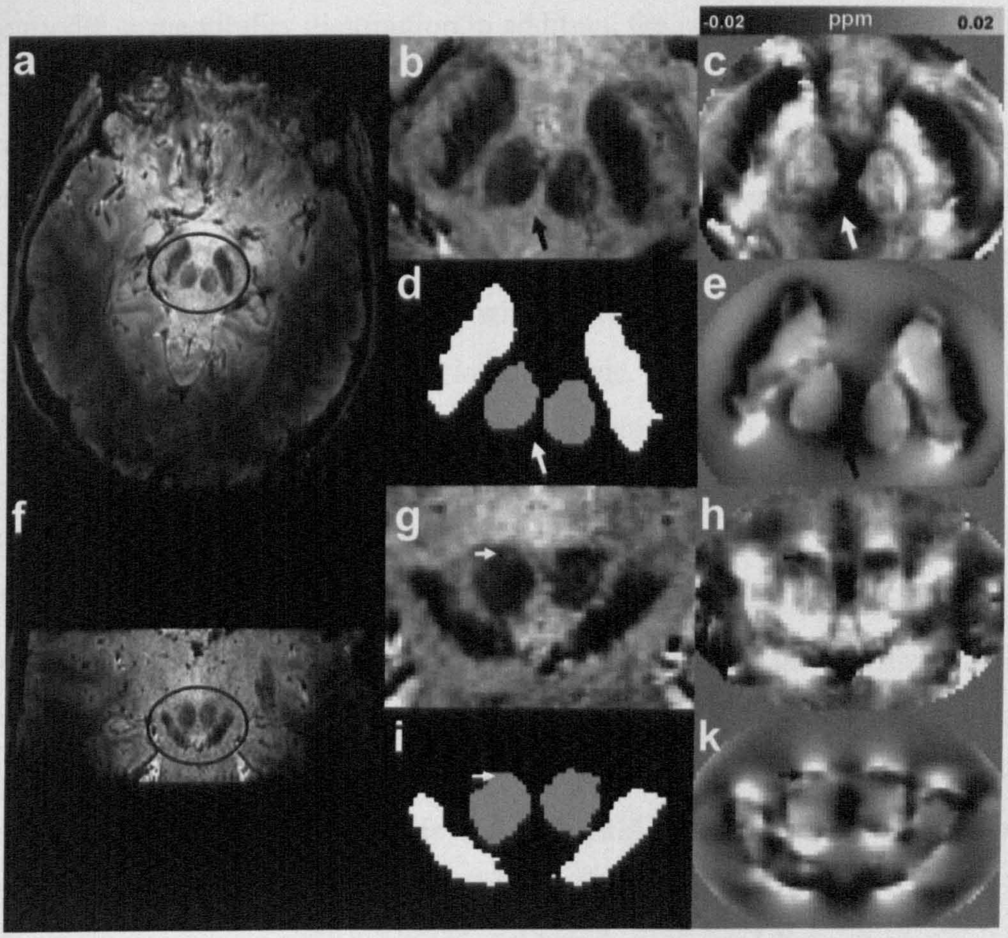

Figure 4.11 ***Comparison of simulated and experimentally measured frequency maps spanning the substantia nigra and red nuclei. Magnitude images from axial (a) and coronal (f) slices in which the region that was studied in detail is highlighted. Zoomed magnitude images from the highlighted region are shown in axial (b) and coronal (g) formats. Segmentation of these data yielded the simple model of the substantia nigra (white) and red nuclei (grey) shown in (d) and (i). Experimentally measured (high-pass-filtered) frequency maps (in ppm) from axial (c) and coronal (h) slices along with simulated data from similar slices are shown. Arrows mark positions in the corresponding axial (b–e) and coronal (f–i) slices.***

Figs. 4.11d and i show the model susceptibility distribution that was used for the simulations. This was derived from the structures shown in the modulus images. The experimentally measured and calculated phase/field variation in representative axial (Figs. 4.11c and e) and coronal (Figs. 4.11h and k) slices are also shown. Many of the features that are evident in the experimental data, such as the dark rings around the red nuclei and medial to lateral decrease in frequency on moving across the substantia nigra are reproduced in the simulated data although they were not present in the model susceptibility distribution.In addition, the coronal maps (Figs. 4.11c and e) show clear evidence of dipolar field patterns formed around the red nuclei and indicate that despite the application of high-pass filtering, significant frequency variation is projected into regions above and below the red nuclei and substantia nigra. There is greater heterogeneity in the experimentally measured phase maps, particularly within the substantia nigra, which presumably reflects local variations in susceptibility that are not represented in the simple, two compartment model used in the simulations. Averaging over the compartments defined as the substantia nigra and red nuclei based on the modulus images, the frequency difference between SN and RN is found to be −0.0034 ppm in the experimental data and −0.0040 pm in the simulations. These values are opposite in sign to the susceptibility difference between the SN and RN of $\Delta\chi$ = +0.05 ppm that was used in the simulations and have a magnitude that is 20 and 24% of the value of $|\Delta\chi|/3$. Thus the structures of the RN and SN have relative field perturbations of the opposite sign to the susceptibility values used to populate them. This effect should be carefully considered when inspecting phase images in this region of the brain.

These findings indicate that care should be exercised when relating structural features in phase or susceptibility weighted images to underlying anatomy. For example the rings seen around the red nuclei in experimental measurements might be assumed to correspond to a layer of reduced susceptibility at the surface of these structures, but in fact the simulations show that the ring results from a pattern of frequency variation that is generated around an approximately spherical region with a uniform magnetic susceptibility that differs from that in the surrounding volume. In addition, the medial to lateral variation of frequency across the substantia nigra could be interpreted as reflecting different iron content in the inner and outer regions, but the simulations show that this variation can be generated by a homogeneous structure and is merely a consequence of its shape. Further, the frequency variation that is produced outside compact structures like the SN and RN, means that anatomical features may appear projected into the slices above and below the relevant structures, producing apparent anatomical features. The rather weak correspondence of anatomical structure and frequency variation in the region spanning the SN and RN stands in some contrast to the situation in superior regions of the cortex, where the frequency maps follow anatomical features quite closely. Some insight into the reasons for this behaviour can be found by considering the relationship between field and susceptibility described in Chapter 3. The GM/WM boundaries in the cortex run, very approximately, parallel to the main magnetic field when viewed in the transverse plane. The field perturbation due to this geometry is analogous to that of an infinite cylinder running parallel to B_0 for which the field shift is local and closely reflects the underlying $\Delta\chi$ distribution (see Table 3.1). The RN and SN structures, however, are more closely approximated by spheres for which the field shift is entirely non-local and gives very little direct information of the underlying $\Delta\chi$ distribution (see Table 3.1).

4.2.5 The Effect of Rotation on Phase Contrast

The previous simulations and discussions of field maps have assumed that the susceptibility distribution is fixed relative to the magnetic field. Also, the transverse magnitude and phase images that have been used for segmentation are assumed to be exactly normal to B_0 and by association, the z-axis. In reality, the human subject will move their head until a comfortable and usually subject specific resting position is found. The inter-subject differences, relative to an arbitrary ideal standard space, can be as much as ± 20°. Thus, to create similar transverse images across different subjects the 3D imaging stack is normally rotated to yield a transverse axis parallel to specific, easily identified brain 'landmarks' such as the corpus collosum (CC). The z-axis of the segmented susceptibility distribution based on these images will then have an angular offset, θ, relative to the direction of B_0. The rotation can be viewed in the reference frame of the susceptibly distribution, as a rotation of B_0 relative to a stationary $\chi(\mathbf{r})$. The expression for the field perturbation due to a rotation of B_0 by an angle θ around the x-axis relative to the susceptibility was described by Marques et al. [29] and is given by,

$$\Delta B = B_0 FT^{-1}\left(\left(\frac{1}{3} - \frac{(k_z \cos\theta - k_y \sin\theta)^2}{k_x^2 + k_y^2 + k_z^2}\right) FT(\chi(\mathbf{r}))\right)$$

Eq. 4.13

In the reference frame of $\chi(\mathbf{r})$ the k-space dipole kernel effectively follows the axis of B_0. To investigate the behaviour of phase contrast after changing the orientation of the underlying susceptibility distribution relative to B_0, a simulation experiment was carried out.

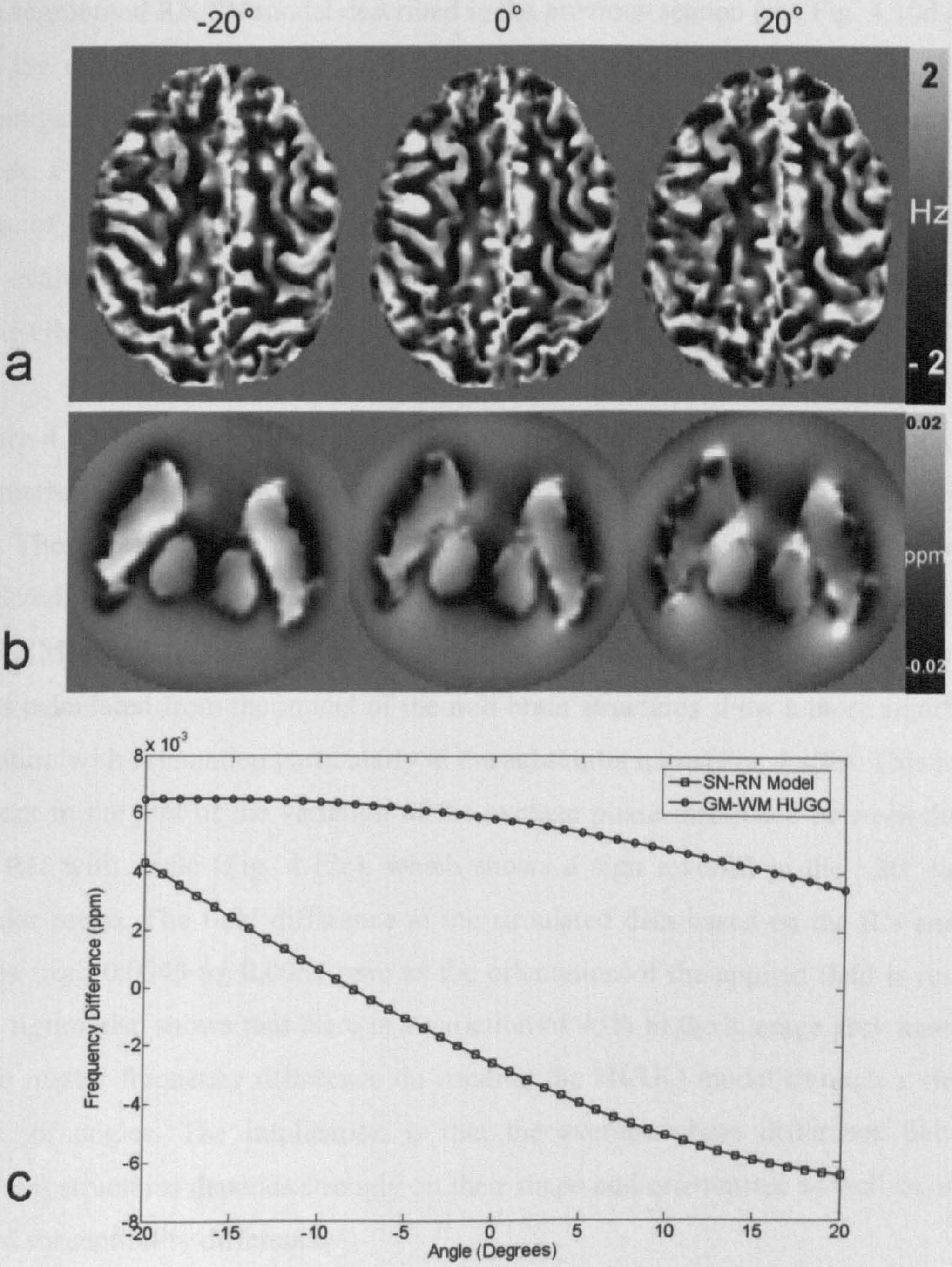

Figure. 4.12. Effect on the simulated frequency maps of changing the field orientation over a 40° range. In each case, the field was rotated relative to the model and filtering (8mm FWHM) was applied in the axial plane of the model data. (a) frequency maps from a central slice of the cortical model arranged at angles of −20°, 0° and 20° with respect to the field; (b) frequency maps from central axial slices of the model of the SN and RN arranged at angles of −20°, 0° and 20° with respect to the field (c) plots of the variation of the average GM/WM and SN/RN frequency difference as a function of the model orientation.

The segmented RN/SN model described in the previous section (see Fig. 4.10d and i) and the digitised brain from the HUGO body model (Section 4.2.2) were used to investigate the effect of rotation in the RN/SN region and GM/WM contrast in the cortex. For each model the field was rotated in steps of 1° about the x-axis over a range of -20° to 20°. The difference of the average field in the SN and RN structures was evaluated at each angle. For the cortex in the HUGO model, ROI's were drawn in the GM and WM to measure average field differences.

Figure 4.12 shows the effect on the simulated data of rotating over a 40° range the orientation of the field with respect to the models of the cortex and of the SN and RN. The maps taken from a central slice in the cortex (Fig. 4.12a) show subtle localized changes in frequency, which lead to the modulation of the average GM/WM phase difference with angle that is shown in Fig. 4.12c. The frequency maps calculated from the model of the mid-brain structures show a more significant variation with orientation particularly in the substantia nigra (Fig. 4.12b). This is also evident in the plot of the variation of the average phase difference between the SN and RN with angle (Fig. 4.12c), which shows a sign reversal in the −20° to 20° angular range. The field difference in the simulated data based on the RN and SN varies from 0.0043 to−0.0065 ppm as the orientation of the applied field is rotated. This figure also shows that there is a variation of 45% in the average grey matter to white matter frequency difference on rotating the HUGO model through a similar range of angles. The implication is that the average phase difference between different structures depends strongly on their shape and orientation, as well as on the actual susceptibility difference.

4.2.6 Conclusions on the Relationship between Field Maps Based on Phase Contrast and the Underlying Susceptibility Distribution

Simulations of the frequency perturbation generated by model susceptibility distributions representing the cortex and mid-brain structures have been used to explore the relationship between anatomy and phase variation in high-pass filtered gradient echo images. The results indicate that susceptibility effects can explain many of the features of experimental data, including the sharp boundaries between grey and white matter regions in the cortex and the ring-shaped region of reduced frequency which appears around the red nuclei in axial images. Analysis of the results of the simulations has shown that care must be exercised when relating features in measured phase maps to anatomical structures, since for example a simple model of the substantia nigra and red nuclei and surrounding white matter consisting of three homogeneous compartments generates complex features in the frequency maps, such as the rings around the red nuclei. In addition evaluation of the average frequency difference between tissue compartments in the simulations shows that there can be a strong dependence on the shape and orientation of structures with respect to the field. This could cause difficulties when attempting to relate average changes in phase in anatomically defined regions in experimental data to changes in regional iron concentration. For SWI, the assumption that positive field offsets reflect local positive susceptibility differences is valid when considering small venous blood vessels perpendicular to the field sampled using long thin voxels. For larger structures, however, the simulation results suggest that the same relationship does not hold, particularly in large deep grey matter regions such as the RN and SN. For these reasons, inverting the field maps to yield a local susceptibility distribution would be preferable to reading phase values directly. The following chapters are devoted to exploring susceptibility mapping as a means to measure quantitative information about differences in the composition of tissues in the human brain.

4.3 References

1. Weisskoff, R.M. and S. Kiihne, *MRI susceptometry: Image-based measurement of absolute susceptibility of MR contrast agents and human blood.* Magnetic Resonance in Medicine, 1992. **24**(2): p. 375-383.
2. Haacke, E.M., G. Herigault, H. An, W. Lin, D.M. Armao, and D.K. Kido, *Visualizing white matter tracts and brain structure using phase imaging.* Radiology, 2001. **221**: p. 344-344.
3. Haacke, E.M., Y.B. Xu, Y.C.N. Cheng, and J.R. Reichenbach, *Susceptibility weighted imaging (SWI).* Magnetic Resonance in Medicine, 2004. **52**(3): p. 612-618.

4. Haddar, D., E.M. Haacke, V. Sehgal, Z. Delproposto, G. Salamon, O. Seror, and N. Sellier, *Susceptibility weighted imaging. theory and applications.* Journal De Radiologie, 2004. **85**(11): p. 1901-1908.
5. Haacke, E.M., S. Mittal, Z. Wu, J. Neelavalli, and Y.C.N. Cheng, *Susceptibility-Weighted Imaging: Technical Aspects and Clinical Applications, Part 1.* American Journal Of Neuroradiology, 2009. **30**(1): p. 19-30.
6. Duyn, J.H., P. van Gelderen, T.Q. Li, J.A. de Zwart, A.P. Koretsky, and M. Fukunaga, *High-field MRI of brain cortical substructure based on signal phase.* PNAS, 2007. **104**(28): p. 11796-11801.
7. Fukunga, M., T.-Q. Li, P. van Gelderen, J.A. de Zwart, K. Shmueli, B. Yao, J. Lee, D. Maric, M.A. Aranova, G. Zhang, R.D. Leapman, J.F. Schenck, H. Merkle, and J.H. Duyn, *Layer-specific variation of iron content in cerebral cortex as a source of MRI contrast.* PNAS, 2010. **107**(8): p. 3834-3839.
8. Hammond, K.E., M. Metcalf, L. Carvajal, D.T. Okuda, R. Srinivasan, D. Vigneron, S.J. Nelson, and D. Pelletier, *Quantitative In Vivo Magnetic Resonance Imaging of Multiple Sclerosis at 7 Tesla with Sensitivity to Iron.* Annals Of Neurology, 2008. **64**(6): p. 707-713.
9. Petridou, N., S.J. Wharton, A. Lotfipour, P. Gowland, and R. Bowtell, *Investigating the effect of blood susceptibility on phase contrast in the human brain.* NeuroImage, 2010. **50**(2): p. 491-498.
10. Lee, J., K. Shmueli, M. Fukunga, P. van Gelderen, H. Merkle, A.C. Silva, and J.H. Duyn, *Sensitivity of MRI resonance frequency to the orientation of brain tissue microstructure.* PNAS, 2010. **107**(11): p. 5130-5135.
11. Yao, B., T.-Q. Li, P.v. Gelderen, K. Shmueli, J.A. de Zwart, and J.H. Duyn, *Susceptibility contrast in high field MRI of human brain as a function of tissue iron content.* Neuroimage, 2009. **44**(4): p. 1259-66.
12. He, X. and D.A. Yablonskiy, *Biophysical mechanisms of phase contrast in gradient echo MRI.* PNAS, 2009. **106**(32): p. 13558-13563.
13. Zhong, K., J. Leupold, D. von Elverfeldt, and O. Speck, *Themolecular basis for gray and white matter contrast in phase imaging.* Neuroimage, 2008. **40**(4): p. 1561-1566.

14. Deistung, A., A. Rauscher, J. Sedlacik, J. Stadler, S. Witoszynskyj, and J.R. Reichenbach, *Susceptibility Weighted Imaging at Ultra High Magnetic Field Strengths: Theoretical Considerations and Experimental Results.* Magnetic Resonance In Medicine, 2008. **60**(5): p. 1155-1168.
15. Jenkinson, M., *Fast, automated, N-dimensional phase-unwrapping algorithm.* Magnetic Resonance In Medicine, 2003. **49**(1): p. 193-197.
16. Smith, S.M., *Fast robust automated brain extraction.* Human Brain Mapping, 2002. **17**(3): p. 143-155.
17. Woolrich, M.W., S. Jbabdi, B. Patenaude, M. Chappell, S. Makni, T. Behrens, C. Beckmann, M. Jenkinson, and S.M. Smith, *Bayesian analysis of neuroimaging data in FSL.* NeuroImage, 2009. **45**(1, Supplement 1): p. S173-S186.
18. Smith, S.M., M. Jenkinson, M.W. Woolrich, C.F. Beckmann, T.E.J. Behrens, H. Johansen-Berg, P.R. Bannister, M. De Luca, I. Drobnjak, D.E. Flitney, R.K. Niazy, J. Saunders, J. Vickers, Y. Zhang, N. De Stefano, J.M. Brady, and P.M. Matthews, *Advances in functional and structural MR image analysis and implementation as FSL.* NeuroImage, 2004. **23**(Supplement 1): p. S208-S219.
19. Wang, Y., Y. Yu, D. Li, K.T. Bae, J.J. Brown, W. Lin, and E.M. Haacke, *Artery and vein separation using susceptibility-dependent phase in contrast-enhanced MRA.* Journal of Magnetic Resonance Imaging, 2000. **12**(5): p. 661-670.
20. Koopmans, P.J., R. Manniesing, W.J. Niessen, M.A. Viergever, and M. Barth, *MR venography of the human brain using susceptibility weighted imaging at very high field strength.* Magnetic Resonance Materials in Physics Biology And Medicine, 2008. **21**(1-2): p. 149-158.
21. Zhao, F.Q., T. Jin, P. Wang, X.P. Hu, and S.G. Kim, *Sources of phase changes in BOLD and CBV-weighted fMRI.* Magnetic Resonance In Medicine, 2007. **57**(3): p. 520-527.
22. Haacke, E.M., M. Ayaz, A. Khan, E.S. Manova, B. Krishnamurthy, L. Gollapalli, C. Ciulla, I. Kim, F. Petersen, and W. Kirsch, *Establishing a baseline phase behavior in magnetic resonance imaging to determine normal*

vs. abnormal iron content in the brain. Journal of Magnetic Resonance Imaging, 2007. **26**(2): p. 256-264.

23. Haacke, E.M., N.Y. Cheng, M.J. House, Q. Liu, J. Neelavalli, R.J. Ogg, A. Khan, M. Ayaz, W. Kirsch, and A. Obenaus, *Imaging iron stores in the brain using magnetic resonance imaging.* Magnetic Resonance Imaging, 2005. **23**(1): p. 1-25.
24. Ogg, R.J., J.W. Langston, E.M. Haacke, R.G. Steen, and J.S. Taylor, *The correlation between phase shifts in gradient-echo MR images and regional brain iron concentration.* Magnetic Resonance Imaging, 1999. **17**(8): p. 1141-1148.
25. Xu, X., Q. Wang, and M. Zhang, *Age, gender, and hemispheric differences in iron deposition in the human brain: an in vivo MRI study.* Neuroimage, 2008. **40**(1): p. 35-42.
26. Collins, C.M., B. Yang, Q.X. Yang, and M.B. Smith, *Numerical calculations of the static magnetic field in three-dimensional multi-tissue models of the human head.* Magnetic Resonance Imaging, 2002. **20**(5): p. 413-424.
27. Haacke, E.M., Z.S. DelProposto, S. Chaturvedi, V. Sehgal, M. Tenzer, J. Neelavalli, and D. Kido, *Imaging cerebral amyloid angiopathy with susceptibility-weighted imaging.* American Journal of Neuroradiology, 2007. **28**(2): p. 316-317.
28. Hallgren, B. and P. Sourander, *The Effect of Age on the Non-Haemin Iron in the Human Brain.* Journal of Neurochemistry, 1958. **3**(1): p. 41-51.
29. Marques, J.P. and R. Bowtell, *Application of a Fourier-based method for rapid calculation of field inhomogeneity due to spatial variation of magnetic susceptibility.* Concepts In Magnetic Resonance Part B-Magnetic Resonance Engineering, 2005. **25B**(1): p. 65-78.

CHAPTER 5

Susceptibility Mapping
Using Threshold-Based *k*-Space Division

The first section of this chapter describes the theoretical basis of susceptibility mapping in MRI. The ill-posed inversion involved in calculating the susceptibility distribution from the field map is discussed in detail, as is a method for conditioning this problem using simple k-space thresholding. A novel filtering method for removing background fields that was developed to improve the quality of inverted susceptibility maps is also introduced and tested using simulated data. The second part of this chapter discusses the application of susceptibility mapping to an agar phantom and also to 7T phase data acquired *in vivo* from the human brain. The sensitivity to errors and the reproducibility of this method are also investigated in detail.

5.1 Susceptibility Mapping Theory

Several approaches for calculating the magnetic susceptibility from magnetic field measurements made using MRI have been proposed. The simplest of these are based on the assumption that anatomical features of interest can be modelled as simple, uniform, geometrical structures (e.g., spheres or long cylinders) for which analytic forms of the induced magnetic field are known [1-3]. It is then possible to fit the measured field variation to the analytic expression, with the susceptibility as the variable parameter. This approach can be extended to structures of more complex shape by using numerical methods to calculate the induced field variation [1, 2]. The main limitation of these approaches is the requirement for exact prior knowledge of the geometry of the desired susceptibility distribution. In 2005, a paper by Marques et al. [3] describing the practical application of the Fourier method for simulating field maps outlined the possibility of inverting this method to yield a susceptibility map. The potential advantages of rotating the sample relative to the main magnetic field of the scanner were also proposed. Such an inversion, when fully developed, would allow the reconstruction of a susceptibility distribution from its associated field map without the need for *a priori* information about the geometry of the desired solution. Here, this simple idea is investigated further and a way of overcoming the ill-posed nature of this inversion is presented in the form of k-space thresholding.

5.1.1 Calculating Susceptibility From Field Maps

In the Fourier domain, the field perturbation, $\Delta B_z(\mathbf{r})$, produced by a susceptibility distribution, $\chi(\mathbf{r})$, that is exposed to a magnetic field, $B_0\hat{\mathbf{z}}$, is given by the simple, local expression which was described in detail in Chapter 3,

$$\Delta B_z(\mathbf{k}) = B_0\chi(\mathbf{k})\left(\frac{1}{3} - \cos^2\beta\right) \qquad \text{Eq. 5.1}$$

where β is the angle between the k-vector and the static magnetic field. Rearranging this expression yields $\chi(\mathbf{r})$ as a function of $\Delta B_z(\mathbf{r})$

$$\chi(\mathbf{k}) = \frac{\Delta B_z(\mathbf{k})}{B_0\left(\frac{1}{3} - \cos^2\beta\right)} = \frac{\Delta B_z(\mathbf{k})}{B_0} \times \frac{1}{C(\mathbf{k})} \qquad \text{Eq. 5.2}$$

where $C(\mathbf{k}) = 1/3\text{-}\cos^2\beta$ represents the Fourier transform of the convolution kernel that links the susceptibility and magnetic field. It is worth noting that the values of C(k) lie in the range -2/3 to 1/3. The susceptibility distribution, $\chi(\mathbf{r})$, can therefore be calculated by: (i) measuring the field map, $\Delta B_z(\mathbf{r})$, from a phase map; (ii) substituting the Fourier transform of $\Delta B_z(\mathbf{r})$ into Eq. 5.2; (iii) applying an inverse Fourier transform to the resulting $\chi(\mathbf{k})$ distribution. Although this approach appears straightforward, there are several limitations associated with its use:

1. Using MRI it is only possible to map the field perturbation, $\Delta B_z(\mathbf{r})$, in regions that generate an NMR signal. For example, in head imaging, the fields inside

the brain can be mapped, but the external fields present in the skull and air surrounding the head remain unknown. This means that the representation of $\Delta B_z(\mathbf{k})$ is inherently inaccurate since it is formed from the 3D Fourier transform of $\Delta B_z(\mathbf{r})$ measured over a region of limited spatial extent.

2. Equation 5.2 assumes that the measured magnetic field perturbation results entirely from the effect of magnetization in the ROI, which is characterized by $\chi(\mathbf{r})$ and $B_0\hat{\mathbf{z}}$, whereas in reality there are always contributions to the measured field perturbation from magnetic field sources outside the ROI [4]. To limit the effect of externally generated fields, it can be beneficial to apply the inversion to a portion of the signal-generating region of the object that is distant from external sources, although this clearly impacts upon the severity of limitation (1).

3. The most significant problem is that the denominator in Eq. 5.2 goes to zero when $\beta = 54.7^\circ$ or 125.3°, often referred to as the 'magic' angles. This means that $\chi(\mathbf{k})$ tends to infinity on two conical surfaces in k-space and there is significant amplification of any noise or errors arising from the measured $\Delta B_z(\mathbf{k})$ in the region adjacent to these surfaces.

In this work, a simple approach involving the introduction of a threshold parameter, α, such that $\Delta B_z(\mathbf{k})$ is set to zero in regions of k-space where $|C(\mathbf{k})| < \alpha$ is proposed. This has the effect of nulling $\chi(\mathbf{k})$ around two conical surfaces in k-space, as shown in Fig. 5.1a. The volume of this region (denoted as the conical mask) decreases as α gets smaller. The effect of varying α on the accuracy of the calculated susceptibility maps is explored in the following sections and the calculation of susceptibility maps from measurements made with $\chi(\mathbf{r})$ oriented at one, two, or three angles relative to B_0 is also investigated.

5.1.2 The Effect of Rotation: *Two Orientations*

As described in Section 4.2.5, in the case where $\Delta B_z(\mathbf{k})$ is measured with B_0 rotated by an angle θ about the x-axis of a coordinate system defined relative to $\chi(\mathbf{r})$, the Fourier transform of the convolution kernel becomes [3]:

$$C(\mathbf{k},\theta)=\left(\frac{1}{3}-\frac{\left(k_z\cos\theta-k_y\sin\theta\right)^2}{|\mathbf{k}|^2}\right) \qquad \text{Eq. 5.3}$$

where θ is the angle that k_z makes with respect to B_0.

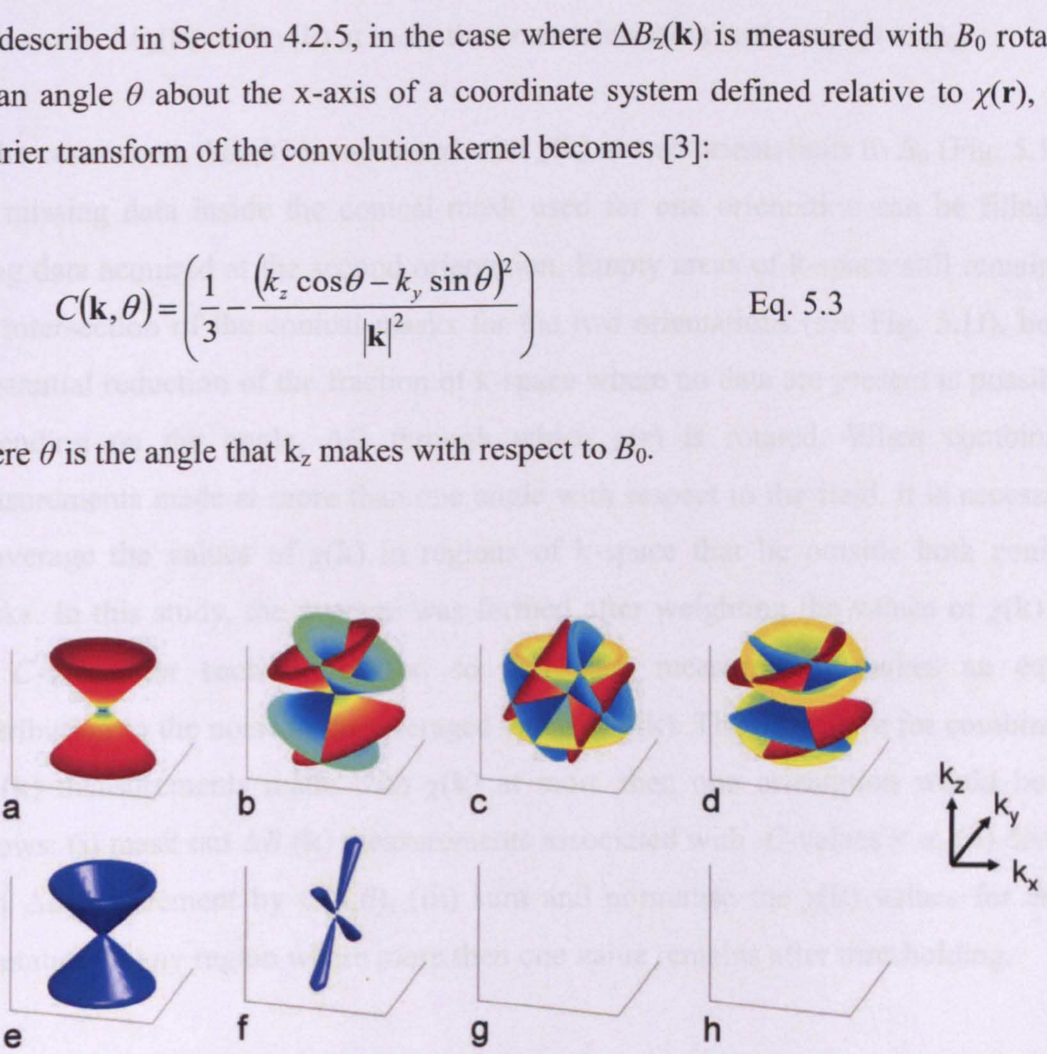

***Figure 5.1** 3D surface diagrams showing the conical masks with α = 0.07 applied to $\chi(k)$ to avoid noise amplification in regions of k-space close to the surfaces lying at the magic angle to the field direction. (a) The mask applied to $\chi(k)$ sampled at a single orientation; (b) the masks applied to $\chi(k)$ sampled at a two orientations separated by a rotation $\Delta\theta$ = 40° about the x-axis with; (c) the masks for three orientations produced by rotations about the x-axis of -60°, 0°, and +60°; (d) the masks for three orientations produced by sequential rotations about the x- and y-axes such that (θ,ϕ)= (20°,0°), (-10°,17°), and (-10°,-17°); (e-h) show surface plots representing the regions of k-space that remain empty after combination of the measurements made at different orientations as described in (a-d), respectively.*

Thus, the principal axis of the conical mask follows the direction of B_0 after a rotation. This rotational property makes it advantageous for susceptibility mapping to measure $\Delta B_z(\mathbf{k})$ with $\chi(\mathbf{k})$ at more than one orientation with respect to B_0.

In the case where $\Delta B_z(\mathbf{k})$ is measured with $\chi(\mathbf{k})$ at two orientations to B_0 (Fig. 5.1b), the missing data inside the conical mask used for one orientation can be filled in using data acquired at the second orientation. Empty areas of k-space still remain at the intersection of the conical masks for the two orientations (see Fig. 5.1f), but a substantial reduction of the fraction of k-space where no data are present is possible, depending on the angle, $\Delta\theta$, through which $\chi(\mathbf{r})$ is rotated. When combining measurements made at more than one angle with respect to the field, it is necessary to average the values of $\chi(\mathbf{k})$ in regions of k-space that lie outside both conical masks. In this study, the average was formed after weighting the values of $\chi(\mathbf{k})$ by the C-value for each orientation so that each measurement makes an equal contribution to the noise in the averaged value of $\chi(\mathbf{k})$. The procedure for combining $\Delta B_z(\mathbf{k})$ measurements made with $\chi(\mathbf{k})$ at more then one orientation would be as follows: (i) mask out $\Delta B_z(\mathbf{k})$ measurements associated with C-values $< \alpha$, (ii) divide each $\Delta B_z(\mathbf{k})$ element by $C(\mathbf{k},\theta)$, (iii) sum and normalise the $\chi(\mathbf{k})$ values for each orientation in any region where more then one value remains after thresholding.

5.1.3 The Effect of Rotation: *Three Orientations*

In 2009, Liu et al. [5] showed that it is possible to define $\chi(\mathbf{k})$ over the whole of *k*-space when $\Delta B_z(\mathbf{r})$ is measured with $\chi(\mathbf{r})$ at three different orientations produced by rotation about a single axis that is perpendicular to B_0. In their approach an iterative method was used to solve the inverse problem. The details of this method are discussed in Chapter 7 along with other iterative techniques. In the approach presented here, as with the approach used by Liu et al., $\chi(\mathbf{k})$ can be defined after three rotations provided that α is small enough to ensure that there is no overlap between the three conical masks. Liu et al. [5] also defined a condition number, κ, for the calculation of $\chi(\mathbf{r})$, which is given by the ratio of the maximum and minimum values of $|C(\mathbf{k})|$ that are used in evaluating $\chi(\mathbf{k})$ via Eq. 5.2. The condition number characterizes error propagation in discrete inverse problems. Larger values of κ imply greater amplification of the noise from the measured field maps in some regions of k-space and hence a reduction in the quality of the calculated susceptibility map. By searching for the minimum value of the condition number, Liu et al. then showed that the optimum set of orientations produced by rotation about a single axis corresponded to rotation angles of -60°, 0°, and +60°, with a corresponding κ value of 2.03. This arrangement is shown in Fig 5.1c. While this set of angles provides high-quality χ-maps, it requires that the object be rotated through 120°, an angular range that is impractical for in vivo imaging of the human head. In our study, we found that the maximum angular range of head rotation that volunteers could comfortably achieve was about ±20°, which yields a much larger condition number ($\kappa \approx 30$), for rotation about a single axis.

The limitations imposed by the restricted range of achievable head rotation can be largely overcome by allowing rotations about more than one axis. We consider the case where three measurements are again combined, but now consider orientations generated by rotations about two orthogonal axes (the x- and y-axes) (Fig 5.1d). For a rotation about the x-axis by angle θ, followed by a rotation about the y-axis by ϕ, the Fourier transform of the convolution kernel becomes

$$C(\mathbf{k},\theta,\phi)=\left(\frac{1}{3}-\frac{(k_z\cos\theta\cos\phi-k_y\sin\theta\cos\phi+k_x\sin\phi)^2}{|\mathbf{k}|^2}\right).$$

Eq.5.4

Using Eq. 5.4, we can calculate the condition number for the case of rotations about two axes and compare with the single-axis case. To allow a fair comparison, the magnitude of the final angle that k_z makes with respect to B_0, $|A(\theta,\phi)|$, was also considered, where

$$A(\theta,\phi)=\tan^{-1}\left(\frac{\sqrt{\cos^2\theta\sin^2\phi+\sin^2\theta}}{\cos\theta\cos\phi}\right) \quad .$$

Eq. 5.5

Figure 5.2 shows the condition number for three orientations produced by rotation about the x-axis plotted against the angular range θ. The figure also shows the variation of the condition number for three orientations produced by rotation about two axes, plotted against the angle $|A(\theta,\phi)|$. For the two-axis case, we only considered the situation where the field vectors for the three different orientations were equally spaced around a conical surface, making an angle of $|A(\theta,\phi)|$ with respect to k_z. So, for example, the situation where $|A(\theta,\phi)|$ = 20° corresponds to rotation angles (θ,ϕ) = (20°, 0°), (-10°, 17°) and (-10°, -17°). For the single axis case, the angles were also distributed evenly, e.g., for $|A(\theta,\phi)|$ = 20°, the rotations were θ = 20°, 0°, -20°. The plot shows that for $|A(\theta,\phi)|$ values in the 0 to 40° range, the two-axis rotation produces lower condition numbers than rotation about a single axis. $|A(\theta,\phi)|$ = 20°, the two-axis rotation gives $\kappa = 3.1$, a factor of 9.6 times less than for the single-axis case for the same range of motion.

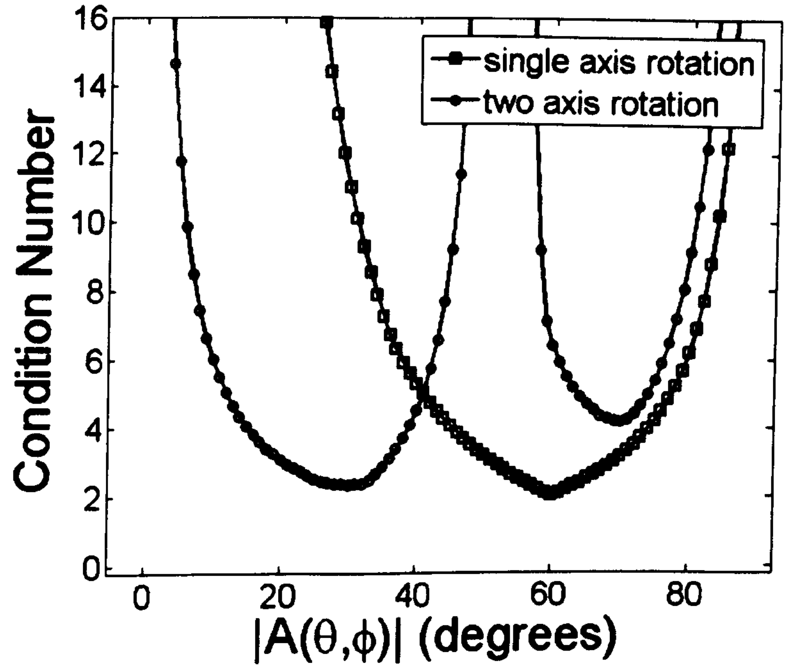

***Figure 5.2** Plots of the condition number for the susceptibility calculation based on combination of phase data sampled at three orientations produced by rotation about a single axis or two orthogonal axes. The condition number is plotted against the magnitude of angle through which the k_z-axis is rotated relative to B_0.*

The condition number becomes very large for the two-axis rotation when $|A(\theta,\phi)|$ is approximately equal to the magic angle since in this case the conical masks for the three different orientations have a large overlap. Overall, the results suggest that when movement is restricted to small angles of revolution, a two-axis rotation will yield data whose inversion is less susceptible to noise propagation.

5.1.4 Effects of High-Pass Filtering

Several different approaches to high-pass filtering techniques for removing unwanted background fields were introduced in the previous chapter: (i) Fourier filtering, where the complex data are low-pass filtered in the Fourier domain and divided into the original data to yield a high-pass-filtered version from which phase can then be calculated [6, 7]; (ii) a similar approach in which the filtering is applied to unwrapped phase data [8]; (iii) subtraction of a low-order polynomial fit from the unwrapped phase data [9]. While these methods have been shown to be very effective in phase and susceptibility-weighted imaging [10], for the purposes of the work carried out within this thesis it was found that the field due to the air/tissue interfaces of the sinuses in the ROI spanning the red nuclei (RN) and substantia nigra (SN) varied so rapidly that the level of filtering required to remove the unwanted field shift resulted in an unacceptable loss of contrast in the filtered field map (see Section 4.2.3).

Recently, a more sophisticated method of eliminating the effect of such fields has been proposed, which involves using structural images of the head to simulate and then remove, via least-squares fitting, the dipolar fields due to air/tissue interfaces in the sinuses [11]. This method has the advantage of incorporating fast spatially varying fields into the fitting process. The disadvantage of this method is the need for information about head structure in the region around the brain. In the work of Neelavalli et al., this information was collected through acquisition of additional high-resolution T1-weighted images [11]. For the work described here and in the following chapters, no such structural information was available, so a new filtering technique was developed for the removal of the rapidly varying fields produced in the ROI by nearby external sources such as the air/tissue interfaces of the sinuses.

5.1.5 Dipole High-Pass Filter

The proposed method involves modelling the unwanted fields using one or more dipole point sources orientated parallel to B_0 and positioned outside the ROI. As described in Chapter 3, Eq. 5.6 shows how the field shift $\Delta B_z(\mathbf{r})$ at position **r** due to a magnetic dipole point source can be expressed as a function of four parameters, the strength of the dipole, P, and the position of the dipole, $\mathbf{r}_d = x_d\hat{\mathbf{x}} + y_d\hat{\mathbf{y}} + z_d\hat{\mathbf{z}}$

$$\Delta B_z^{dip}(\mathbf{r}) = \frac{P}{|\mathbf{r}-\mathbf{r}_d|^3}\left(3\left(\frac{(\mathbf{r}-\mathbf{r}_d)\cdot\hat{\mathbf{z}}}{|\mathbf{r}-\mathbf{r}_d|}\right)^2 - 1\right) \quad . \qquad \text{Eq. 5.6}$$

The field shift at $\mathbf{r} = \mathbf{r}_d$ is ill defined, but this is not a problem since the dipole resides outside the ROI. The first stage of the filtering method is to carry out a least-squares fit for the position and strength of a single dipole, located outside the ROI. This fitting was implemented by iteratively varying the four parameters P, x_d, y_d and z_d until a minima was reached in the error between the estimated dipole field and the field map derived from phase data.

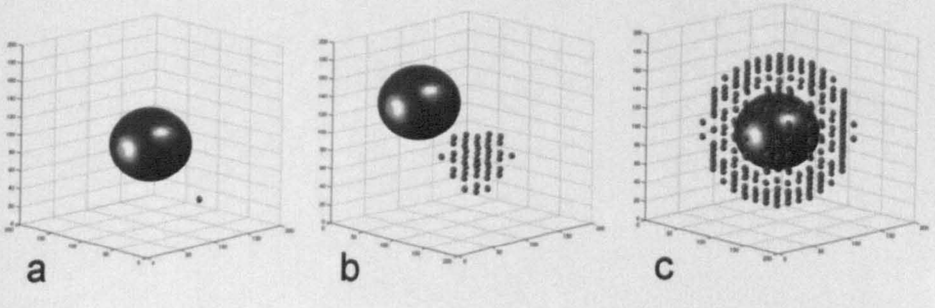

Figure 5.3 3D representation of possible dipole (small spheres) arrangements relative to a chosen ROI (large spheres): (a) a single dipole; (b) a localised group of dipoles, (c) a uniform arrangement of dipoles surround the ROI.

In some cases, this first stage shown in Fig. 5.3a may be sufficient, yielding a relatively flat field map free from large length-scale field variation and thus dominated by the local field shifts due to the susceptibility distribution in the ROI. However, in most cases the sinus field shift cannot be sufficiently well modelled by a single dipole and more dipoles must be incorporated into the fitting. To speed up the process, the new dipoles can be arranged in fixed positions around the original dipole, again restricted to locations outside the ROI, see Fig. 5.3b. The dipoles are placed on a grid with spacing's equal to 10 voxels assuming the ROI has an approximate diameter of 100 voxels. This reduces the number of parameters being fitted to just the strength of each dipole. The minimizations for this study were carried out using a standard least-squares algorithm implemented in Matlab (MathWorks Inc., Natick, MA). The strengths of each dipole were fitted simultaneously by inverting a large matrix with each of the dipole contributions to the inside of the ROI set as the matrix columns. As the dipole fields are linear in form they do not interact with each other, making the inversion of the matrix relatively simple. Once the dipole strengths producing the best fitting field have been found, the total $\Delta B_z^{\mathrm{dip}}$ can be calculated and subtracted from the measured ΔB_z to yield the filtered field map, $\Delta B_z^{\mathrm{filt}}$, which should contain only the field-shift components due to the susceptibility distribution within the ROI. In the case where the external sources of unwanted field shifts are not restricted to a particular region of space, the fitting approach can be extended by distributing the external dipoles more uniformly around the ROI, as shown in Fig. 5.3c. Incorrectly adjusted shim fields present another problem as they generally show a slow spatial variation over the ROI and are therefore not easily modelled by isolated dipoles. In the presence of such fields, a low-order, 3D polynomial can be incorporated into the fitting, yielding a hybrid of the dipole and polynomial fitting methods that is capable of describing slowly varying fields over the whole ROI and more rapidly varying fields toward its edge.

5.1.6 Comparison of Dipole High-Pass Filter to Other Filtering Methods

An evaluation of the performance of the new dipole filtering method described in the previous section was carried out by applying it to simulated data from the SN and RN comprising a known combination of realistic, internally and externally generated fields. The 3D model of the RN and SN created via segmentation of T_2*-weighted modulus image data, as described in Section 4.2.2, with 0.5 mm isotropic resolution was utilised for this simulation-based experiment (Fig. 5.4a). Based on previous comparison of simulations and experimental measurements, the RN and SN were allocated susceptibility values that were 0.09 and 0.15 parts per million (ppm) larger than the surrounding white matter. These structures occupied a region of approximately 60 x 60 x 30 voxels' extent that was then set inside a 200 x 200 x 200 matrix of zeros. The field shift associated with this susceptibility distribution, ΔB_z^{RNSN}, was then calculated using Eq. 3.55 as described in Chapter 4. The resulting field map is shown in Fig. 5.4b. The HUGO body model (Medical VR Studio GmbH, Lörrach) was used for simulation of the rapidly varying fields due to the air/tissue interface of the sinuses. The highest-resolution version of the model in which each voxel in the head has dimensions of 1 x 1 x 1 mm^3 and is assigned to one of six tissue types (including bone, fat, and muscle) was employed. The head occupied a region of approximately 200^3 voxels' extent that was set inside a 512^3 matrix of zeros (see Fig. 5.4g). The field shift due to the head model, ΔB_z^{HUGO}, was then simulated using the Fourier method, producing the result shown in Fig. 5.4c. The ΔB_z^{HUGO} data were then interpolated to 0.5 mm isotropic resolution for ease of combination with ΔB_z^{RNSN}. An ellipsoidal mask, spanning approximately 80 x 80 x 60 voxels, large enough to enclose the RN and SN structures and a surrounding region of approximately 10 voxels' thickness, was applied to both ΔB_z^{RNSN} and ΔB_z^{HUGO}. In the case of ΔB_z^{HUGO}, the mask was applied at a position corresponding to the approximate location of the RN and SN to capture the typical, externally generated field shifts, ΔB_z^{EXT}, as shown in Fig. 5.4d. The body of the HUGO model was excluded to speed up the simulation. This truncation will affect the field values measured in the brain. However, for the purposes of this simulation the rapidly varying fields due to the close proximity of the sinuses will tend to dominate the field map in the RNSN region.

Addition of ΔB_z^{RNSN} and ΔB_z^{EXT} produces a composite field map, ΔB_z^{COMP} (Fig. 5.4e), which shows good correspondence to experimental data acquired from the SN/RN in vivo (Fig. 5.4f). We can now assess the effect of high-pass filtering, represented by the filter function, F, on the two contributions to ΔB_z^{COMP}, since for a linear filter

$$F\left(\Delta B_z^{COMP}\right)=F\left(\Delta B_z^{RNSN}+\Delta B_z^{EXT}\right)=F\left(\Delta B_z^{RNSN}\right)+F\left(\Delta B_z^{EXT}\right)\ . \tag{Eq. 5.7}$$

We used two parameters to characterize the performance of each filter: a contrast parameter,

$$f_c=\frac{F\left(\Delta B_z^{RNSN}\right)}{\Delta B_z^{RNSN}} \tag{Eq. 5.8}$$

describing how much of the internally generated field shift is eliminated by filtering, and an error parameter,

$$f_e=\left|F\left(\Delta B_z^{COMP}\right)-F\left(\Delta B_z^{RNSN}\right)\right|=\left|F\left(\Delta B_z^{EXT}\right)\right| \tag{Eq. 5.9}$$

describing how much of the externally generated field shift remains after filtering. In the ideal case, $f_c = 1$ and $f_e = 0$. Using these definitions, the performances of Fourier, polynomial, and dipole filtering were assessed by calculating values of f_e and f_c for each voxel within the ellipsoidal mask and then averaging over voxels. Values were measured for each of the filtering methods while varying the relevant filter parameters: the full width at half maximum of the real-space Gaussian function used in the Fourier filter (see Section 4.1.3), the maximum order of 3D polynomial in the polynomial filtering, and the number of dipoles used in the dipole fitting procedure. All filters were applied in 3D for a fair comparison. To avoid denominator values close to 0, f_c values were only measured in voxels with $\left|\Delta B_z^{RNSN}\right| > 0.005$ ppm.

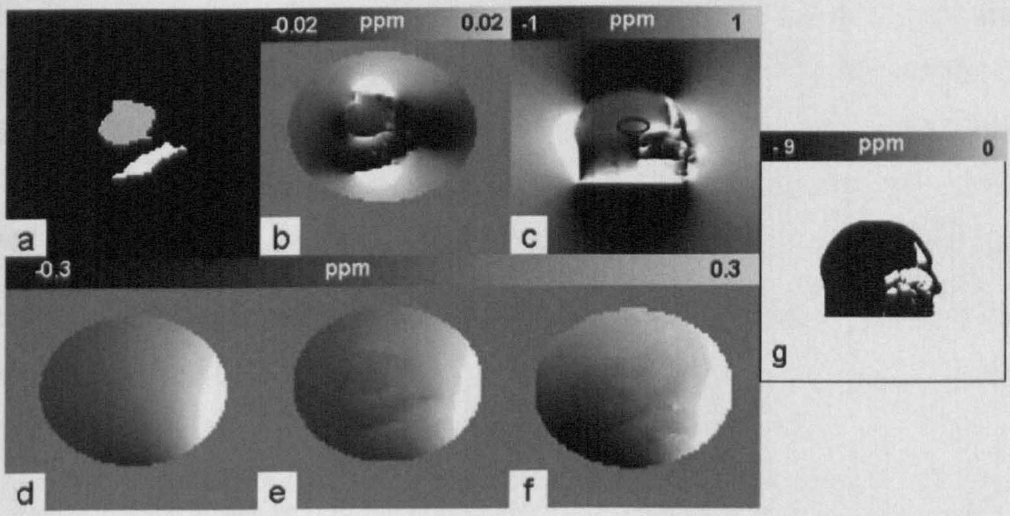

***Figure 5.4** The steps used to create simulated field maps for assessing the performance of the different high-pass filters. a: Sagittal slice through the model (gray = RN; white = SN); (b) map (in ppm) of the simulated field produced by the SN/RN model,* ΔB_z^{RNSN}*, in this slice; (c) the simulated field map for the HUGO digitized head model; the ellipse indicates the approximate location of the SN and RN; (d) the field variation produced by the head model in the ROI shown in (c), which was used to model the externally generated rapid spatially varying field due to the sinuses,* ΔB_z^{EXT}*; (e) the composite field map produced from the sum of (b) and (d),* ΔB_z^{COMP}*; (f) sagittal field map measured in vivo from a region spanning the SN and RN; (g) the susceptibility values for the HUGO model used to create (c).*

Figure 5.5 shows plots of f_c against f_e for the polynomial-, complex Fourier-, and dipole-based filters. Figure 5.6a-c shows the results of filtering the simulated field map ΔB_z^{COMP} using each of the different filter methods. The approximate optimal filter parameters were chosen by varying the filter parameters and visually inspecting the filtered field maps created. The plots of f_c versus f_e were used to give an approximate starting range of filter parameters to speed up the visual inspection process. The optimal parameters were chosen as: 6 mm full width at half maximum for the complex Fourier method, a 3rd-order polynomial fit, and 10 dipoles for the multi-dipole filter. It should be noted that these values will not be optimal for all applications. Increasing the number of dipoles in the multi-dipole fit did tend to reduce contrast in the filtered field maps but the differences in the results of the multi-dipole fit incorporating 1-50 dipoles were relatively small (see ellipsoid in Fig. 5.5). For comparison, the unfiltered field shift produced by the SN/RN structures, ΔB_z^{RNSN}, is also shown in Fig. 5.6d. The results indicate that dipole filtering outperforms both polynomial and Fourier filtering in preserving contrast while removing unwanted field shifts.

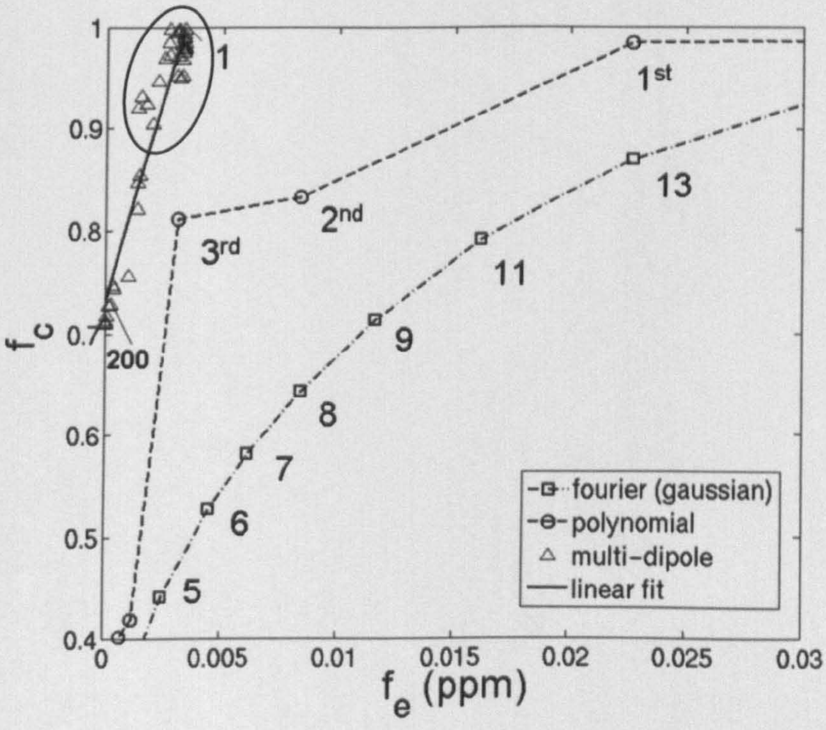

***Figure 5.5** f_c is plotted against f_e for each of the different approaches to high-pass filtering: the results for the Fourier filter are plotted for decreasing full width at half maximum (millimeters), the results for the polynomial based filter are plotted with inclusion of increasing orders, and the dipole filter results are plotted for increasing numbers of dipoles. Data labels indicate some of the parameters used in the filtering process. The results of Dipole filtering using 1-50 dipoles are highlighted by an ellipsoid.*

Another important indicator of the filter performance is the effect that the filtering has on calculated susceptibility values. To evaluate this effect, field maps were simulated after changing the orientation of the RN/SN model relative to B_0 by rotation about the x-axis through angles of -60, 0, and 60°. Combination of the data from these three orientations allowed the effect of the filtering to be evaluated independent of any effect of setting elements of $\Delta B_Z(\mathbf{k})$ equal to zero through application of the conical mask. The sinus artifact, ΔB_z^{EXT}, was also simulated at each angle and superimposed on the RN/SN field maps. The field maps were then filtered using each of the three methods, with the filter parameters set to the optimum values described above. After filtering, the susceptibility maps were calculated and the χ-values in the RN and SN structures were analyzed.

Table 5.1 details the average and standard deviation of the susceptibility values found in the RN and SN, measured relative to the average susceptibility value in the surrounding white matter, for the three different filtering methods. The dipole filtering produces susceptibilities that are closest to the model values and show the smallest spatial variation over the uniform structures. There is a significant underestimation (by nearly 40%) of the susceptibility in the data that have been subjected to Fourier or polynomial filtering, suggesting that these methods significantly attenuate the field produced by the susceptibility distribution inside the ROI. However, the polynomial and complex Fourier filters are less computationally intensive. For the volumes of about 100^3 voxels size used in this study, these methods ran in approximately 10 sec on a 64-bit Linux system with a 2-GHz Dual Core AMD processor and 8 GB of random access memory, while the dipole-based filter incorporating 300 dipoles required a computational time of about 2 min.

The comparison of high-pass-filtering methods showed that the dipole-based technique could be a powerful tool for removing unwanted magnetic field perturbations from field maps measured *in vivo*. This potential is highlighted particularly well by the representative filtered field maps shown in Fig. 5.6a-c. The Fourier-based filter fails to deal with rapidly varying, externally generated fields, such as those created by the air/tissue interface of the sinuses. The arrow in Fig. 5.6a indicates the residual field from the sinuses that remains after filtering; this filtered field map also shows reduced contrast, when compared to the field map shown in Fig. 5.6d, which depicts the field perturbation produced by the RN and SN alone.

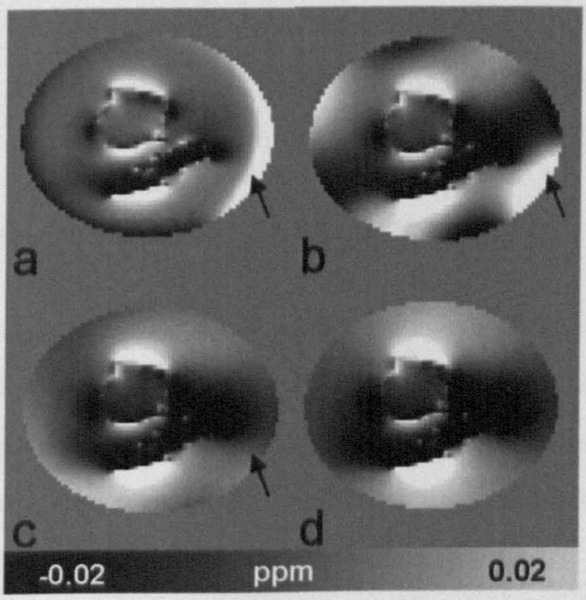

Figure 5.6 ***Representative field maps showing the results of filtering the simulated composite field map ΔB_z^{COMP} (see Fig. 5.4e) (a): After Fourier filtering with full width at half maximum = 6 mm; (b) after polynomial filtering using a 3rd-order fit; (c) after multi-dipole filtering using 40 dipoles; (d) map of the field, ΔB_z^{RNSN}. The arrows show residual externally generated fields that could not be filtered out by either the polynomial- or Fourier-based filters.***

	Fourier (± σ)	Polynomial (± σ)	Dipole (± σ)	Model Value
RN (ppm)	0.051 ± 0.016	0.065 ± 0.014	0.083 ± 0.007	0.09
SN (ppm)	0.082 ± 0.019	0.122 ± 0.015	0.143 ± 0.008	0.15

Table 5.1 Average $\Delta\chi$ Measured in Simulations of the RN and SN for optimal filter parameters.

The polynomial-based filter preserves contrast but shows poor performance in removing the fields from the sinuses (arrowed region in Fig. 5.6b). The dipole-based filter outperforms these methods, preserving contrast and removing the sinus artifact, with little residual field at the edge of the ROI. The dipole-filter also performed well on the phantom data (Fig. 5.7c). With a larger ROI, the effect of poorly adjusted shim fields becomes an issue, which can be addressed by incorporation of a 2nd order polynomial into the filtering process. The resulting hybrid dipole/polynomial filter could also have applications in susceptibility weighted imaging [7, 10].

5.1.7 Effects of Restricting the Extent of the ROI

In the simulations discussed previously within this section, and in the experimental data investigated in the next section, a small ellipsoidal ROI was always used for the processing of data acquired *in vivo*, so as to avoid the fields due to large blood vessels and other structures near to the surface of the brain that produce relatively large field shifts and also to speed up the dipole fitting process. Imposing a mask on a field map inevitably reduces the amount of available information for the susceptibility calculations. However, if the edge of the ROI is a reasonable distance from the structures of interest, the effect of the mask is usually not significant. This is a consequence of the high-pass filtering that is routinely applied to field maps, which means that field shifts produced by sources outside the ROI are forced to zero due to their slowly spatially varying nature. This assumption was tested by analyzing field maps generated using the model of the SN and RN. The results of this simulation based experiment are shown in Figure 5.7. First, the field perturbation produced by the model when oriented at three different angles (-60, 0, and 60°) to B_0 was simulated over a 256^3 matrix. The field map at 0° is shown in Fig 5.7a. Gaussian noise with a variance of 1×10^{-5} B_0 was then added to the field maps as shown in Fig 5.7b. These were subsequently high-pass filtered using the Fourier-method with a FWHM of 6 mm and then masked using ellipsoids of various sizes ranging from 200 x 200 x 200 voxels to 80 x 80 x 60 voxels in extent as shown in Fig 5.7c. The susceptibility was calculated by combining the data from the three orientations with α set to 0.07, and the susceptibilities of the RN/SN structures were then evaluated. The susceptibility maps created with ellipsoid masks 200 x 200 x 200, 140 x 140 x 140, and 80 x 80 x 80 voxels in size are shown in Fig 5.7d-f. The results showed a change in the calculated $\Delta\chi$ values of less than 1% on varying the extent of the masked region, thus validating the assumption that the restricted ROI sizes used here have little effect on the average measured susceptibility. The measured values are, however, reduced by the effect of the Fourier-based high pass filtering to approximately 70% of the actual values.

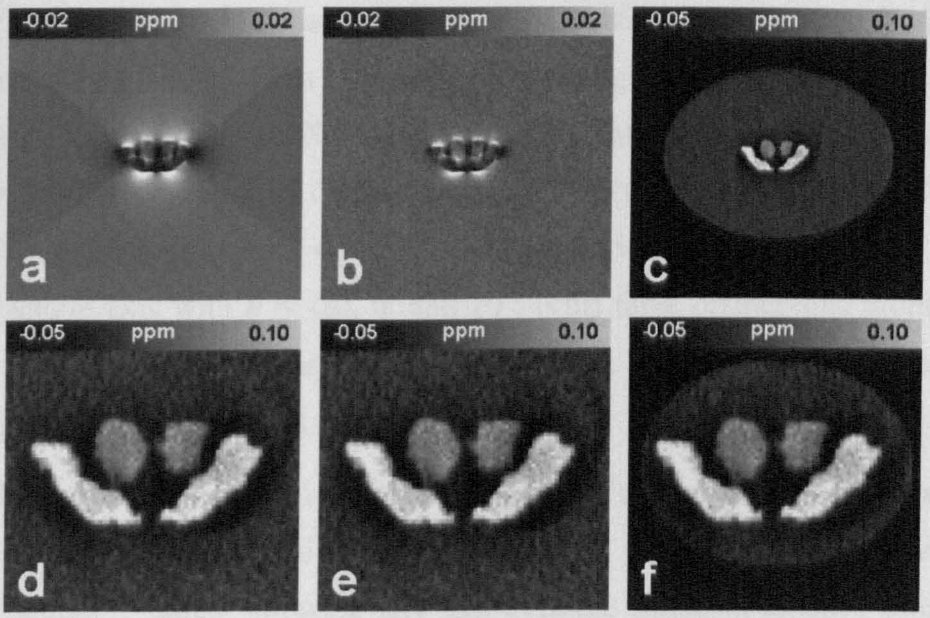

***Figure 5.7** Coronal images showing the effect of a restricted ROI: (a) Simulated field map; (b) (a) plus noise; (c) susceptibility map created in restricted ROI; (d), (e), and (f) zoomed in susceptibility maps created in a 200x200x200, 140x140x140, 80x80x80 ellipsoid respectively.*

5.2 Application of Susceptibility Mapping to Experimental Data

In the previous section a *k*-space threshold method for calculating susceptibility maps from field map data was proposed. Also, a new high pass filtering method was introduced. In this section the results of applying these methods to experimental data from an agar phantom and *in vivo* data acquired from human subjects are presented and discussed.

5.2.1 Phantom Validation: Methods

The spherical agar gel phantom described in Section 4.2.2 containing cylindrical inclusions doped with two concentrations of an iron oxide based contrast agent was used to validate the *k*-space threshold method. Images were acquired at 7T using a 3D spoiled GE FLASH sequence with 0.5 mm isotropic resolution, 128 x 128 x 65 mm^3 field of view, TE/TR = 16/45 ms, and a flip angle of 16°. The phantom was imaged at multiple orientations to B_0, and susceptibility maps were calculated from nine different data combinations: (i) a single orientation scanned once (Number of Experiments [NEX] = 1); (ii) a single orientation imaged with NEX = 2; (iii) a single orientation imaged with NEX = 3; (iv) two orientations where the angle, $\Delta\theta$, between the first and second orientations was 20°; (v) two orientations with $\Delta\theta$ = 40°; (vi) two orientations with $\Delta\theta$ = 60°; (vii) three orientations produced by rotation about a single axis with θ = -20, 0, and 20°; (viii) three orientations produced by rotation about two axes, first a rotation θ about the x-axis followed by a rotation ϕ about the y-axis, where (θ,ϕ) = (20°,0°), (-10°,17°), and (-10°,-17°); and (ix) three orientations produced by rotation about a single axis only, with θ = -60, 0, and 60°. Arrangements (i), (ii), and (iii) were used to assess the effect of signal averaging without sample rotation, allowing any improvement in signal-to-noise ratio to be compared with that produced when combining data acquired at different orientations.

Phase images were unwrapped and then scaled to yield field maps in ppm. The modulus images acquired at each orientation were coregistered using the FLIRT registration tool in FSL [12]. The transformation parameters were then applied to the phase data to bring all of the phase maps into the same space. The rotational parameters from the registration were used to calculate the field direction relative to each data set. The dipole-based method was used for high-pass spatial filtering of the field data, as described in the previous section. For the susceptibility calculations, the measured field maps were placed inside large empty matrices of zeros at least twice as large, in each dimension, as the original map. This ensured that effects of the finite extent of the space considered in the Fourier transform (see Chapter 3) were not significant. The susceptibility values calculated using the approach described here are always subject to an arbitrary offset since they stem from measurement of a frequency difference relative to an arbitrarily set base frequency, and in any case the form of Eq. 3.29 means that $\chi(\mathbf{k})$ is not defined at $\mathbf{k} = 0$. It is therefore necessary to work in terms of a susceptibility difference between regions or compartments, which we denote as $\Delta\chi$. For the phantom, ROIs were drawn inside the doped cylinders and also in adjacent regions of the surrounding agar, allowing the difference in susceptibility between the doped and undoped agar compartments to be calculated.

5.2.2 Phantom Validation: Results

Figure 5.7a-c shows typical modulus, unfiltered, and filtered phase images acquired with the phantom at a single orientation to the field. Figure 5.8a shows the $\Delta\chi$-values calculated for the agar cylinders doped with 0.5 mM and 1 mM concentrations of contrast agent for case (i), a single orientation imaged once, plotted against the threshold parameter, α. The associated χ maps calculated for this case with α = 0.0003, 0.07, and 0.33 are shown in Fig. 5.7d-f. For further analysis, we focused on the contrast-to-noise ratio (CNR) of the susceptibility measurements (defined as the ratio of the average to the standard deviation of the $\Delta\chi$ values in a particular compartment).

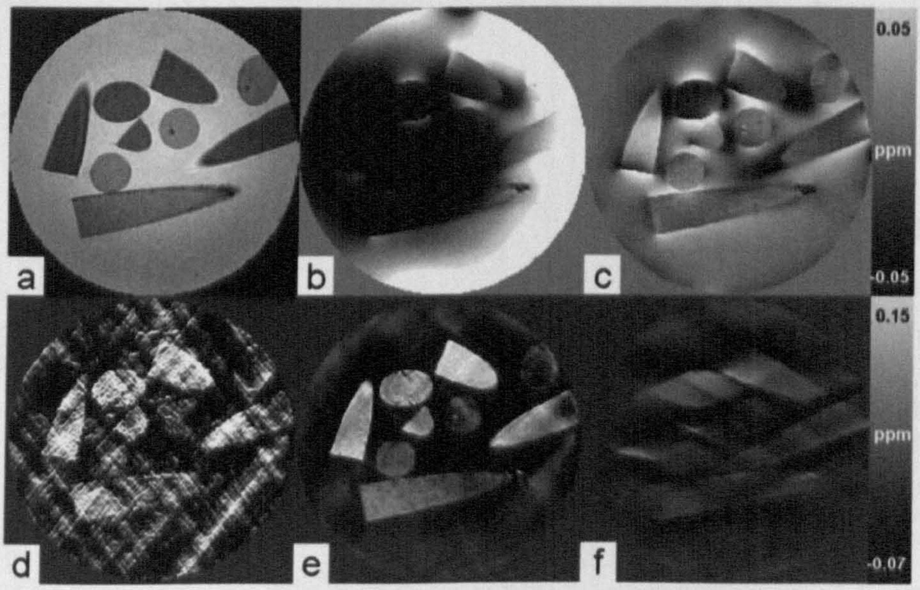

<u>Figure 5.7</u> Modulus data, phase data, filtered phase data, and calculated χ maps for the agar phantom containing iron oxide–doped cylinders. a: Coronal modulus data; (b) unwrapped phase data; (c) phase data filtered using the hybrid dipole/ polynomial filter with 300 dipoles, incorporating a 2^{nd}-order, 3D polynomial function; (d) calculated χ map for the phantom imaged at a single orientation to B0 with α = 0.0003; (e) calculated χ map with α = 0.07; (f) calculated χ map with α = 0.33.

The variation of CNR with α for a single orientation imaged once is shown in Fig. 5.8b, and the plot suggests an optimum value of α = 0.07. Figure 5.8c shows the variation of CNR with α for the nine data combinations (i-ix) described in Section 5.2.1. To simplify the plot, only the results obtained from the cylinders doped with a 1 mM concentration of the contrast agent are shown. The optimum α value, along with the measured $\Delta\chi$ values for the 0.5-mM and 1-mM doped cylinders, are listed in Table 5.2. Figure 5.9 shows representative χ maps for each arrangement that were obtained by using the optimum threshold values.

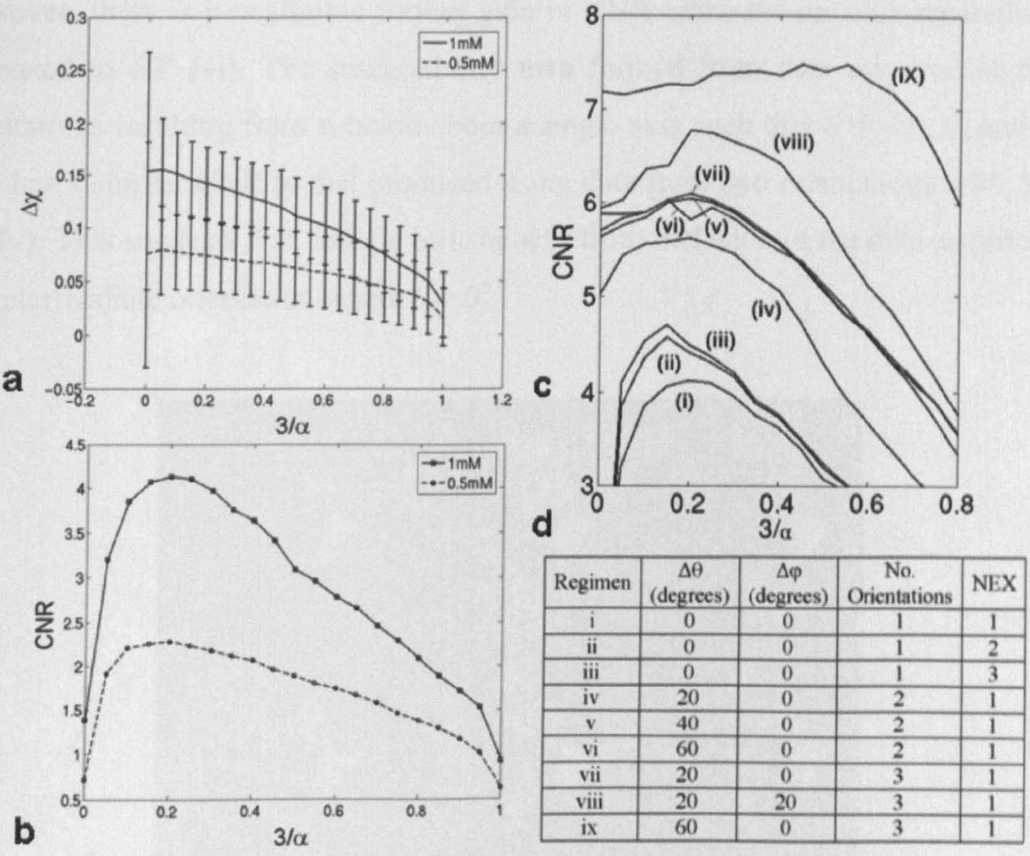

Regimen	Δθ (degrees)	Δφ (degrees)	No. Orientations	NEX
i	0	0	1	1
ii	0	0	1	2
iii	0	0	1	3
iv	20	0	2	1
v	40	0	2	1
vi	60	0	2	1
vii	20	0	3	1
viii	20	20	3	1
ix	60	0	3	1

<u>Figure 5.8</u> a: $\Delta\chi$ and (b) CNR values measured from the agar cylinders doped with 0.5-mM and 1-mM concentrations of the contrast agent are plotted against α. The susceptibility values were calculated from phase data produced with the phantom at a single orientation to B_0. c: CNR calculated from the cylinders doped with 1 mM of contrast agent, plotted against α. Plots are based on $\Delta\chi$ measurements made from data acquired with the phantom for data combinations (i-ix). A description of the different regimen is listed in the table in d.

The results show that averaging data acquired at a single orientation (i-iii) produces a small gain in CNR, but that the CNR increases more slowly than the square root of the number of averages. Larger gains in CNR can be achieved by combining data acquired at different orientations, implying that errors in reconstruction are the dominant source of spatial heterogeneity in the $\Delta\chi$ values calculated from data acquired at a single orientation. The map calculated from data acquired at two orientations with $\Delta\theta = 20^\circ$ (iv) shows increased CNR over the single orientation data (i), with further improvement for $\Delta\theta = 40^\circ$ (v), reflecting the increase in the proportion of k-space for which $\chi(\mathbf{k})$ data are available with these arrangements.

However, there is a negligible further gain in CNR when the angular separation is increased to 60° (vi). The susceptibility map formed from data acquired at three orientations resulting from rotation about a single axis such that θ = -20, 0, and 20° (vii) has a similar CNR to that produced using data from two orientations with $\Delta\theta =$ 40° (v). This suggests that there is little benefit from inclusion of the data acquired at the intermediate orientation where $\theta = 0^\circ$.

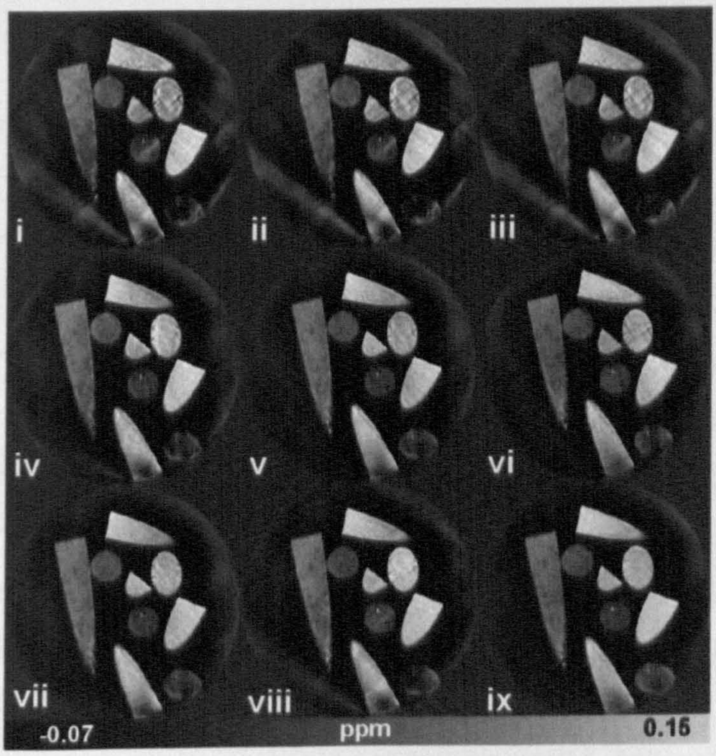

Figure 5.9 *Representative χ maps produced using data combinations (i-ix). The associated α values were set to the optimum values for each arrangement, as described in Table 5.2. For definitions of i-ix see table in Fig. 5.8.*

The map generated from data acquired at three orientations produced by rotations about two orthogonal axes (viii) shows a noticeable improvement in CNR over the previously described data combinations (i-vii). This is an important result as the range of motion, ±20°, is small enough to be reproduced in *in vivo* measurements on the human head. In agreement with the simulations, the susceptibility maps produced from data acquired at three orientations produced by rotation about a single axis such that θ = -60, 0, and 60° (ix) produced the best CNR of all of the data combinations that were evaluated here. The larger optimal value of α for combination (ix) results from the large angular separation of the cones formed by thresholding $C(\mathbf{k})$ in k-space (Fig. 5.1c). However, the range of motion required for this combination makes its use in head imaging unrealistic. The measured values for the 0.5- mM and 1-mM doped cylinders for all of the data combinations were generally in good agreement with the expected values of 0.075 ± 0.01 ppm and 0.15 ± 0.01 ppm, respectively, with a slight general increase in the measured $\Delta\chi$ value seen on stepping through combinations (i) to (ix) (see Table 5.2).

Regimen	$\Delta\chi\,(\pm\sigma)\times10^8$ 0.5-mM cylinders	$\Delta\chi\,(\pm\sigma)\times10^8$ 1-mM cylinders	Optimal α
i	7.41 ± 3.01	14.20 ± 3.14	0.07
ii	7.54 ± 3.01	14.74 ± 3.08	0.05
iii	7.55 ± 3.06	14.74 ± 3.13	0.05
iv	8.04 ± 2.68	15.20 ± 2.70	0.07
v	7.92 ± 2.51	15.25 ± 2.52	0.05
vi	7.93 ± 2.39	15.74 ± 2.61	0.05
vii	8.07 ± 2.47	15.19 ± 2.49	0.07
viii	8.06 ± 2.47	15.71 ± 2.31	0.07
ix	7.99 ± 2.22	15.55 ± 2.08	0.14

Table 5.2 ***Average $\Delta\chi$ values measured in the 0.5-mM and 1-mM agar cylinders relative to the surrounding nondoped agar for each of the nine data combinations.***

The phantom results show the sensitivity of the susceptibility calculation to the choice of the *k*-space threshold parameter, α. A small threshold value yields χ-maps of poor quality, as shown in Fig. 5.7d, due to the presence of streaking artifacts produced by the amplification of noise in k-space regions associated with large values of $1/C$. A high value of the threshold parameter yields a low-contrast χ-map, as shown in Fig. 5.9f, due to the nulling of $\chi(\mathbf{k})$ over a significant fraction of *k*-space. The optimal α value of 0.07 appears to give a good compromise between maintenance of contrast and avoidance of significant noise amplification. Similar behavior was seen in the *in vivo* data, along with a broadly similar variation of CNR with α. Analysis of simulated data (not shown here) indicates that the optimal value of α increases in size as the signal-to-noise ratio in the phase data decreases, but the reduction in CNR produced by using $\alpha = 0.07$, rather than the optimum value, is always small for realistic noise levels. α values identified from the phantom experiments are thus also appropriate for use with in vivo data.

Surprisingly, the χ-map calculated using data acquired with the phantom at a single orientation to B_0 and $\alpha = 0.07$ (Fig. 5.9i) yielded $\Delta\chi$ values for the agar cylinders doped with 0.5-mM and 1-mM concentrations of the contrast agent that agree with the expected values within experimental error. This suggests that despite portions of $\chi(\mathbf{k})$ having been nulled (see Fig. 5.1a,e) there is sufficient remaining information to allow proper definition of the real-space structures. The χ maps are not perfect (see Fig. 5.9i); streaking artifacts can be seen to occur along directions defined by the geometry of the *k*-space mask. However, at the optimum threshold value ($\alpha = 0.07$) these artifacts are not dominant and the structure of the susceptibility distribution can be clearly discerned. The CNR plots, shown in Fig. 5.8c, highlight the advantages of using data acquired at multiple orientations in calculating susceptibility maps, but perhaps more importantly, also show the redundancy of using large rotations, $\Delta\theta > 40^\circ$, in the case where field maps are acquired at two orientations. The results also demonstrate the limited gains produced by using data acquired at three orientations, produced by small rotations about a single axis ($\theta = -20^\circ$, 0°, and 20° corresponding to case (vii) shown in Fig. 5.9c), compared with use of data acquired at two orientations $\Delta\theta = 40^\circ$, corresponding to case (v) in Fig. 5.9c.

5.2.3 Susceptibility Mapping *in vivo*: Methods

The RN and SN brain regions were investigated *in vivo* due to the relativity high concentration of iron attributed to these structures [13]. Images were acquired at 7T using a 3D spoiled GE FLASH sequence with 0.5 mm isotropic resolution, 200 x 200 x 50 mm^3 field of view, TE/TR = 20/45 ms, and a flip angle of 16°. Head images were also acquired on a 3T Philips Achieva scanner, using a similar protocol with TE/TR = 45/74 ms, and 0.65 mm isotropic resolution. The first stage of the *in vivo* experimentation was to image a single healthy subject at 7 T with their head at multiple orientations to B_0. Susceptibility maps were calculated from three different data combinations: ($\mathrm{i}_{in\text{-}vivo}$) a single orientation; ($\mathrm{ii}_{in\text{-}vivo}$) two orientations with the difference produced by a nodding motion with $\Delta\theta$ = 25°; and ($\mathrm{iii}_{in\text{-}vivo}$) three orientations produced by rotation about two axes (θ,ϕ) = (14°,0°), (-7°,12°), and (-7°,-12°), corresponding to a condition number of $\kappa = 4.5$. The same healthy subject was then scanned four times using arrangements ($\mathrm{i}_{in\text{-}vivo}$) and ($\mathrm{ii}_{in\text{-}vivo}$) so as to assess the reproducibility of the calculated susceptibility maps. For each repeated scan, the subject was imaged, removed from the scanner, and then repositioned in the scanner, ready for acquisition of the next image. Two healthy subjects were also imaged at 3 and 7 T in the ($\mathrm{ii}_{in\text{-}vivo}$) arrangement, to allow a comparison of the susceptibility values calculated at the two different fields. The $\Delta\theta$ values were typically 20 ± 10° for the ($\mathrm{ii}_{in\text{-}vivo}$) arrangement. For the in vivo data, the modulus images were used to draw ROIs inside the RN, SN, and the surrounding WM. This allowed calculation of the difference in the susceptibility of the RN and SN relative to the surrounding WM.

5.2.4 Susceptibility Mapping *in vivo*: Results

Figure 5.10c-e,h-j shows χ maps calculated from one healthy subject, using three different data combinations ($\mathrm{i}_{in\text{-}vivo}$-$\mathrm{iii}_{in\text{-}vivo}$). The value of α used in all of the susceptibility calculations on *in vivo* data were fixed at 0.07, based on the study of the phantom. For comparison, the filtered phase data for a single orientation are also shown in Fig. 5.10b,g. Table 5.3 lists the measured $\Delta\chi$ values for the RN and SN, relative to the surrounding WM, for each of the three combinations. $\Delta\chi$ was measured as the average over the entire RN and SN structures. The calculated susceptibility maps clearly show structures matching the RN/SN geometries found in the modulus data, even in the map calculated from phase data produced by imaging at a single orientation with NEX = 1 ($\mathrm{i}_{in\text{-}vivo}$). In contrast, the associated phase/field map appears to be dominated by field shifts projected outside the structures, an effect that is particularly obvious in the coronal images (Fig. 5.10b). The χ-map produced from data acquired at two orientations with $\Delta\theta = 25^\circ$ ($\mathrm{ii}_{in\text{-}vivo}$) shows improved contrast over the single orientation case, with a particular reduction in the heterogeneity of the measured susceptibility in white matter. The map calculated from data acquired at three orientations produced by rotating the head about two axes ($\mathrm{iii}_{in\text{-}vivo}$) showed a further enhancement of contrast and a reduction in WM heterogeneity.

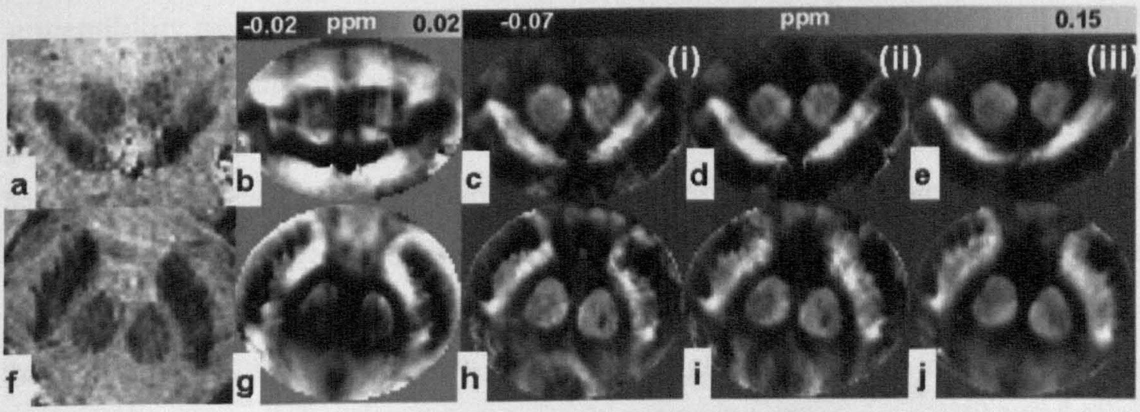

<u>Figure 5.10</u> Field and susceptibility maps acquired from a healthy subject. Images on the top row (a-d) are from representative coronal slices, while the bottom row (e-h) shows representative axial slices from the same data sets. (a,f) modulus data for a single orientation; (b,g) field map for a single orientation; (c,h) χ map calculated from data acquired with the head at a single orientation to B_0; (d,i) χ map calculated from data acquired at two orientations to B0 with $\Delta\theta = 25^\circ$; (e,j) χ map calculated from data acquired at three orientations to B_0, produced by rotation about two axes such that $(\theta,\phi) = (14^\circ,0^\circ)$, $(-7^\circ,12^\circ)$, and $(-7^\circ,-12^\circ)$.

Regimen	RN (ppm)		SN (ppm)	
	$\Delta\chi$	σ	$\Delta\chi$	σ
$\mathrm{i}_{in\text{-}vivo}$	0.05	0.03	0.09	0.06
$\mathrm{ii}_{in\text{-}vivo}$	0.05	0.03	0.11	0.06
$\mathrm{iii}_{in\text{-}vivo}$	0.04	0.02	0.10	0.04

Table 5.3 ***Average in vivo $\Delta\chi$ measured over the whole RN and SN structures relative to the surrounding WM for three different data combinations. The standard deviation, σ, of $\Delta\chi$ calculated over the regions is also shown.***

The situation where calculations are based on a single orientation imaged once ($\mathrm{i}_{in\text{-}vivo}$) is of particular relevance, as the possibility of making quantitative $\Delta\chi$ measurements *in vivo* using a single data set would open up many applications of susceptibility mapping and would also be particularly useful in large medical studies where head rotation may be impractical. Recently, de Rochefort et al. [14] showed that a weighted gradient regularization approach using prior knowledge, such as that based on magnitude image data, yields accurate, high-quality χ maps that show no noticeable streaking artifacts, from a single-phase map acquired *in vivo*. This method is described in more detail in Chapter 7. Here, it has been shown that simple *k*-space thresholding used in conjunction with improved high-pass filtering can also produce quantitative χ maps from a single data set (Fig. 5.10c,h). The χ-map calculated from phase data acquired at two orientations ($\mathrm{ii}_{in\text{-}vivo}$), with $\Delta\theta = 25^\circ$ (Fig. 5.10d,i), exhibits increased homogeneity within the WM and the SN relative to that produced using phase data from a single orientation. The χ-map calculated from data acquired at three orientations ($\mathrm{iii}_{in\text{-}vivo}$) (Fig. 5.10e,j) shows a further increase in homogeneity within the separate compartments associated with the WM, RN, and SN and also yielded a susceptibility distribution that is free of streaking artefacts. It would appear that for the three-angle case, the WM/RN and the WM/SN interfaces are very slightly smoothed. This smoothing is most likely due to the increased number of co-registration steps required to combine the data acquired at the three orientations, resulting in slight errors in alignment. Such smoothing was not evident in the phantom data, for which image alignment is more straightforward. Co-registration was made more difficult by EPI related distortions due to the close proximity of the sinus fields. To improve the quality of the registered data, masks were applied to inform the co-registration software (FLIRT) of the important ROI for this work i.e. the RNSN region. In these data, the average calculated $\Delta\chi$-values for the RN and SN were found to be 0.05 ± 0.02 and 0.10 ± 0.05 ppm, respectively. Making the assumption that the susceptibility difference results from the elevated iron content of these structures and that the iron is in the form of ferritin, which has a susceptibility of 1.4 ppm/mg/gram-tissue [9], these susceptibility measurements would correspond to an increased ferritin content relative to the surrounding WM of 0.04 ± 0.02 and 0.07 ± 0.04 mg/g-tissue for the RN and SN, respectively. The relatively large standard deviation of the susceptibility values measured across the RN and SN indicates a degree of heterogeneity in these structures, which is greater than is seen in the data from the phantom. This may well reflect true variation of susceptibility due to heterogeneity of iron content in the SN and RN, but further work is needed to test this hypothesis. Splitting the SN into different sub-regions, such as the pars compacta, would probably yield smaller standard deviation values.

5.2.5 Susceptibility Mapping *in vivo*: Reproducibility

Table 5.4 summarizes measurements made on susceptibility maps that were produced from data acquired at one or two orientations ($\mathrm{i}_{in\text{-}vivo}$ and $\mathrm{ii}_{in\text{-}vivo}$) over four separate scanning sessions. The standard deviation quoted for each individual measurement was calculated from the square root of the sum of the variance of χ over voxels in the relevant compartment (SN or RN) and in the reference WM region, while the value quoted in association with the average is calculated from the variation of the compartmental average across repeats. The results shown in Table 5.4, which were produced by imaging the same subject in four separate sessions, provide evidence that the susceptibility measurements show a reasonable degree of intra-subject reproducibility, with the mean $\Delta\chi$ values of the RN and SN varying by no more than 0.03 ppm for calculations based on phase data acquired in one or two orientations. In general, the susceptibility values in the RN were more constant across repeats than those measured in the SN, perhaps reflecting the comparatively simple geometry of the sphere-like RN and the lesser spatial heterogeneity of the measured susceptibility in the RN.

Session	One Orientation		Two Orientations	
	RN $\Delta\chi\pm\sigma$(ppm)	SN $\Delta\chi\pm\sigma$(ppm)	RN $\Delta\chi\pm\sigma$(ppm)	SN $\Delta\chi\pm\sigma$(ppm)
Scan 1	0.05 ± 0.03	0.09 ± 0.06	0.05 ± 0.02	0.11 ± 0.06
Scan 2	0.05 ± 0.05	0.10 ± 0.08	0.06 ± 0.05	0.12 ± 0.07
Scan 3	0.05 ± 0.06	0.08 ± 0.08	0.06 ± 0.05	0.09 ± 0.07
Scan 4	0.05 ± 0.05	0.10 ± 0.08	0.07 ± 0.04	0.12 ± 0.06
Average	0.05 ± 0	0.09 ± 0.01	0.06 ± 0.01	0.11 ± 0.01

***Table 5.4** Average $\Delta\chi$ measured in vivo in the RN and SN relative to the surrounding WM for susceptibility maps calculated from phase data acquired at one or two orientations, recorded over four separate scanning sessions.*

The $\Delta\chi$-values calculated from data acquired at a single orientation were slightly lower than the results for data acquired at two orientations, which is a consequence of the increased k-space data available for the susceptibility calculation after averaging the measurements made at different orientations. In this preliminary study only two subjects were scanned as a large scale study was beyond the scope of this work. The small number of subjects used here may mean the mean susceptibility values are not representative of a larger population. Further work should be carried out to establish mean susceptibility values for larger numbers of subjects, taking into account important factors such as age.

5.2.6 Susceptibility Mapping *in vivo*: Cross-Field Results

Table 5.5 details the results of measuring $\Delta\chi$ in two healthy subjects, using phase data acquired at two orientations ($\text{ii}_{in\text{-}vivo}$) at 3 and 7 T. The $\Delta\chi$-values appear to be independent of field strength, with only small variations of the order of ±0.02 ppm in the average values. The results listed in Table 5.5, which were produced from the two healthy subjects who were imaged at two orientations at 3 and 7 T, suggest that the calculated $\Delta\chi$ values within the RN and SN are independent of field strength in the 3-7 T range. This observation agrees well with recent work by Yao et al. [15], who showed a linear increase in measured frequency offset with field strength over the range of 1.5 to 7 T for deep gray matter structures, including the putamen, caudate nucleus, globus pallidus, and thalamus.

Region, field (T),	RN		SN	
$\Delta\chi \pm \sigma$ (ppm)	3	7	3	7
Subject 1	0.05 ± 0.05	0.05 ± 0.02	0.11 ± 0.07	0.10 ± 0.06
Subject 2	0.09 ± 0.06	0.08 ± 0.06	0.12 ± 0.08	0.12 ± 0.07

***Table 5.5** Average $\Delta\chi$ measured in vivo in the RN and SN relative to the surrounding WM at 3 and 7 T for two healthy subjects.*

The results obtained at 3 T are encouraging since the average $\Delta\chi$ values are consistent with those measured at 7 T, despite the reduced SNR associated with the lower field strength. As discussed above, the relatively small number of subjects used in this study may mean the susceptibility values listed here are not fully representative. Further work should be carried out to establish the relationship between field strength and measured susceptibility in all brain regions for a large subject pool.

5.2.7 General Comments on Susceptibility Mapping using a *k*-Space Threshold

A robust method for using phase image data to map the susceptibility distribution in samples with complex geometries has been presented. The method was validated using a phantom and than applied successfully to brain images acquired at 7 T. For susceptibility mapping based on phase data acquired at a single orientation, the choice of *k*-space threshold is the most important consideration. The results presented in this chapter suggest a threshold of $a \approx 0.07$ gives a good compromise between contrast and noise. For susceptibility mapping based on phase data acquired at multiple orientations, the size of the angle through which the sample is rotated, as well as the choice of a, ultimately determine the quality of the reconstructed χ-map. For *in vivo* imaging in a standard high field MRI scanner the range of motion is limited. In this case small rotations about two axes give better results when compared to small rotations about a single axis. The reproducibility of the method was shown to be good, and in conjunction with the consistency of the cross-field measurements suggests that this technique could be used to analyze data from clinical studies. In Chapter 6, the threshold method is used to create susceptibility maps based on phase data acquired from patients with Parkinson's disease and multiple sclerosis. In Chapter 7, more sophisticated mapping methods based on iterative techniques are discussed that allow whole-brain susceptibility mapping.

5.3 References

1. de Rochefort, L., R. Brown, M.R. Prince, and Y. Wang, *Quantitative MR susceptibility mapping using piece-wise constant regularized inversion of the magnetic field.* Magnetic Resonance in Medicine, 2008. **60**(4): p. 1003-1009.
2. de Rochefort, L., T. Nguyen, R. Brown, P. Spincemaille, G. Choi, J. Weinsaft, M.R. Prince, and Y. Wang, *In vivo quantification of contrast agent concentration using the induced magnetic field for time-resolved arterial input function measurement with MRI.* Medical Physics, 2008. **35**(12): p. 5328-5339.
3. Marques, J.P. and R. Bowtell, *Application of a fourier-based method for rapid calculation of field inhomogeneity due to spatial variation of magnetic susceptibility.* Concepts in Magnetic Resonance Part B-Magnetic Resonance Engineering, 2005. **25B**(1): p. 65-78.
4. Jezzard, P. and S. Clare, *Sources of distortion in functional MRI data.* Human Brain Mapping, 1999. **8**(2-3): p. 80-85.
5. Liu, T., P. Spincemaille, L. de Rochefort, B. Kressler, and Y. Wang, *Calculation of Susceptibility Through Multiple Orientation Sampling (COSMOS): A Method for Conditioning the Inverse Problem From Measured Magnetic Field Map to Susceptibility Source Image in MRI.* Magnetic Resonance In Medicine, 2009. **61**(1): p. 196-204.
6. Haacke, E.M., N.Y. Cheng, M.J. House, Q. Liu, J. Neelavalli, R.J. Ogg, A. Khan, M. Ayaz, W. Kirsch, and A. Obenaus, *Imaging iron stores in the brain using magnetic resonance imaging.* Magnetic Resonance Imaging, 2005. **23**(1): p. 1-25.

7. Haacke, E.M., Y.B. Xu, Y.C.N. Cheng, and J.R. Reichenbach, *Susceptibility weighted imaging (SWI).* Magnetic Resonance in Medicine, 2004. **52**(3): p. 612-618.
8. Deistung, A., A. Rauscher, J. Sedlacik, J. Stadler, S. Witoszynskyj, and J.R. Reichenbach, *Susceptibility Weighted Imaging at Ultra High Magnetic Field Strengths: Theoretical Considerations and Experimental Results.* Magnetic Resonance In Medicine, 2008. **60**(5): p. 1155-1168.
9. Duyn, J.H., P. van Gelderen, T.Q. Li, J.A. de Zwart, A.P. Koretsky, and M. Fukunaga, *High-field MRI of brain cortical substructure based on signal phase.* PNAS, 2007. **104**(28): p. 11796-11801.
10. Haacke, E.M., S. Mittal, Z. Wu, J. Neelavalli, and Y.C.N. Cheng, *Susceptibility-Weighted Imaging: Technical Aspects and Clinical Applications, Part 1.* American Journal of Neuroradiology, 2009. **30**(1): p. 19-30.
11. Neelavalli, J., N.C. Yu-Chung, J. Jing, and E.M. Haacke, *Removing background phase variations in susceptibility-weighted imaging using a fast, forward-field calculation.* Journal of Magnetic Resonance Imaging, 2009. **29**(4): p. 937-948.
12. Jenkinson, M. and S. Smith, *A global optimisation method for robust affine registration of brain images.* Medical Image Analysis, 2001. **5**(2): p. 143-156.
13. Hallgren, B. and P. Sourander, *The Effect of Age on the Non-Haemin Iron In The Human Brain.* Journal of Neurochemistry, 1958. **3**(1): p. 41-51.
14. de Rochefort, L., T. Liu, B. Kressler, J. Liu, P. Spincemaille, V. Lebon, J. Wu, and Y. Wang, *Quantitative susceptibility map reconstruction from MR phase data using bayesian regularization: Validation and application to brain imaging.* Magnetic Resonance in Medicine, 2010. **63**(1): p. 194-206.
15. Yao, B., T.-Q. Li, P.v. Gelderen, K. Shmueli, J.A. de Zwart, and J.H. Duyn, *Susceptibility contrast in high field MRI of human brain as a function of tissue iron content.* Neuroimage, 2009. **44**(4): p. 1259-66.

CHAPTER 6

Preliminary Results of Susceptibility Mapping In Clinical Applications

Research in MRI is ultimately driven by the need for accurate information for medical research and diagnosis. Clinicians working in the field of medical imaging are continuously looking for new ways to visualise disease pathologies. With the development of MRI over the last 25 years, common neurodegenerative diseases such as Parkinson's disease and multiple sclerosis (MS) have been subject to intense research [1-8]. Despite this growing body of research, an accurate 'bio-marker' of disease progression, to enable the diagnosis and management of these neurodegenerative diseases, has yet to be found [9, 10]. Iron concentration in brain tissues has been proposed as a possible biomarker for disease progression in Parkinson's and MS. The sensitivity of susceptibility mapping to iron levels makes it a potentially important technique for determining the relationship between iron deposits and disease pathology. Here, preliminary results generated by applying susceptibility mapping, based on the approach described in Chapter 5, to data acquired from healthy subjects and patients with MS and Parkinson's disease are presented.

6.1 Forming User Friendly Susceptibility Mapping Software

Most of the data presented in this chapter has been analysed by investigators who were unfamiliar with the underlying theory of susceptibility mapping. For this reason, software was created that would enable these researchers to use susceptibility mapping without specialist knowledge.

6.1.1 Establishing the Users Needs

After several discussions with the investigators who would ultimately be processing the data, a set of user needs were established:

1. The processes should be automated as much as possible.
2. For the processes that could not be automated the user input should be kept to a minimum.
3. When the user is asked to perform a task it should be simple and require no specialist knowledge.

These simple needs are all based on reducing the total amount of time the user spends on analysing data. A more general requirement is that the total processing time is made as short as possible.

6.1.2 Flow Diagram of Mapping Procedure

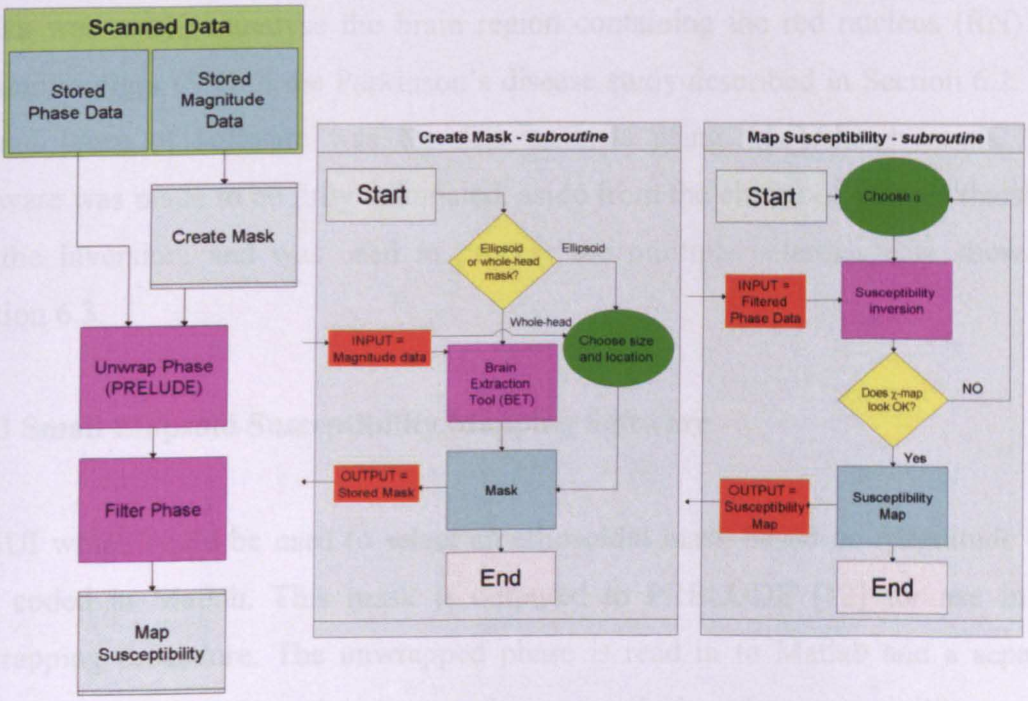

***Figure 6.1** Flow diagram of the susceptibility mapping procedure.*

In order to determine the inputs required from a user it is often useful to form a flow diagram. Figure 6.1 shows the flow diagram associated with forming a susceptibility map based on MRI phase and magnitude data. There are three or four main user inputs in the procedure (four if an ellipsoidal mask is selected). The first input is the choice of mask type in the mask creation subroutine. If the user chooses to use a whole head mask then the brain extraction tool (BET) [11] can be used to create a mask, as described in Chapter 4. However, if the user chooses a small ellipsoidal mask further inputs are required. To generate an ellipsoid the central coordinate and associated axial radii must be defined by the user using magnitude data. The other major user input is the choice of k-space threshold, α, in the susceptibility mapping routine, described in Chapter 5.

Based on the user needs, and the necessary user inputs derived from the flow chart, it was decided to create two separate pieces of software. One would be used for data analysis involving small ellipsoidal masks. This software would have a graphic user interface (GUI) that would help guide the user through the necessary steps for forming a χ-map based on a small mask. The software incorporating small ellipsoidal masks was used to analyse the brain region containing the red nucleus (RN) and substantia nigra (SN) in the Parkinson's disease study described in Section 6.2. The second piece of software was for data analysis using whole-head masks. This software was made to be fully automated, aside from the choice of k-space threshold for the inversion, and was used to process the multiple sclerosis data shown in Section 6.3.

6.1.3 Small Ellipsoid Susceptibility Mapping Software

A GUI which could be used to select an ellipsoidal mask based on magnitude data was coded in Matlab. This mask is outputed to PRELUDE [12] for use in the unwrapping procedure. The unwrapped phase is read in to Matlab and a separate GUI is then used to filter the phase and create and view the susceptibility map. A representative whole-brain 3D phase and magnitude data set is used here to demonstrate the layout of the GUI's. Figure 6.2 shows the layout of the first GUI that appears after the user has chosen the data sets to be analysed. This GUI allows the user to select the location and size of the ellipsoidal mask to be used for unwrapping and filtering. To help explain the GUI the key inputs and displays have been numbered from 1-16 on Fig 6.2. The magnitude image is displayed in transverse (Fig 6.2:8), sagittal (Fig. 6.2:11), and coronal planes (Fig. 6.2:14) at slice numbers defined by the boxes next to each image (Fig. 6.2:10, 13&16). There are also zoom buttons (Fig. 6.2:9, 12&15) that will enlarge the associated image to a larger size. The location of the mask is defined by three central coordinates, *x*, *y*, and *z* (Fig. 6.2:2) which can be updated in real time. The size of the mask is defined by the three radii, *a*, *b*, and *c* (Fig 6.2:3) which can also be updated.

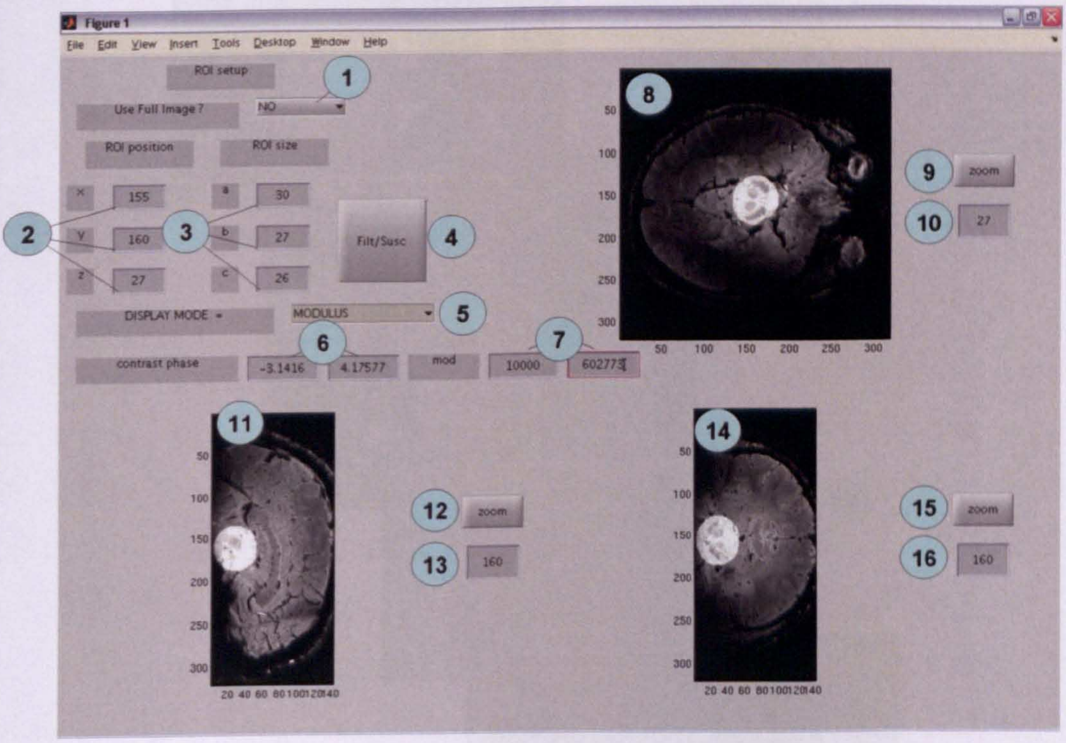

***Figure 6.2** GUI for mask selection (white ellipsoid) based on transverse, coronal, and sagittal magnitude data. The different parts of the GUI are labelled 1-16.*

The mask is superimposed over the magnitude data as a region of hyper-intensity. This lighter region changes if the central coordinates or radii values are updated, and can be made invisible or visible by switching the box labelled 1 in Fig 6.2. There are also adjustable contrast settings that control how the magnitude is displayed (Fig 6.2:6&7). The image display can be switched between the magnitude and phase data by changing the box labelled as 5 in Fig 6.2. Once the mask is selected it can be saved to memory by pressing the large square button (Fig 6.2:4). This mask can then be used by Prelude [12] to unwrap only the phase data that are important, greatly speeding up the procedure from a number of hours to a few minutes. In the example above, the RN/SN region has been selected for analysis as this was the region used in the Parkinson's study.

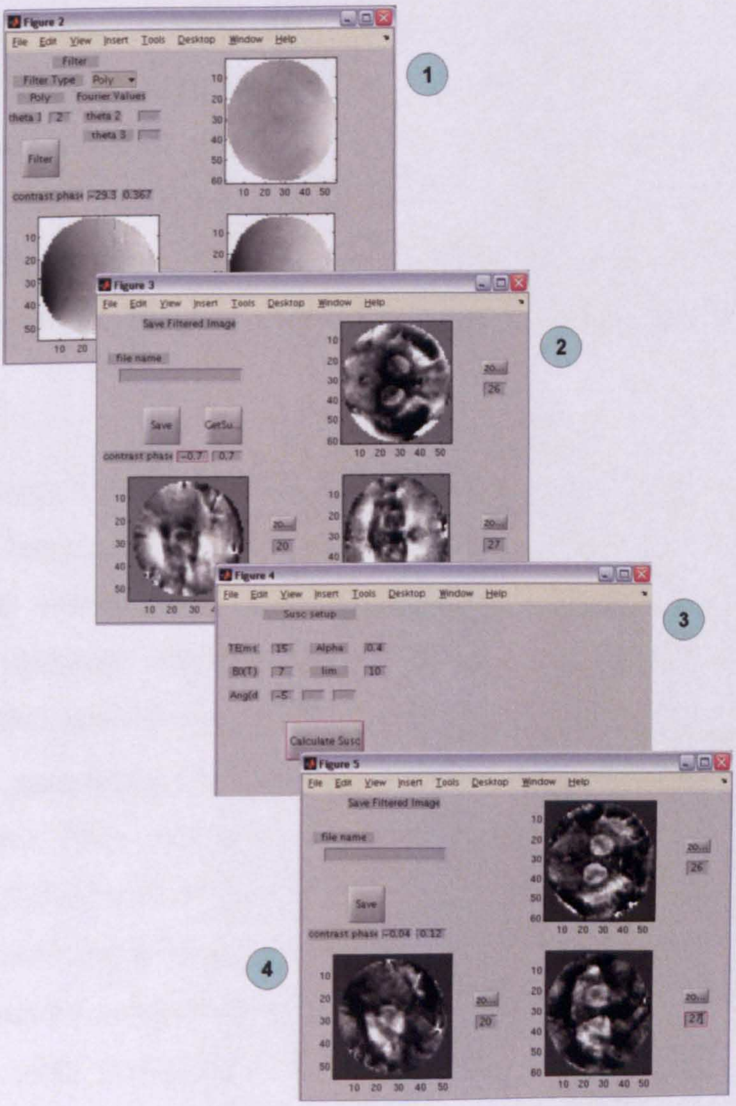

Figure 2

Filter Type: Poly

theta 1: 2

contrast phase: -29.3 0.367

Figure 3

contrast phase: -0.7 0.7

Figure 4

TE(ms): 15

Alpha: 0.4

B(T): 7

lim: 10

Ang(d: -5

Figure 5

contrast phase: -0.04 0.12

__Figure 6.3__ Screen shots of the various GUI's used for filtering and susceptibility mapping: (1) GUI displaying unwrapped phase; (2) GUI displaying filtered phase with saving option; (3) GUI asking the user to choose the parameters for susceptibility mapping; (4) GUI displaying calculated susceptibility map.

After the unwrapping stage, the phase data (now forming a scaled field map) must be filtered to remove unwanted background fields, as described in Chapter 4. A GUI was formed (Fig 6.3:1) that displays the unwrapped phase in a similar format to that used in the masking GUI. The default filtering parameters were chosen to be a dipole fit incorporating 40 dipoles, placed in the approximated region of the sinuses, combined with a 2^{nd} order 3D polynomial, as described in Section 5.1.5. These values were chosen in a small preliminary study involving four healthy subjects. Combining the polynomial filter with the dipole filter was found to slightly improve the filtering of the large scale sinus fields. These default filtering parameters proved to be highly successful in removing the unwanted field for all subjects analysed using this software. The filtering is carried out when the user selects the '*Filter*' button. The GUI shown in Fig 6.3:2 then appears and displays the filtered phase data. The user can save this data set by choosing a filename and pressing the '*Save*' button.

If the user is happy with the filtering, the susceptibility can be calculated by pressing the '*Get Susc*' button. This will then make the GUI shown in Fig 6.3:3 appear. This GUI allows the user to define all the parameters for the *k*-space threshold based susceptibility mapping procedure (Chapter 5), including: B_0, TE, a, and the orientation of the image relative to B_0 characterised by angles θ, ϕ. Once the user has selected these parameters the '*Calculate Susc*' button is pressed to initiate the inversion process. The result of the susceptibility mapping is then displayed in the GUI shown in Fig 6.3:4. If the user is happy with the result, the χ-map can be saved to memory by defining a filename. If the user is unhappy with the result, this GUI can be closed and the parameters can be re-defined on the previous GUI to repeat the process. The total processing time for the procedures discussed above is approximately 30 minutes per data set.

6.1.4 Whole-head Susceptibility Mapping Software

For the case where no specific region of the brain is selected, the region of interest becomes the whole brain. For this application, automated software was written with the only user input being the choice of the *k*-space threshold, a. The first stage in the mapping procedure is to use BET [11] (see Chapter 4) to create a mask of the brain. This mask is then used to define the region of space to be unwrapped using PRELUDE [12]. For large 3D data sets (typically 400 x 400 x 200 voxels), the main computational cost is in the unwrapping procedure which can take several hours. However, no user input is required and the unwrapping can usually be left running over night. After unwrapping, the masked phase data must be filtered to remove unwanted background fields.

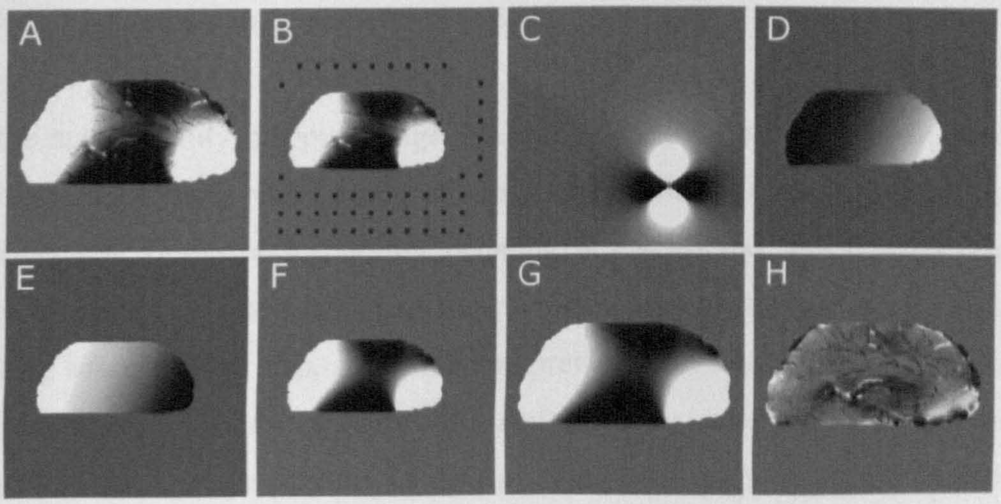

***Figure 6.4** Wholehead filtering steps: (A) sagittal slice of masked and unwrapped phase data; (B) down-sampled phase (A) with position of dipoles for filtering; (C) example of dipole field; (D) fitted multi-dipole field; (E) fitted 2^{nd} order polynomial; (F) total fitted field = D + E; (G) Interpolated fit (F) to yield same resolution as (A); filtered phase = A-G.*

Figure 6.4 shows the different steps involved in filtering the whole brain phase data. The unwrapped and masked phase (Fig 6.4A) is down-sampled by a factor of 2 in each dimension to yield a lower resolution data set (Fig 6.4B). This reduces the total processing time as the number of voxels being fitted is cut by a factor of 8 (2^3). Approximately 700 dipoles were then placed on a grid around the brain in the reduced phase data. This number of dipoles was chosen as a compromise between a large computation time, as the fitting time scaled with the number of dipoles squared, and having enough dipoles to accurately map the unwanted externally generated fields. The dipoles were placed non-uniformly (Fig 6.4B) so as to give more dipoles underneath the brain to better model, and remove, the unwanted fields due to the air/tissue interface of the sinuses. To demonstrate the field due to a dipole that would be fitted inside the brain, a single dipolar field is shown in Fig 6.4C. The fields due to these dipoles were then fitted in combination with a 2^{nd} order 3D polynomial, as described in Chapter 5. The fitted dipole field, 3D polynomial field, and composite total field are shown in Fig 6.4D, E&F respectively. The composite total fitted field is then interpolated back to the original resolution, see Fig 6.4 G. Finally, the fitted field is subtracted from the original unwrapped phase to yield a filtered phase/field map, as shown in Fig 6.4H.

For the susceptibility mapping stage the user defines the orientation of the image relative to B_0 (usually read directly off the scanner) and the *k*-space threshold, α, for the inversion. Before susceptibility mapping is carried out, the filtered phase is placed in a matrix of zeros 25% larger in each dimension then the original mask. The resulting susceptibility map, as well as the previously created filtered phase data is than saved to memory for further analysis. The total processing time is approximately 10 hours for a large data set. However, the user is only required to input a small amount of information over the course of the processing, taking no more than 5 minutes.

6.2 Magnetic Susceptiblity of Substantia Nigra in Parkinson's Disease: A 7T *In Vivo* MRI Study

Parkinson's disease (PD) is a common neurodegenerative disease that is associated with dopaminergic cell loss in the substantia nigra (SN) [10]. In normal aging or Parkinson's disease, loss of these neurons occurs concurrently with the accumulation of iron [13]. The pars compacta (PC), the medial subregion of the SN, has the greatest concentration of dopaminergic neurones in the SN [14].

6.2.1 Previous MRI Studies on the Substantia Nigra in Parkinson's Disease

There have been a number of attempts to use MRI to study changes in the SN in PD [1-6] . In the SN there is a relatively homogeneous distribution of iron in the form of ferritin and a heterogeneous distribution of iron in the form of neuromelanin and haemosiderin, which give rise to inhomogeneities in the magnetic field in and around the SN. The transverse relaxation rates, R_2 and R_2*, decrease with increasing iron concentration, due to spin dephasing in the microscopic field inhomogeneities induced in regions where the distribution of iron is heterogeneous. Decreased R_2 [15-17] and R_2* [18] have been observed in the pars compacta of the SN of patients with PD, particularly on the most affected side. It has been proposed that the field dependence of R_2 is a direct measure of ferritin, and using this measure it was suggested that the concentration of ferritin is increased in the SN in early onset PD patients, whereas the reverse is true for late onset patients [19].

Unfortunately R_2 and R_2* are affected not only by iron but also by water binding, and so R_2' (the difference between R_2 and R_2*) has been proposed as a parameter that is sensitive to field inhomogeneities due to iron, without any confounding effects of changes in water binding. Wallis et al [20] found an increase in R_2' in PD patients compared to healthy controls which correlated with motor symptoms, but not disease duration. The SN has a long T_1 compared to the surrounding brain tissue. Some studies have found this to be reduced in PD and have interpreted this finding as being related to a change in cell density [21], although the finding is not consistent between studies [2, 17].

In summary, most MR contrasts that have been studied in PD depend indirectly on the effect of the magnetic susceptibility of iron on the dephasing of NMR signal, and will show a complex dependence on the microscopic distribution of iron. Therefore there is a need for a more direct, *in vivo* measure of iron in the brains of PD patients. The magnetic susceptibility of the tissue also depends on iron content but is less dependent on the spatial distribution of the iron. Susceptibility mapping may provide an indirect marker of neuronal loss and the spatial pattern of neuronal loss in the SN. The aim of this study was therefore to determine whether susceptibility mapping at 7T could distinguish susceptibility differences between PD patients and normal control subjects.

6.2.2 Methods

This study received approval from the local ethics committee. Fourteen patients with Parkinson's disease and thirteen controls were recruited. Data from five patients and

2 controls were subsequently excluded due to movement, leaving 9 PD patients and 11 controls. MRI scans were acquired at 7T using a 3D spoiled gradient echo FLASH sequence with EPI factor 3, TR = 45ms, TE ≈ 20ms, flip angle 15°, resolution ≈ 0.55x0.55x0.55 mm^3, water fat shift ≈ 25 pixels. Approximate values are quoted as the scan parameters varied slightly due to hardware upgrades throughout the study. Magnitude and phase images were reconstructed from the data. The processing and software steps for susceptibility mapping based on small ellipsoidal masks, as described in Section 6.1.3, were then applied to the data by an investigator. Through trial and error, a *k*-space threshold of $\alpha = 0.13$ was found to give the best compromise between contrast and noise. ROI's inside the SN, PC, and nearby white matter (WM) were drawn on 6 transverse slices using the magnitude data, as shown in Figure 6.5.

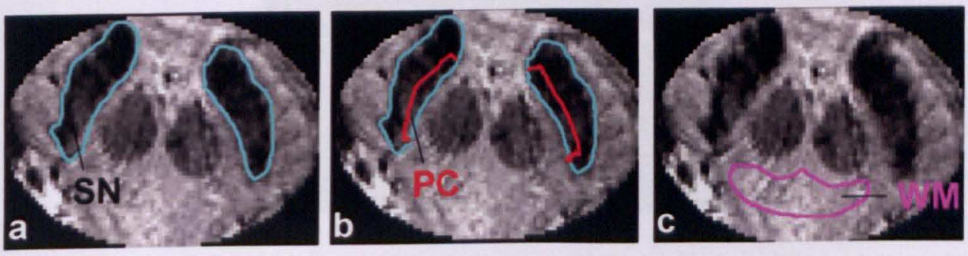

***Figure 6.5** ROI's used for Parkinson's study: (A) SN;(B) PC+SN;(C) WM.*

The PC was analysed as a separate region from the SN due to the particularly high concentration of dopaminergic neurones present within this structure. The WM was used as a reference point such that the susceptibility inside the SN and PC would be measured as $\Delta\chi$-values relative to WM. A reference point is necessary due to the removal of the centre of *k*-space inherent in the χ-mapping procedure, see Chapter 5. To visualise the spatial variations of magnetic susceptibility within the SN for PD patients and controls, data from one subject from each group with similar average susceptibility was chosen to be rendered and visualised in 3D.

6.2.3 Results and Discussion

Figure 6.6 shows representative transverse slices of typical susceptibility maps from a control subject (Fig. 6.6c&d) and a PD patient (Fig. 6.6a&b). The contrast is shown in both greyscale (Fig. 6.6a&c) and artificial colour (Fig. 6.6b&d) to help enhance the subtle differences between the two images. The PD patient has more positive $\Delta\chi$-values in the SN relative to the control, perhaps suggesting increased iron content. Figure 6.7 shows the result of averaging $\Delta\chi$ values in the SN and PC for all controls and PD patients. The average values of $\Delta\chi$ in the SN was higher for the PD vs controls, but not significantly so ($p = 0.1755$). The average $\Delta\chi$ value in the PC was higher for the PD vs controls, and the difference was found to be significant ($p = 0.0415$). The apparent split in $\Delta\chi$ values measured in the PC for PD subjects was not found to correlate with either age or disease duration.

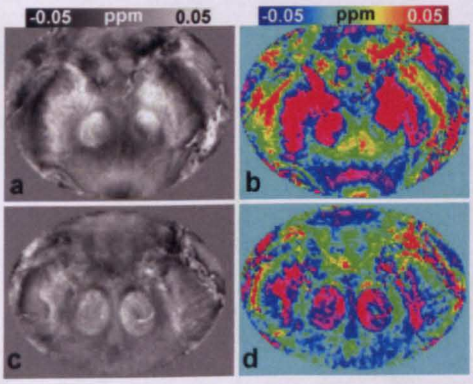

Figure 6.6 ***Typical susceptibility maps from a control subject (c&d) and PD patient (a&b). The contrast is shown in standard grey scale (a&c) and also artificial colour (b&d).***

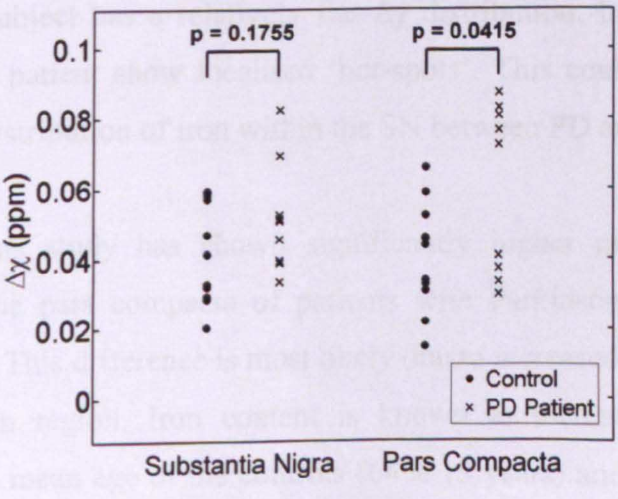

***Figure 6.7** Average $\Delta\chi$ values for PD and controls in the substantia nigra and pars compacta regions.*

Figure 6.8 shows 3D rendered surface plots of the SN for a control and PD patient. The segmentation of the surface was carried out by hand using the magnitude data as a guide. The surface intensity was calculated by averaging the value of $\Delta\chi$ within each half of the SN along the right-left axis (see top of Fig. 6.8) and then dividing the results by the mean value for the whole SN to yield normalised values.

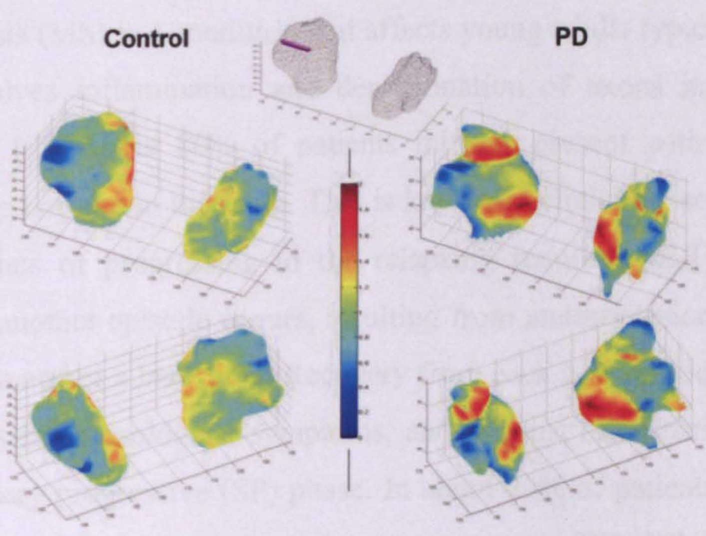

***Figure 6.8** 3D surface plots of the SN for a control and PD patient.*

From the mean normalised surface plots shown in Fig. 6.8, it can be seen that the SN of the control subject has a relatively flat $\Delta\chi$ distribution. In contrast, the surface plots of the PD patient show localised 'hot-spots'. This could be an indication of changes in the distribution of iron within the SN between PD and controls.

In summary, this study has shown significantly higher magnetic susceptibility differences in the pars compacta of patients with Parkinson's disease relative to control subjects. This difference is most likely due to increased iron deposition in PD within this brain region. Iron content is known to increase with age, but the difference in the mean age of the controls (64 ± 13 years) and PD patients (59 ± 8) was not significant. The surface plots show that the 3D spatial distribution of iron within the SN, and not just the bulk average, may be of particular importance. These preliminary results suggest that susceptibility mapping is potentially a useful tool for investigating Parkinson's disease. Further work should be carried out on larger test populations using 3D surface plotting in longitudinal studies to better understand the relationship between iron deposition and the progression of Parkinson's disease.

6.3 Magnetic Susceptibility Mapping in Deep Grey Matter Structures of Patients with Multiple Sclerosis

Multiple Sclerosis (MS) is a condition that affects young adults typically aged 20-40 years, and involves inflammation and demyelination of axons in the brain and nervous system [9]. About 80% of patients initially present with a single acute episode affecting one site in the brain. This is known as clinically isolated syndrome (CIS). The chance of progressing to the relapsing remitting (RR) phase of MS increases when another episode occurs, resulting from another lesion appearing at a different location and at a later time. Recovery from each new episode is incomplete leading to persistent neurological symptoms, and in most cases patients eventually enter the secondary progressive (SP) phase. In about 20% of patients, the disease is progressive from onset and known as primary progressive (PP). While inflammation and demyelination dominate the early stage of disease, the progressive phase involves neurodegenaration, axonal loss and atrophy [9, 22, 23].

6.3.1 MRI and Multiple Sclerosis

MRI has played an important role in the diagnosis of MS [7] and has also been used to monitor drug efficacy in treatment trials. However white matter lesion burden, as conventionally detected on MRI, can only explain up to 10-15% of clinical disability and it is thought that this could be partly due to the diffuse disease which occurs outside 'visible' lesions in normal appearing brain tissue. In addition, MS patterns differ from subject to subject, between lesions within the same subject, and in the same lesion at different time points. MS lesions are thought to be related to iron deposition although it is not well understood if iron deposition occurs as a result of pathological changes of MS disease, or whether iron deposition causes the neurological degenerations in brain tissue to occur due to iron oxidative stress [24]. A recent study of relapsing remitting MS patients using MR phase data indicated an increase in the iron content of the deep GM structures [8]. However, as discussed in previous chapters the non-local relationship between local field shift measurements and the underlying susceptibility distribution confounds any conclusions that are based on direct measurements of phase alone. Susceptibility mapping could yield further insight into these differences by eliminating confounding effects of the non-local relationship between field measurements and the underlying $\Delta\chi$-offsets, as described in Chapters 3 and 4.

The aims of this study were to determine whether susceptibility changes occur in the earliest phases of MS, by measuring the susceptibility of deep grey matter structures in patients with Clinically Isolated Syndrome at 7T and comparing these measurements with similar measurements from Relapsing-Remitting patients and age-matched healthy subjects.

6.3.2 Methods

Twenty patients with CIS (11 females, 9 males; mean age 36.7 years; age range 22-54), and seventeen patients with RR (11 females, 6 males; mean age 38.6 years; age range 20-55 years) were recruited from Nottingham University Hospital, along with twenty, age-matched healthy controls (7 females, 13 males; mean age 34.6 years; age range 21-58). All groups gave consent according to local ethics committee approval. MRI data were acquired at 7T using a spoiled gradient echo FLASH sequence with: TR/TE = 150/20ms, flip angle = 14°, SENSE factor = 2, EPI factor = 3, Number of excitations (NEX) = 1, and a total imaging time of 8.5 minutes. Two hundred transverse slices were acquired in 4 interleaved stacks to achieve whole head coverage with a relatively long TR. A long TR was desirable as this generally improves contrast in the magnitude data (see Chapter 2). The spatial coverage was 192x164x25 mm^3 per stack with 0.5 mm isotropic voxel size. Susceptibility mapping was carried out by an investigator using the whole-head susceptibility mapping software described in Section 6.1.4. A k-space threshold of $\alpha = 0.13$ was found to give the best compromise between contrast and noise.

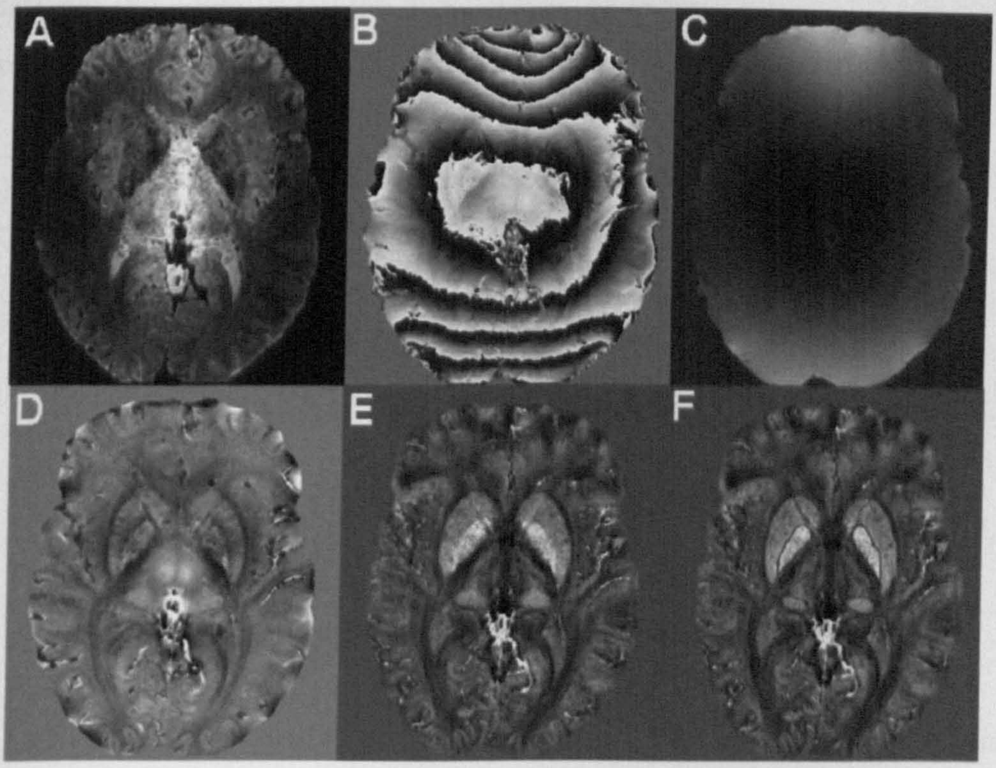

***Figure 6.9** Results of each processing step used to map susceptibility in MS patients: (A) magnitude data; (B) phase data; (C) unwrapped phase data using BET mask; (D) filtered phase data; (E) calculated χ-map; (F) E with ROIs (red = CN, green = PU, blue = GP, purple = IC, orange = TH, dark red = PV).*

Figure 6.9 shows the results of each step of the data processing. ROIs covering the Caudate Nucleus (CN), Putamen (PT), Globus Pallidus (GP), Internal Capsule (IC), Pulvinar part of the thalamus (PV), and the remaining part of the Thalamus (TH) (Fig. 6.9F) were defined in both hemispheres on five transverse slices for all subjects and the susceptibility values in the ROIs were averaged. Since susceptibility can only be measured relative to other tissues, the difference in susceptibility of each structure relative to the IC was then calculated.

6.3.3 Results and Discussion

Table 6.1 lists the average $\Delta\chi$ values in each grey matter structure (relative to the IC) for the CIS, RR, and control groups. The table also lists the p-values associated with each brain region for two significance tests: (i) the difference in $\Delta\chi$ values between CIS patients and controls; (ii) the difference in $\Delta\chi$ values between RR patients and controls.

Region	Controls $\Delta\chi \pm \sigma$ (ppm)	CIS $\Delta\chi \pm \sigma$ (ppm)	RR $\Delta\chi \pm \sigma$ (ppm)	CIS vs Controls *p*-value	RR vs Controls *p*-value
CN	0.085±0.016	0.103±0.020	0.101±0.019	$p < 0.017^*$	$p < 0.03^*$
PT	0.081±0.016	0.096±0.015	0.099±0.013	$p < 0.017^*$	$p < 0.03^*$
GP	0.118±0.024	0.134±0.024	0.145±0.019	$p > 0.05$	$p < 0.017^*$
TH	0.053±0.009	0.051±0.009	0.053±0.014	$p > 0.05$	$p > 0.05$
PV	0.077±0.013	0.090±0.018	0.085±0.023	$p > 0.05$	$p > 0.05$

***Table 6.1* Average $\Delta\chi$ values for each structure and for each group. Also included is a list of p-values for CIS vs controls and RR vs controls. Differences that were found to be significant are highlighted '*'. The p-values were corrected for multi-comparisons.**

In the case of the CN $\Delta\chi$ was found to be significantly higher in CIS and RR patients than in controls. Similarly, for the PT $\Delta\chi$ was found to be significantly higher in both patient groups than in controls. For the GP, $\Delta\chi$ was found to be significantly higher in RR patients than in controls but there was no significant difference between controls and CIS patients. For the TH and PV regions no significance was found.

In summary, high resolution susceptibility mapping has shown that the susceptibility in the caudate nucleus and putamen is significantly higher ($p<0.05$) in both CIS and RR patients than in healthy subjects, suggesting that iron accumulation occurs in the early phases of MS in these regions. Significant susceptibility changes were only found in the globus pallidus at later stages of MS disease, suggesting that iron accumulation occurs in the later phases of MS in this region. These preliminary results suggest that susceptibility mapping could be a worthwhile tool in mapping the progression of MS. Further work needs to be carried out, utilising longitudinal studies with large patient groups, to establish the relationship between MS and iron deposition measured via susceptibility mapping fully.

6.4 General Conclusions on Preliminary Clinical Results

Software which enables investigators with no specialist knowledge to apply susceptibility mapping in clinical studies has been presented in this chapter. Preliminary results produced by applying this software to data acquired at 7T from patients with Parkinson's disease and multiple sclerosis have also been presented.

Through discussions with investigators it was established that the software must be automated where possible and require minimal user input. With this in mind, two pieces of software were produced. Firstly, software was produced which allowed the user to define a small mask guided by magnitude data. Secondly, a separate piece of software was produced that used the whole brain as a mask. The main difference between the two approaches is processing time. The total processing time for the small mask method is approximately 30 min, compared to up to 10 hours for the whole brain approach using a PC with a 2 GHz Dual Processor and 8GB of RAM. Although the user is only required interact with the wholehead software for $\approx$ 5 min, the total processing time is still an important factor when analysing large amounts of information in a limited time. The main 'bottle neck' in the whole-head software is the 3D unwrapping stage which takes $\approx$ 8 hours using PRELUDE. At the time of writing this thesis, PRELUDE is the most robust and widely available algorithm for unwrapping MRI phase data. Recently, however, other algorithms have been proposed that, when fully developed, could dramatically reduce the total processing time [25]. More efficient algorithms combined with advances in parallel computing could certainly help to remove the unwrapping bottle neck in the whole-head approach.

In the Parkinson's disease study, significantly higher $\Delta\chi$ values were measured in the pars compacta region of the substantia nigra in PD patients relative to controls. This is consistent with the accumulation of higher concentrations of non-heme iron within this deep gray matter structure in PD. The study involved a relatively small number of subjects (9 PD and 11 controls) meaning that conclusions on the relationship between iron deposition and disease progression are limited. It is, however, an indicator that iron differences are important in PD, and also shows that susceptibility mapping is sensitive enough to detect these differences.

In the MS study, significantly higher $\Delta\chi$ values were measured in the CN, PU, and GP regions. The GP, unlike the CN and PU, only showed significantly higher susceptibility offsets for the later stage relapsing and remitting MS patients. This suggests that iron deposition may occur at different stages of the disease in different regions of the brain. The data presented here is based on specific subjects being imaged once. Only through longitudinal studies, where the same subject is imaged at different time points (e.g. once a year), can iron deposition in MS be fully understood. However, the results do show that susceptibility mapping of the whole brain is feasible, and sensitive enough to measure significant differences between patients with MS and healthy controls.

6.5 References

1. Minati, L., M. Grisoli, F. Carella, T. De Simone, M.G. Bruzzone, and M. Savoiardo, *Imaging Degeneration of the Substantia Nigra in Parkinson Disease with Inversion-Recovery MR Imaging.* AJNR, 2007. **28**(2): p. 309-313.
2. Menke, R.A., J. Scholz, K.L. Miller, S. Deoni, S. Jbabdi, P.M. Matthews, and M. Zarei, *MRI characteristics of the substantia nigra in Parkinson's disease: A combined quantitative T1 and DTI study.* Neuroimage, 2009. **47**(2): p. 435-441.
3. Vaillancourt, D.E., M.B. Spraker, J. Prodoehl, I. Abraham, D.M. Corcos, X.J. Zhou, C.L. Comella, and D.M. Little, *High-resolution diffusion tensor imaging in the substantia nigra of de novo Parkinson disease.* Neurology, 2009. **72**(16): p. 1378-1384.
4. Gattellaro, G., L. Minati, M. Grisoli, C. Mariani, F. Carella, M. Osio, E. Ciceri, A. Albanese, and M.G. Bruzzone, *White Matter Involvement in Idiopathic Parkinson Disease: A Diffusion Tensor Imaging Study.* American Journal of Neuroradiology, 2009. **30**(6): p. 1222-1226.

5. Chan, L.L., H. Rumpel, K. Yap, E. Lee, H.V. Loo, G.L. Ho, S. Fook-Chong, Y. Yuen, and E.K. Tan, *Case control study of diffusion tensor imaging in Parkinson's disease.* Journal of Neurology Neurosurgery and Psychiatry, 2007. **78**(12): p. 1383-1386.

6. Yoshikawa, K., Y. Nakata, K. Yamada, and M. Nakagawa, *Early pathological changes in the parkinsonian brain demonstrated by diffusion tensor MRI.* Journal of Neurology Neurosurgery and Psychiatry, 2004. **75**(3): p. 481-484.

7. Wattjes, M.P. and F. Barkhof, *High field MRI in the diagnosis of multiple sclerosis: high field–high yield?* Neuroradiology, 2009. **51**: p. 279-292.

8. Hammond, K.E., M. Metcalf, L. Carvajal, D.T. Okuda, R. Srinivasan, D. Vigneron, S.J. Nelson, and D. Pelletier, *Quantitative In Vivo Magnetic Resonance Imaging of Multiple Sclerosis at 7 Tesla with Sensitivity to Iron.* Annals Of Neurology, 2008. **64**(6): p. 707-713.

9. Alastair Compston and A. Coles, *Multiple sclerosis.* Lancet, 2008. **372**: p. 1502-1517.

10. Jankovic, J., *Parkinson's disease: clinical features and diagnosis.* Journal of Neurology, Neurosurgery & Psychiatry, 2008. **79**(4): p. 368-376.

11. Smith, S.M., *Fast robust automated brain extraction.* Human Brain Mapping, 2002. **17**(3): p. 143-155.

12. Jenkinson, M., *Fast, automated, N-dimensional phase-unwrapping algorithm.* Magnetic Resonance In Medicine, 2003. **49**(1): p. 193-197.

13. Gutteridge, J.M.C., *Iron and oxygen radicals in brain.* Annals of Neurology, 1992. **32**(S1): p. S16-S21.

14. Piccini, P. and D.J. Brooks, *New developments of brain imaging for Parkinson's disease and related disorders.* Movement Disorders, 2006. **21**(12): p. 2035-2041.

15. Kosta, P., M.I. Argyropoulou, S. Markoula, and S. Konitsiotis, *MRI evaluation of the basal ganglia size and iron content in patients with Parkinson's disease.* J Neurol, 2006. **253**(1): p. 26-32.

16. Martin, W.R., M. Wieler, and M. Gee, *Midbrain iron content in early Parkinson disease: a potential biomarker of disease status.* Neurology, 2008. **70**(16 Pt 2): p. 1411-7.

17. Vymazal, J., A. Righini, R.A. Brooks, M. Canesi, C. Mariani, M. Leonardi, and G. Pezzoli, *T1 and T2 in the brain of healthy subjects, patients with Parkinson disease, and patients with multiple system atrophy: Relation to iron content.* Radiology, 1999. **211**(2): p. 489-495.

18. Kosta, P., M. Argyropoulou, S. Markoula, and S. Konitsiotis, *MRI evaluation of the basal ganglia size and iron content in patients with Parkinson's disease.* Journal of Neurology, 2006. **253**(1): p. 26-32.

19. Bartzokis, G., J.L. Cummings, C.H. Markham, P.Z. Marmarelis, L.J. Treciokas, T.A. Tishler, S.R. Marder, and J. Mintz, *MRI evaluation of brain iron in earlier- and later-onset Parkinson's disease and normal subjects.* Magnetic Resonance Imaging, 1999. **17**(2): p. 213-222.

20. Wallis, L.I., M.N. Paley, J.M. Graham, R.A. Grunewald, E.L. Wignall, H.M. Joy, and P.D. Griffiths, *MRI assessment of basal ganglia iron deposition in Parkinson's disease.* J Magn Reson Imaging, 2008. **28**(5): p. 1061-7.

21. Hutchinson, M. and U. Raff, *Structural changes of the substantia nigra in Parkinson's Disease as revealed by MR imaging.* American Journal of Neuroradiology, 2000. **21**: p. 697-701.

22. Alastair Compston and Alasdair Coles, *Multiple sclerosis.* The Lancet, 2002. **359**: p. 1221-1231.

23. Hafler, D.A., *Multiple Sclerosis.* The Journal of Clinical Investigation, 2004. **113**: p. 788-794.

24. LeVine, S.M., *Iron deposits in multiple sclerosis and Alzheimer's disease brains.* Brain Research, 1997. **760**(1-2): p. 298-303.

25. Bagher-Ebadian, H., Q. Jiang, and J.R. Ewing, *A modified fourier-based phase unwrapping algorithm with an application to MRI venography.* Journal of Magnetic Resonance Imaging, 2008. **27**(3): p. 649-652.

26. MacDonald, D., N. Kabani, D. Avis, and A.C. Evans, *Automated 3-D Extraction of Inner and Outer Surfaces of Cerebral Cortex from MRI.* NeuroImage, 2000. **12**(3): p. 340-356.

CHAPTER 7

Susceptibility Mapping Using Iterative Inversion Methods

The previous chapters have described the application of susceptibility mapping through a direct *k*-space division conditioned by a threshold parameter. This direct inversion is simple and fast to implement, but is rather naïve in its treatment of noise. In this chapter a different type of inversion method based on an iterative algorithm is presented. Specifically, the conjugate gradient method is used due to its favourable computational efficiency. Whole-brain susceptibility maps are created by applying the conjugate gradient iterative technique applied to data acquired at single and multiple-orientations to the main magnetic field.

7.1 Conjugate Gradient Methods

There is a large number of iterative methods that can be used in solving inversion problems [1]. Iterative methods involve guessing a solution, comparing the results of using this first guess solution to the actual measured result, and then adjusting the guess to yield a more accurate result. For susceptibility mapping, the inversion problem is complicated by two main factors: (i) the inversion is ill-posed; (ii) the forward field calculation operation cannot be explicitly formed as a matrix multiplication. Conjugate gradient methods form a type of iterative algorithm designed to deal with inversions suffering from this sort of problem. This section will introduce the theory of conjugate gradient methods and describe how this approach can be applied to magnetic susceptibility mapping.

7.1.1 Susceptibility Mapping: A Sparse Problem

As discussed in previous chapters, susceptibility mapping involves the inversion of a convolution,

$$\Delta B(\mathbf{r}) = IFT(C(\mathbf{k}) \cdot FT(\chi(\mathbf{r}))) \qquad \text{Eq. 7.1}$$

where $\Delta B(\mathbf{r})$ is the field map, $C(\mathbf{k})$ is the point dipole field kernel, and $\chi(\mathbf{r})$ is the susceptibility distribution. The direct inversion approach, presented in Chapter 5, takes advantage of this simple Fourier expression to perform a deconvolution operation by applying the reciprocal of this expression to the field map in the Fourier domain (see Eq. 5.2). Another way of visualising the problem is as a least squares minimisation, where we are trying to solve an equation of the form,

$$\min_x \|Ax - b\|^2 \qquad \text{Eq. 7.2}$$

where b is the measured data, x is the desired unknown, A is a matrix representing an operation of some kind, and $\|...\|$ is the Euclidean or '*L2*' norm given by

$$\|y\| = \sqrt{\sum_{i=1}^{n} (y_i)^2} \quad . \qquad \text{Eq. 7.3}$$

For susceptibility mapping Eq. 7.2 takes the form

$$\min_\chi \|C\chi - \Delta B\|^2 \qquad \text{Eq. 7.4}$$

where the matrix C represents the dipole convolution operation:

$$C\chi(\mathbf{r}) = IFT(C(\mathbf{k}) \cdot FT(\chi(\mathbf{r}))) \quad . \qquad \text{Eq. 7.5}$$

Often a first step in any minimisation, like Eq. 7.4, is to form the matrix C and then apply various operations or analyses to it such as in single value decomposition (SVD) [2], or Moore-Penrose pseudo inversion [3]. In susceptibility mapping, the matrix C represents a 3D convolution with the point dipole field. In this case, C is an N x M matrix where N is the number of voxels in the field map, and M is the number of voxels over which the dipole kernel is defined. For a 128 x 128 x 128 matrix N = 128^3 = 2,097,152, and the kernel is defined over the same volume meaning M =

2,097,152. Thus, for a relatively small 128^3 MRI data set the matrix C will have 4,398,046,511,104 elements. This is beyond the data storage capabilities of most computers. Hence, for reasonably sized data sets the matrix C can never be explicitly formed as it is too large. Another problem is that if C were to be formed it would have a large number of elements that were close or exactly equal, to zero. This is because of the $\cos^2\theta$-1/3 spatial modulation implicit in the dipole field (see Chapter 3). Matrices that have large regions of zero values are called 'sparse' and are inherently difficult to invert without some form of conditioning.

7.1.2 The Conjugate Gradient Method

There are a number of algorithms for matrix equations involving large and sparse A matrices [1]. Perhaps the most well-known of these is the Conjugate Gradient Method (CGM) [4]. The main advantage of this method is that A does not have to be explicitly formed, instead only the product Ax (see Eq. 7.2) needs to be calculated. However, in cases where A is non-symmetric, the product A^*x also has to be calculated, where '*' is the conjugate transpose of A. The generalised form of the CGM algorithm for a non-symmetric matrix, A, is given by [1]:

```
Choose initial guess solution: $x^{(0)}$
Find first residual: $r^{(0)} = b - Ax^{(0)}$
Apply conjugate matrix to residual: $p^{(0)} = A^* r^{(0)}$
For $i = 1, 2, 3, \ldots, N_{IT}$ compute:
    $\alpha_i = \frac{\left\| A^* r^{(i)} \right\|^2}{\left\| A p^{(i)} \right\|^2}$
    $x^{(i+1)} = x^{(i)} + \alpha_i p^{(i)}$
    $r^{(i+1)} = r^{(i)} - \alpha_i p^{(i)}$
    $\beta_i = \frac{\left\| A^* r^{(i+1)} \right\|^2}{\left\| A^* r^{(i)} \right\|^2}$
    $p^{(i+1)} = A^* r^{(i+1)} + \beta_i p^{(i)}$
If $i = N_{IT} \rightarrow$ End                                Eq. 7.6
```

Within each iteration the result of applying A and A^* must each be calculated once. This algorithm is designed to successively minimise the square of the norm of the residual, $\left\|r^{(i)}\right\|^2$. Hence, it is commonly referred to as a 'least-squares' fitting algorithm. In the CGM algorithm, low frequency components tend to converge faster than high frequency components. This means the CGM algorithm has an in-built regularisation property that can be used to deal with sparse problems, i.e. by adjusting the number of iterations N_{IT}.

7.1.3 Applying CGM to Susceptibility Mapping

The CGM algorithm (Eq. 7.6) can be applied to susceptibility mapping fairly easily by replacing: (i) the operator A with the Fourier dipole convolution operation, C, described in Eq. 7.5; (ii) the vector b with a field map; (iii) $x^{(i)}$ with the successive estimates of χ. As the dipole kernel is symmetric across its central point, the matrix C will be symmetric such that $C^* = C$. This simplifies the CGM algorithm to the symmetric form [1]. There is, however, additional information about the distribution of noise in the phase that we can add to the least squares fit carried out by the CGM algorithm. The SNR of the associated measured phase is proportional to the signal magnitude [5]. Thus, the magnitude information can be used to weight the fitting algorithm to form a 'weighted least-squares' fit. The weighted minimisation can be written as:

$$\min_{\chi}\left\|W(C\chi-\Delta B)\right\|^2 \qquad \text{Eq. 7.7}$$

where W is the weighting matrix. Multiplying out the bracket gives,

$$\min_{\chi}\left\|WC\chi-W\Delta B\right\|^2 \qquad \text{Eq. 7.8}$$

The CGM method (Eq. 7.6) can then be utilised for this minimisation by replacing b with $W\Delta B$, and replacing A with WC. As W is a point-wise multiplication it can be represented by a symmetric diagonal matrix, such that $W = W^*$. However, the product WC is not symmetric. Using matrix algebra it can be shown that:

$$(WC)^* = (WC)^T = C^T W^T = CW \qquad \text{Eq. 7.9}$$

where the conjugate transpose, *, can be replaced by the standard matrix transpose, ^{T}, as all matrices considered here are real. Thus, the order of the operators has been reversed. A weighted CGM algorithm can then be constructed by setting $A = WC$, and $A^* = CW$. Figure 7.1 shows a simple simulation experiment to demonstrate the application of weighted, and non-weighed, CGM fits.

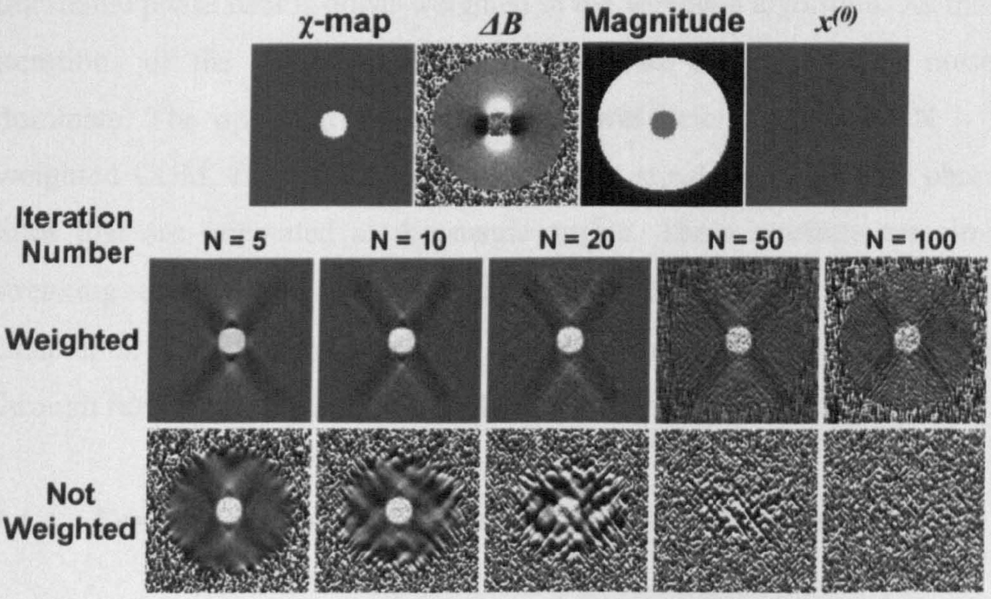

***Figure 7.1** Application of weighted and non-weighted CGM fitting based on a spherical susceptibility distribution using a field map with added Gaussian noise with a variance proportional to the reciprocal of the magnitude data.*

The chosen χ-map was a small digitised unit sphere placed in an empty matrix of zeroes. The field map, *ΔB*, was simulated using the standard Fourier method (see Chapters 3 and 4). For the simulated magnitude data, a large unit sphere was set inside a matrix and surrounded by voxels with values close to 0 (= 0.01). Voxels in the region corresponding to the unit sphere of the susceptibility distribution were set to a value of 0.25 in the simulated magnitude data. This reduction of magnitude in a region with a high positive $\Delta\chi$ offset is consistent with the effect of reduced T_2* measured *in vivo* in iron-rich structures like the SN and RN (see Chapters 4 and 5). To simulate real data, Gaussian noise with zero mean and a variance inversely proportional to the magnitude data was added to the field map. The initial guess ($x^{(0)}$) was set to a matrix of zeros. For the weighted algorithm the weighting matrix, W, was set equal to the simulated magnitude data.

The results of applying the weighted, and non-weighted, CGM fits are shown at the bottom of Fig 7.1. Fitted χ-maps are shown for increasing iteration numbers. Generally, the results show that the fitted χ-maps based on the weighted algorithm are of a higher quality compared to the non-weighted maps. This is because unreliable phase data is down-weighted in the weighted algorithm. As the number of iterations of the CGM algorithm is increased, high frequency noise starts to dominate. The optimum iteration number was determined to be N $\approx$ 20 for the weighted CGM. Even at this optimum value, streaking effects are observed along lines that are orientated at the magic angles. These artefacts are similar to the streaking effects seen with the threshold-based inversion method presented in Chapter 5. They occur due to the sparse nature of C, and can only be removed through further conditioning or regularisation of the minimisation problem.

7.1.4 Conditioning using an Iterative Multiple-Orientation Method

In Chapter 5, the concept of rotating the sample relative to B_0 to condition the inverse problem was introduced. The same methodology can be applied to susceptibility mapping using an iterative CGM algorithm. This approach has been most fully explored by Liu et al. [6] who introduced the COSMOS (calculation of susceptibility through multiple-orientation sampling) method and applied it to simple phantoms and excised tissue. The multiple-orientation minimisation can be written as:

$$\min_{\chi}\left(\|O_1\|^2+\|O_2\|^2+\|O_3\|^2\ldots+\|O_n\|^2\right) \qquad \text{Eq. 7.10}$$

where O_n is the norm for the n^{th} orientation given by

$$O_n = W_n\left(C_n\chi-\Delta B_n\right) \qquad \text{Eq. 7.11}$$

where W_n is the weighting matrix for the n^{th} orientation, ΔB_n is the measured field map at the n^{th} orientation, and C_n is the dipole convolution operator for the n^{th} orientation and is given by

$$C_n\chi = IFT\left(\left(\frac{1}{3}-\frac{\left(k_z\cos\theta_n\cos\phi_n - k_y\sin\theta_n\cos\phi_n + k_x\sin\phi_n\right)^2}{|\mathbf{k}|^2}\right)\cdot FT(\chi)\right)$$

Eq. 7.12

where (θ_n, ϕ_n) are the angles defining the n^{th} sample orientation relative to B_0. A sensible choice in setting the values of W_n is to use the modulus signal amplitude, as described in the previous section.

7.1.5 Conditioning using an Iterative Regularised Single Orientation Method.

Another method for stabilising the inversion problem is to incorporate prior knowledge of the susceptibility distribution to form a regularisation problem requiring only data acquired at a single orientation. This approach has been most fully explored by de Rochefort et al. [7], who introduced the use of edge information extracted from modulus data as effective priors. The iterative method which these authors used to find the best fitting solution is based on a least-squares, CGM algorithm. In this approach, the expression that χ must satisfy can be written as

$$\min_\chi\left(\|O_1\|^2 + \alpha^2\|M_{outer}\chi\|^2 + \beta^2\|W_g G\chi\|^2\right)$$

Eq. 7.13

where α and β are regularisation parameters, and M_{outer} is a mask which defines the region outside of the brain/phantom where the susceptibility is assumed to be zero. The final, regularisation term can be expanded as

$$\|W_g G\chi\|^2 = \|W_{gx}G_x\chi\|^2 + \|W_{gy}G_y\chi\|^2 + \|W_{gz}G_z\chi\|^2$$

Eq. 7.14

where W_g is made up of a set of weighting matrices linked to each Cartesian direction, and $G_i = \frac{\partial}{\partial_i}$ is the gradient operator which is used to extract edge information from χ along the i^{th} dimension. de Rochefort et al. [7] showed that the inverse of the gradient of the modulus data is a good choice for W_g as it is rich in structural detail and its use allows the inversion to be carried out without the acquisition of additional scans. In each iteration, a field map is simulated, and the gradient along each dimension of χ measured. The effect of the gradient weighting terms is to allow the χ distribution to vary in regions where the modulus signal varies with position, but to force it to be smooth in regions where the modulus data shows little spatial variation.

7.2 Whole-brain Susceptibility Mapping at 7T: A Comparison of Multiple-and Single-Orientation Methods

Several conditioning strategies have been proposed for ameliorating the ill-posed field map to susceptibility problem. These include combining data obtained with the susceptibility distribution orientated at multiple angles with respect to the main magnetic field [6, 8], regularisation of the inversion problem via the incorporation of prior knowledge of the form of the susceptibility distribution [7, 9], and utilisation of a simple *k*-space thresholding approach [8, 10]. The first method requires multiple data acquisitions and will be referred to as the multiple-orientation (MO) method. For this study, the iterative MO method (Section 7.1.4) was chosen for its more robust treatment of noise over the direct method proposed in Chapter 5. The MO method has the obvious disadvantage of increased scanning time and is also dependent on the ability of subjects to rotate their heads between scans. Despite these drawbacks the MO method deals with noise robustly and consistently produces high quality susceptibility maps. The second and third methods require only a single acquisition and will be referred to as the regularised single-orientation (RSO) method, and the threshold-based single-orientation (TSO) method, respectively. The RSO method was implemented as described in Section 7.1.5. The application of the

TSO method is described in detail in Chapter 5. The RSO and TSO methods, although requiring less scanning time and no head rotation, are more sensitive to noise than the MO method.

The aims of the study described here were firstly, to optimise the performance of each susceptibility mapping method for the calculation of high quality quantitative susceptibility maps from whole-brain phase and modulus data acquired at 7 T, and secondly, to investigate by comparison the strengths and weaknesses of the different methods. The methods and their optimisations were validated by analysis of data from a phantom containing different compartments of known susceptibility, and then applied to brain data acquired in vivo at 7 T.

7.2.1 Materials and Methods

Initial experiments were carried out on the spherical agar phantom described in Chapter 4. The 10 cm diameter phantom contained a random arrangement of small cylindrical sections of agar that had been doped with an iron-oxide based contrast agent. In separate experiments, the susceptibility of this agent was measured to be 0.15±0.01 ppm/mM at 7 T. Small cylindrical sections containing two different concentrations of the contrast agent (0.5 and 1 mM) were used, yielding a test sample showing a structured variation of magnetic susceptibility that spanned similar values to those found in the human brain. Subsequent *in vivo* studies, involved scanning five, healthy, male subjects aged between 25 and 30 years. The study was approved by the local ethics committee. Data processing was carried out using a 64-bit Linux system with a 2 GHz Dual Core AMD processor and 8 GB of RAM. Data fitting and simulations were carried out in Matlab (The Mathworks Inc, Massachusetts).

Images were acquired on a 7 T scanner (Philips Medical Systems, Best, the Netherlands) using a 3D spoiled GE FLASH sequence with 0.7 mm isotropic resolution, 200×200×100 mm3 FOV with axial slab orientation, TE/TR=15/23 ms, EPI factor=3, SENSE factor=2, a flip angle of 12° and a scan time of 210 s per acquisition. The phantom was imaged at four orientations to $B_0\mathbf{z}$: (i) rotated −10°

about the x-axis from an arbitrary starting position, (ii) rotated +10° about the x-axis, (iii) rotated +10° about the y-axis, and finally (iv) rotated −10° about the y-axis. Similarly, for the *in vivo* experiments each subject was scanned with their head at four orientations to $B_0\mathbf{z}$: (i) tipped back by ~10°, corresponding to a rotation about the right-left axis (x-axis) from a neutral head position, (ii) tipped forward by ~ 10°, (iii) tipped to the side by ~10°, corresponding to a rotation about the anterior-posterior axis (y-axis), and (iv) tipped to the opposite side by ~10°. Approximate angles are quoted, as the subjects rotated their heads by varying angles ranging from 5° to 15° in each direction. As each scan required 210 s the total scan time for the five orientations was approximately 20 minutes.

7.2.1.1 *Iterative High-pass filtering*

Before susceptibility mapping can be carried out, high-pass spatial filtering of the field maps must be performed to remove unwanted background fields. In Chapter 5, a filtering method based on fitting and removing fields due to multiple dipoles positioned outside the brain was introduced. This approach can be extended using iterative CGM algorithms to fit dipole fields using the Fourier-based forward field calculation described in Chapter 3. The speed of the Fourier method enables millions of dipole fields to be fitted using an acceptable amount of computational resources. The iterative dipole fitting approach was first proposed by de Rochefort et al. [7]. In the work described here, a similar approach was employed, with the addition of a low-order polynomial fit. The polynomial fit was found to improve the filtering process by removing the large-scale variations related to B_1 inhomogeneity and susceptibility sources situated a large distance from the brain that the fitted dipoles alone could not accurately remove. Figure 7.2 shows the steps involved in filtering the phase data using this approach. This involves identifying the susceptibility distribution outside the region of interest which generates a field that best fits the measured field variation inside the region of interest. The filtering was carried out by solving a minimization problem analogous to that described for the RSO method (Eq. 7.13):

$$\min_{\chi,p}\left(\left\|W_1\left(C_1\chi + Vp - \Delta B_1\right)\right\|^2 + \alpha^2\left\|M\chi\right\|^2\right) \qquad \text{Eq. 7.15}$$

using an iterative CGM algorithm. Here M is a mask that is only non-zero inside the region of interest (i.e. telling the algorithm where, for the purposes of modelling background fields, susceptibility is not allowed to exist); V is a matrix describing low-order polynomials in x, y, and z; p is a vector describing the polynomial coefficients associated with these orders; ΔB_1 is the measured field map; and χ is the susceptibility distribution outside the region of interest. The polynomial was incorporated into the filtering process in order to account for the slowly varying fields produced by B_0-inhomogeneity.

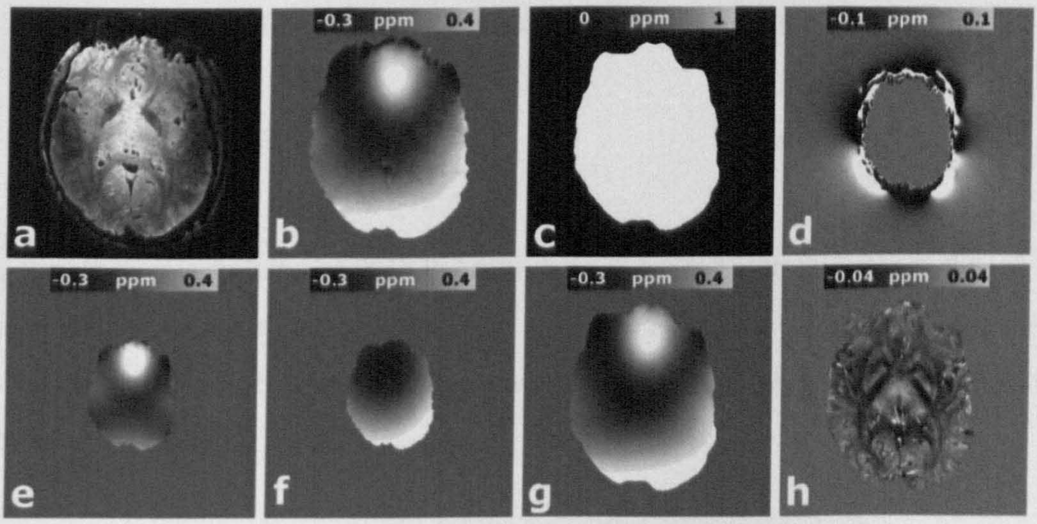

***Figure 7.2** The steps used in high-pass filtering of field maps. (a) Axial modulus image. (b) Unwrapped phase data. (c) Mask of brain region, M. (d) Fitted susceptibility, χ_{fit}, (e) Simulated dipole field, $C_1\chi_{fit}$ (f) Fitted 2^{nd} order polynomial, Vp_{fit} (g) Interpolated and cropped, fitted field map based on (e)+(f), ΔB_{fit} (h) High-pass filtered field map calculated from (b) to (g).*

The BET tool in FSL [11] was applied to the modulus data (Fig. 7.2a) to create a mask of the brain, M (Fig. 7.2c). To decrease the computation time the field map (Fig. 7.2b) was masked by M and resampled to yield a lower resolution field map, ΔB_1, with isotropic voxels of 2.1 mm size. The weighting matrix, W_1, was set equal to the modulus data, after being masked and resampled to match the resolution of ΔB_1. M was also resampled to match ΔB_1 and W_1. To allow room for susceptibility offsets to be populated around the field map, ΔB_1, W_1, and M were zero padded to form matrices twice as large in each dimension as the originals. The matrix V was set up to describe polynomials up to 2nd order over the region of space defined by M, so that p contained 10 coefficients. Before the fitting could take place an appropriate value for the regularisation parameter, α, had to be found. To help simplify this choice for different acquisitions/subjects, W_1 was normalised by dividing each element of W_1 by the mean value of W_1 over the region of space defined by M. An acceptable value of $\alpha = 1000$ was established by trial and error. This was the lowest value at which the masking term restricted the susceptibility fitted in the region defined by M, to numerical values close to zero (< 0.0001 ppm). It was found that after 2000 iterations of the fitting algorithm, taking about 5 hours, acceptable values for χ and p were identified to produce a fitted field, ΔB_{fit}, given by

$$\Delta B_{fit} = C_1\chi + Vp \quad . \qquad \text{Eq. 7.16}$$

ΔB_{fit} was then interpolated back to 0.7 mm isotropic resolution and cropped back to a matrix size identical to the original ΔB_1, see Fig. 7.2g. The fitted field map, ΔB_{fit}, was subtracted from ΔB_1 to yield a high-pass filtered field map, ΔB_{fit} as shown in Fig. 7.2h.

7.2.1.2 *Measuring Orientation*

Before susceptibility maps can be calculated it is necessary to establish the exact orientation of each measured data set relative to B_0. To do this, the modulus data sets were first co-registered using the FLIRT tool in FSL [12]. This process yields rotation matrices describing the transformation of each data set to a common space. Combining this information with the angle of each imaging stack to B_0, recorded directly from the scanner, it was possible to characterise the orientations accurately in terms of angles θ and ϕ that can then be used to describe C_n via Eq. 7.12.

7.2.1.3 *Susceptibility Calculations*

For the phantom and *in vivo* studies, the MO method was applied to data acquired at four orientations. The minimisation described in Eq. 7.10 was slightly modified by the addition of a mask-related term, identical to that used in the RSO method Eq. 7.13, which was found to improve the stability of the fitting algorithm:

$$\min_{\chi}\left(\|O_1\|^2+\|O_1\|^2+\|O_1\|^2+\|O_1\|^2+\alpha^2\|M_{outer}\chi\|^2\right) \quad \text{Eq. 7.17}$$

The mask was calculated from modulus data acquired at one of the orientations and following the process used for the high-pass filtering, the weighting matrices were set equal to the modulus data for each orientation and mean normalised. In a similar method to that used in defining the high-pass phase filter, an acceptable value for the regularisation parameter was established at $\alpha = 10$.

For the RSO method, similar weighting and masking matrices were extracted from the modulus data and the mask regularisation parameter, α, was set to a value of 15. The next stage was to establish an acceptable value for the regularisation parameter, β (see Eq. 7.13), and also for an extra noise-related parameter. The latter is used to clip the maximum value of W_g, as defined in Eq. 7.14, to a chosen threshold level [7]. This threshold defines what is considered to be a significant gradient in the modulus image. Preliminary experiments were carried out on the phantom data to determine the best values for the noise threshold and regularisation parameters. These experiments involved varying each parameter and inspecting the associated susceptibility map within carefully chosen ROIs.

In contrast to the MO and RSO methods the TSO method requires less preparation, the only variable parameter being the *k*-space threshold value. Preliminary experiments, similar to those used for the RSO parameter selection, were carried out on the phantom data to determine the best value for this threshold. The first data set acquired (with the head/phantom tipped back by a rotation about the right-left/*x*-axis of about 10°) was used for the susceptibility calculations in the single-orientation methods.

7.2.1.4 *ROI Selection*

For the phantom, ROIs were drawn inside the doped cylinders, and also in adjacent regions of the surrounding agar allowing the difference in susceptibility between the doped and undoped agar compartments to be calculated. Several brain areas divided across lower (red nucleus (RN) and substantia nigra (SN)), middle (internal capsule (IC), globus pallidus (GP), putamen (PU), thalamus (TH), and caudate nucleus (CN)) and upper (grey matter (GM) regions in the cortex) sections were targeted in the in vivo data. The upper GM regions in the cortex were divided into those located in the frontal lobe (GM_{FL}), anterior parietal lobe (GM_{APL}), and posterior parietal lobe (GM_{PPL}). ROI were drawn on transverse slices of susceptibility maps created using the three different methods and then combined so that only voxels common to all ROI were included in the final composite ROI.

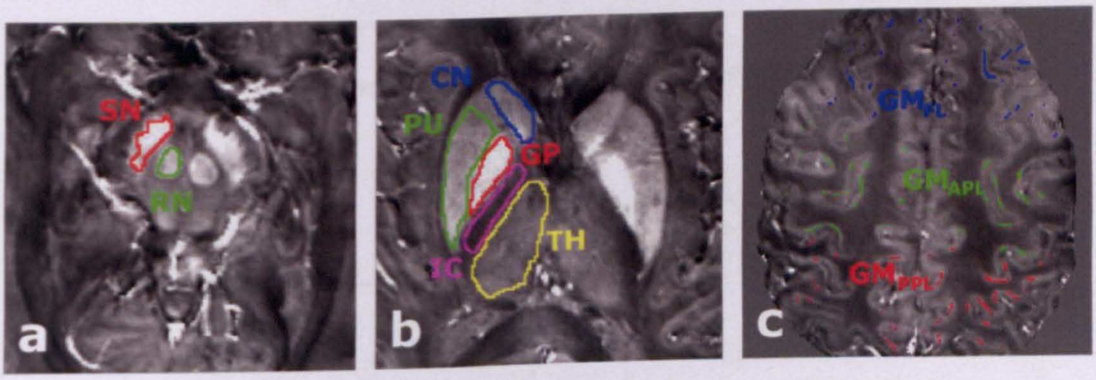

<u>Figure 7.3</u> ROIs (coloured lines) used for data analysis superimposed on (a–c) transverse slices of a susceptibility map from a single subject created using the MO method.

Figure 7.3 shows a representative set of ROI drawn on axial susceptibility maps (created using the MO method) from each of the three sections. Although this figure only shows ROIs on the left side of the brain for lower and middle sections, the data analysis included the average of ROI drawn on 4–5 slices at each brain level on both the right and left sides. As discussed above, it is important to choose a reference susceptibility value for meaningful data analysis. Here, ROI were drawn in WM throughout the brain for each subject. The average susceptibility value measured in the WM was then subtracted from the values measured in each of the brain structures listed above to yield values of $\Delta\chi$ relative to WM.

7.2.2 Results

7.2.2.1 *Phantom Results*

Figure 7.4 shows susceptibility values and associated errors calculated from maps produced in preliminary phantom experiments by using the RSO and TSO methods. Results are plotted for varying values of the noise threshold parameter and edge information regularisation parameter, *β*, for the RSO method, and for different values of the *k*-space threshold parameter for the TSO method.

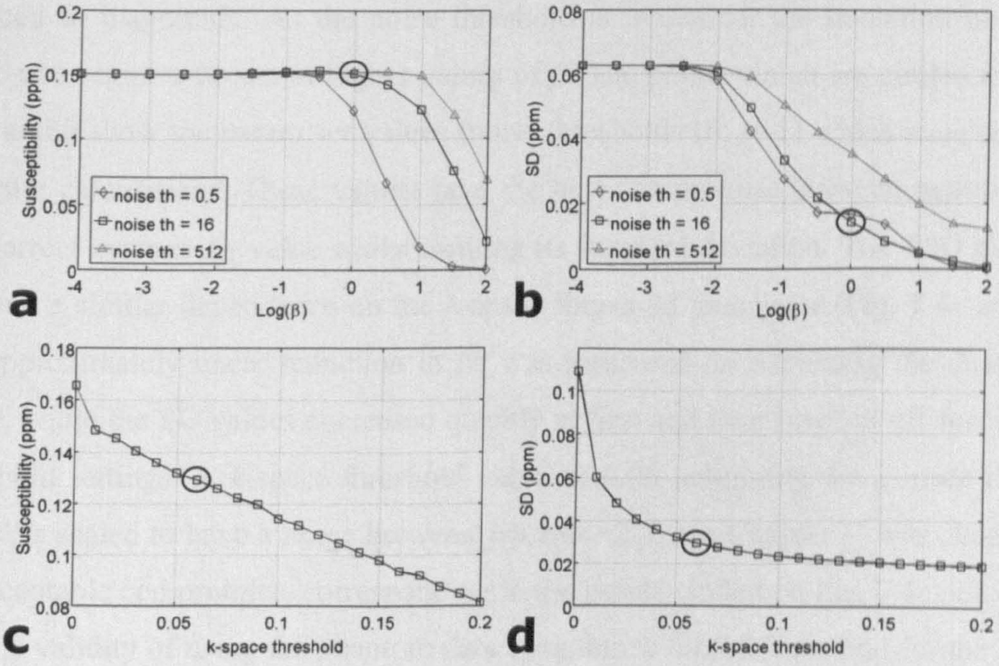

***Figure 7.4** Measured susceptibility differences (a and c) and associated standard deviations (b and d) in the compartments of the agar phantom doped with 1mM contrast agent, for the RSO (a and b) and TSO (c and d) susceptibility mapping methods, plotted against different values of relevant mapping parameters. The noise threshold and regularisation parameter, β, were varied in the RSO method, while the k-space threshold was altered in the TSO method. The circled values in each figure correspond to the chosen optimal values of the k-space threshold and the regularisation parameter.*

To simplify the plots, only the results obtained from the ROI in cylinders doped with a 1 mM concentration of the contrast agent are shown. As discussed above, these cylinders have an expected $\Delta\chi$ of 0.15 ± 0.01 ppm relative to the surrounding undoped agar. The $\Delta\chi$ values produced using the RSO method, for three different noise thresholds (0.5, 16, and 512) are plotted against $\log(\beta)$ in Fig. 7.4a, while Fig. 7.4b shows plots of the associated averaged standard deviations (SD) within the ROI. These plots show that small values of β yield accurate $\Delta\chi$ values, but also produce a high standard deviation that indicates significant variation of the calculated susceptibility within what should be homogeneous compartments, while a high value of β yields a low SD, but also produces $\Delta\chi$ values that are significantly reduced in magnitude. As the noise threshold is increased, the transition between these two regimes occurs at higher values of β. The points which are circled on Fig. 7.4a and b show the parameter values (noise threshold=16; β=1) which were used in the later calculations. These values gave the best compromise between maintaining the correct average $\Delta\chi$ value whilst limiting its standard deviation. The TSO method showed a similar dependence on the *k*-space threshold parameter (Fig. 7.4c and d). An approximately linear reduction in $\Delta\chi$ was measured on increasing the threshold value, while the SD values decreased quickly at first and then levelled off for higher threshold settings. A *k*-space threshold value of 0.06 (assuming the *k*-space dipole kernel is scaled to have a range between 1/3 and −2/3, see Chapter 3) was chosen as an acceptable compromise, corresponding to the points circled on Fig. 7.4c and d. To test the validity of using the phantom data to optimise the TSO method for the brain studies, similar analysis was carried out on the *in vivo* data using the susceptibility values in all ROI.

	MO $\Delta\chi \pm\sigma$	RSO $\Delta\chi \pm\sigma$	TSO $\Delta\chi \pm\sigma$
1 mM	0.16 ± 0.01	0.15 ± 0.01	0.13 ± 0.03
0.5 mM	0.076 ± 0.009	0.067 ± 0.009	0.07 ± 0.02

<u>Table 7.1</u> Susceptibility differences measured for the two differently doped compartments of the agar phantom using the three different mapping methods.

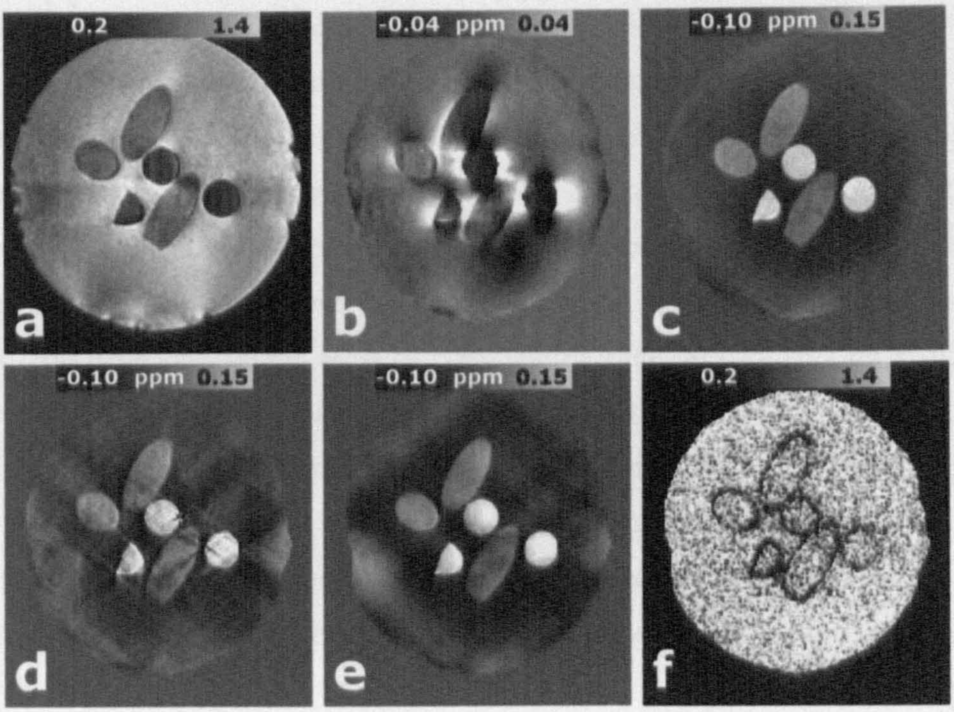

<u>Figure 7.5</u> Representative coronal images acquired from the agar phantom and the corresponding susceptibility maps calculated using the optimised MO, RSO, and TSO methods. (a) Mean-normalised modulus data from a single orientation. (b) Filtered field map from a single orientation. (c) χ-map calculated using the MO method. (d) χ-map calculated using the optimised TSO method. (e) χ-map calculated using the optimised RSO method. (f) Combined weighting matrix used to impose spatial priors based on the gradient of (a) in the RSO method $(W_{gx}^2 + W_{gy}^2 + W_{gz}^2)^{1/2}$, with a noise threshold=16.

The results showed a similar dependence of susceptibility on the threshold parameter, supporting the use of a threshold of 0.06 for the in vivo data analysis. Figure 7.5 shows representative coronal images of the phantom along with susceptibility maps calculated using the optimal parameter settings for the three different methods. Fig. 7.5a shows the mean normalised modulus data acquired at one orientation, which was used for weighting in the MO and RSO methods. Fig. 7.5b shows a corresponding field map which was calculated from spatially filtered phase data. Fig.7.5c shows the susceptibility map calculated by applying the MO method to data acquired with the phantom at four different orientations to B_0. No parameter selection was necessary for this method as the data from each orientation were weighted equally in the minimization problem given in Eq. 7.17. Calculation of the susceptibility map required 400 iterations, taking approximately 3 h of computation time. Fig. 7.5d shows the susceptibility map calculated using the TSO method with a *k*-space threshold value of 0.06. The total computation time for this method was about 2 min. The susceptibility map calculated using the RSO method with a noise threshold of 16 and $\beta=1$ is shown in Fig.7.5e. This calculation required around 200 iterations, taking ~2 h of computation time, to converge on a solution. The combined magnitude of the weighting matrices $(W_{gx}^2 + W_{gy}^2 + W_{gz}^2)^{1/2}$, which was used to impose edge information in the RSO method, is also shown in Fig. 7.5f. Table 7.1 lists the average $\Delta\chi$ values measured in cylinders containing 0.5 and 1 mM concentrations of contrast agent for the MO, RSO, and TSO methods. The phantom results show that the TSO method underestimated $\Delta\chi$ values, while the RSO and MO methods gave more accurate susceptibility estimates. The MO method produced higher quality susceptibility maps compared to the RSO method, as shown in Fig 7.5. The MO seemed to slightly overestimate the $\Delta\chi$ value in the 1mM cylinders. This may be a result of doping errors but is still accurate to within error (±0.01ppm).

7.2.2.2 *In vivo Results*

Figure 7.6 shows representative axial brain images drawn from the lower, middle and upper sections. The modulus data and field maps, upon which the susceptibility calculations are based, are shown in Fig.7.6a, f and k, and b, g and l, respectively. χ-maps calculated using the MO (Fig.7.6c, h and m), RSO (Fig. 7.6d, i and n), and TSO (Fig.7.6e, j and o) methods are also shown. For the RSO method the noise threshold and regularisation parameters were set to the optimum values derived from the phantom data (noise threshold=16; $\beta=1$). Similarly, for the TSO method the *k*-space threshold was set to the optimum value of 0.06. Table 7.2 lists the average $\Delta\chi$ values in each of the brain regions measured relative to the white matter reference region using the three different methods. ΔB values taken from the field maps are also detailed. The numbers quoted are the average over the five subjects along with the standard deviations of the means across subjects. The χ-map calculated using the MO method shows excellent structural detail, with high contrast in areas associated with large susceptibility offsets such as the GP and SN. Veins are also easily discernable as areas of positive susceptibility, consistent with a high deoxyhemoglobin content.

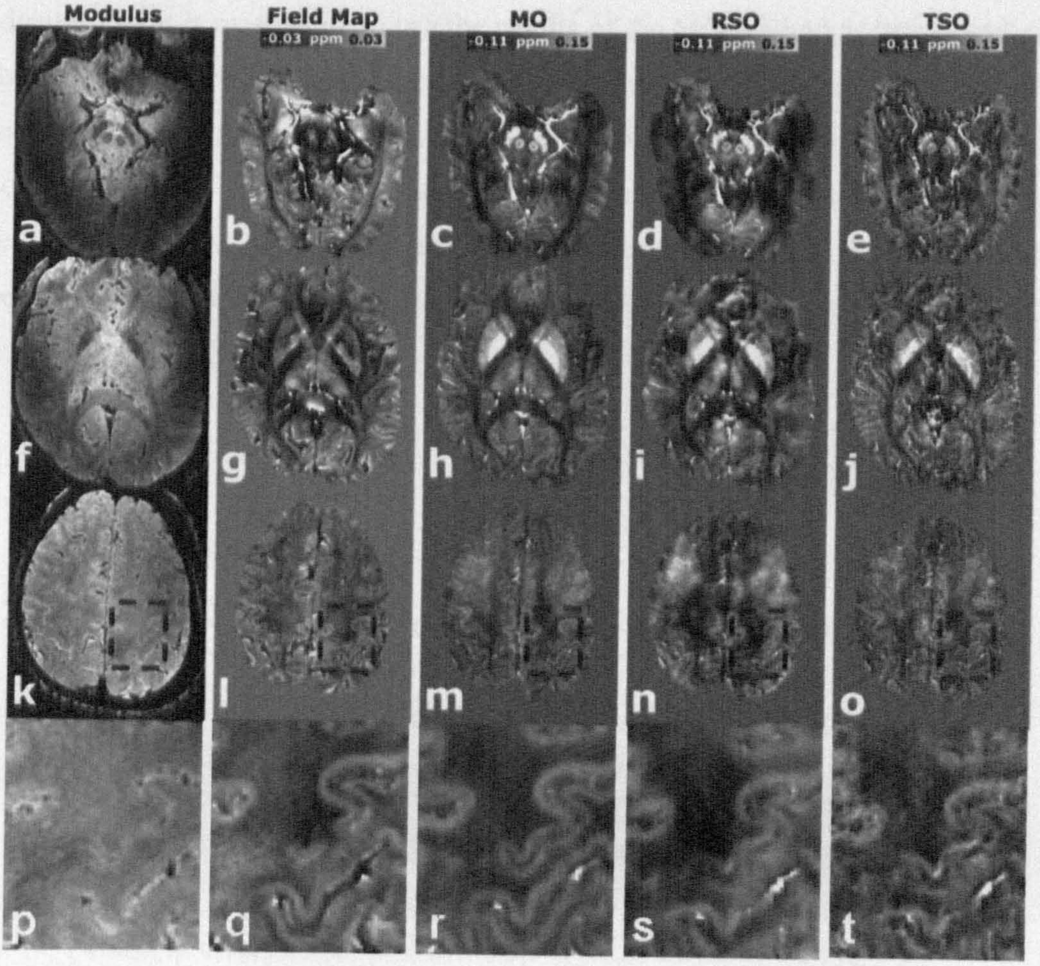

Figure 7.6 ***Transverse modulus images, fieldmap data, and susceptibility maps for a single subject at three levels in the brain. (a, f and k) Modulus data. (b, g and l) Field map data. (c, h and m) Susceptibility maps calculated using MO method. (d, i and n) Susceptibility maps calculated using RSO method. (e, j and o) Susceptibility maps calculated using TSO method. (p, q, r, s, and t) Zoomed in GM/WM region from dashed box shown in k, l, m, n, and o.***

The RSO method shows similar large scale detail to the MO method, with the GP, SN, and large veins having high, positive $\Delta\chi$ values relative to the surrounding tissue. However, the finer, more subtle detail present in the MO data, such as the

GM/WM contrast in the mid and upper brain regions, is attenuated. This attenuation is highlighted in the zoomed in GM/WM regions shown in Fig. 7.6p-t. The χ-map calculated using the TSO method shows increased artefacts relative to the other methods, particularly around blood vessels. Analysis of the phantom experiments indicates that it is reasonable to use the results of the MO method as benchmark data when assessing the other susceptibility mapping methods. In Figure 7.7 we therefore plotted the susceptibility differences measured in the different brain regions using each of the three mapping methods against the results produced using the MO method. For comparison, differences measured directly from the field map are also shown. In each case a linear fit was carried out and is depicted as a dashed line on the plot.

	MO $\Delta\chi \pm$ SD (ppm)	RSO $\Delta\chi \pm$ SD (ppm)	TSO $\Delta\chi \pm$ SD (ppm)	Field Map $\Delta B \pm$ SD (ppm)
SN	0.15 ± 0.02	0.11 ± 0.02	0.11 ± 0.03	0.009 ± 0.008
RN	0.11 ± 0.03	0.07 ± 0.02	0.08 ± 0.03	0.007 ± 0.003
IC	-0.035 ± 0.005	-0.04 ± 0.02	-0.04 ± 0.01	-0.022 ± 0.001
GP	0.19 ± 0.01	0.182 ± 0.006	0.15 ± 0.02	0.010 ± 0.003
PU	0.08 ± 0.02	0.07 ± 0.01	0.067 ± 0.009	0.006 ± 0.002
CN	0.07 ± 0.02	0.07 ± 0.02	0.07 ± 0.02	0.011 ± 0.002
GM$_{PPL}$	0.044 ± 0.008	0.05 ± 0.01	0.05 ± 0.01	0.013 ± 0.001
GM$_{APL}$	0.04 ± 0.02	0.04 ± 0.01	0.04 ± 0.01	0.013 ± 0.003
GM$_{FL}$	0.02 ± 0.01	0.02 ± 0.01	0.03 ± 0.01	0.009 ± 0.001

Table 7.2 Measured susceptibility differences averaged over the five subjects using each mapping method, for each of the different brain regions. The measured field differences for each ROI are also listed for comparison.

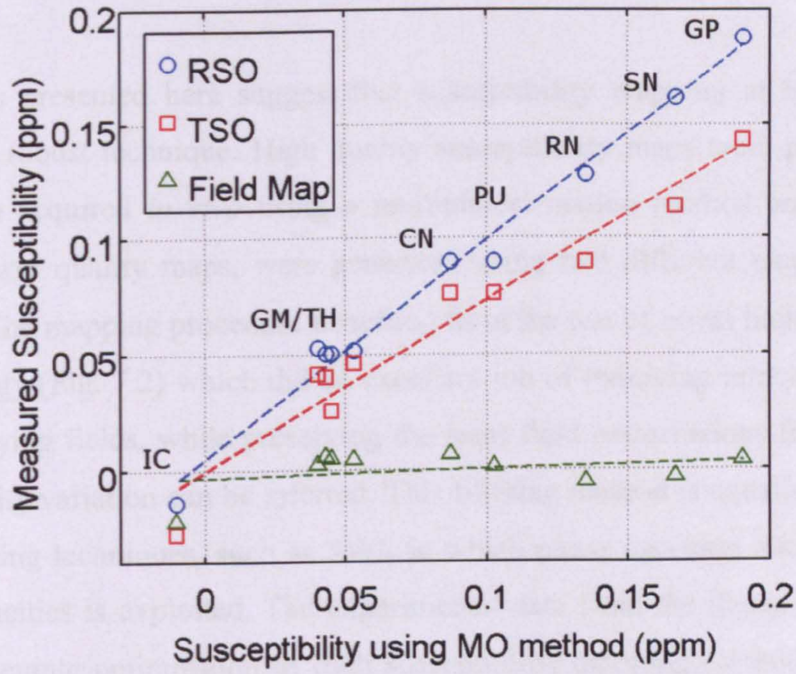

***Figure 7.7** Δχ values measured in each brain region using the RSO (blue), and TSO (red) methods plotted against the results for the MO method. For comparison the measured field differences are plotted against the MO results (green). The dashed lines represent least-squares linear fits.*

Table 7.3 details the linear fits, along with the correlation coefficient produced by comparing the RSO, TSO, and field map values to the results of the MO method. The RSO method yielded average susceptibility offsets in good agreement with the MO results. The TSO method however, underestimated the susceptibility values compared to the MO method.

	Linear Fit to MO (ppm)	Correlation to MO data
RSO	$0.8645 \times \Delta\chi_{MO} - 0.0070$	0.97
TSO	$0.7602 \times \Delta\chi_{MO} + 0.0054$	0.98
Field Map	$0.0841 \times \Delta\chi_{MO} - 0.0000$	0.53

***Table 7.3** Calculated linear fits and correlation coefficients of RSO, and TSO methods to the MO method. For comparison, the field map fit and correlation are also included.*

7.2.3 Discussion

The results presented here suggest that susceptibility mapping at high field is a viable and robust technique. High quality susceptibility maps were produced from image data acquired *in vivo* using a multiple-orientation method and similar, but slightly lower quality maps, were generated using two different single-orientation methods. The mapping procedure benefited from the use of novel high-pass filtering methodology (Fig. 7.2) which did an excellent job of removing remotely generated, slowly varying fields, while preserving the local field perturbations from which the susceptibility variation can be inferred. This filtering method is equally applicable to other imaging techniques, such as SWI, in which phase variation due to local field inhomogeneities is exploited. The experimental data from the doped agar phantom allowed accurate optimisation of each susceptibility mapping method to be carried out. For the MO method, the phantom results showed that an accurate χ-map could be created from data measured at four different orientations produced by small rotations about two orthogonal axes (Fig. 7.5c). For the RSO method, the phantom data allowed the correct choice of regularisation parameters to be made (Fig. 7.5e and f). Similarly, the phantom data allowed an acceptable k-space threshold to be chosen for the TSO method that gave the best compromise between contrast and noise (Fig. 7.5d).

Comparing the results produced from the phantom using the different methods, it is clear the MO method yielded the highest quality susceptibility map. This is free of noise-related artefacts and shows susceptibility values which are in good agreement with those expected from the known concentrations of contrast agent (Table 7.1). The TSO method slightly underestimated the susceptibility values and produced maps showing "streaking" artefacts, but which still contain readily interpretable structural information about the underlying susceptibility distribution. The RSO method, while not achieving quite the same quality of χ-map as the MO method, outperformed the TSO method in reducing artefacts and producing accurate average susceptibility values. This is a consequence of the RSO method's utilisation of the structural information present in the modulus data.

The in vivo experiments showed that high quality whole-brain susceptibility mapping at 7 T is feasible, and allowed further characterisation of the strengths and weaknesses of the different mapping methods in the context of human brain imaging. The susceptibility maps created by the MO method show exquisite detail, with particularly high positive $\Delta\chi$ values in the GP, PU, CN, SN, and RN regions, as well as a negative offset in the IC, as shown in Fig.7.6c, h and m and in Table 7.2. The rich structural detail and high contrast to noise present in the field map are improved upon, in the χ-map generated using the MO method. This is particularly emphasised in the upper brain slice, shown in Fig. 7.6m and the zoomed in region in Fig. 7.6r, where the χ-map shows clear boundaries between GM and WM in the parietal lobe. In contrast, the field map of the same region, shown in Fig. 7.6p, displays varying field shifts at the GM/WM interfaces which make boundaries harder to discern relative to those in the χ-map. Another impressive property of the χ-map produced using the MO method is the visualisation of veins. The characteristic dipole artefacts that occur in and around large blood vessels [13] in field maps are completely eliminated in the susceptibility map which shows high, positive, and localised $\Delta\chi$-offsets in the veins. This effect is particularly clear in the large vessels close to the SN/RN region in the lower brain slices shown in Fig. 7.6b and c. The susceptibility maps calculated using the RSO method display similar large scale structure to the MO χ-map with the GP and SN regions particularly visible. However, finer more subtle detail such as GM/WM boundaries in the cortices appear less well defined. The behaviour of the RSO method can be explained to some extent by considering the definition of compartments in the associated modulus data (Fig. 7.6a, f and k). Since the regularisation algorithm uses spatial priors based on the gradient of the modulus data, structures that are clearly defined in the modulus data, such as the GP shown in Fig. 7.6f and the cylindrical compartments of the phantom depicted in Fig. 7.5a, are likely to be better represented in the final χ-map, than less clearly defined structures, such as the GM and WM in the upper brain sections (Fig. 7.6k).

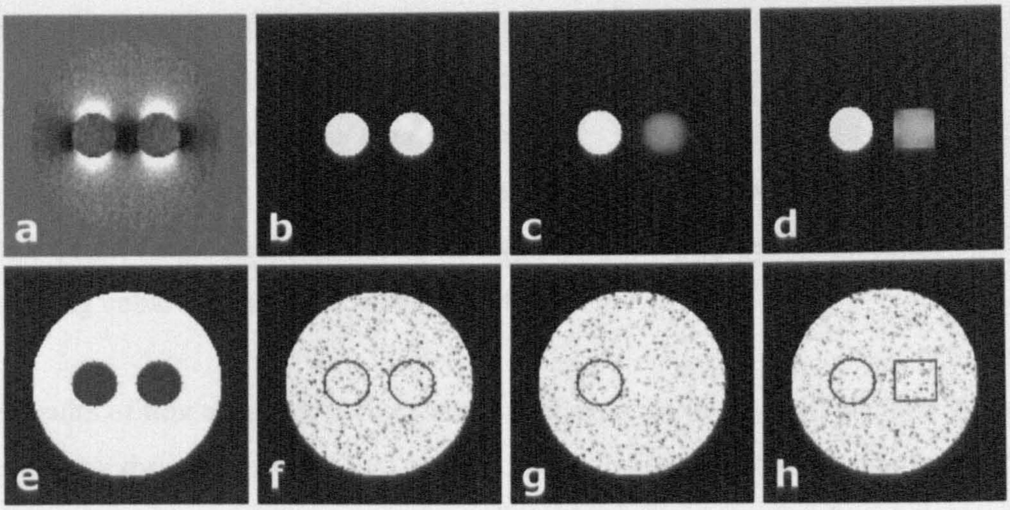

<u>Figure 7.8</u> Results of simulations demonstrating the dependence of the RSO method on the choice of spatial priors. (a) Simulated field map. (e) Simulated modulus data. (f) Composite spatial prior based on (e). (b) χ-map calculated using (a) and (f). (g) Spatial prior with one sphere removed from the modulus data. (c) χ-map calculated using (a) and (g). (h) Spatial prior based on modulus data with one sphere replaced with a cube. (d) χ-map calculated using (a) and (h).

To demonstrate the dependence of the RSO method on the choice of spatial priors, some simple simulations were carried out, the results of which are shown in Fig. 7.8. A digital phantom containing two small spheres of 12 voxels in radius were set inside a larger sphere of radius 50 voxels, itself set inside a 128^3 matrix of zeros. The small spheres were given susceptibly values of 1 ppm relative to a value of zero for the rest of the phantom. A field map was simulated using the Fourier method (Chapter 3) and masked using the larger sphere and Gaussian noise with a standard deviation of 0.02 ppm was added (Fig. 7.8a). Modulus data were also created by giving the small spheres signal magnitudes of 0.2, and the larger sphere a magnitude of 1, Gaussian noise with standard deviation 0.01 was then added (Fig. 7.8e). The RSO method was then used to calculate a χ-map (Fig. 7.8b) utilising edge information from the modulus data to form the spatial priors (Fig. 7f). As would be expected from such high quality spatial priors, the RSO method yields an excellent χ-map, retrieving accurate susceptibility values within the spheres. If one of the spheres is removed from the modulus data, the spatial prior (Fig. 7.8g) contains no edge information and the RSO method yields a smoothed susceptibility map in this region (Fig. 7.8c). This is analogous to the low contrast between GM and WM in the cortex in the in vivo modulus data sets (see Fig. 7.6k). We can also add erroneous modulus information by changing one of the spheres to a cube. Use of this incorrect spatial prior (Fig. 7.8h), yields a susceptibility map (Fig. 7.8d) reflecting the underlying cubic region in the modulus data.

The results of this experiment suggest the performance of the RSO method is highly sensitive to the choice of spatial priors. Accordingly, the RSO method should be strongly dependent on the imaging parameters used to acquire the modulus data, such as TE, TR and flip angle. Investigating this dependence on scanning parameter selection was beyond the scope of this work, but forms an important area for future study. It should also be noted that there are no restrictions on the image contrast that is used to generate the spatial priors. Here, the modulus signal was used as it comes free with the phase information, but other image data could also easily be used (e.g. T_1- or T_2-weighted images). Recently, Yao et al. [14] showed that R_2* measurements at high field are highly correlated with iron content, making R_2* -maps a potentially rich source of susceptibility-based structural information for driving RSO calculations.

Susceptibility maps calculated using the TSO method showed similar bulk structure to the MO χ-maps, but also displayed "streaking" artefacts especially around areas of the brain with large $\Delta\chi$-offsets, such as veins (Fig. 7.6e, j and o). Veins which appear clearly with high, positive $\Delta\chi$-offsets in the χ-maps produced using the MO and RSO methods are harder to visualise in the TSO-generated map. The artefacts around veins most likely result from the over-simplified treatment of noise in the TSO method. Both the MO and RSO methods employ weighting matrices to reduce the contribution of phase measurements in regions where the noise is high. In contrast, the TSO method does not use noise information and weights all phase measurements equally. Thus, in areas of high noise such as around veins, where the magnitude signal has significantly decayed due to the short T_2* of venous blood, the susceptibility maps calculated using the TSO method show severe artefacts. The *in vivo* susceptibility measurements shown in Table 7.2 and Fig. 7.7 indicate that the

TSO method underestimated $\Delta\chi$ by about 20% relative to the MO and RSO methods. This is most likely due to the unavoidable removal of *k*-space data that is implicit to the TSO method. The measured $\Delta\chi$ values for the TSO method in this study are higher than those found in recent work by Shmueli et al. [10]. However, the threshold parameter used here (0.06) was significantly lower than the equivalent truncation value used by Shmueli et al. (0.2), meaning that less *k*-space data were effectively nulled in our study. This comparison highlights the importance of keeping a fixed threshold parameter when carrying out studies of multiple subjects.

In this study, the single-orientation methods utilised a single data set which was acquired in about 3 min, while the MO method utilised four data sets which took a total of 12 min to acquire. Field maps acquired at a single orientation over 12 min would obviously have a higher signal to noise ratio (SNR) and use of such maps might provide a fairer comparison with the MO data. However, we note that just increasing the SNR of the field maps cannot compensate for the ill-posed nature of the deconvolution problem. This point was discussed in detail in Chapter 5 where it was shown that averaging over multiple scans at a single orientation yielded little gain in the quality of the final χ-map created using a threshold-based method.

Comparison of the field measurements to the $\Delta\chi$ values produced using the MO method, in particular the low correlation coefficient listed in Table 7.3, highlights the effects of the non-locality of the field perturbations arising from a given susceptibility distribution. This illustrates the fact that care must be taken when interpreting differences in phase or field measurements between brain regions. Although the correlation of field and susceptibility is lower than in other phase based studies [10, 15] the use of different filtering approaches and ROI definitions in the different studies make direct comparison difficult.

In general, the in vivo susceptibility maps produced in this work, showed large $\Delta\chi$ offsets and well resolved structural detail in the GP, SN, RN, IC, PU, and CN regardless of the mapping method utilised. This suggests that these brain regions have particularly large $\Delta\chi$ offsets relative to surrounding tissues. The positive offsets in the GP, SN, RN, PU, and CN are most likely due to the high concentration of non-heme iron known to exist in these brain areas [16, 17]. Figure 7.9 shows the average susceptibility values calculated from the MO method plotted against the estimated non-heme iron content based on the work of Hallgren and Sourander [16], for brain regions common to both studies. The excellent correlation ($r = 0.96$) between susceptibility and estimated iron content suggests that susceptibility differences in the human brain are closely linked to iron content [10]. The slope of the plot is found to be 0.75 ± 0.1 ppm per mg iron per g tissue agreeing within error with the value of 0.72 ppm per mg iron per g tissue that has previously been quoted [18]. The negative $\Delta\chi$-offset of the IC could be attributed to the effect of the large amount of myelin in the IC [19, 20]. As would be expected from Fig. 7.7, a plot of field rather than susceptibility against non-heme iron content produces a much poorer correlation ($r = 0.43$).

The sensitivity of susceptibility mapping to iron and myelin rich regions could be particularly beneficial in clinical studies. Recently, for example, field shifts based on phase data measured in the GP, PU, and CN, of patients with multiple sclerosis were shown to be significantly different to those measured in healthy subjects [21]. Susceptibility mapping could yield further insight into these differences by eliminating confounding effects of the non-local relationship between field measurements and the underlying $\Delta\chi$-offsets. In addition, changes in the levels of non-heme iron present in the SN are thought to be closely linked with the progression of Parkinson's disease [22]. High resolution susceptibility mapping could form a useful tool for accurately characterising these changes.

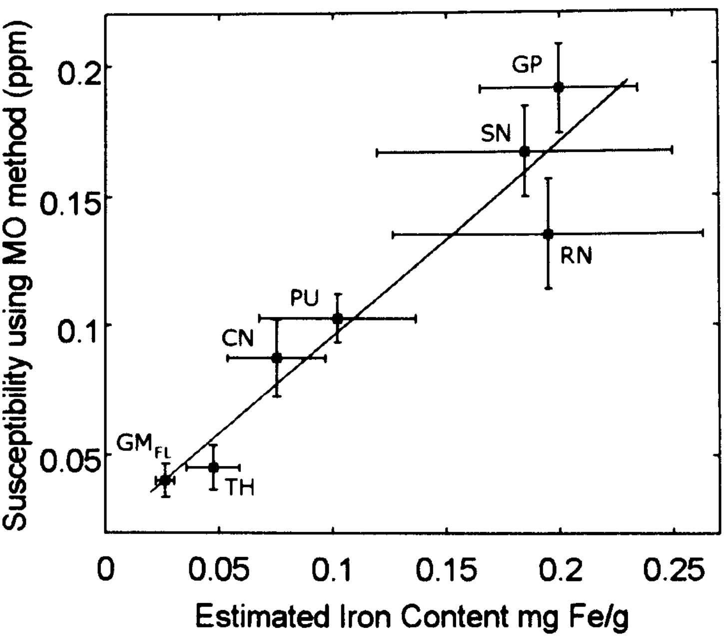

***Figure 7.9** Average susceptibility values calculated from the MO method plotted against estimated non-heme iron content [16] for GM_{FL}, TH, PU, CN, RN, SN, and GP brain regions.*

While this work focuses on 7 T data, Liu et al. [23] recently applied a method that is similar to the RSO method utilised here to data acquired at 1.5 T and measured susceptibility values of 0.18 and 0.13 ppm in the GP and SN, respectively. These results, which are in good agreement with values calculated in our study (see Table 7.2), suggest that despite the coarser spatial resolution available at lower field strengths, acceptable bulk susceptibility values can be measured in reasonably sized brain structures, potentially making susceptibility mapping a viable tool at 1.5 and 3T.

Finally, we speculate that the methodology used here to compare the different susceptibility mapping methods could also be beneficially utilised in studies involving longitudinal measurements and/or large numbers of subjects in which the MO method may not be suitable due to the need for subjects to execute head rotations. Instead, a small number of subjects could be scanned at multiple orientations with the desired FOV and voxel size, in preliminary experiments. χ-

Maps calculated by applying the MO method to these data could then be used to calibrate a single-orientation method, such as the RSO method. The calibration would involve choosing appropriate regularisation parameters, as well as the selection of scanning parameters such as TE, TR and flip angle which would yield modulus data showing the structural information required by the RSO method. The bulk of the subjects in the study could then be scanned at a single-orientation and χ-maps calculated using the calibrated RSO method.

7.2.4 Conclusions

Three susceptibility mapping methods have been optimised for application to whole-brain modulus and phase data acquired at 7 T. These are a multiple-orientation method, a regularised single-orientation method, and a threshold-based single-orientation method. Comparison of these methods showed that the multiple-orientation method yielded high quality susceptibility maps, out-performing the single-orientation methods. The threshold-based single-orientation approach was fast and simple to use, but underestimated susceptibility values and showed significant noise-related artefacts. The regularised method yielded contrast dependent on the choice of spatial priors, but demonstrated the potential to yield single-orientation susceptibility maps of a similar quality to those calculated using data acquired at multiple orientations to the field.

7.3 References

1. Westlake, J.R., *A Handbook of Numerical Matrix Inversion and Solution of Linear Equations* 1968, New York: JOHN WILEY & SONS.
2. Golub, G. and C. Reinsch, *Singular value decomposition and least squares solutions*. Numerische Mathematik, 1970. **14**(5): p. 403-420.
3. Penrose, R. and J.A. Todd, *On best approximate solutions of linear matrix equations*. Mathematical Proceedings of the Cambridge Philosophical Society, 1956. **52**(01): p. 17-19.

4. Hestenes, M.R. and E. Stiefel, *Methods of Conjugate Gradients for Solving Linear Systems.* Journal of Research of the National Bureau of Standards, 1952. **49**(6): p. 409.
5. Haacke, E.M., R.W. Brown, M.R. Thompson, and R. Venkatesan, *Magnetic Resonance Imaging: Physical Principles and Sequence Design.* 1999, New York: WILEY-LISS.
6. Liu, T., P. Spincemaille, L. de Rochefort, B. Kressler, and Y. Wang, *Calculation of Susceptibility Through Multiple Orientation Sampling (COSMOS): A Method for Conditioning the Inverse Problem From Measured Magnetic Field Map to Susceptibility Source Image in MRI.* Magnetic Resonance in Medicine, 2009. **61**(1): p. 196-204.
7. de Rochefort, L., T. Liu, B. Kressler, J. Liu, P. Spincemaille, V. Lebon, J. Wu, and Y. Wang, *Quantitative susceptibility map reconstruction from MR phase data using bayesian regularization: Validation and application to brain imaging.* Magnetic Resonance in Medicine, 2010. **63**(1): p. 194-206.
8. Wharton, S., A. Schäfer, and R. Bowtell, *Susceptibility mapping in the human brain using threshold based k-space division.* Magnetic Resonance in Medicine, 2010. **63**: p. 1292-1304.
9. Kressler, B., L. de Rochefort, T. Liu, P. Spincemaille, Q. Jiang, and Y. Wang, *Nonlinear Regularization for Per Voxel Estimation of Magnetic Susceptibility Distributions From MRI Field Maps.* IEEE Transactions on Medical Imaging. 2010. **29**(2): p. 273-281.
10. Shmueli, K., J.A. de Zwart, P. van Gelderen, T. Li, S.J. Dodd, and J.H. Duyn, *Magnetic susceptibility mapping of brain tissue in vivo using MRI phase data.* Magnetic Resonance in Medicine, 2009. **62**(6): p. 1510-1522.
11. Stephen, M.S., *Fast robust automated brain extraction.* Human Brain Mapping, 2002. **17**(3): p. 143-155.
12. Jenkinson, M. and S. Smith, *A global optimisation method for robust affine registration of brain images.* Medical Image Analysis, 2001. **5**(2): p. 143-156.
13. Deistung, A., A. Rauscher, J. Sedlacik, J. Stadler, S. Witoszynskyj, and J.R. Reichenbach, *Susceptibility Weighted Imaging at Ultra High Magnetic Field*

Strengths: Theoretical Considerations and Experimental Results. Magnetic Resonance In Medicine, 2008. **60**(5): p. 1155-1168.

14. Yao, B., T.-Q. Li, P.v. Gelderen, K. Shmueli, J.A. de Zwart, and J.H. Duyn, *Susceptibility contrast in high field MRI of human brain as a function of tissue iron content.* Neuroimage, 2009. **44**(4): p. 1259-66.
15. Xu, X., Q. Wang, and M. Zhang, *Age, gender, and hemispheric differences in iron deposition in the human brain: an in vivo MRI study.* Neuroimage, 2008. **40**(1): p. 35-42.
16. Hallgren, B. and P. Sourander, *THE EFFECT OF AGE ON THE NON-HAEMIN IRON IN THE HUMAN BRAIN.* Journal of Neurochemistry, 1958. **3**(1): p. 41-51.
17. Haacke, E.M., N.Y. Cheng, M.J. House, Q. Liu, J. Neelavalli, R.J. Ogg, A. Khan, M. Ayaz, W. Kirsch, and A. Obenaus, *Imaging iron stores in the brain using magnetic resonance imaging.* Magnetic Resonance Imaging, 2005. **23**(1): p. 1-25.
18. Duyn, J.H., P. van Gelderen, T.Q. Li, J.A. de Zwart, A.P. Koretsky, and M. Fukunaga, *High-field MRI of brain cortical substructure based on signal phase.* PNAS, 2007. **104**(28): p. 11796-11801.
19. Mori, S., S. Wakana, L.M. Nagae-Poetscher, and P.C.M. van Zijl, *MRI Atlas of Human White Matter.* AJNR Am J Neuroradiol, 2006. **27**(6): p. 1384-a-1385.
20. Fukunga, M., T.-Q. Li, P. van Gelderen, J.A. de Zwart, K. Shmueli, B. Yao, J. Lee, D. Maric, M.A. Aranova, G. Zhang, R.D. Leapman, J.F. Schenck, H. Merkle, and J.H. Duyn, *Layer-specific variation of iron content in cerebral cortex as a source of MRI contrast.* PNAS, 2010. **107**(8): p. 3834-3839.
21. Hammond, K.E., M. Metcalf, L. Carvajal, D.T. Okuda, R. Srinivasan, D. Vigneron, S.J. Nelson, and D. Pelletier, *Quantitative In Vivo Magnetic Resonance Imaging of Multiple Sclerosis at 7 Tesla with Sensitivity to Iron.* Annals of Neurology, 2008. **64**(6): p. 707-713.
22. Sofic, E., P. Riederer, H. Heinsen, H. Beckmann, G.P. Reynolds, G. Hebenstreit, and M.B.H. Youdim, *Increased iron (III) and total iron content in post mortem substantia nigra of parkinsonian brain.* Journal of Neural Transmission, 1988. **74**(3): p. 199-205.

23. Liu, T., L. de Rochefort, I. Khalidov, M. Prince, and Y. Wang, *Quantitative susceptibility mapping by regulating the field to source inverse problem with a sparse prior derived from the Maxwell Equation: validation and application to brain*, in *18th Annual Meeting of the ISMRM.* 2010: Stockholm.

CHAPTER 8

Conclusions

8.1 Summary

The primary focus of the work described in this thesis was to extract as much useful information as possible from phase images acquired using gradient-echo-based MRI techniques. The excellent contrast seen in these phase images is related to susceptibility differences between brain tissues. These susceptibility differences induce field perturbations in the main magnetic field of an MRI scanner causing a spatial variation of the NMR frequency. The field shifts due to a distribution of susceptibility, χ, scale with the main magnetic field, B_0. For this reason, phase images at ultra-high field strengths (7T) show particularly exquisite anatomical detail. The main aim of this work was to convert the contrast seen in these 'pretty pictures' into quantitative χ-maps.

Susceptibility mapping is hampered by two main sources of potential error in phase images. First, phase images are confounded by artefacts that must be removed before any attempt is made to form χ-maps. These artefacts include: (i) discrete, 2π, phase jumps; (ii) unwanted large-scale background field offsets. The second source of error is the non-local relationship between field perturbations, measured in phase images, and the underlying χ. It is hoped that the work presented here will convince the reader that, while these problems are severe, with careful processing and conditioning of the phase data, high quality χ-maps can be formed that contain useful quantitative information on tissue composition.

The early sections of this thesis described a recently proposed Fourier method for calculating the non-local field perturbations caused by a χ-distribution with an arbitrary geometry. The derivation of this simple Fourier relationship was a large step forward in the field of phase imaging as it allowed the simulation of high-resolution field maps in matter of minutes. The method was validated using χ-

distributions with simple geometries and known analytical solutions. After the steps for creating field maps from phase data were outlined, *in vivo* field maps were compared to simulations generated from digitised phantoms using the Fourier method. The results of these comparisons led to several important conclusions: (i) the level of high-pass filtering, used to remove unwanted fields, will strongly affect the contrast seen in phase images; (ii) χ-maps with relatively simple geometries can create complex field perturbations; (iii) changing the orientation of the sample relative to B_0 can dramatically alter phase contrast; (iv) care must be taken if direct phase measurements are used to infer local $\Delta\chi$ changes. The final conclusion has important implications for investigations involving phase imaging, such as studies utilising susceptibility weighted imaging (SWI) where phase data is multiplied directly into modulus data.

The simple Fourier relationship between field maps and χ-maps can be inverted to allow the calculation of susceptibility maps. However, the inversion is ill-posed and, left unconditioned, will amplify any noise present in the phase. In Chapter 5, a threshold based method for conditioning the inversion problem is presented. The method is shown to yield high quality susceptibility maps of the substantia nigra and red nucleus brain regions from data acquired at a single orientation. These regions were chosen as they are thought to be rich in paramagnetic, non-heme iron. As part of this work a novel filtering method was introduced to model and remove the dipolar field due to the sinuses. The advantages of combining data at multiple-orientations to B_0 were also investigated. The results of the study suggested that if the sample can only be rotated by small angles, as is the case for head imaging in MRI, rotations about two orthogonal axes were more effective than rotations about a single axis.

In Chapter 6, preliminary results of applying the threshold-based method to clinical data are presented. In these studies susceptibility mapping was used to probe iron deposition as a possible bio-marker for disease pathology. As part of this work, software was produced that enabled investigators to perform susceptibility mapping with no specialist knowledge. In the multiple-sclerosis (MS) study, higher $\Delta\chi$ values were measured in the globus pallidus, caudate nucleus, and putamen for MS versus controls. The globus pallidus, however, only showed increased levels in patients with more advanced MS, suggesting that iron deposition may occur at different stages of the disease in different regions of the brain. For the Parkinson's disease (PD) study, significantly higher $\Delta\chi$ values were measured in the pars compacta region of the substantia nigra for PD versus controls. The results of these studies suggest that susceptibility mapping could be a useful tool in measuring iron as a possible bio-marker for these neurodegenerative diseases.

Finally, the concept of iterative susceptibility mapping was introduced. The advantage of iterative methods, such as the conjugate gradient method algorithm used here, is that they enable the incorporation of *a priori* knowledge. Possible priors useful for susceptibility mapping include: (i) a weighting term giving the distribution of noise in the phase data; (ii) a mask of the region in which susceptibility is allowed to exist; (iii) edge information from the magnitude data. As part of this work, a novel iterative filtering method for removing background fields was also presented. An investigation was carried out to compare an iterative multiple-orientation (MO) method, an iterative regularised single-orientation (RSO) method, and the previously described single-orientation threshold (TSO) method. The three techniques were optimised for whole-brain phase and modulus data. The results showed that high quality whole brain χ-maps could be produced using the MO method, but slightly lower quality maps were formed using the RSO and TSO method. Of the single orientation methods, the RSO method dealt with noise and reproduced bulk $\Delta\chi$ offsets more robustly that the TSO method.

8.2 Future Work

Susceptibility mapping has many potentially important clinical applications. Further work should be carried out to fully explore how high quality χ-maps can be used to gain useful information about disease pathologies. Specifically, the diseases relevant for susceptibility mapping are likely to be those associated with changes in iron deposition. These diseases include multiple sclerosis, Parkinson's disease, and Alzheimer's disease. An important factor for these diseases is the time dependence of iron deposition as the disease progresses. Future work should therefore be focused on measuring susceptibility differences in single subjects at multiple time points.

Another direction for future work will be to investigate the validity of newly proposed alternatives to magnetic susceptibility as the dominant source of contrast in gradient echo phase images. Recently, three new contrast mechanisms have been proposed that could potentially contribute to phase contrast. In 2009, He and Yablonskiy [1] proposed that orientational order within the microstructure of tissues could yield a phase offset that is not simply proportional to the volume susceptibility. In WM in the human brain, long axons are grouped together to form fibre bundles and myelin producing cells called oligodendrocytes, which contain high concentrations of iron, tend to line up with these bundles [2]. This means that within an imaging voxel magnetisable material is potentially orientated along the fibres. Such large scale order, even if it is at the microscopic scale, can theoretically change the phase offset. Previous treatment of field maps assumed that the bulk susceptibility of tissues on the macroscopic scale was the only contributor, but microstructure can yield a field offset that is independent of the average susceptibility. Another source of phase contrast, proposed by Zhong et al. [3], is the exchange of magnetisation between water molecules and large macromolecules. This exchange results in an effective chemical shift that yields an offset in field maps produced from phase data. This contrast mechanism is completely independent of the magnetic susceptibility of tissues and rather reflects the relative concentrations of water and macromolecules. Most recently, Liu et al. [4] and Lee et al. [5] have shown that that magnetic susceptibility of white matter has a measurable anisotropy. This means that the susceptibility of some biological materials could change with the orientation of the sample relative to the magnetic field of the MRI scanner, producing an additional sensitivity of phase measurements to the orientation of structures. To accommodate this effect in susceptibility mapping, the magnetic susceptibility must be viewed as a tensor with component values that depend on the orientation of structures in the frame of reference in which measurements are made.

While these newly proposed contrast mechanisms may seem to confound the use of susceptibility mapping in analysing phase images, they could also allow the extraction of a plethora of new information related to microstructure and chemical exchange. It should be noted that the mechanisms described above are unlikely to significantly affect the use of susceptibility mapping in iron-rich, deep grey matter regions such as the globus pallidus and substantia nigra. This is because the iron is unlikely to show orientational order on the micrometer scale, and also because these regions are not thought to exhibit particularly strong exchange effects relative to surrounding tissues. The important brain areas for these new mechanisms are white matter regions containing axonal fibre bundles and grey matter/white matter cortical regions. The most important tool for separating the effects of each contrast mechanism is rotation of the sample relative to the main magnetic field.

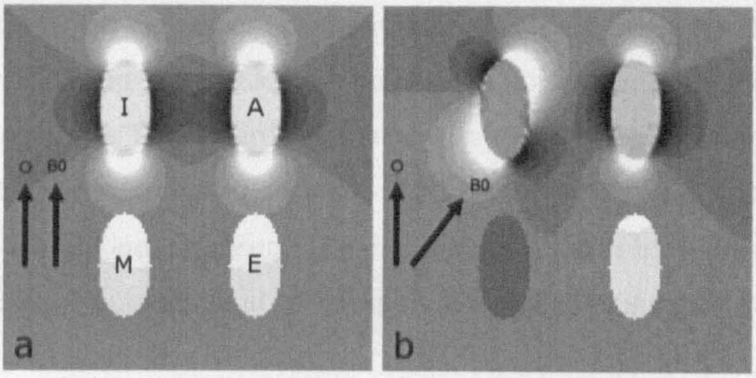

<u>Figure 8.1</u> Simulated phase offset due to ellipsoidal inclusions populated with isotropic susceptibility (I), anisotropic susceptibility (A), microstructure offset (M), exchange offset (E). For two B_0 orientations: (a) 0^o, (b) 45^o. The O axis shows the directions of order and anisotropy for M and E.

Figure 8.1 shows simulations of the phase offsets produced by four ellipsoids, each containing material that manifests one of the different contrast mechanisms, for two different orientations to B_0. Phase offsets due to exchange (E) are independent of orientation. The phase offset due to microstructural effects (M) varies as $\cos^2\theta$-1/3, where θ is the angle between B_0 and the axis characterising the orientation of the microstructure. The susceptibility-related offsets (I, A) are given by convolutions with dipole field kernels that vary with orientation. However, the anisotropic offset (A) is modulated by an additional term, $\sin(2\theta_T)$, where θ_T is the angle between the axis of anisotropy and B_0. The phase offsets produced by M and E, and by I and A, are fairly similar in Fig. 8.1a and it is only by rotating B_0 relative to the ellipsoids (Fig. 8.1b) that the differences become clear. To isolate each contribution it is likely that acquisitions at multiple angles to B_0 will be necessary [4].

8.3 Final Conclusions

Over the course of my PhD work the methodology of susceptibility mapping in MRI has been developed to a point where it is now possible to create high quality whole-brain susceptibility maps *in vivo*. I have shown in the earlier chapters of this thesis that care must be taken when carrying out studies based on gradient echo phase data due to the non-local relationship between phase contrast and susceptibility mapping. I then showed that the technique of susceptibility mapping can be used to invert this non-local relationship to yield quantitative information on the underlying composition of tissue. The linearity of phase with the strength of the main magnetic field makes the methods I have developed applicable at lower field strengths, such as those used in clinical environments. The preliminary results I have presented suggest that susceptibility mapping could be an important tool in using iron deposition as a biomarker in neurodegenerative diseases.

8.4 References

1. He, X. and D.A. Yablonskiy, *Biophysical mechanisms of phase contrast in gradient echo MRI.* PNAS, 2009. **106**(32): p. 13558-13563.
2. Todorich, B., J.M. Pasquini, C.I. Garcia, P.M. Paez, and J.R. Connor, *Oligodendrocytes and myelination: The role of iron.* Glia, 2009. **57**(5): p. 467-478.
3. Zhong, K., J. Leupold, D. von Elverfeldt, and O. Speck, *The molecular basis for gray and white matter contrast in phase imaging.* NeuroImage, 2008. **40**(4): p. 1561-1566.
4. Liu, C., *Susceptibility tensor imaging.* Magnetic Resonance in Medicine, 2010. **63**(6): p. 1471-1477.

5. Lee, J., K. Shmueli, M. Fukunga, P. van Gelderen, H. Merkle, A.C. Silva, and J.H. Duyn, *Sensitivity of MRI resonance frequency to the orientation of brain tissue microstructure.* PNAS, 2010. **107**(11): p. 5130-5135.